

HUNGARIAN ACADEMY OF SCIENCES
CENTRE FOR ENERGY RESEARCH

29-33 KONKOLY-THEGE MIKLÓS ÚT

1121 BUDAPEST, HUNGARY

PROGRESS REPORT
ON RESEARCH ACTIVITIES
IN 2019

DEAR READER,

Welcome to the 2019 yearbook published by the MTA Centre for Energy Research (MTA EK), summarizing the scientific results of its three institutions and highlights in 2019. This booklet provides a summary of the research personals and equipment of departments and research groups working in the Centre.

The year 2019 was an unusual one in terms of awarded grants and new opportunities. The Centre and the whole Research network of MTA were working on the transition of reorganization into a new research network origination. According to the decision of the Hungarian Government the new network had to become independent from the Hungarian Academy of Sciences. The new organization was named after the great Hungarian physicist Loránd Eötvös. The Loránd Eötvös Research Network took over the research network from the MTA on the 1st of September 2019. Information on this new organization can be found at the URL: <http://www.elkh.org/>. The transition was relatively smooth, but gave very busy period to the involved leaders and personals of the Centre.

Three important, research works were selected for highlights this year. One of them is from the field of insecticides contaminated water cleaning and energy saving. Our researchers managed to show that the from the advanced oxidation methods the high energy radiation treatment is using more than a hundred times less energy than the Ultra Violet or Vacuum Ultra Violet + TiO₂ catalyst treatment for the same insecticides contaminated water.

The other work described a new magnetic method to study nuclear reactor steels' rigidity changes due to high irradiation field. The researchers managed to correlate the magnetic parameter value of the reactor steels to the usual Charp test results, which determine the rigidity of the steels. This new method is non-destructive thus the same sample can be used for several other tests.

The three-year long Zirconium Materials Science Studies project was successfully completed in 2019. Cladding materials of nuclear fuel, including accident tolerant fuel were tested in different experimental facilities under extreme conditions and their microstructure was investigated by a large number of examination techniques. The experimental database, containing several thousands of samples was applied in the development and validation of numerical models used for the simulation of fuel behavior in nuclear power plants.

The BNC researchers continued their work in various EU funded projects such as IPERION CH, E-RIHS, BrightnESS and CHANDA and all of them were ended this year. This year we had to work on the proposals to renew them for another period. The CHANDA project has been replaced with the H2020 ARIAL project, which instead of research support concentrates on teaching people interested in nuclear data research. The Centre is involved in the European Spallation Source project aimed at constructing the new neutron source facility in Sweden. Member countries were invited to contribute on an *in-kind* basis, and the expenditures of the participating Institutions in Hungary are compensated from the membership fee of the country. The work in the ESS project continued on designing neutron detectors and their shielding.

We celebrated the 60th anniversary of the Budapest Research Reactor in a one-day event in the prestigious building of the Hungarian Academy of Sciences. For this occasion, a brochure was printed to summarise the most important achievements of the past 60 years in the neutron science.

Ákos Horváth
Director General
horvath.akos@energia.mta.hu

CONTENTS

Dear Reader.....	2
Contents.....	3
Mission Statement of MTA Centre for Energy Research.....	7
Scientific Advisory Board of the MTA Centre for Energy Research.....	7
Organization Structure of the MTA Centre for Energy Research.....	8
Quality Management.....	9
Budapest Research Reactor.....	10
Environmental Protection Service.....	12
I. EU, NKFIH OR GOVERNMENT SUPPORTED RESEARCH ACTIVITIES.....	13
The ALLEGRO Project and the Operational States.....	14
Neutron Irradiation of Zirconium Alloys in the Budapest Research Reactor.....	15
Corrosion of Zirconium Cladding in Autoclave.....	16
Testing of Accident Tolerant Fuel Cladding at High Temperature.....	17
High Pressure Steam Oxidation of Zirconium Cladding.....	18
Oxidation Kinetics Measurements of Zirconium Alloys in Air Atmospheres.....	19
Investigations of Phenomena During High Temperature Ballooning and Burst of Nuclear Fuel Claddings.....	20
Simulation of Station Blackout Transient in the CODEX Facility.....	21
Normal Operating and Design Basis Accident Conditions in the TRANSURANUS Fuel Performance Code.....	22
Improvements of the Code FUROM in the Framework of the Zirconium Material Research Project.....	24
Identification of Summertime Short-Term Particulate Matter Pollution Episodes in Budapest.....	25
Strategic Research Group for the Challenges of Renewable Energy Based Systems.....	26
CORTEX – Core Monitoring Techniques and Experimental Validation and Demonstration.....	27
CONCERT-European Joint Programme for the Integration of Radiation Protection Research.....	28
Medium Scale Experiment for VVER-440 Nozzle Mock-Up.....	29
Non-destructive Evaluation System for the Inspection of Operation-Induced Material Degradation in Nuclear Power Plants – NOMAD.....	30
Radiological Characterization in View of Nuclear Reactor Decommissioning: On-site Benchmark of a Biological Shield.....	31
Uncertainties of Atmospheric Dispersion Calculations.....	32
Integrated Platform for the European Research Infrastructure on Culture Heritage (IPERION CH).....	34
H2020 European Union Project: INnovative CLUster on raDIological and Nuclear emerGencies (INCLUDING).....	35
Science & Innovation with Neutrons in Europe in 2020.....	36
Performance Evaluation of the Boron Coated Straws Detector with Geant4.....	37
Reduction of Scattered Neutron Background in Boron-Carbide Converter Based Neutron Detector.....	38
Comparison of Measured and Simulated Neutron Activation of Concrete Samples.....	39
Neutronic Design of the First Built Experimental Cave for the European Spallation Source.....	40
Concrete Activation Study for the European Spallation Source.....	41
Full Simulation of Detector Performance of Neutron Instrumentation at ESS.....	42
II. RESEARCH AND DEVELOPMENT RELATED TO NUCLEAR POWER PLANTS.....	43
Activities of EK as Main Consultant of Paks NPP.....	44
Release of the FUROM 2.2 Code Version.....	45
SURET Calculation of a New Type of Fuel Assembly Having Spacer Grid with Mixing Vane.....	46
Working Fluids.....	47

Numerical Modelling of Fuel Rod Behaviour.....	48
Numerical Simulation of Mandrel Tests of Zirconium Cladding Samples with Different Hydrogen Contents	49
Solution of the VVER-1000 Full Core Calculation Benchmark by the KARATE Code System.....	50
The Effect of Chemical Composition of Concrete on its Long-term Performance in An Irradiated Environment (V4-Korea RADCON).....	51
Flow Redistribution in Unequally Heated Parallel Channels.....	53
Extension, Application and Validation of the In House KIKO3DMG Nodal Code for Fast Reactor Core Analyses.....	54
III. NUCLEAR SECURITY, DOSIMETRY AND SPACE RESEARCH.....	55
Nuclear Forensic Analysis of Sealed Radioactive Sources	56
Source-Activity Measurements with Scintillation Crystal Detectors.....	57
IAEA Coordinated Research Project: Applying Nuclear Forensics Science to Respond to a Nuclear Security Event.....	58
Review and Assess of Radiation Protection in Nuclear Installations - Training Course at the Centre For Energy Research.....	59
Assessment of Capacity for Gamma Spectrometric Measurement of Environmental Samples.....	60
Determination of Uncertainties and Characteristic Limits of the Environmental Radiation Measurements.....	61
Determination of Uncertainties in the Estimation of Internal Exposure.....	62
Effects of Inhaled Radon Progeny Modelled at the Tissue Level.....	64
Environmental Radiation Monitoring with Detectors in a New Generation Scalable Network - DoziNet.....	65
Numerical Modelling of Individual Radiosensitivity.....	66
Characterization of Radiation Exposure and its Biological Effects at Different Spatial Scales.....	67
Environmental and Radiation Transport Modelling of Space Radiation Telescopes - PhD Progress Report	68
Space Dosimetry for Human Spaceflight	69
Dose Distribution Inside the International Space Station-3D / DOSIS 3D	70
Research & Development Activities in Space Weather	71
Upgrade of the Space Research Test Laboratory	73
IV. ENERGY AND ENVIRONMENTAL STUDIES.....	74
Utilization of Cu and Fe Complexes in Water Oxidation.....	75
Methane Dry Reforming over Novel Bimetallic Catalysts.....	76
Bimetallic Gold Catalysts in Aerobic Selective Oxidation of Alcohols.....	77
Catalytic Properties of 2D MoSSe During Electrolysis of Water	78
Preventing the Development of Antibiotic Resistance in Wastewater Matrices by High Energy Irradiation	79
High Energy Ionizing Radiation Induced Degradation of Amodiaquine in Dilute Aqueous Solution: Radical Reactions and Kinetics.....	80
Optimizing the Use of Renewable Energy Sources in the Energy Mix of Hungary	81
Biogenic Carbon Content Determination of Catalytically Converted Biomass.....	83
Electric Power Grid Failures	84
Modelling Development of Power System Infrastructure	85
Study of Public Energy Preferences and the Valuation of Criteria for the Utilization of Multi-criteria Decision Weighted Factors.....	86
Atomic Structure and Chemical Durability of U-Containing Glass Composites.....	87
Characterization of Iron Adsorption on Clay Minerals.....	88
Preparation and Characterization of Nanoparticle Systems Considered for Plant Nutrition Experiments.....	89
Exploring the Impact of Nanoparticles on Productivity, Metal Uptake and Iron Metabolism of Plants.....	90
Structure of Oxy-Halide Compositions for Solid State Batteries.....	91
V. NUCLEAR ANALYSIS AND CHEMISTRY	92
Rapid Separation of Actinides from Soil and Sediment Matrices by Extraction Chromatography	93
Applications of Nuclear Analytical Techniques.....	94

Development of Nuclear Analytical Techniques, Nuclear Data Measurements & Dissemination Activities.....	96
Phase Analysis and Activity of Iron and Gold Particles Probed by Mössbauer Spectroscopy and Other Methods.....	97
Nanostructure Research by Small Angle Neutron Scattering	98
Radiography and Tomography at BRR	99
Non-destructive, Spatially-resolved Element Analysis of Structured Samples (OTKA K124068)	100
IAEA Coordinated Research Project on Photonuclear Data and Photon Strength Functions.....	101
VI. RESEARCH AND DEVELOPMENT IN INSTITUTE OF TECHNICAL PHYSICS AND MATERIAL SCIENCES.....	102
Non-destructive Evaluation (NDE) System for the Inspection of Operation-induced Material Degradation in Nuclear Power Plants.....	103
Transition Metal Chalcogenide Single Layers as an Active Platform for Single-atom Catalysis.....	105
Visible-frequency Graphene Plasmons in Extremely Nanocorrugated Graphene Sheets	107
Ultra-flat Twisted Superlattices in 2D Heterostructures	109
Anisotropic Strain Effects in Small-twist-angle Graphene on Graphite.....	111
Optical Detection of Vapour Mixtures Using Structurally Coloured Butterfly and Moth Wings.....	113
Reproducible Phenotype Alteration due to Prolonged Cooling of the Pupae of <i>Polyommatus icarus</i> Butterflies	115
Combinatorial Investigation of WO ₃ -MoO ₃ Mixed Layers by Spectroscopic Ellipsometry Using Different Optical Models ..	117
Sensing Layer for Ni detection in Water Created by Immobilization of Bio-engineered Flagellar Nanotubes on Gold Surfaces	119
Optical Properties of Hydrogenated Amorphous Si _{1-x} Ge _x for the Entire Range of Compositions	121
Determination of Complex Dielectric Function of Ion-implanted Amorphous Germanium by Spectroscopic Ellipsometry ..	122
Optical Spectroscopy Studies on Nanoparticles.....	123
Robust Contact Angle Determination for Sessile Drops Without Apex.....	125
Contact Angle Determination on Super Hydrophilic Surfaces by Using Capillary Bridges.....	127
Makyoh Topography	129
Optimization of Co-sputtered Cr _x Al _{1-x} N Thin Films for Piezoelectric MEMS Devices.....	130
Energy Harvester Powered Vibration Analyser.....	131
Wireless Environmental Radiation Monitoring System – DOZINET.....	133
Bicycle Traffic Monitoring System	134
Nanometer-scale Resistive Switches	135
Optimization of VO ₂ Thin Films for Memristors.....	136
Optimization of Superconducting Microwave Resonators and High Spatial Resolution Bottom Gates.....	137
Atomic Layer Deposition and Characterisation of Ga ₂ O ₃ Films	139
Radiative Damping of Surface Plasmon Resonance in Gold Nanoparticles: the Influence of Shape, Size, and Substrate Material.....	141
Investigation of Atomic or Molecular Processes Induced by Ultrashort Laser and/or Electron Pulses.....	142
Low Power Consumption-type Nano-sensors for Gas Detection in Harsh Environment.....	143
Design and Development of a 3D Flex-to-Rigid Compatible Force Sensor	145
Manufacturing Implantable Microelectrode Arrays.....	147
Polymer Based Autonomous Microfluidic Systems for Medical Diagnostics	149
Microfluidic Sample Preparation System for Rapid Urine Bacteria Analysis	150
Microfluidically Integrated SERS Active Cell Trap Array for Analysis Red Blood Cells.....	153
Modelling and Analysing of Fluid Dynamic Phenomena in Two-phase Microfluidic Systems.....	155
Near InfraRed LED Devices for Spectroscopic Applications: Development and Small Scale Production of Near Infrared LEDs and LED Based Devices	157
Adhesion Force Measurements on Functionalized Microbeads: An In-depth Comparison of Computer Controlled Micropipette and Fluidic Force Microscopy	159

Spring Constant and Sensitivity Calibration of FluidFM Micropipette Cantilevers for Force Spectroscopy Measurements...	160
A Practical Review on the Measurement Tools for Cellular Adhesion Force	161
Modelling of Label-free Optical Waveguide Biosensors with Surfaces Covered Partially by Vertically Homogeneous and Inhomogeneous Films	162
Biomimetic Dextran-Based Hydrogel Layers for Cell Micropatterning over Large Areas Using the FluidFM BOT Technology	163
Oxidization Increases the Binding of EGCG to Serum Albumin Revealed by Kinetic Data from Label-free Optical Biosensor with Reference Channel.....	164
In vitro SOD-like Activity of Mono- and di-copper Complexes with a Phosphonate Substituted SALAN-type Ligand	165
An Improved 96 Well Plate Format Lipid Quantification Assay for Standardisation of Experiments with Extracellular Vesicles.....	166
Graphene Added Multilayer Ceramic Sandwich (GMCS) Porous Structure Prepared by HIP and SPS Techniques.....	167
An Economic and Facile Method for Graphene Oxide Preparation from Graphite Powder	169
Examination of Novel Electrosprayed Biogenic Hydroxyapatite Coatings on Si ₃ N ₄ and Si ₃ N ₄ /MWCNT Ceramic Composite	171
Eco-friendly AlON Processing.....	172
Development of Multiwall Carbon Nanotube Reinforced Yttria Stabilized Zirconia Composites	174
Novel Method for the Production of SiC Micro and Nanopatterns.....	175
Investigation of the Nanostructural Background of Functionality in the Case of Biogenic and Biocompatible Mineral Apatite	176
Nanostructure Investigation of Mg-NbO-carbon Nanotube Composite Materials for Hydrogen Storage Applications	178
Structural and Electrical Properties of AlN Thin Films on GaN Substrates Grown by Plasma Enhanced-Atomic Layer Deposition	179
Structure, Mechanical Properties and Thermal Stability of WBC and MoBC Coatings.....	180
Influence of Bath Additives on the Thermal Stability of the Nanostructure and Hardness of Ni Films Processed by Electrodeposition.....	182
TEM Study of Nickel Silicides	183
A Micro-combinatorial Study of the Optical Properties of a-SiGe: H Towards a Database for Optoelectronics.....	184
Ceramic Dispersion Strengthened Sintered Stainless Steels After Thermal Ageing	186
Si(B) a Prospective Material for Quantum Electronic Applications.....	188
Bursts in Three-strategy Evolutionary Games on a Square Lattice.....	190
Seasonal Payoff Variations and the Evolution of Cooperation in Social Dilemmas.....	192
Critical Synchronization Dynamics of the Kuramoto Model on Connectome and Small World Graphs	194
ABBREVIATIONS	195

MISSION STATEMENT OF MTA CENTRE FOR ENERGY RESEARCH

- Research and development in the field of nuclear science and technology for facilitating the adoption and the safe use of nuclear technology in Hungary.
- To participate in international research effort aiming at the establishing a new generation of nuclear power plants and closing the fuel cycle.
- Maintaining and improving competence in nuclear science and technology, especially in the field of nuclear safety, security, health physics, nuclear and isotope chemistry.
- To guarantee the safe operation of Budapest Research Reactor (BRR), and to ensure the open access to the research facilities around the reactor operated by the Budapest Neutron Centre.
- Research activities to improve nuclear analytical and imaging methods and their applications for energy and materials science.
- Perform studies in the field of environmental physics related to energy generation, renewable energies, energy storage and their impact on public health, and on environmental safety.
- Research and development in the field of low carbon energy technologies and of energy saving in industrial technologies.
- Interdisciplinary research on complex functional materials and nanometer-scale structures, exploration of their physical, chemical, and biological principles, exploitation their operations in integrated micro- and nanosystems, and in the development of characterization techniques.
- Dissemination of the results in international programs, education and industrial research.

SCIENTIFIC ADVISORY BOARD OF THE MTA CENTRE FOR ENERGY RESEARCH

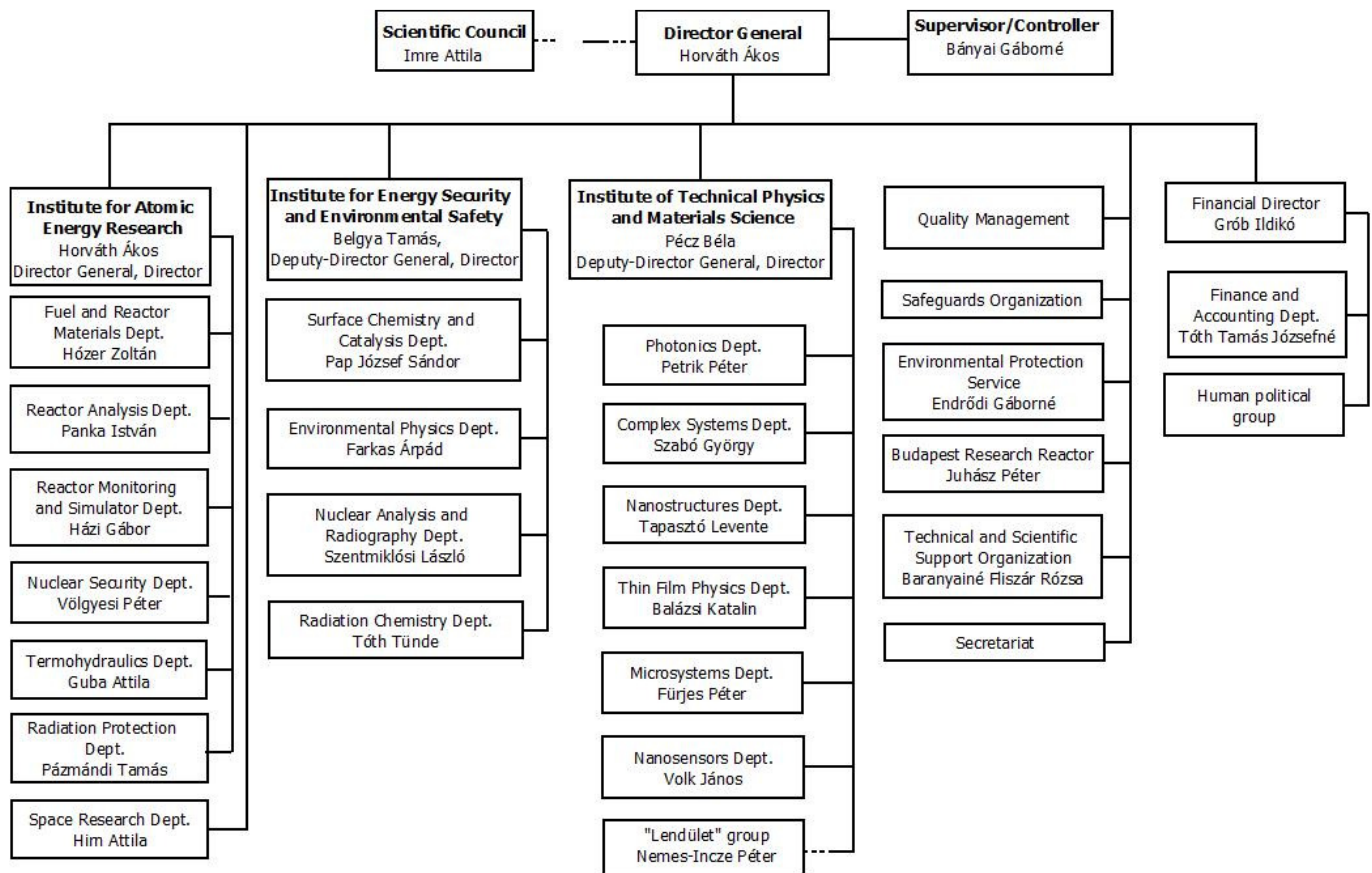
The Board consists of five Hungarian and two foreign leading scientists. The last meeting of the board took place in Budapest at MTE EK, on the 12th of June 2019. The results of year 2018 was presented and discussed.

In 2020, we do not have yet a Board meeting on the results of the year 2019. It is related to the still ongoing reorganization into the ELKH research network. The Board is also about to be reorganized.

Members of the Board in 2019:

- Prof. Dr. László Keviczky (Chair), MTA Institute for Computer Techniques and Automation
- Dr. Hervé Bernard, Deputy Chairman, Centre French Alternative Energies and Atomic Energy Commission (CEA)
- Dr. Maximilian Fleischer, Head of Department of Corporate Technology, Siemens AG
- Prof. Dr. Ádám Kiss, Eötvös Loránd University
- Dr. Zoltán Homonnay, Head of Laboratory of Nuclear Chemistry, Eötvös Loránd University
- Mr. István Hamvas, Director General, Paks Nuclear Power Plant
- Dr. József Rónaky, Scientific Advisor, Hungarian Atomic Energy Authority

ORGANIZATION STRUCTURE OF THE MTA CENTRE FOR ENERGY RESEARCH



QUALITY MANAGEMENT

In order to achieve the highest quality of research, development, design, condition monitoring and valuation, engineering, contracting and managing in design, production, implementation and inspection, the Research Centre’s quality management system has continuously been upgraded by the recommendations of ISO 9001 standard since 1994. Reviewing our QM system by integral audits and management reviews, evaluating improvement opportunities, maintaining project documentation, infrastructure, supporting communication, ensuring the competence of workers the management improves the Centre’s QM system. For the new organization structure, our Quality Policy has been renewed. Many new employees induced a need to upgrade our QM tuition practice. We organised the work and fire safety educations. Our QM system has been certified by Hungarian Standards Institution, IQNet, MVM Paks NPP and MVM Paks II NPP. The last one gives concrete certifications for special topics; up to now four of them were awarded, one of these documents is shown below.



Certifications by Hungarian Standards Institution, IQNet, and MVM Paks NPP and MVM Paks II

BUDAPEST RESEARCH REACTOR

One of the most important strategic large scale research facilities in Hungary is the Budapest Research Reactor (BRR). It serves the needs of an extensive and diverse scientific community by supporting R&D opportunities, helping innovation and providing a strong foundation for training and education.



Bird's eye view of the Budapest Research Reactor

The BRR is a VVR-type reactor that uses light water as moderator and cooling fluid. The power of the reactor is 10 MW provided from low enrichment uranium fuel, and its main purposes – as established during the feasibility/functionality study – are radioisotope production, production of thermal and cold neutron beams for research and applications in all areas, primarily development of new functional materials and neutron activation analysis.

The core is designed to have about 120 reactor-days per year, having time-spans of 10 days or 4 days in a week. We are committed to long-term safety and responsible operations, taking care of the wastes from the spent fuel coming from the reactor. Besides the temporary spent fuel storage pool, we also operate a long-term spent fuel storage building for the physical and environmental separation between the reactor and the spent fuel storage.

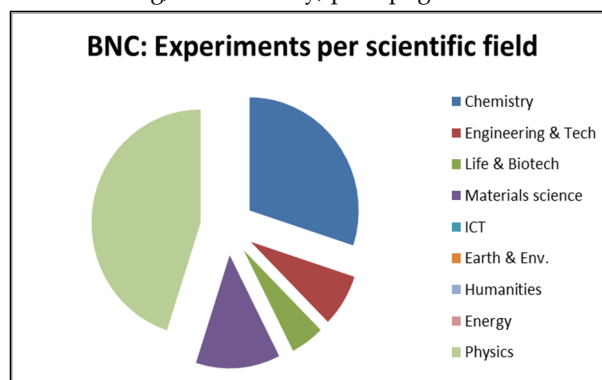


Top view of the research reactor



Layout of the BRR's facilities

The reactor hosts three kind of activities: the research activities utilizing neutron beams, production of radioisotopes for industrial and research purposes, and providing national and international training. We are proud of our innovative flagship research topics, which are carried out with a network of neutron beam stations, including beam-lines of thermal neutrons, experiments on powder and residual stress diffractometry, TOF neutron spectroscopy, radiography, biological irradiations and beam-lines of cold neutrons for experiments on small angle neutron scattering, reflectometry, prompt gamma activation analysis and nuclear data measurements. In accordance with recent worldwide trends, we are open to establishing new industrial relations, and supporting innovation. The BRR's experimental facilities are open for science based on excellence for researcher all over the world. We aim to increase our competence on special topics, to implement new technologies and develop new materials, to promote and exploit our R&D capacity at the national and regional/international level. During the past years the BRR hosted several international schools on various technical and research topics, special trainings in the field of reactor physics, reactor operation, nuclear measurement techniques, and safety and environmental issues. Typical distribution of research topics is shown in the figure to the right.



The BRR is used by groups of different scientific communities from medical, environmental, material, archaeological, nuclear sciences and industry, as well as several Hungarian Universities. Neutron beams are uniquely suited to study the structure and dynamics of materials at the atomic level. The Budapest Neutron Centre (BNC) coordinates the scientific utilization of the research reactor. Some of main research topics currently are:

- neutron scattering, used to examine changes of sample properties under different conditions such as variations in vacuum or pressure, high and low temperature, and magnetic field, modelling real-world conditions.
- using prompt and delayed neutron activation analysis, it is possible to measure the concentration of elements in ppm and ppb levels even for small samples. Atoms of a sample become radioactive by exposure to neutrons from the reactor. They decay by gamma-rays characteristic for each element that can be detected by suitable detectors
- neutron activation is also used to produce different radioisotopes, widely used in industry and medicine. For example, Y-90 microspheres to treat liver cancer are produced by bombarding Y-89 with neutrons, which capture those. Production of radioisotopes for different applications such as medicine, sterilization and industrial use.
- testing reactor materials; materials are subjected to intense neutron irradiation which cause radiation damage of their crystalline structure. For instance, some steels become brittle. Thus, the so-called high-entropy alloys resist embrittlement are to be used in nuclear reactors.
- applied research using neutron beams to produce images of material interior. Examples are the visualization of porosities in materials or changes of density inside the sample. Dynamic neutron radiography of cooling system of refrigerator or visualization of fuel burn in engine system of a car and tomography of different materials and items.

The BNC provides researchers with 15 neutron instruments; 13 instruments are installed directly on the horizontal beam ports of the reactor or to the thermal and cold neutron guides, while the other 2 are placed at the vertical irradiation channels. The instruments are supported by a variety of sample environments and data analysis and visualization capabilities.

The BNC provides access to the international neutron user community through a peer-review system. Local scientists assist researchers and industrial users to find the appropriate neutron techniques that meet their research needs. The various neutron scattering instruments in BNC cater to a large number of users from Europe and has grown in strength and stature over the years.

BNC is a member of the League of advanced European Neutron Sources and CERIC-ERIC, and partner in recent EU Framework Programme projects (NMI3-II, CHANDA, IPERION CH, SINE2020, ESS-BrighthESS, E-RIHS, H2020 ARIAL).

BNC is strongly committed to the training of future professionals inland and all over the world in co-operation with the International Atomic Energy Agency. We cooperate with Hungarian universities (Budapest University of Technology and Economics, Eötvös Loránd University (ELTE), Pannon University, ...), BNC accommodates students for laboratory practice for studying nuclear-based techniques. A specialized course was developed for geology students of the ELTE to introduce nuclear analytical techniques into their education. BNC organizes the Central European Training School on Neutron Scattering annually, to train young scientists for neutron physics and to attract new users. The school provides insight into neutron scattering, element analysis and imaging techniques and their applications to study the structure and dynamics of condensed matter.

The Budapest Research Reactor is open to the public. Members of the local communities and high school and university students visit us regularly and learn more about the amazing nuclear science possibilities available at BRR.



Research staff of the Budapest Research Reactor facilities in the operator's room.

ENVIRONMENTAL PROTECTION SERVICE

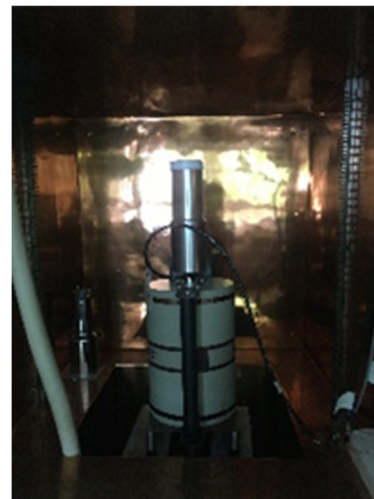
During the use of nuclear energy, radioactive contamination of the air and the aquatic environment must be checked. As part of the Centre for Energy Research, this task is performed by the Environmental Protection Service for the entire area of the KFKI Campus.



Environment controlling gamma probe

Our Environmental Policy, developed on the basis of the relevant legislation, specifies the characteristics and frequency of the examinations for various sample types. These tests include monitoring of airborne gamma radiation, examinations of atmospheric fallout, and gamma spectrometry and total-beta activity of air aerosol particles. By the use of our own resources and tenders, we intend to develop our equipment and instrumentation in order to perform our tasks with high reliability.

During the year, a high-sensitivity ORTEC Model GEM C40 detector with an efficiency of 40% was purchased, and we also expanded the capacity of the spectrum analyser. Thus, with the expansion, we can currently operate four detectors in parallel, so we can perform up to date long-term tests. By purchasing an uninterruptible power supply, we were able to eliminate measurement restarts caused by short-term power outages.



ORTEC Model GEM C40 detector

In addition to checking the external environment, we also monitor the external and internal radiation exposure of employees exposed to radiation. Besides official TLD tests, the external radiation exposure is checked with RADOS type thermoluminescent dosimeters used by the Service under its own authority. The system has been continuously improved, so besides the reading device, they also have a heating furnace and an irradiation device.



TLD Oven

To determine the internal radiation exposure, we have a measuring system designed for whole-body examination. We constantly develop this system to get more accurate and detailed results. To minimize background radiation, we use specially designed ventilation equipment.

A detailed report of the work of the Service carried out in 2019 is available on the EK website.



Whole body measuring point

*Gáborné, Endródi
Head of Service
endrodi.gaborne@energia.mta.hu*



I. EU, NKFIH OR GOVERNMENT SUPPORTED RESEARCH ACTIVITIES



THE ALLEGRO PROJECT AND THE OPERATIONAL STATES

János Gadó, János Sebestyén Jánosy, Gusztáv Mayer

Objective

Corresponding to the European initiative on launching research in the field of Generation IV nuclear reactors, the nuclear research institutes of the Visegrad 4 (V4G4) countries and the French CEA started a co-operation on the development of the Gas Cooled Fast Reactor demonstration reactor ALLEGRO in 2010. The ALLEGRO Project Preparatory Phase was launched by the consortium of the nuclear research institutes of the V4G4 countries in 2015. The final objective of the co-operation is to build up and operate this reactor but the construction has to be preceded by a long period of research and development related to various technological issues and the design of the reactor has to be prepared in several steps. ALLEGRO can start operation not earlier than in 2030.

As the Hungarian National Nuclear Research Program (NNKP) was completed in 2018, these works were financed by the budget of EK. Correspondingly, the contribution of EK to V4G4 efforts in 2019 was more modest than earlier.

Methods

Elaboration of ALLEGRO Design Specification is one of the most important works in the preparatory phase of the ALLEGRO Project (2015-2025). Until recently, the ALLEGRO safety analysis was concentrated on transients from the nominal plant state (100 % power). As the fundamental safety functions have to function in all operational states and for all accident scenarios, the scope of safety analysis has to be broadened. First the operational states of the ALLEGRO reactor have to be defined. This is an iterative process in ALLEGRO development, because the outcome of the results of the safety calculations at different operational states may indicate the need of further design changes.

Results

As a first step of the iterative process, 10 preliminary operational states were identified by EK taking into account the specific features of the gas cooled fast reactor technology which were discussed by the V4G4 Project Coordination Team. During the discussions several key design modification needs were identified. The most urgent topic is the design of the fuel handling and storage system. As part of the iterative process, an updated ALLEGRO Design Specification document was prepared which partially takes into account the new development directions of ALLEGRO [1].

Remaining work

The definition of the operational states has to be finalized and all the emerging needs for design changes have to be identified. The basic design features of the fuel handling and storage system have to be elaborated.

Related publication

[1] G. Mayer: *APP-DSR15-411-01 Rev8 Design Specifications Draft 10-20*, presented at the 14th V4G4 meeting

NEUTRON IRRADIATION OF ZIRCONIUM ALLOYS IN THE BUDAPEST RESEARCH REACTOR

Ildiko Szenthe, Márta Horváth, Ferenc Gillemot

Objective

The failure of the fuel elements' clad of fission reactors under normal and extreme operating conditions causes large economic loss for the plant owner. To avoid it requires to perform and evaluate a large number of simulations covering all operation and accidental situations in order to understand the expected behaviour of the fuel pipes. These simulations must be carried out with validated computer programs supported by experimental results. The effect of the different ageing mechanisms should be studied, including the neutron irradiation damage.

Methods

Within the framework of a research and development contract sponsored by the National Research, Development and Innovation Fund of Hungary (NKFIH), two types of cladding tubes' material had been selected (named E110 and E110G) to be studied. The project was entitled „Effect of material structure changes on zirconium alloys used in nuclear power plants on fuel element integrity and environmental load”. As part of the contract, Centre for Energy Research irradiated Zirconium alloys. Before the irradiation, different treatments were performed to simulate the environmental ageing effects during operation and accidental cases, to evaluate the combined effect of irradiation, heat treatment and corrosion.

The irradiation was performed in the BAGIRA (Budapest Advanced Gas-cooled Irradiation Rig with Aluminium structure) irradiation rig in the core of the BRR (Budapest Research Reactor). To fulfil the irradiation campaign the number, type and material of the samples had to be selected, prescribing the time and temperature of the irradiation together with the other parameters (e.g.: heat removal, coding, handling and storage of the active samples). The rig capacity is 6 pieces of 65*21*25 mm targets. The target must be designed in such a way that it can be easily dismantled under hot-cell conditions. To simulate the different burnout states, the samples were placed in axial positions to receive different fast neutron fluxes. After the pre-treatments the E110 and E110G samples were cleaned and filled into the targets. A dosimetry (Cu, Fe, Al-Co1 %, Nb) monitor package for measuring flux was included in each sample packet.

Results

The E110 and E110G cladding tube materials had been irradiated for 1752 hours. The recorded data taken at every 15 seconds are: date and time, temperatures on 6 levels, pressure of cooling gas, absorbed powers of 4 electric heaters, and alarm messages. From the recorded data the average temperatures are evaluated, and summarized in Table 1.

Table 1: Measured and averaged temperatures during the relevant irradiation cycles, at the thermocouples

Cycle	Hours	Hours	T1	T2	T3	T4	T5	T6
1.	26.09.2017-06.10.2017	240	297	276	241	211	181	149
2.	10.10.2017-20.10.2017	240	300	282	246	206	172	148
3.	07.11.2017-21.11.2017	336	298	280	244	201	166	144
4.	28.11.2017-17.12.2017	456	300	295	265	215	174	152
5.	06.02.2018-16.02.2018	240	291	294	281	240	176	136
6.	27.02.2018-09.03.2018	240	285	293	286	250	188	148
Total hours		1752						

During the irradiation campaign of the E110 and E110G alloys no critical alarm was detected. After the campaign the rig was lifted from the reactor, the targets were reloaded separately and transported into the hot-cell with a special remote controlled system. In the hot cell, the licensed and trained staff removed the samples from the dismantled targets. Appropriate assistance mechanisms, specially designed for this purpose, helped the work in the hot-cell. The irradiated samples are stored in labelled, covered aluminium holders.

Remaining work

The dosimetry data, the flux, fluence and dpa values of the irradiation campaign will be calculated and evaluated. The irradiated samples must be stored in hot-cell for the decay time, until their activities will be reduced enough to test them. The design and production of the testing devices are under way.

CORROSION OF ZIRCONIUM CLADDING IN AUTOCLAVE

Tamás Novotny, Erzsébet Perezné Feró, Zsolt Kerner

Objective

The aim of our project was to perform pressurized water reactors' modelling test series on corrosion-modelling zirconium rings, type E110 (cladding alloy produced from electrolytic zirconium) and E110G (made from metal sponge). We simulated hot and cold leg environments in an autoclave and compared corrosion rates. Four different solutions – specific to the phases of the campaign – and ultrapure water were used for the experiments.

Methods

The E110 and E110G samples were weighed on an XS205 type analytical balance before the treatment. To prepare parallel samples, 2 pcs of 8 mm rings of the same alloy were placed simultaneously into the autoclave in stainless steel capsules (Fig. 1). The temperature and pressure in the capsules were the same as those measured in the autoclave.



Figure 1: Stainless steel sample capsules

The capsules containing zirconium samples were approx. half-filled with the solutions of different compositions. These capsules were placed in a PARR 4552 high-pressure autoclave and the samples were treated at 270 °C and 300 °C with their corresponding saturated water vapour pressure (86 and 54 bar) for a long time. The rate of corrosion was calculated from the weight gain data.

Results

The cladding samples were treated for a maximum of 112 days. After treatment at 270 °C for 14 days, a coloured oxide layer was formed on the rings. At 300 °C, a dark grey layer was formed on the surface of the rings after one week of treatment and after 14 days there were black coherent oxide layers in all cases. After the same treatment time, there was no visible difference between E110 and E110G alloys.

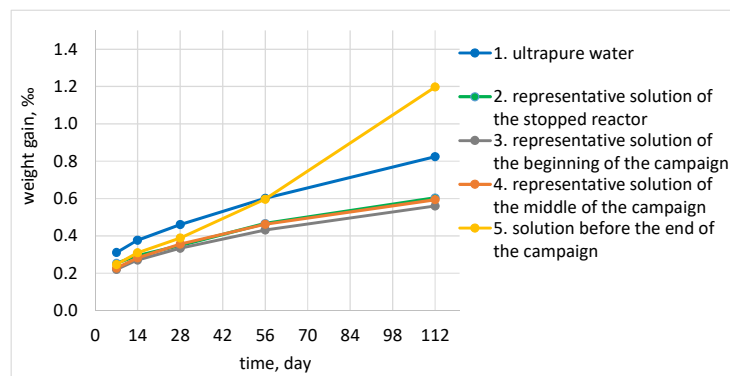


Figure 2: Weight gain of E110G samples treated in different solutions at 300 °C and 86 bar

We found that the weight gain due to corrosion was small for both alloys, especially after treatment in solutions with a composition typical of the campaign phases (Fig. 2). In case of E110G, a slightly higher degree of oxidation occurred in the ultrapure water. In the long-term (112-day) corrosion test at 300 °C, the weight gain of the samples is characterized by cubic oxidation kinetics in almost all solutions, except for solution No. 5 (solution before the end of the campaign) where the rate of oxidation accelerated after approx. day 24. For E110G, the kinetics in solution No. 5 is nearly linear.

There was no significant difference between the behaviour of E110 and E110G claddings after the same treatment time. It can be stated that the corrosion rate of both alloys was very low after the treatment in solutions characterized by the campaign.

Remaining work

The work is completed in the reporting year. Objectives in the project have been fulfilled.

Related publication

[1] T. Novotny, E. Perezné Feró, Zs. Kerner: *Cirkónium burkolat korróziója autoklámban*, Nukleon **XII/2.**, 219 (2019)

TESTING OF ACCIDENT TOLERANT FUEL CLADDING AT HIGH TEMPERATURE

Zoltán Hózer, Tamás Novotny, Erzsébet Perez-Feró, Márta Horváth,
Anna Pintér Csordás, Péter Szabó, Levente Illés, Martin Ševeček*

*Czech Technical University in Prague

Objective

The International Atomic Energy Agency (IAEA) launched a Coordinated Research Project (CRP) on the Analysis of Options and Experimental Examination of Accident Tolerant Fuels (ACTOF) for Water Cooled Reactors for the period 2015-2019. The aim of our studies was to investigate the consequences of high temperature oxidation on the chromium coated E110 type cladding material.

Methods

The 60 mm long test specimens provided by the Czech Technical University were Cr-coated samples with about 25 μm coating. The tube specimens were closed by two plugs, so one-side oxidation took place. The specimens were oxidized in steam mixed with 12 vol.% argon or in pure air atmosphere under isothermal conditions, at 1200 °C and 1100 °C. At the end of oxidation, the sample was quenched.

After the oxidation tests the tube samples were cut into five pieces. Three 8 mm long rings and two 14 mm long plugs were produced for further testing. From each sample two rings were used for radial ring compression tests which were carried out with a standard INSTRON 1195 type tensile test machine at 135 °C.

Results

The mass gain of Cr coated samples was very low compared to the reference Zr samples oxidised under similar conditions. The mass gain for Zr samples was 0.3-0.4 g, while the Cr coated samples showed only 0.01-0.04 g increase in steam atmosphere. The results of the ring compression tests showed significant differences between the reference Zr cladding and the Cr coated tubes.

The Cr coated IAEA-03 sample oxidised at 1100 °C for 3600 s indicated ductile behaviour. The ductile plateau continued after the plastic deformation for a long displacement. The Zr reference sample IAEA-02 reached 450 N maximum load. After that, less and less load was enough to cause further deformation, but no clear breakdown was observed for this sample (Figure 1, left)).

The oxidation at 1200 °C for 1800 s resulted in brittle Zr IAEA-05 samples with maximum force of ≈ 300 N. The large breakdown at 1.5 mm displacement indicated brittle fracture of the specimen. The Cr coated IAEA-06 rings could withstand loads above 500 N and remained ductile (Figure 1, right).

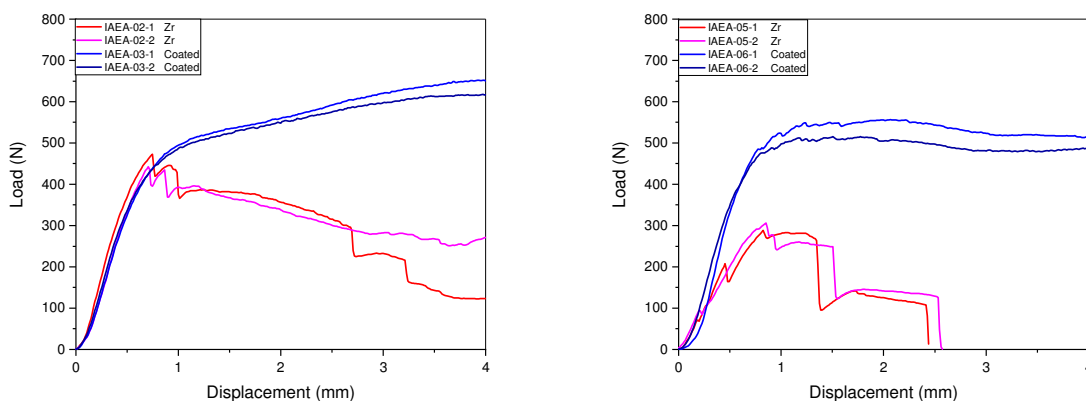


Figure 1: Load-displacement curves of ring compression tests with standard E110 Zr alloy and Cr coated E110 alloy samples after oxidation at 1100 °C for 3600 s (left) and after oxidation at 1200 °C for 1800 s (right)

Remaining work

Further testing with other methods (e.g. mandrel or ballooning) is planned if more coated cladding materials become available.

Related publication

- [1] Z. Hózer, T. Novotny, E. Perez-Feró, A. Pintér Csordás, M. Horváth, P. Szabó: *Testing of Cr coated Zr cladding for accident tolerant fuel*, MTA EK-FRL-2019-231-1-1-M0

HIGH PRESSURE STEAM OXIDATION OF ZIRCONIUM CLADDING

*Erzsébet Perez Feró, Tamás Novotny, Valér Gottlasz,
Gábor Baranyai*

Objective

This project was aimed at investigating the effect of hot steam pressure on the high temperature oxidation of zirconium fuel claddings. The experimental results can be used for model development of small break LOCA (loss of coolant accidents). This experimental program was initiated in 2018. It was part of the Zirconium Material Science Studies (CAK) project.

Methods

Two test series were conducted to study the impact of pressure on the oxidation kinetics of sponge-based E110G alloy at 800 °C. The first test series were carried out in the old equipment with limited capability. In 2019, a new autoclave was designed and manufactured, which allowed us to perform a new test series with E110G and an additional experiment with traditional E110 cladding [1]. The steam oxidation tests were carried out preferably at 50 bar, but some tests were performed at lower (15 bar and 30 bar) and higher (100 bar) pressures. Samples with 8 mm length were oxidized for different times (390 s – 1800 s) on both sides. The extent of the oxidation (ECR% - Equivalent Cladding Reacted) was calculated on the basis of the mass increase.

Results

The results of oxidation tests performed at 800 °C for various steam pressures are presented in Fig.1. For comparison this figure also contains previous data obtained in atmospheric pressure.

The steam pressure has a significant impact on the high temperature oxidation kinetics of E110G. At this temperature, the extent of oxidation increases with increasing steam pressure.

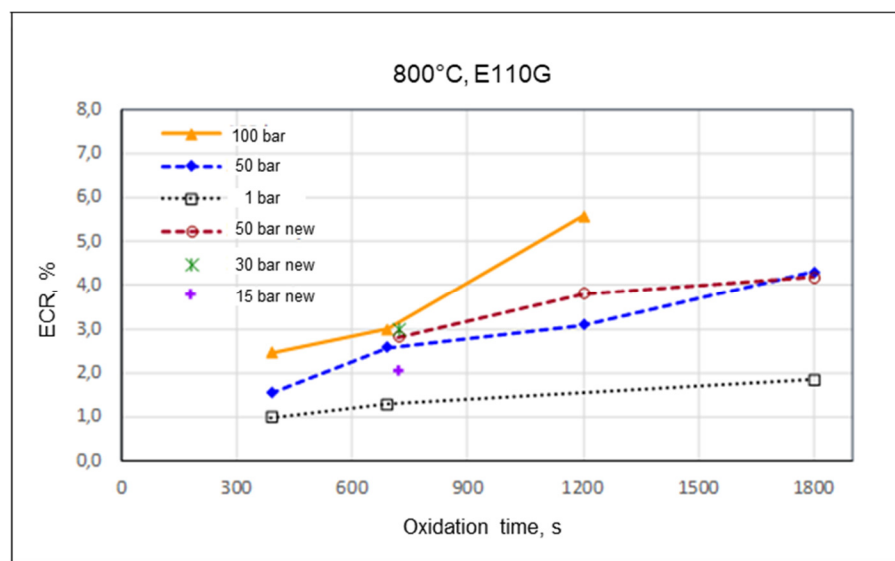


Figure 1: Influence of pressure on the oxidation kinetics of E110G alloy in steam at 800 °C

On the basis of the additional experiment with E110 alloy, the steam pressure effect was much higher for traditional E110 than for E110G under these conditions.

Remaining work

This project has been completed.

Related publication

- [1] E. Perez Feró, T. Novotny, V. Gottlasz, G. Baranyai: *Steam oxidation of Zr cladding at high pressure II*, MTA EK-FRL-2019-232-1-1-M0, in Hungarian (2019)

OXIDATION KINETICS MEASUREMENTS OF ZIRCONIUM ALLOYS IN AIR ATMOSPHERES

Nóra Vér, Martin Steinbrück⁽¹⁾, Ulrike Stegmaier⁽¹⁾, Alajos Ö. Kovács⁽²⁾

⁽¹⁾ Karlsruhe Institute of Technology, Karlsruhe, Germany

⁽²⁾ Eötvös Loránd University, Budapest, Hungary

Objective

The oxidation kinetics of E110 and E110G cladding materials have thoroughly been studied mainly in steam but also in air, mixed steam – air, steam – nitrogen and pure nitrogen atmospheres over a wide temperature range (600 – 1200 °C) at the Centre for Energy Research (EK). The reaction kinetics of the zirconium alloys were determined from the discrete weight gain values (weight gain for one oxidation time interval per one cladding specimen/measurement) in these isothermal tests. The aim of the present work was to determine the oxidation kinetics of E110 and E110G alloys in high temperature air atmospheres by thermogravimetric analysis which allows the continuous measurement of mass changes (mass gains) of the zirconium sample during high temperature oxidation. These thermogravimetric (TG) measurements were intended to make comparison in reaction kinetics between E110 and E110G alloys in high temperature air and in the obtained results between the two measurement groups. The work was performed in the frame of the Zirconium Material Science Studies project (contract number: NVKP_16-1-2016-0014).

Methods

Original E110 and E110G fuel cladding tubes cut into 8 mm long specimens were used for the measurements. The specimens were open tube segments allowing external and internal oxidation. Both E110 and E110G are Zr-1% Nb alloys. Traditional E110 (produced by electrolytic method) and sponge base E110G cladding materials were provided by Paks Nuclear Power Plant in 2015. The isothermal air oxidation measurements were performed between 800 and 1200 °C in 100 °C steps plus at 950 °C. Two measurement series were performed in a NETZSCH STA 409 thermal analyser at air flow rates of 10 and 30 l/h at Karlsruhe Institute of Technology (KIT), Germany. Another measurement series was conducted in a SETARAM TGA 92 thermal analyser at an air flow rate of 40 l/h at Eötvös Loránd University (ELTE).

Results

The results of the high temperature oxidation measurements proved that traditional E110 cladding materials are more susceptible to the breakaway oxidation (i.e. to form non-protective, porous/spalling oxide scale) than sponge base E110G alloy. The test conditions can significantly influence the measured oxidation kinetics of zirconium alloys in air mainly in the breakaway regime (at 900 – 1000 °C) and at high temperatures (1100 – 1200 °C). In the breakaway regime of the Zr-1% Nb alloys (at 900 – 1000 °C), the higher air flow rate extended the time for the breakaway transition, i.e. for initiation the accelerated oxidation kinetics. However, after the breakaway transition the higher air flow rate with more available oxygen quantity promoted higher mass increase in the second part of the oxidation process (Fig. 1). At high temperatures (1100 – 1200 °C), where zirconium reacts with oxygen and nitrogen simultaneously from the beginning of the oxidation process, the higher air flow rate resulted in higher mass gains of the zirconium alloys (Fig. 2). The oxidation kinetics measured at these high temperatures were highly dependent on the temperature where the oxide scale started to grow. This temperature can be lower than the measurement temperature (e.g. in the EK measurements where the cold samples placed in a relatively big sample holder were shifted into the preheated furnace) or higher (e.g. in the TG measurements where the preheated samples were started to oxidise in air and significant temperature overshooting took place at the beginning of the tests). The oxide scale which formed first significantly influenced the measured oxidation rates at these high temperatures (Fig. 2).

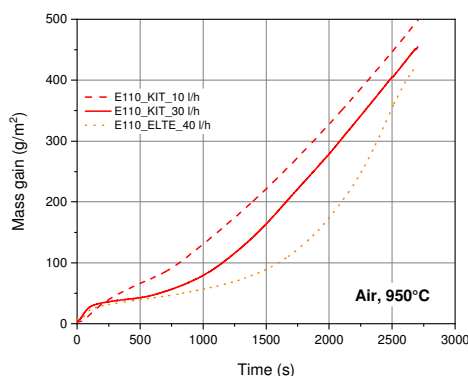


Figure 1: Comparison of mass gain of E110 tube segments oxidised at 950 °C at different air flow rates in TG

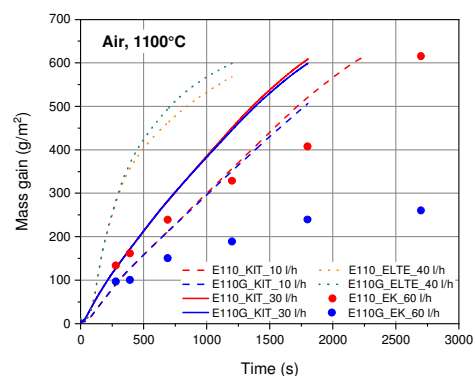


Figure 2: Comparison of mass gain of E110 and E110G tube segments oxidised in air at 1100 °C in different measurements

Remaining work

There is no remaining work.

INVESTIGATIONS OF PHENOMENA DURING HIGH TEMPERATURE BALLOONING AND BURST OF NUCLEAR FUEL CLADDINGS

Márton Király, Richárd Nagy, Tamás Szepesi

Objective

The objective of the Zirconium Material Science Project was to gain deeper knowledge on the nuclear fuel cladding materials used in Paks NPP. In this subtask the high temperature ballooning and burst were investigated. The fragmentation and dispersion of the fuel pellet was numerically modelled by foreign institutes, in this project we developed experimental methods to model the dispersion.

Methods

The fragmented fuel pellet was modelled with small ceramic balls of varying diameter. They were structured into layers to account for the different fragmentation in the middle and at the edge of the pellet (Figure 1). The layers were divided by thin polylactic acid (PLA) tubes, as this material disintegrates at high temperatures and the products are mostly gases that leave the structure intact. The balls themselves were either completely free or glued together with sodium-silicate solution.

The burst experiments were recorded by high-speed infrared cameras to capture the local heat-up of the cladding before the burst and during the burst at the cracktips. This heat-up was previously captured by monochrome high-speed cameras as the bulge area and the edge of the crack was brighter than the rest of the cladding sample.

Results

The modelled pellet fragments could be seen on the high-speed camera recordings exiting through the crack in the cladding. The average speed of the ceramic balls was determined to be around 30 m/s. The slightly glued pellet model behaved similarly to the real fuel pellet, fractured into chunks and free balls, and some of the pieces remained in the sample. However, the free, unglued balls completely dispersed out of the cladding sample, driven by the exiting high pressure argon gas, so their retention was minimal. This behaviour could approximate the fine fragmentation of the fuel at high burnup, above 70 MWday/kgHM. The dispersion also depends on the overpressure at the time of the burst, and the length and width of the crack depends on the testing temperature, so the effect of these variables needs to be further investigated.

The infrared images revealed many interesting features. The emissivity coefficient of the zirconium tube and the thin zirconium-dioxide layer on its surface was estimated based on the different cooling of the oxide scales (Figure 1). The difference in emissivity was small, so the temperature of both materials could be given at each moment. The cladding tube showed signs of heating up at the bulge on the tube a few seconds before the burst. After the burst, the tips and the edge of the crack were 20-30 °C hotter than the rest of the sample. This is in agreement with the previous tests where the surface of the samples seemed brighter as if caused by local temperature difference.

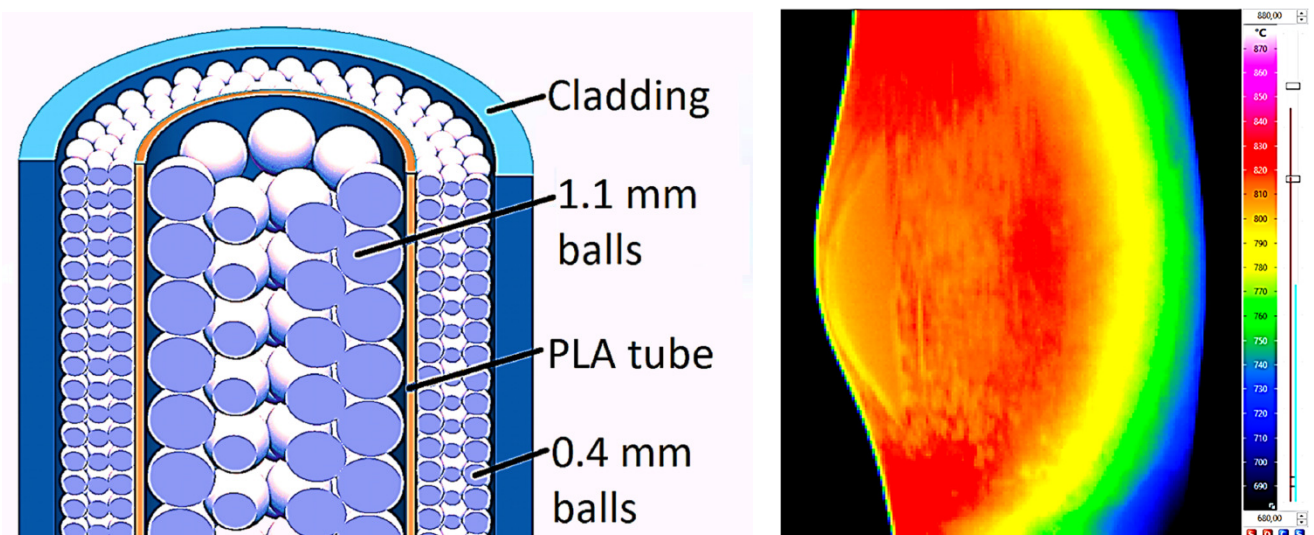


Figure 1: The model of the fragmented fuel pellet (left) and the infrared image of the cladding after burst (right).

Remaining work

The Zirconium Material Science Project was completed, but the burst test will continue with different cladding materials (e.g. Zircaloy-4) and the new thin-walled E110G cladding proposed by Paks NPP.

SIMULATION OF STATION BLACKOUT TRANSIENT IN THE CODEX FACILITY

Imre Nagy, Róbert Farkas, Nóra Vér, Zoltán Hózer, Péter Szabó, Gergely Szabó

Objective

The station blackout (SBO) transient was numerically simulated by NUBIKI experts for the Paks NPP. The objective of the integral test carried out in the CODEX facility was the experimental simulation of the same event in order to provide additional details on the measured transient data for the validation of severe accident codes.

Methods

The CODEX-SBO experiment was performed with an electrically heated seven rod bundle. The hexagonal arrangement of the bundle was fixed by original spacer grid elements. Three different Zr alloys were applied in order to see the differences in their behaviour. ZrO_2 and Al_2O_3 pellets and tungsten heaters were used.

The experiment consisted of two phases:

- During the first phase 800 °C temperature was reached in the dry core when water injection from the bottom arrived. This injection simulated the operation of hydroaccumulators. At the end of the first phase the facility was cooled down and filled by water. Burst of central rod took place due to pressure increase in the rod before the maximum temperature was reached.
- The second phase simulated the operation of the active core cooling system, which took place after another dry period. The maximum temperature during this phase was 1900 °C and strong hydrogen production was observed.

After the experiment, visual examination of the bundle was carried out using endoscopy. Later the bundle was fixed with epoxy and horizontal cross sections were prepared for metallographic examinations.

Results

The station blackout transient was successfully simulated in the CODEX facility. The planned maximum temperatures in both phases were reached. The mass of hydrogen produced due to Zr-steam reaction was 32 g.

The bundle state after the experiment showed strong oxidation and degradation of the bundle, especially in the upper part of the test facility where the temperatures were high. Some fuel rods fragmented and the broken segments indicated high degree of oxidation.



Figure 1: Broken cladding pieces from the top of the bundle (left) and cross section of the bundle at 550 mm elevation

Remaining work

Further examination of the bundle using SEM and optical microscopy will be carried out.

Related publication

- [1] I. Nagy, R. Farkas, N. Vér, Z. Hózer, P. Szabó, G. Szabó: *The CODEX-SBO severe accident experiment*, MTA EK-FRL-2019-235-1-1-M0, in Hungarian (2019)

NORMAL OPERATING AND DESIGN BASIS ACCIDENT CONDITIONS IN THE TRANSURANUS FUEL PERFORMANCE CODE

Eszter Barsy, Barbara Somfai

Objective

In 2019 two projects were aimed at using the TRANSURANUS fuel performance code for simulating normal operating (project 293) and design basis accident (project 237) scenarios for the cladding type Zr1%Nb.

In the framework of a contract with the Hungarian Atomic Energy Authority, our aim was to test the new code version by performing a simulation of the Halden experiment IFA-789.1.

The simulation of the DBA (design basis accident) scenario was supported by the National Research, Development and Innovation Fund of Hungary (contract number:: NVKP_16-1-2016-0014). The goal was to simulate a LOCA (loss-of-coolant accident) that was carried out as an experiment at EK called CODEX-LOCA-200.

Methods

One of the numerical simulation codes used by EK is TRANSURANUS, which makes it possible to model fuel behaviour in not only normal operation but also accidents such as LOCA. In recent years, we used the code version 2015, but now – in the framework of the project "Independent simulation of nuclear fuel behaviour with the TRANSURANUS code" – we have acquired the 2019 version.

Version 2015 was used for the simulation of LOCA. 115 simulations were made for an experimental scenario where a double-ended guillotine break occurs and most of the coolant leaves the system (called LOCA 200%).

The code requires a user-generated input file, which determines the material properties, the used models and the timeline of parameters. The 115 versions of this file were made to analyse the following:

- the sensitivity of the experiment to the changes of the main parameters (temperature, pin pressure, system pressure),
- the difference in high-temperature oxidation of Zr1%Nb cladding variants (E110 and sponge-based E110*),
- the accuracy of the simulations compared to the CODEX-LOCA-200 experimental results.

Later on, (in the scope of the other project) the new TRANSURANUS code version was tested. First, our high-temperature oxidation kinetics correlation of the sponge-based E110 was built into the code (it is not yet included in it by default, but it will be done in the future). Then a simulation was run with the fuel from Loviisa I nuclear power plant which was irradiated during 4 cycles and the average burnup of the rod was 48.6 MWdkgU. Then we simulated the basic irradiation again, but with the short sections which were used in the Halden Reactor. Using the RESTART function in the input, we modified the appropriate parameters and continued the simulation with the IFA-789 experiment. The calculations were compared with the results of the examinations and measurements available to us after both the Loviisa and the Halden irradiation.

*The fuel rod cladding used in the Hungarian NPP Paks is a Zirconium alloy called E110, which is quite resistant to corrosion under normal conditions. The supplier has licensed a new sponge-based modification of the alloy. The new cladding has identical geometry to E110 and similar elemental composition. The main difference is in the high temperature oxidation kinetics.

Results

Code version 2015 simulation results for the LOCA scenario provided conservative estimates for the behaviour of the bundle. The analysis of the key parameters helped us to better understand their effect on the results (Figure 1), it showed that the code can be used in the planning phase of experiments.

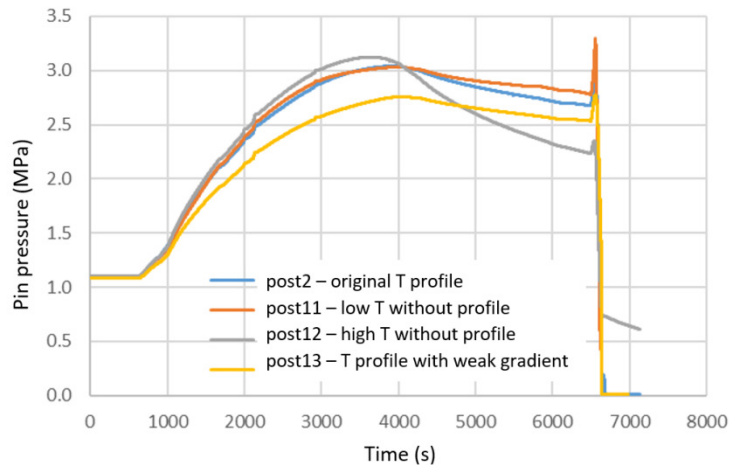


Figure 1: Effect of axial temperature profile on pin pressure and burst (simulations)

The 2019 version of the TRANSURANUS fuel behaviour code successfully simulated the base irradiation (Figure 2) and its continuation. It is capable of independent simulation of the behaviour of nuclear fuel.

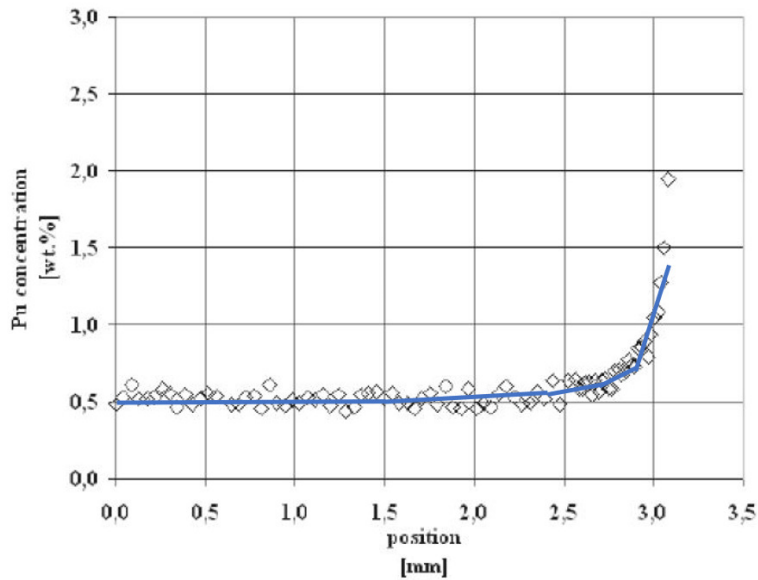


Figure 2: Radial plutonium profile of Loviisa rod (the blue curve is the simulation, the points are measured results)

Based on these results we would like to use the TRANSURANUS in the pre-calculations (for the authorities) of the new “lean” fuel (rod with decreased cladding wall thickness and outer diameter) which will be installed in Paks NPP in the future.

Remaining work

The projects have been completed.

IMPROVEMENTS OF THE CODE FUROM IN THE FRAMEWORK OF THE ZIRCONIUM MATERIAL RESEARCH PROJECT

Katalin Kulacsy, János Gadó, András Ványi

Objective

The code FUROM has been developed in EK to simulate the quasi-static in-reactor behaviour of Pressurized Water Reactor (PWR) fuel. It mostly consists of empirical models that reflect the materials and scientific state of the art of the period when they were created. However, as new technologies are introduced in the production of fuel rods and as new models emerge, the code needs to be validated and sometimes improved to stay up to date. Moreover, it is more and more important to be able to simulate the behaviour of fuel rods not only in reactor but also in dry storage conditions.

A key phenomenon that affects both in-reactor and storage performance is cladding creep. In the framework of the Zirconium Material Research Project two creep models valid for the Russian cladding E110 (Zr1%Nb) have been assessed, implemented in the code and validated, one for storage and the other one for in-reactor conditions.

Methods

Cladding creep depends instantaneously on temperature, stress and fast neutron flux, and cumulatively on fast neutron fluence. For E110 there are a maximum of six underlying mechanisms that are activated in different regimes of the above parameters. A series of papers on the correlations describing each of these mechanisms was published between 1998 and 2004 for storage conditions and in 2008 for in-reactor conditions. These publications have been reviewed, the models have been assessed and evaluated based on experimental data, and implemented in the code FUROM. Finally, validation calculations have been performed with the new models.

Results

The models are sensitive to the grain size of the cladding material. Using a grain size of 4 or of 7 μm causes a difference of 30% in the calculated creep. In addition, the model describing creep in the reactor is also very sensitive to the radiation damage rate, which can be calculated from the fast neutron flux with a rather high uncertainty. Depending on the adopted conversion factor within the range of physically acceptable values, the calculated creep may change by as much as 100%.

In typical storage or in-reactor conditions the calculated results for the E110 cladding produced by the electrolytic technology are in good agreement with or somewhat above the measured values. However, for the E110G cladding produced by the sponge technology, calculated values are conservative, i.e. mostly above measurements (Fig. 1).

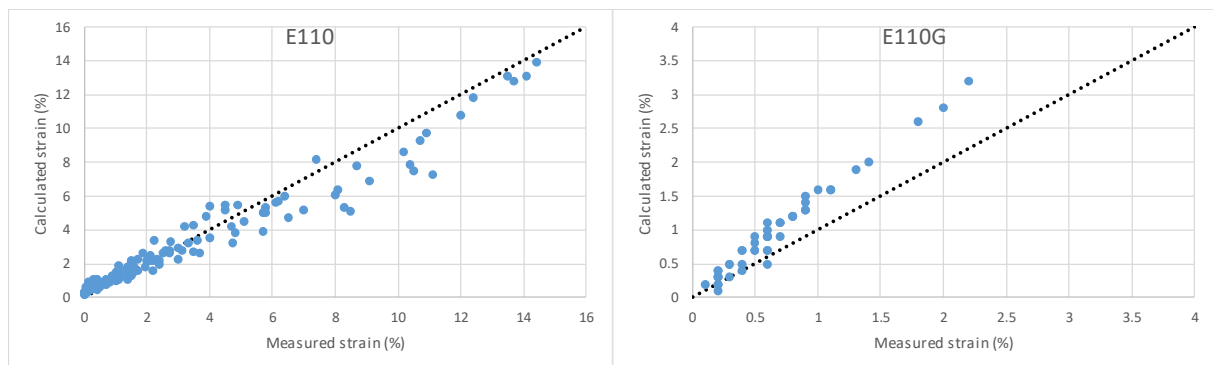


Figure 1: Calculated vs. measured tangential strains for experiments performed in the reactor BOR-60, using the flux to radiation damage conversion that gave the best results

The new model is recommended to be used for storage conditions, but not recommended for in-reactor simulation.

Remaining work

The work has been completed.

Related publications

- [1] A. Ványi, K. Kulacsy: *Zirconium Material Research: Numerical modelling of spent fuel interim storage and final disposal*, MTA EK MTSZSZ-2019-238-01-01-M0, in Hungarian (2019)
- [2] J. Gadó, K. Kulacsy: *Zirconium Material Research: Numerical modelling of normal operation states - 2*, MTA EK MTSZSZ-2019-238-03-01-M0, in Hungarian (2019)

IDENTIFICATION OF SUMMERTIME SHORT-TERM PARTICULATE MATTER POLLUTION EPISODES IN BUDAPEST

János Osán, Endre Börzsök, Ottó Czömpöly, Csenge Dian, Árpád Farkas, Péter Fűri, Veronika Groma, Szabina Török

Objective

European countries have made progress in reducing particulate air pollution in recent decades, being concerned about their harmful health effects. Submicron particles can be especially detrimental due to their ability to reach the alveolar region of the lungs. Ultrafine particles ($d < 100$ nm) deposited in the lungs can even enter directly into the blood circulatory system. Although the size distribution of particulates can be readily investigated by scanning mobility particle sizers (SMPS), the composition and speciation of particles is also of high importance. By a combination of cascade impactor sampling and total-reflection X-ray fluorescence (TXRF) analysis, the elemental composition of the different sized particles can be efficiently determined, of which size distribution of each detected chemical element can be built. The chemical state of metals in aerosol particles can be investigated using X-ray absorption near-edge structure (XANES) in TXRF geometry. Since the size and composition of urban aerosol particles have a high time variability due to their sources and to meteorological conditions, short-term pollution episodes can occur with elevated concentration of ultrafine particles or chemical elements. The aim of this study was to identify aerosol pollution events in the urban environment through analysis of size distributions and of carbonaceous particle concentrations from a series of comprehensive measurements with high time resolution. The health effect of ultrafine particles was addressed through numerical simulations by the Stochastic Lung Model.

Methods

An intense summer measurement campaign was carried out in a green belt area of Budapest (Hungary), 30 July – 9 August 2019. Size fractionated aerosol samples were collected by means of a 9-stage May type cascade impactor covering the size range of 70 nm – 16 μ m, from ultrafine to coarse particles. Sampling was performed onto Si wafers for 4 hours, four times each day (morning, afternoon, evening and night). Simultaneously, the black carbon (BC) concentration and the particle size distribution (by number) were monitored by means of aethalometer, and SMPS, respectively. Particulate matter collected on Si wafers was directly analysed by TXRF, allowing determination of size distributions of major (S, Cl, K, Ca, Fe) and trace (Cu, Zn, As, Se, Br, Pb) elements, with a detection limit down to 0.1 ng/m³ [1]. The chemical state of Cu, Br and Pb was investigated by XANES at the XRF beamline of Elettra (Trieste, Italy). In order to determine the deposition distribution of ultrafine particles in the human respiratory tract, the Radact version of the Stochastic Lung Model [2] was used.

Results

Based on the elemental size distributions obtained by TXRF analysis of cascade impactor samples and BC concentrations by aethalometer, four characteristic short-term particulate matter pollution episodes could be identified [1]: (i) a high-sulphate episode characteristic of secondary aerosols (1 August, morning), (ii) a BC and resuspension, characteristic of traffic (both end-of-pipe and non-end-of-pipe emissions; 2 August, morning), (iii) a high-bromine episode (6 August, morning), and (iv) an elevated lead episode (8 August, afternoon). A high total S concentration peaking in the fine fraction was a major indication of secondary aerosols in episode (i), with the size distribution of trace elements (Zn, Se, Br, Pb) following the S size distribution. During episode (ii), crustal elements (Ca, Fe) and Cu were elevated in the coarse fraction. XANES investigations revealed that Cu(I) and Cu(II) compounds are mixed in this fraction (from resuspension and brake wear) because of the high traffic influence. Episode (iii) was identified due to a 20-fold increase of Br concentrations peaking in the fine fraction, and elements K and Cu followed the same size distribution. Br in the fine fraction was found dominantly as organobromine, while Cu as CuSO₄ and in smaller amount as CuO, underlining the anthropogenic (combustion) origin. Pb in episode (iv) had a wider size distribution peaking at 1 μ m, and was found mostly as PbSO₄.

Stochastic Lung Model calculations revealed that the deposition probability of ultrafine particles is higher in diseased lungs than in healthy ones. The deposited ultrafine particles may cause strong irritation of the diseased airway epithelium [3].

Remaining work

In order to differentiate traffic and wood combustion as main aerosol sources in winter, an intense measurement campaign is planned in January 2020, involving the same instruments.

Related publications

- [1] J. Osán, E. Börzsök, O. Czömpöly, C. Dian, V. Groma, L. Stabile and S. Török: *Experimental evaluation of the in-the-field capabilities of total-reflection X-ray fluorescence analysis to trace fine and ultrafine aerosol particles in populated areas*, *Spectrochimica Acta Part B* **167**, 105852 (2020)
- [2] P. Fűri, Á. Farkas, B.G. Madas, W. Hofmann, R. Winkler-Heil, G. Kudela and I. Balásházy: *The degree of inhomogeneity of the absorbed cell nucleus doses in the bronchial region of the human respiratory tract*, *Radiation and Environmental Biophysics* **59**, 173–183 (2020)
- [3] P. Fűri, V. Groma, S. Török, Á. Farkas and C. Dian: *Deposition distributions of ultrafine urban particles in healthy and diseased lungs*, *Inhalation Toxicology*, submitted (2020)

STRATEGIC RESEARCH GROUP FOR THE CHALLENGES OF RENEWABLE ENERGY BASED SYSTEMS

Bálint Hartmann, Attila Kazsoki, Bálint Sinkovics, Viktória Sugár

Objective

Due to the trends of unification and integration of the European electricity, the market for system-scale services has also received new framework. Alongside the directives written in the Third Energy Package, the EU legislation is affecting the regulatory reserves from 2017 onwards.

The Electricity Balancing (EB GL) and the System Operational Regulation (SO GL) Guidelines define the new reserve market terminology and provide guidance on their obligate quantities. Due to the fact, that the implementation remains in the competence of the Member States, the final reserve planning methodology is still under development.

The primary aim for the third year of the research project is to define a procedure to determine the quantity of the system regulatory reserves, as well as developing of proposals for operation. Also, determining sample networks for the distribution networks was this year's objective.

Methods

In the distribution areas covering more than 50% of the countries we surveyed 1768 supply areas (sample networks). Each network was characterized by 14 parameters, which were reduced to eight after correlation analysis. After analysing the main components, the three with the highest values were used for k-medium clustering. By simultaneously investigating the validation criteria (Calinski-Harabasz, Davies-Bouldin, Silhouette, Gap), we found that the optimal cluster number is 6. In case of the 6 clusters we selected the networks closest to the centre of the cluster.

In the analysis of the expected changes, the transformations of the individual reserve market product and estimations of the effect on the domestic power plant portfolio were presented. In view of the above, and the change in the penetration of the new photovoltaic systems, a new adaptive reserve design procedure has been developed to monitor the changes in the power plant composition.

The proposed algorithm takes into account the historical data of the reserve market and power plant composition, and the domestic technical characteristics of the photovoltaic production (gradient change, time of energy production, etc.)

Results

With the help of principal factors (pf), the main component analysis and the k-medium clustering, we have classified the distribution network topologies. From the groups created we have selected the representative networks to use in simulations. We have carried out the qualitative analysis of the current and expected reserve market planning guidelines, revealing the shortcomings and the domestic effects.

We are introducing a methodological proposal for the implementation of stochastic reserve planning in Hungary.

Remaining work

The research project lasts until 2021 as part of the VEKOP-2.3.2-16-2016-00011 project. The next year's main objective will focus on stochastic simulation of medium voltage networks.

Related publications

- [1] A. Kazsoki, B. Hartmann: *Data Analysis and Data Generation Techniques for Comparative Examination of Distribution Network Topologies*, International Review of Electrical Engineering **14**, 32-43 (2019)
- [2] A. Kazsoki, B. Hartmann: *Typologization of medium voltage distribution networks using data mining techniques: A case study*, in Proc. 7th International Youth Conference on Energy (IYCE) pp. 1-8 (2019)
- [3] A. Kazsoki, B. Hartmann: *Elosztóhálózatok topologizálása adatbányászati módszerek felhasználásával*, in Proc. Tavasz Szél Konferencia 2019 pp. 81-95 (2019)
- [7] B. Hartmann: *Comparing efficiency of various solar irradiance categorization methods*, Renewable Energy **154**, 661-671 (2020)
- [4] A. Kazsoki, B. Hartmann: *Hierarchical agglomerative clustering of selected Hungarian medium voltage distribution networks*, Acta Polytechnica Hungarica - in print
- [5] A. Kazsoki, B. Hartmann: *Methodology for the formulation of medium voltage representative networks in three DSO areas*, Renewable Energy & Power Quality Journal - in print
- [6] B. Hartmann, A. Kazsoki, V. Sugár, B. Sinkovics: *Napsugárzás mintázat kategorizálási módszereinek kritikai szemléletű összehasonlítása*, Magyar Energetika, - in print

CORTEX – CORE MONITORING TECHNIQUES AND EXPERIMENTAL VALIDATION AND DEMONSTRATION

Sándor Kiss and Sándor Lipcsei

Objective

The CORTEX project is a four-year long, wide cooperation among 19 institutes, universities and companies of 11 countries in several working packages. The consortium was strategically structured around the required core expertise from all the necessary actors of the nuclear industry, both within Europe and outside. The project aims at developing an innovative core monitoring technique that allows detecting anomalies in nuclear reactors, such as excessive vibrations of core internals, flow blockage, coolant inlet perturbations, etc. The technique will primarily be based on using the inherent fluctuations in neutron flux recorded by in-core and ex-core instrumentation, from which the anomalies will be differentiated depending on their type, location and characteristics. The method is non-intrusive and does not require any external perturbation of the system. The project will result in a deepened understanding of the physical processes involved. This will allow utilities to detect operational problems at a very early stage and to take proper actions before such problems have had any adverse effect on plant safety and reliability.

Methods

We are participating in Working Package 4 (Application and demonstration of the developed modelling tools and signal processing) focusing on VVER-440 techniques against plant data measured at Paks NPP.

Results

In an earlier phase of the project, three noise measurements were selected of the same fuel cycle of a VVER-440/213 reactor unit. This year, static calculations of the neutron flux were performed for all three measurements using the code provided by the Technical University of Valencia.

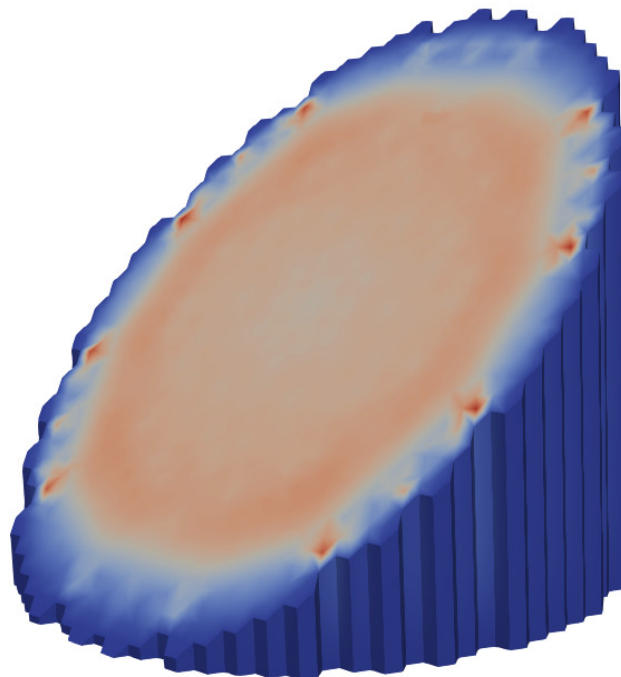


Figure 1: Distribution of thermic neutrons in the reactor core during the measurement made at the end of the fuel cycle

The standard evaluation (with calculating Fast Fourier Transform based auto and cross power spectral density functions) of the measured signals was also fulfilled in this period for later use.

Remaining work

The project finishes in 2021.

Acknowledgement

The research leading to these results has received funding from the Euratom research and training programme 2014-2018 under grant agreement No 754316.

CONCERT-EUROPEAN JOINT PROGRAMME FOR THE INTEGRATION OF RADIATION PROTECTION RESEARCH

Balázs Madas, Emese Drozsdik

Objective

The ‘CONCERT-European Joint Programme for the Integration of Radiation Protection Research’ under Horizon 2020 aims to contribute to the sustainable integration of European and national research programmes in radiation protection. There are seven work packages in CONCERT, and the Centre of Energy Research contributes to four of them. In WP2 (SRA development), we participated in the development of Strategic Research Agendas (SRAs), and in particular, in that of the Multidisciplinary European Low Dose Initiative (MELODI). In WP3 (Joint programming), we contributed to the Second Joint Roadmap for Radiation Protection Research. In WP6 (Access to Infrastructures), we disseminated the results of our survey on data management in radiation protection research and contributed to the preparation of the webhandbook of research infrastructures. In WP7 (Education & Training), we provided electronic surveys for organizers of CONCERT funded training courses to collect feedback from the participants.

Methods

There is an SRA Working Group (WG) in MELODI, which is responsible for the regular update of the MELODI SRA. The WG met two times in person and once through videoconference in 2019 including discussions of the texts drafted by different members. The broad community of radiation protection research was invited for consultation of the SRAs of MELODI and EURADOS (European Radiation Dosimetry Group). There was a meeting in Brussels and multiple videoconferences in order to prepare the joint roadmap which is to be consulted in 2020. In WP6, we had meetings to set up the structure of the web-handbook, and identify persons responsible for drafting the different chapters. In WP7, we prepared electronic feedback forms using a commercial platform and a general template adjusted to the program of the given training course.

Results

As the CONCERT project approaches its conclusion in mid-2020, the first drafts of several publications have been finalized. MELODI now has a significantly revised SRA [1]. We also provided input to the Second joint roadmap for radiation protection research [2], for example the roadmap for the challenge entitled “Understanding and quantifying the health effects of radiation exposure” (Figure 1). In WP6, the final version of the infrastructures “web-handbook including protocols issued from harmonization procedures” has been prepared [3]. Besides this, we also have a new proceedings published about the survey on data management in radiation protection research [4]. Based on the feedback from training course organizers, our electronic survey provided great help for them.

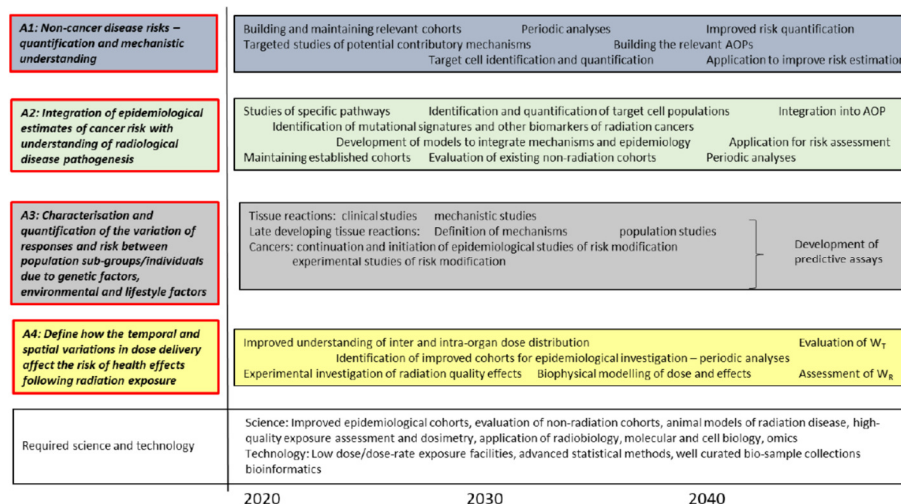


Figure 1: Roadmap for the challenge entitled Understanding and quantifying the health effects of radiation exposure

Related publications

- [1] S. Bouffler, A. Auvinen, E. Cardis, M. Durante, J.R. Jourdain, M. Harms-Ringdahl, et al.: *Strategic Research Agenda of the Multidisciplinary European Low Dose Initiative (MELODI) –2019 1-29* (2019)
- [2] N. Impens, S. Salomaa, S. Bouffler, B. Madas, L. Roy, R. Gilbin, et al.: *Second joint roadmap for radiation protection research*, CONCERT deliverable D3.7 (2020)
- [3] L. Sabatier, L. Ainsbury, P. Auce, R. Benotmane, N. Beresford, M. Birschwilks, et al.: *Publishing the web-handbook including protocols issued from harmonization procedures*, CONCERT deliverable D6.6 (2020)
- [4] B. Madas, U. Kulka, B. Grosche, M. Birschwilks, G. Woloschak, Saigusa S., et al.: *FAIRing the radiation science commons*, BIO Web of Conferences **14**, 08002 (2019)

MEDIUM SCALE EXPERIMENT FOR VVER-440 NOZZLE MOCK-UP

Levente Tatár

Objective

In the framework of the ATLAS+ (Advanced Structural Integrity Assessment Tools for Safe Long Term Operation) EU Horizon2020 project, large-scale experiments are being carried out on mock-ups (MU) representative to reactor coolant pressure boundary components. These experiments are backed up by a large set of numerical studies as well as experiments on laboratory size specimens. Most of these large-scale experiments involve 4 point bending of 1:1 scale pipes. BZN (Bay Zoltán Nonprofit Ltd. for Applied Research) and EK perform an experimental study of crack propagation on a 1:5 scale MU of the VVER-440 main feedwater nozzle manufactured in the framework of the STYLE EU FP7 project. This is a “medium” size experiment, not completely representative considering the size, however it has similar complexity to experiments performed by other partners.

Methods

To perform the experiment a very extensive preparatory work [1] was required. One of the main concerns was obtaining an acceptable balance between the required cross-head force and displacement as both are limited by the available Instron 8850 biaxial testing machine. In addition, the testing machine is not conceived to support large lateral forces, so these had to be dealt with. Required strength of the bolted joints was another issue. Due to these large uncertainties, it had been decided that two pre-mockups were needed to be manufactured to test the experimental set-up before performing the “real” large-scale experiment. However, issues connected with manufacturing lead to using the originally selected STYLE MU. The STYLE MU, as well the two pre-mockups have been manufactured by respecting the technology representative for VVER-440 type reactors. During the experiment, ARAMIS optical measurement system as well as mechanical extensometers had been used.

Results

Despite the concerns, the experiment was a large success. The supporting system had the required strength and rigidity. 3D maps of the local displacement fields had been recorded by the ARAMIS system. All extensometers measured realistic displacement values with very small electrical noise until the end of the experiment. Displacements had automatically been converted to strains. Large crack extension had been observed during the experiment (See Figure 1).

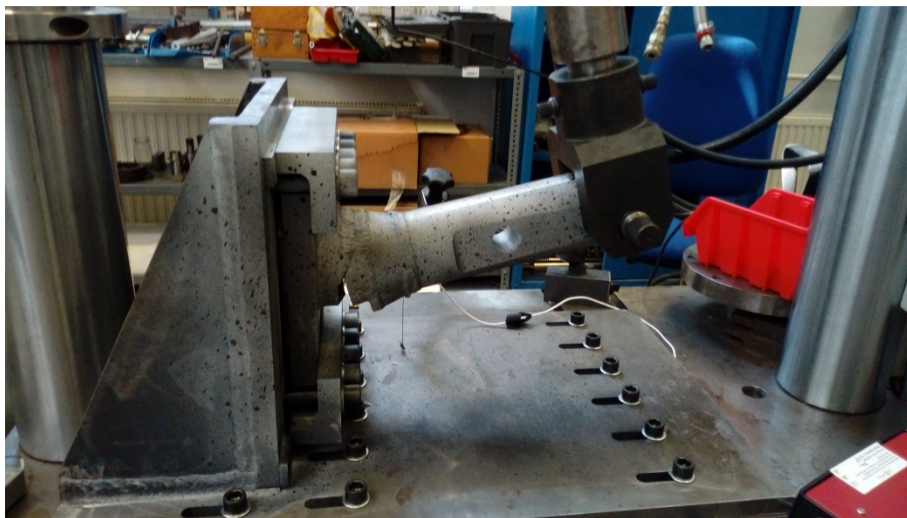


Figure 1: Large crack propagation during the experiment

Remaining work

The obtained results show that the crack propagation differs from predictions done before the experiments.

To assess the discrepancies, new finite element models of the main experiment are being prepared. Before performing the main large-scale experiment, only a very limited number of experiments on specimens taken from the crack zone could be performed due to lack of material, leading to insufficient knowledge of the material properties in the most important zone. New experiments on specimens will be carried out to complement the existing material data. They are required as input for the FE (Finite Element) computations. Fractographic examination of the crack surfaces is ongoing.

Related publication

[1] Advances in the ATLAS+ Project. MTA EK progress report 2019 (2020)

NON-DESTRUCTIVE EVALUATION SYSTEM FOR THE INSPECTION OF OPERATION-INDUCED MATERIAL DEGRADATION IN NUCLEAR POWER PLANTS – NOMAD

Antal Gasparics, Gábor Vértesy, Ildikó Szenthe, Ferenc Gillemot

Objective

NOMAD (Non-destructive Evaluation System for the Inspection of Operation-Induced Material Degradation in Nuclear Power Plants) project focuses on development, demonstration and validation of a non-destructive evaluation (NDE) tool for the local and volumetric characterization of the embrittlement in operational reactor pressure vessels (RPVs).

Methods

EK contributes to the project with a specially designed tool having a sensing yoke for the so called Magnetic Adaptive Testing (MAT). MAT is a method for non-destructive characterization of ferromagnetic materials which is based on systematic measurement and evaluation of minor magnetic hysteresis loops. This method is being tested and evaluated regarding its applicability for the determination of the material changes and the variation of the material properties during exposure to neutron irradiation.

Results

In 2019 measurements were performed on non-irradiated and irradiated, 22NiMoCr37 type base, and on 18MND5 type weld reactor steel material. The non-destructively determined magnetic parameters were compared to the destructively measured ductile-to-brittle transition temperature (DBTT) values.

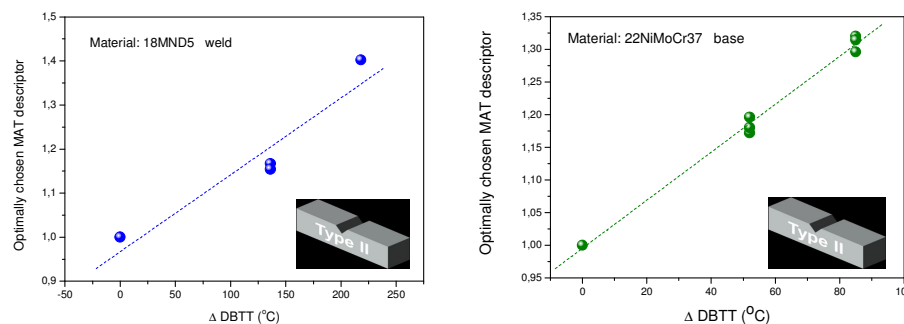


Figure 1: Selected MAT descriptor as a function of the transition temperature shift for the 22NiMoCr37 and 18MND5 materials

The influence of neutron irradiation is reflected on the shift of transition temperature, and this modification of material structure can be followed by the magnetic measurements, as shown in Fig. 1.

Measurements were also performed on clad and unclad blocks made of 15H2NMFA type material. From the base material side regular loops with large amplitude were experienced. On the clad side of the blocks a much weaker, but still evaluable magnetic signal was found: since the cladding is an austenitic, almost paramagnetic material, that represents practically an air gap between magnetizing yoke and ferromagnetic part of sample. Nevertheless, similarly good correlation (as shown above) was observed between DBTT and magnetic parameters in this case, too.

Remaining work

Measurement and evaluation of the irradiated, aged blocks will provide data about the applicability of these methods. A software-based multi-parametric NDE tool will be developed for the inspection of clad RPV material.

Related publications

- [1] G. Vértesy, A. Gasparics, I. Szenthe, F. Gillemot, and I. Uytendhouwen: *Inspection of Reactor Steel Degradation by Magnetic Adaptive Testing*, *Materials* 12 : 6 Paper: 963 , 12 p (2019)
- [2] G. Vértesy, A. Gasparics, I. Szenthe, F. Gillemot: *Magnetic nondestructive inspection of reactor steel clad blocks*, *Global Journal of Advanced Engineering Technologies and Sciences*, 6 : 6 pp. 1-9. , 9 p. (2019)
- [3] G. Vértesy, A. Gasparics, I. Uytendhouwen and R Chaouadi: *Influence of surface roughness on non-destructive magnetic measurements*, *Global Journal of Advanced Engineering Technologies and Sciences*, 6:12, pp. 25-33, 9 p. (2019)
- [4] G. Vértesy, A. Gasparics, B. Bálint, Sz. Gyimóthy and J. Pávó: *Influence of the size of samples in Magnetic Adaptive Testing*, *Global Journal of Advanced Engineering Technologies and Sciences*, 6 : 9 pp. 1-9 , 9 p. (2019)

RADIOLOGICAL CHARACTERIZATION IN VIEW OF NUCLEAR REACTOR DECOMMISSIONING: ON-SITE BENCHMARK OF A BIOLOGICAL SHIELD

István Almási, Zoltán Hlavathy, Nándor Kaposy, Péter Völgyesi

Objective

The aim of the INSIDER (Improved nuclear site characterisation for waste minimisation in decommissioning and dismantling operations under constrained environment) Horizon-2020 EU project is to work out the details of a good common practice to categorize the waste produced during the decommissioning of nuclear sites in an economically reasonable way. The particular case's objective was to investigate the activated biological shield in the Belgian Reactor 3 at SCK•CEN. A specific characterization program was developed, and the measurement campaign was part of an interlaboratory comparison.

Methods

As a starting point for the exercise, three relatively simple and commonly used, fast and straightforward measurement methods were used: dose rate, total gamma measurements and in situ gamma spectrometry. In the benchmarking program 3 fixed points on the shield were chosen [top (A-point), middle (B-point), bottom (C-point) of the reactor pool] and five consecutive measurements were made on each point 5-times. In the case of the dose rate and total gamma measurements the distance between the source and the detector was near to zero and open collimation was used. Between every set, the equipment was removed and repositioned. From the 3 points and the 5x5 measurements on every point, 7

5 single data were obtained. Four different types of detector were used for the dose rate measurements: an ionisation chamber, a proportional counter, Geiger-Müller counters and scintillators. Two measurement systems have been used for the total gamma analysis: proportional counters and scintillators. All measurement teams used their own equipment (mostly germanium detectors) as well as their own calibration procedure and modelling tools (Monte-Carlo based codes) for the in situ gamma spectrometry method.

Results

The mean dose rate values found for all three measurement points, taking the uncertainty bands into account, are very consistent (Fig. 1). Nevertheless, the uncertainty on a single measurement can be very large for certain types of detectors. The most appropriate equipment tested might be the organic scintillator, the BGO (Bismuth Germanate - $\text{Bi}_4\text{Ge}_3\text{O}_{12}$) or even the ionisation chamber since they show smaller relative uncertainties. The results of the total gamma measurements showed that the LaBr_3 detector results in the lowest uncertainty, followed by the organic scintillator with a 20 mm thick crystal. Using the LaBr_3 detector and a measurement time of 30-45 s would considerably reduce the uncertainty at the A, B, C locations. The on-site gamma spectrometry benchmarking exercise showed that the results for high-resolution detectors are generally very consistent, when using proper shielding. The organisers gave us an uncalibrated depth profile of the nuclides in question. The participants had to determine the depth in the wall where the nuclide concentration reached a predetermined value. For solving the problem, the participants had to build up a Monte Carlo model of the wall with the known depth profile and compare the prediction of the model with the calibrated gamma spectrum. The interesting nuclides in the wall interior were Ba-133, Eu-152 and Eu-154; on the surface it was Cs-137. Figure 2 shows the results of Ba-133 and Eu-152. The various modelling tools provide consistent results, too.

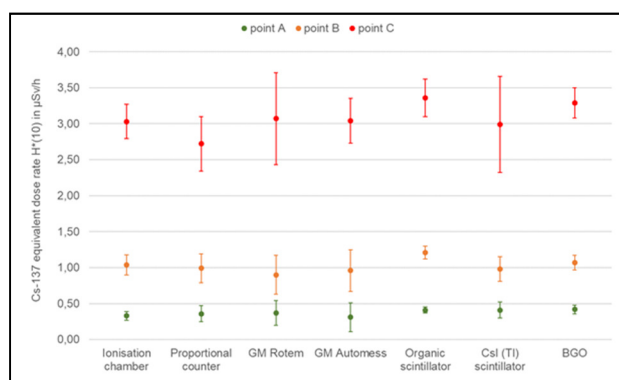


Figure 1: Cs-137 equivalent dose rate $H^*(10)$ for the points A, B and C with various measurement equipment used by the teams. The error bars represent the expanded uncertainty (coverage factor)

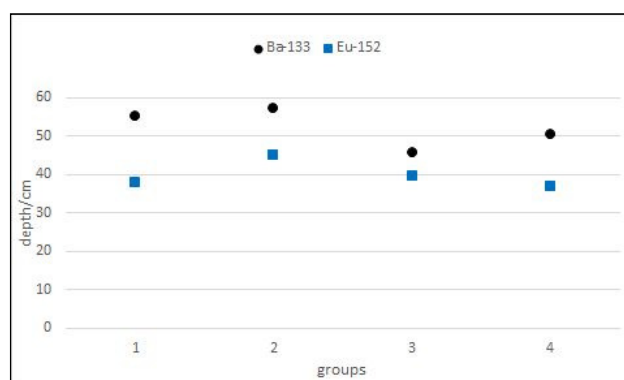


Figure 2: Depth in the concrete wall where the nuclide concentrations drop to 0.1 Bq/g determined by the different teams

Remaining work

This project in Belgium was finished but another in-situ campaign is going on with a measurement campaign in Ispra, Italy, where the aim is to characterize containers filled with liquid radioactive waste.

UNCERTAINTIES OF ATMOSPHERIC DISPERSION CALCULATIONS

Csilla Rudas, Péter Zagvai, Tamás Pázmándi

Objective

The objective of the research of the CONFIDENCE project is to understand, reduce and cope with the uncertainties of meteorological and radiological data and their further propagation in decision support systems, including atmospheric dispersion, dose estimation, food-chain modelling and countermeasure simulation models. Work package 1 (WP1) is focused on the modelling of uncertainties during the emergency phase, from meteorological and source term inputs, and is applied to atmospheric dispersion calculations and dose estimations.

Methods

In the third, final year of the project, the utilization of ensemble input data in operational context was investigated and various methods for reducing the runtime of such assessments were evaluated. A new module for the usage of ensemble input data was integrated into the SINAC (Simulator Software for Interactive Consequences of Nuclear Accidents) decision support system developed in the Centre for Energy Research. The utilization of local meteorological data was demonstrated through a case study with meteorological data sets (ensembles) provided by the Hungarian Meteorological Service. Calculations were made to examine different methods of reducing model run time for a single ensemble member and assess the change in the uncertainty indicators. The simulations were made with the SINAC system and meteorological ensemble data from the HARMONIE-AROME model. Dispersion calculations were performed with Gaussian puff model.

Results

Two simple release cases were simulated with SINAC using local meteorological ensemble data from ALADIN-EPS, interpolated to AROME grid covering the Carpathian Basin with 2.5 km resolution. Possible visualizations of the results for several ensemble calculations were shown to present the effect of meteorological forecast uncertainty in the atmospheric dispersion calculation. [1]

For the investigation of introducing the usage of ensemble input for operational calculation, several methods for the reduction of runtime for one ensemble member were assessed. The usage of simpler but faster dispersion modelling scheme was studied by changing the number of puffs released. Reducing the number of puffs from the original default value of 16 to 4 resulted in a 38% decrease in runtime, and multiplying the number of puffs by 4 more than doubled the runtime. The maximum distance of threshold exceedance for the mean of the ensemble results is shown in Fig. 1 for different quantities and the various number of released puffs. [2]

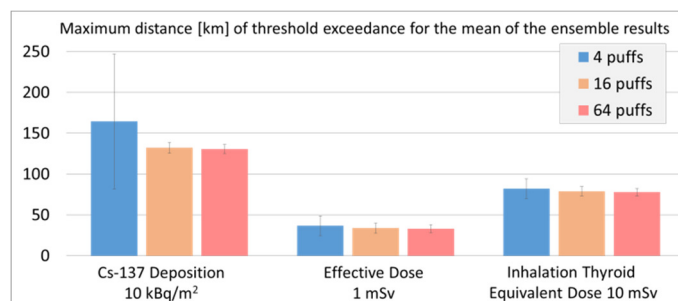


Figure 1: Maximum distance (in km from the source) of threshold exceedance for the mean of the ensemble results, for several model endpoints and for three simulation cases. Bars indicate standard deviation of the results. [2]

Results indicate that considering 64 puffs instead of 16 is not justified, because considering the quantities shown in Fig. 1 the results for the two simulations are very similar. However, with the release of 16 puffs rather than 4 puffs, the standard deviation and thus the uncertainty of the Cs-137 deposition results were significantly reduced.

Simulations were also conducted with decreasing the spatial domain and the grid of the output to 4/9 and 1/9 of its original size, for which the runtime was reduced by about 37% and 13%, respectively, without change occurring in the uncertainty indicators. The temporal resolution of the time integrated activity concentration in air and deposition concentration output was modified from 1 hour to 2 and 4 hours, which resulted in only a 22-26% reduction in total run time. The mean maximum distance and surface values of threshold exceedance were not affected [3].

Papers summarizing the results of the WP1 obtained throughout the entire projects are currently under review [4][5][6].

Remaining work

This project has been completed.

Related publications

- [1] Cs. Rudas, T. Pázmándi, P. Szántó, M. Szűcs, B. Szintai: *The application of meteorological ensembles in the SINAC decision support system*, 19th International Conference on Harmonisation within Atmospheric Dispersion Modelling for Regulatory Purposes, Bruges, Belgium (2019)

- [2] Cs. Rudas, P. Szántó, T. Pázmándi, P. Zagyvai: *Efficiency savings in model setup for an ensemble approach used to describe atmospheric dispersion model uncertainty*, CONFIDENCE Dissemination workshop, Bratislava, Slovakia (2019)
- [3] P. Bedwell, I. Korsakissok, S. Leadbetter, R. Périllat, C. Rudas, J. Tomas, J. Wellings: *Guidelines for the use of ensembles in the description of uncertainty in atmospheric dispersion modelling: operational applications in the context of an emergency response*, CONCERT CONFIDENCE Report D9.5.5 (2019)
- [4] P. Bedwell, I. Korsakissok, S. Leadbetter, R. Périllat, C. Rudas, J. Tomas and J. Wellings: *Operationalising an ensemble approach in the description of uncertainty in atmospheric dispersion modelling and an emergency response*, Radioprotection (under review)
- [5] I. Korsakissok, S. Andronopoulos, P. Astrup, P. Bedwell, E. Berge, T. Charnock, H. De Vries, G. Geertsema, F. Gering, T. Hamburger, I. Ievdin, H. Klein, S. Leadbetter, O. C. Lind, T. Pázmándi, R. Périllat, C. Rudas, B. Salbu, S. Schantz, R. Scheele, A. Sogachev, N. Syed, J. Tomas, M. Ulmoen, J. Wellings: *Uncertainty propagation in atmospheric dispersion models for radiological emergencies in the pre- and early release phase: summary of case studies*, Radioprotection (under review)
- [6] S. J. Leadbetter, S. Andronopoulos, P. Bedwell, K. Chevalier-Jabet, I. Korsakissok, A. Mathieu, R. Périllat, J. Wellings, G. Geertsema, F. Gering, T. Hamburger, A. R. Jones, H. Klein, T. Pázmándi, C. Rudas, A. Sogachev, P. Szanto, J. Tomas, C. Twenhöfel, H. de Vries: *Ranking Uncertainties in Atmospheric Dispersion Modelling Following the Accidental Release of Radioactive Material*, Radioprotection (under review)

INTEGRATED PLATFORM FOR THE EUROPEAN RESEARCH INFRASTRUCTURE ON CULTURE HERITAGE (IPERION CH)

Zsolt Kasztovszky, László Szentmiklósi, Boglárka Maróti, Ildikó Harsányi, Zoltán Kis, Veronika Szilágyi, Katalin Gméling

Objective

IPERION CH is a project funded by the European Commission, H2020-INFRAIA-2014-2015, under Grant No. 654028. It offers Transnational Access (TNA) to world-class laboratories and knowledge distributed in 11 countries with the submission of single or multi-technique proposals. The TNA program offers a vast portfolio of services, including the FIXLAB platform for large-scale facilities. BNC took part with its advanced neutron-based instrumentation and expertise.

Methods

Prompt Gamma Activation Analysis (PGAA) – to determine the bulk elemental composition, mostly for major components, and some trace elements with high neutron absorption cross-section, Prompt Gamma Activation Imaging (PGAI) – to determine the elemental distribution within a large heterogeneous sample. Neutron Activation Analysis (NAA) – to determine the elemental composition of a sample taken from a larger object, mostly for trace elements. Neutron imaging on NIPS-NORMA (Neutron-Induced Prompt Gamma-ray Spectroscopy & Neutron Optics and Radiography for Material Analysis) and on RAD (Static/Dynamic thermal-neutron and X-ray Imaging Station) instruments – to map the 2D or 3D macro-structure of the objects. Time-of-flight neutron diffraction (ToF-ND) – for atomic-scale structure determination.

Results

In this calendar year, we provided 37 beam-days at PGAA, 9 at NIPS-NORMA, 5 at RAD and 9 at the NAA laboratory. During the four years of the entire project, we delivered 279 beam days for 54 projects, 74% more than originally planned. The distribution of the users based on the nationalities of the PI and the breakdown of the projects based on the investigated materials are shown in Figures 1 and 2.

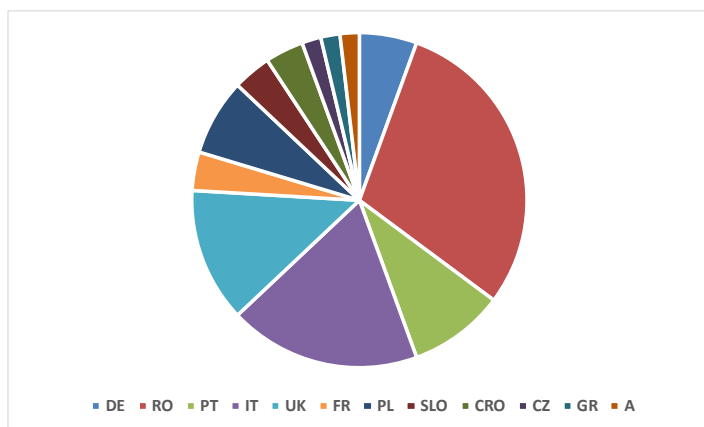


Figure 1: Distribution of the users based on the nationalities of the PI

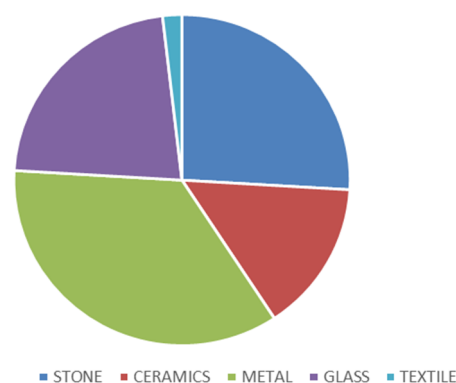


Figure 2: Distribution of the projects based on the investigated material

In a recent highlight project, pieces of a processional cross, coming from the abbey of Chiaravalle (close to Milan, Italy) and dated to the 13th century were measured by XRF, PIXE and PGAA. We succeeded in verifying the use of an amalgam technique (blend of Au and Hg) applied on a silver sample [1].

Remaining work

The Cultural Heritage community will continue the collaboration within the follow-up project IPERION HS (2020-2022), and on a longer run within the E-RIHS ERIC, in which our group will continue to participate.

Related publication

- [1] D. Di Martino, E. Perelli Cippo, A. Scherillo, Z. Kasztovszky, I. Harsányi, I. Kovács, Z. Szőkefalvi-Nagy, R. Cattaneo, G. Gorini: *An Archaeometallurgical Investigation on Metal Samples from the Chiaravalle Cross*, *Heritage* **2** (1), 836–847 (2019)

H2020 EUROPEAN UNION PROJECT: INNOVATIVE CLUSTER ON RADIOLOGICAL AND NUCLEAR EMERGENCIES (INCLUDING)

Éva Kovács-Széles, András Kovács, Péter Völgyesi

Introduction

Radiation and nuclear emergencies are by far the most feared by people and difficult to face by the authorities, and the radiological threat is now recognized as a high, if not the highest, priority in the global agenda for nuclear security and an important element in the broad spectrum of hybrid threats pursued by terrorist groups. The beginning of radiological and nuclear terrorism dates back to 1995 in Moscow, when Chechen rebels alerted the international media regarding a canister containing Cs-137, which they threatened to detonate, thus bringing to the public domain the concept of a “dirty bomb” or Radiological Dispersive Device. The European Union aimed to prevent nuclear terror attacks and fighting with nuclear terrorism. Therefore, more projects were started to focus on this area due to the continuously evolving threats in this field worldwide.

Objective of INCLUDING project

In the above explained context, training and exercise is probably the most important element that can make the difference between life and death, preservation and loss, incident and tragedy. As a matter of fact, training in the Radioactive and Nuclear security sector is a multifaceted activity involving several actors, demanding appropriate infrastructures and resources that are not publicly available, even at European level. As a step towards a full-fledged and comprehensive training at European level, the Consortium proposes the creation of an INnovative CLUster for raDIological and Nuclear emerGencies (INCLUDING).

INCLUDING connects 14 Partners from 10 EU Member States (MS), bringing together infrastructure, equipment and experts coming from Medical Organizations, Fire Corps, Government Departments, Municipalities, Governmental and Civilian Research Institutes, Centres of Excellence, Academia, Industries and subject matter experts. The project started in August 2019.

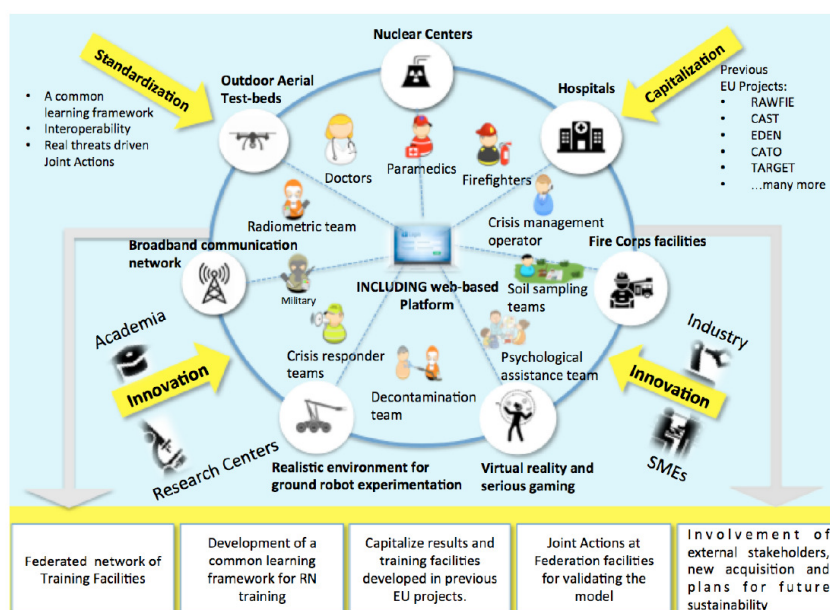


Figure 1: INCLUDING will develop an innovative approach to the management of a network of training facilities and be based on a Federated model.

Activity of Centre for Energy Research in INCLUDING in 2019

Due to the fact that this 5-year project only started in August 2019, there were not many opportunities for effective work this year. The Centre for Energy Research gave all details about its testbed into the project database (all capabilities, equipment, laboratories and facilities available at the Centre to serve the purpose of the project, i.e. training and exercises for nuclear security). Besides, in Work Package 4, the Centre for Energy Research conducted a study to overview previous EU funded projects to find similarities and thus avoid duplication. The Centre for Energy Research also undertook a lecture at the first Joint Action of the project in Rome, in January 2020 on: “Interactive Trainings for Nuclear Security in Hungary”.

Remaining work

The main task of the Centre for Energy Research in the project is the organization of a multiple Joint Action for training and demonstration based on a dirty bomb explosion scenario in 2022. In the frame of the Joint Action, the Annual Meeting of the project will be also held in Hungary that year.

SCIENCE & INNOVATION WITH NEUTRONS IN EUROPE IN 2020

Rózsa Baranyai

SINE2020, world-class Science and Innovation with Neutrons in Europe in 2020 project finished in September, 2019. The Budapest Neutron Centre (BNC) was a member of the SINE2020 consortium. The aims and the fields of the project, where the partners worked together were put on one slide (Fig.1). BNC was active mainly in the area of e-learning & schools (WP3) and Industry Consultancy (WP4). SINE2020 WP3 was dedicated to education and training, support was launched for Advanced Schools every second year, and for Introductory Schools every year.

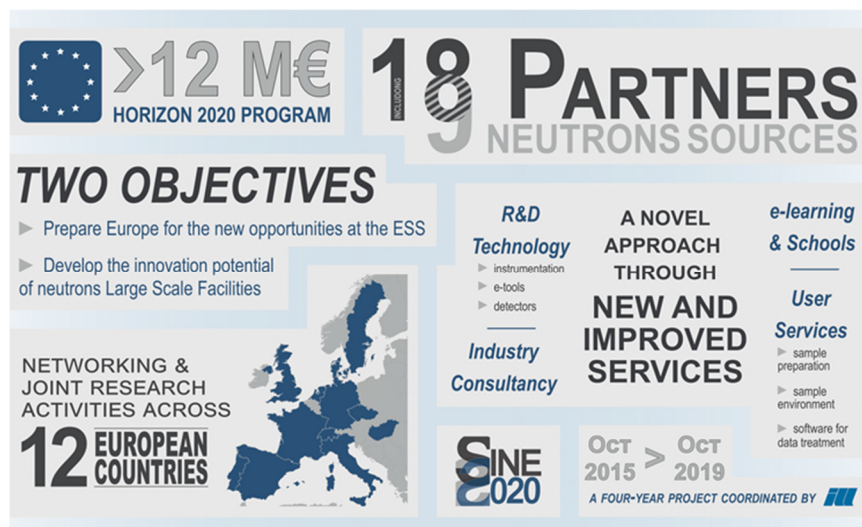


Figure 1: SINE2020 project (source: www.sine2020.eu)

Majority of the attendees were PhD students, post-doc fellows, young scientists, and some newcomers, especially from research centres. SINE2020 supported 71 school days and 232 students in 2019. During the project time, SINE2020 schools trained over 1800 people in the neutron community.

SINE2020 Industrial Consultancy workpackage gave opportunities to introduce neutron techniques to industrial users. Eight neutron centres offered about 90 days over 4 years for feasibility studies or test measurements. SINE2020 collected 49 requests, out of these requests 37 were considered for feasibility studies, and 35 were actually carried out providing 55 neutron beam days. Among the 35 granted studies, mostly the stress scanning, imaging (radiography and tomography) and SANS techniques were used.

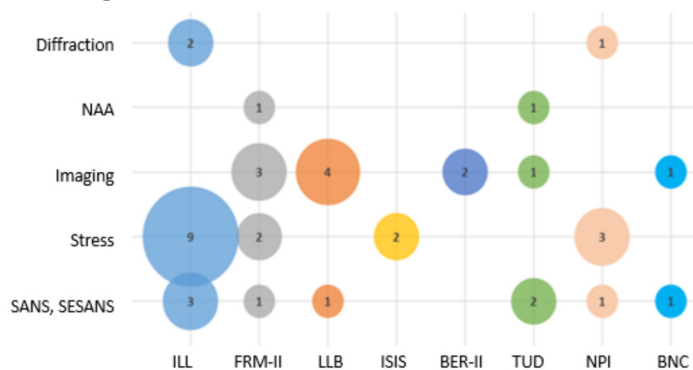


Figure 2: Distribution of feasibility studies among the neutron facilities

The distribution of measurements among the neutron centres shows slight regional influence; more than half of the requests coming from France-based companies were carried out in France (Fig. 2). There were only two Scandinavian companies that used all available facilities.

During the project BNC focused on the automotive industry and its suppliers. BNC participated in the Automotive Exhibition as an exhibitor and sponsored the Techtogether competition. The Techtogether aims to build closer ties between the automotive firms and the university students. BNC offered a one-day introductory program to the neutron techniques available at BNC for the winner team, which was the Formula Racing Team, Miskolc University.

To strengthen the industrial relationship we organized a one-day conference titled “Science, innovation, competitiveness”, in May 2019. The conference was devoted to applications of neutrons for industry, healthcare and Cultural Heritage. We expected attendees from universities with strong industrial relationships, academia and industry. Research infrastructures, neutron methods and their applications for materials research were presented. Invited speakers covered a wide range of topics using neutron techniques. The conference presentations and a conference video can be reached on the BNC webpage, <https://www.bnc.hu/ind4con19/en/program> and https://www.bnc.hu/?q=industry_day_2019.

Sine2020 partners worked together to prepare a “Sustainability Report” in which we could show what has been achieved and what should be done to ensure legacy. The SINE2020 Sustainability Report can be downloaded from the SINE2020 webpage (www.sine2020.eu).

PERFORMANCE EVALUATION OF THE BORON COATED STRAWS DETECTOR WITH GEANT4

Milán Klausz, Péter Zagyvai

Objective

Building the European Spallation Source (ESS), the most powerful neutron source in the world, requires significant technological advances at most fronts of instrument component design. Detectors are not exceptions. The existing implementations at current neutron scattering facilities are at their performance limits and sometimes barely cover the scientific needs. At full operation, the ESS will yield unprecedented neutron brilliance. This means that one of the most challenging aspects for the new detector designs is the increased rate capability and in particular the peak instantaneous rate capability, i.e. the number of neutrons hitting the detector per channel, pixel or cm^2 at the peak of the neutron pulse. The purpose of this PhD work is to define rate requirements and to characterise the planned detectors, detector systems for ESS instruments to ensure that they fit the high scientific requirements of ESS. The current work focuses on the boron coated straws (BCS) neutron detectors manufactured by Proportional Technologies Inc., a commercial product designed for use in homeland security and neutron science. A detailed Geant4 simulation study of the BCS is presented that investigates various aspects of the detector performance, e.g. efficiency, activation, absorption and the impact of scattering on the measured signal. The suitability of the BCS detector for Small Angle Neutron Scattering (SANS) and direct chopper spectrometry is discussed.

Methods

A generic BCS detector model is implemented for Geant4 simulations. With this, a complex analysis is carried out in order to evaluate various aspects of the BCS detector performance. This study is made in the context of most realistic applications that might be envisaged at ESS. The aim is to have a complete set of generally applicable results. The study includes the efficiency of the detectors, the absorption and activation of the materials thereof, and the impact of the material budget on scattering.

Results

The detection efficiency of a single straw, and even that of complete detector tubes with seven straws are shown to be low, as expected. Therefore, overlapping layers (panels) of detectors are needed to achieve an acceptable efficiency. The cost-efficient number of panels depends on the application and the relevant neutron wavelength range.

The absorption (not resulting in conversion to detectable particles) in B_4C is 6.5–8 times higher than in Al and Cu combined. The absorption from these two structural materials in the detector is in the range of 1.5–4.5% of the incident neutrons depending on the wavelength. Pure unalloyed material was modelled in the study; alloyed materials and impurities may significantly increase it and need to be considered. At lower wavelengths the fraction of neutrons transmitted through the detector is high (50%–60% at 0.6 Å) and therefore absorbent shielding behind the detector is a must for applications below 5 Å.

Neutron activation analysis of such a detector has been implemented. The activation is dominated by copper, as expected, with a cooling time of few days. The radiation background from activated materials will not interfere with the data acquisition. The activation during operation at ESS is not expected to be a limitation for maintenance. The calculated numbers have been presented in a fashion that could be scaled to real applications.

The scattering has been studied in detail, namely its effect on δX , δY , δTOF , $\delta\theta$, $\delta\Phi$, $\delta\lambda$, δE and δQ in terms of the fraction of neutrons that end up as signal, scattered background, transmission through the detector or absorbed and non-detected. The effect of the detector geometry on the natural shape of the resolution function is shown. Scattering is highest at low wavelengths and is significant below the Bragg cut-off. It can be considered to be at acceptable levels for applications such as SANS and diffraction, however, scattering may be significant for applications which are highly sensitive to it such as spectroscopy. Any application for spectroscopy would need detailed consideration of its effect on performance.

A polyethylene “afterburner” block placed behind the detector was investigated and found to increase signal by up to 4%, however, background correspondingly increased up to 15%. Therefore this is not a good solution for most applications. It also re-emphasises the need for the layer of shielding closest to the detector to be made of materials with very low neutron albedo.

Remaining work

This work is a part of the four-year PhD with the same title. The results are well interpreted, published and will be part of the PhD thesis.

Related publication

- [1] M. Klausz, K. Kanaki, P. Zagyvai, R.J. Hall-Wilton, "Performance evaluation of the Boron Coated Straws detector with Geant4", *Nuclear Inst. and Methods in Physics Research*, A 943 (2019), 162463

REDUCTION OF SCATTERED NEUTRON BACKGROUND IN BORON-CARBIDE CONVERTER BASED NEUTRON DETECTOR

Eszter Dian, Péter Zagyvai, Szabina Török

Objective

The European Spallation Source (ESS) aspires to be the brightest neutron source of the world. Its establishment and commissioning requires joint and organised effort of the neutronic community, as well as research and development in fields like neutron instrumentation, especially detector development, in order to make use of the potential of the ESS. In addition, the recent ^3He -shortage necessitates the development of new types of neutron detectors replacing ^3He where it is reasonably achievable. As part of this effort, investigation and development of the Multi-Grid, a novel, solid $^{10}\text{B}_4\text{C}$ -converter-based, Ar/ CO_2 -filled detector is performed. The Multi-Grid detector is a large area neutron detector for chopper spectrometry, invented by researchers of ILL (Institut Laue-Langevin) and now jointly developed by ILL and ESS. Since the intensity of the signal of the inelastic instruments is a few orders-of-magnitude lower than the one of the elastic instruments, the high signal-to-background ratio (SBR) is a key issue for the detectors at these instruments. The aim of the current study is to develop an internal shielding to reduce the intrinsic scattered neutron background of the detector.

Methods

Thanks to the recent development of neutron simulation tools, detailed and realistic Geant4-based Monte Carlo simulation studies were performed for the Multi-Grid detector. For the first time, thermal neutron scattering background sources were modelled in a detailed simulation of detector response. The applicability and background-reduction capacity of typical shielding types like end-shielding and side-shielding, and shielding materials like B_4C , Cd, LiF and Ga_2O_3 have been determined. The background-reduction capacities of common shielding geometries, end-shielding, interstack-shielding and side-shielding are compared by applying a black material. On the basis of the obtained results, optimisation of internal detector shielding was started, in order to increase the SBR via background-suppression.

Results

It is demonstrated that the dominant shielding geometries are the end-shielding, absorbing 10 - 60% of neutrons above 5.1 meV, and the side-shielding, absorbing 5 - 10% of neutrons through the whole energy range. In order to develop a combined internal shielding, common shielding materials B_4C , Cd, Gd_2O_3 and LiF are tested for each shielding type, and 1 mm of B_4C or Cd is proven to provide equally good shielding as the total absorber. It is shown that with these materials as a combination of end-, side- and interstack-shielding, the SBR can be raised by 50 - 106% for the 0.8 - 511 meV region, respectively.

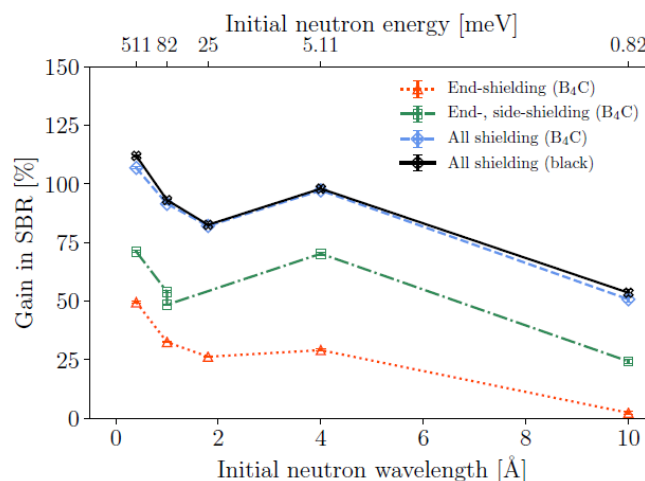


Figure 1: Simulated Signal-to-Background Ratio with combined shielding with boron-carbide compared to black material, normalised to the unshielded reference detector.

Remaining work

This project has been completed.

Related publication

1. E. Dian, K. Kanaki, A. Khaplanov, T. Kittelmann, P. Zagyvai, R Hall-Wilton, *Suppression of intrinsic neutron background in the Multi-Grid detector*, Journal of Instrumentation, **14** Paper: P01021, 24 p. (2019) [doi:10.1088/1748-0221/14/01/P01021](https://doi.org/10.1088/1748-0221/14/01/P01021)

COMPARISON OF MEASURED AND SIMULATED NEUTRON ACTIVATION OF CONCRETE SAMPLES

Dávid Hajdú, Péter Zagvai

Objective

Different shielding concrete samples were studied for the European Spallation Source (ESS). The aim of the current study was to reveal if the nominal composition (provided by the manufacturer) consists enough elements for realistic activation-related safety simulations, or more detailed composition is needed for such purposes. It was also tested if simulations using measured composition with energy-dispersive X-ray fluorescence (EDXRF) technique - as a relatively cheap and easy-to-use analytical technique - can reproduce the measured activity concentration, or different analytical methods are required for this purpose.

Methods

First, neutron activation experiments were carried out at the Budapest Research Reactor. The prepared samples were irradiated for 2 hours. Decay gamma spectra of the samples were measured with a Canberra HPGe detector 5 times after 4 to 16 days of cooling for identifying both short- and long-lived radioisotopes. In total, 30 isotopes were identified from 12 hours (^{42}K) to 13.5 years (^{152}Eu) of half-life.

EDXRF elemental analysis measurements were carried out with an Epsilon 5 triaxial polarising XRF device.

Monte Carlo N-Particle eXtended (MCNPX) and Cinder90 codes were used for irradiation simulations. The nominal and the EDXRF-based compositions were used in the simulations. Simulation results were then compared to the measured values.

Results

The comparison of the measured total activity concentration and the simulated ones with nominal composition and with EDXRF-based composition is presented in Figure 1 for the reference concrete. EDXRF-based curves show better agreement with the measured data than nominal ones; the latter produced only 8-27% of the measured activity concentrations. Beside these promising results, it must be noted that the parent elements of the two measured neutron activation products with the longest half-lives: ^{60}Co (5.3 y) from cobalt and ^{152}Eu (13.5 y) from europium were not measured by EDXRF. Europium was below detection limit (1 ppm), while cobalt was not measurable because of the spectral overlapping with the high iron content of the samples. For this reason, a complementary analytical method is required for the investigation of concretes from radioactive waste management point of view. For example, different XRF techniques with higher spectral resolution might enable the measurement of cobalt.

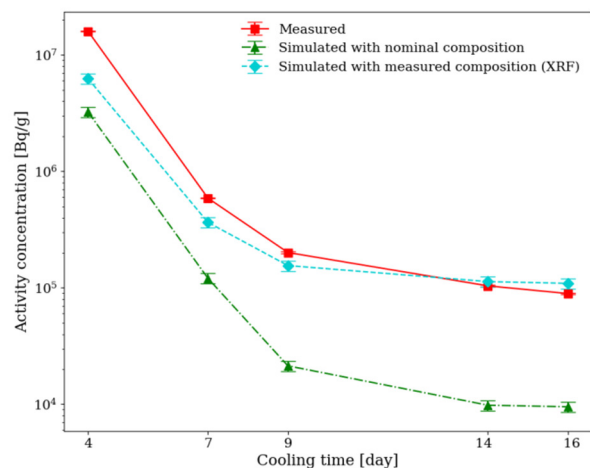


Figure 1: Measured total activity concentrations of the reference concrete after irradiation in the BRR

Remaining work

This project has been completed, but it is possible that further XRF measurements will be carried out on concrete samples, focusing on the measurement of the identified key elements.

Related publications

Manuscript is submitted to Journal of Neutron Research.

A manuscript of a more comprehensive study was prepared as well, including these results. It is under submission, currently available on arXiv: arXiv:1909.12794.

NEUTRONIC DESIGN OF THE FIRST BUILT EXPERIMENTAL CAVE FOR THE EUROPEAN SPALLATION SOURCE

Eszter Dian, Tamás Bozsó, Szabina Török, Péter Zagyoai, Viktória Sugár

Objective

The Neutron Macromolecular Diffraction (NMX) Experimental Cave is being built as first of a kind in the European Spallation Source (ESS) in Lund, Sweden. The experimental cave provides the biological shielding to personnel staying outside its walls. The task for 2019 was the justification of the compliance with radiological rules of ESS of the detailed cave design. This implies modelling for solid walls and estimate the effect of chicanes and cable inlets. A new analytical model was developed to calculate dose increases around chicane areas. The cable inlets were optimized by using additional steel plates and *Mirrobor*TM covers.

Methods

The cave and its door have to comply with radiological constraint of 3 $\mu\text{Sv/h}$ contact dose rate at every 20cmx20cm surface area. This year the final task before the approval of the detailed cave design was the modelling of transmission through multileg chicanes of the 90 cm concrete wall and the cable inlets.

Results

The existing cave model was modified many times since numerous additional engineering constrains were issued by ESS regarding the envelope, the crane access and the hutch position. As already decided in 2019, cave walls and roof are made of reinforced concrete structure assembled from premanufactured units. Value engineering meant also cost optimization. For this purpose, other material (like boron coating of walls) than standard 2,3 density concrete was supposed to be avoided as much as possible except for the steel door and cable inlets.

The detailed study using MCNP6 simulation of NMX experimental cave shielding of the detailed design confirmed that the proposed version with 90 cm concrete wall thickness and a 65 mm steel door behind a blade wall provides sufficient shielding at all the operational (H1) and accidental (H2) scenarios. The simulated dose rates outside of the experimental cave do not exceed the predefined 1.5 $\mu\text{Sv/h}$ (safety factor 2) limit for the Monte Carlo simulations and 1 $\mu\text{Sv/h}$ (safety factor 3) limit for the analytical calculations.

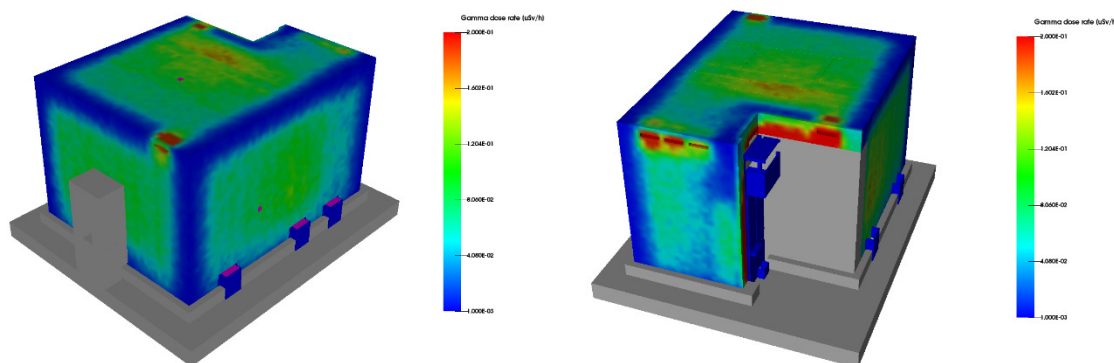


Figure 1: Contact dose rate at front and rear side of experimental cave in accidental scenario with strong neutron scatterer. After optimization the highest dose rate at the lower door cable inlet could be reduced to 1.48 $\mu\text{Sv/h}$.

Remaining work

By April 2020 the full cave of 330m³ concrete has been assembled. The radiological report on the cave was approved and is suitable for licencing. The shielding calculations for the 140 m guide and the two chopper pits of NMX have to be completed in 2020

Related publications

- [1] T. Bozsó, E. Dian and Sz. Török: NMX Cave - Shielding calculations report, 2019ESS-1066585
- [2] <https://www.youtube.com/watch?v=6ohJVWkfp34&feature=youtu>

CONCRETE ACTIVATION STUDY FOR THE EUROPEAN SPALLATION SOURCE

Eszter Dian, Katalin Gméling, Dávid Hajdú, János Osán, Péter Zagyoai

Objective

The European Spallation Source (ESS) aspires to be the brightest neutron source of the world, which requires joint and organised effort of the neutronic community, as well as research and development in fields like shielding.

A new PE-B4C-concrete (polyethylene, boron-carbide) has been developed as part of the SINE2020 project in order to improve the neutron absorption effect of concrete below 10 MeV, where iron has resonances in the cross section. It is essential to know the activation of the shielding material, like concrete and metal components, considering both short-term effects on exposure of personnel during the operation phase, and long-term effects on the decommissioning of the ESS facility. The aims of the current study are to compare the neutron activation properties of the new PE-B4C-concrete to those of the reference concrete, to quantify the impact of the trace elements on the produced activity and the decay gamma background, and to obtain concrete composition for performing conservative Monte Carlo activity simulations.

Methods

In order to take into account the activation products of shielding concretes more realistically in Monte Carlo simulations, the composition of all three concretes were determined with three analytical methods (NAA, PGAA and EDXRF). Based on the performed neutron activation measurements, the 15 most important gamma emitting radioisotopes were identified, for the comparison of their measured and simulated activities. Activation simulations were performed with MCNP and Cinder90 codes for all the measured and nominal compositions (given by the manufacturer) of the three concretes.

The importance of realistic material cards was also demonstrated in terms of radiation safety: decay gamma dose rates were calculated for a single concrete wall of the ESS West Hall with a realistic irradiation scenario for the Reference concrete and the current concrete composition used for bunker simulations in the ESS.

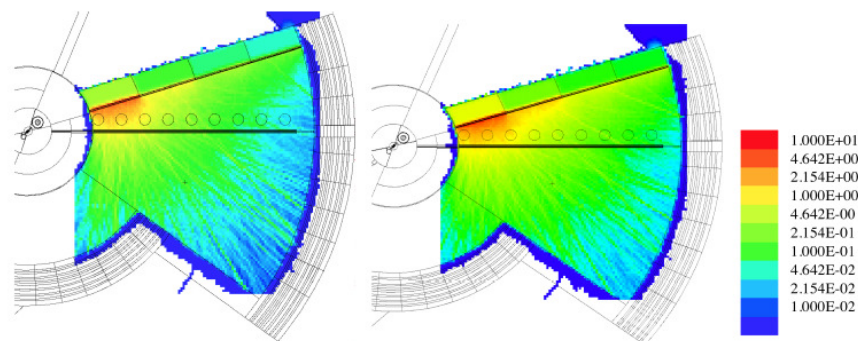


Figure 2: Simulated dose rate maps [$\mu\text{Sv/h}$] from the segmented axial wall made of Reference concrete. Simulations were performed with nominal (left) and recommended (right) initial concrete compositions.

Results

It was proven that the simulations based solely on the nominal composition underestimate the measured activities with one order of magnitude, highlighting the importance of trace elements in terms of activation. On the basis of the measured composition, MCNP material cards were developed and validated for the PE-B4C- and the Reference concretes that are recommended for activation calculations.

In terms of decay gamma dose rates, it was found that after 3 days of cooling i.e. in an assumed maintenance period of an ESS instrument, the decay gamma dose rates simulated with the recommended, measurement-based material card of the Reference concrete resulted in 29-72% higher dose rates than the nominal composition which does not contain trace elements. This underlines that reliable input compositions are essential for activation simulations and that the presence of trace elements can enhance the simulated activities and decay gamma doses, approaching the double conservative allowance of Monte Carlo safety simulations, required in the ESS.

Remaining work

This project has been completed; acceptance of final paper is pending.

Related publication

[1.] Report D8.16 SINE2020

FULL SIMULATION OF DETECTOR PERFORMANCE OF NEUTRON INSTRUMENTATION AT ESS

Milán Klausz, Péter Zagyvai

Objective

Building the European Spallation Source (ESS), the most powerful neutron source in the world, requires significant technological advances at most fronts of instrument component design. Detectors are no exception. The existing implementations at current neutron scattering facilities are at their performance limits and sometimes barely cover the scientific needs. At full operation the ESS will provide unprecedented neutron brilliance. This means that one of the most challenging aspects for the new detector designs is the increased rate capability and in particular the peak instantaneous rate capability, i.e. the number of neutrons hitting the detector per channel, pixel or cm² at the peak of the neutron pulse. The purpose of this PhD work is to define rate requirements and to characterise the planned detectors and detector systems for ESS instruments to ensure that they fit the unprecedentedly high scientific requirements of ESS. The instruments being studied are LOKI, a Small Angle Neutron Scattering (SANS) instrument using the Boron Coated Straws (BCS) detector technology, and BIFROST, an indirect geometry, cold neutron spectrometer employing a complex multi-channel analyser-detector system.

Methods

Full simulation models of the LOKI and BIFROST instruments from source to detector position were implemented with the use of several simulation software packages. These models were used to carry out analyses of the detector rate requirements and rates in different operational scenarios. The simulations schema in both cases consisted of the simulation of the beam transport and conditioning system using the pre-existing McStas model of the instrument, and the Geant4 simulation of the scattering characterization system including various experimental samples and the detectors. The connection between the two simulation software is facilitated by the MCPL package. In addition, the scattering characterization system of the BIFROST instrument was also implemented in McStas to enable comparison of the McStas and Geant4 simulation results. A generic BCS detector model was also implemented for Geant4 simulations. With it, a complex analysis was carried out in order to evaluate various aspects of the BCS detector performance.

Results

The analysis of the BCS detectors showed that the detection efficiency of a single straw, and even of complete detector tubes with seven straws are all low, as expected. Therefore, overlapping layers of detectors are needed to achieve a decent efficiency. The absorption in B₄C is 6.5–8 times more than in Al and Cu combined. The absorption from these two metal support materials in the detector is in the range of 1.5–4.5% of the incident neutrons depending on the wavelength. At smaller wavelengths the fraction of neutrons transmitted through the detector is high (50%–60% at 0.6 Å) and therefore absorbent shielding behind the detector is a must for applications below 5 Å. Activation analysis of such a detector has been implemented. The activation is dominated by copper, as expected, with a cooling time of a few days. The radiation background from activated materials will not interfere with the data acquisition. The activation during operation at ESS is not expected to be a limitation for maintenance. The scattering has been studied in detail, and found to be highest at low wavelengths and significant below the Bragg cut-off. It can be considered to be at acceptable levels for applications such as SANS and diffraction, but may be considerable for applications which are highly sensitive to it such as spectroscopy.

On the question of using BCS detector tubes for the LOKI instrument, it was found that for instrument configurations representing realistic operational conditions, the instantaneous detection rate can be as high as 458 kHz for a functional unit of the detector, a single straw. Given that such a straw is expected to start saturating at 50–100 kHz, these results show that a detector system of BCS tubes with the conventional parameters cannot satisfy the high requirements set by the exceptional flux at the ESS since it would limit the scientific performance at higher source power.

The incident detector rates of the BIFROST instrument were determined for various samples and instrument configurations. For parameters representing worst-case conditions, it was determined that the instantaneous rate can be on the order of 1–1.7 GHz for a single detector tube with the time-averaged rates of 40–70 MHz, well over the capabilities of the standard He-3 tubes. The results of the McStas and Geant4 simulations of the scattering characterization system were compared using various single crystal samples. The results showed almost perfect agreement, with the only exception being the transmission through the sample where a difference of 10% is found in one case, due to the more detailed modelling of absorption in Geant4.

Remaining work

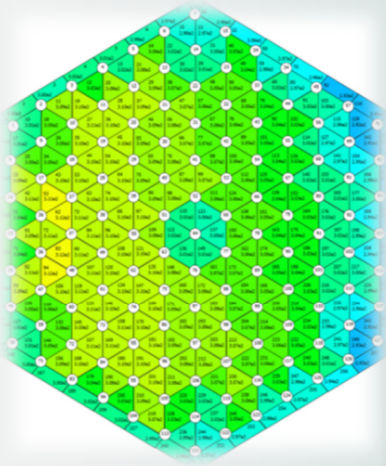
This project is a part of the four-year PhD with the same title. The results are well understood, published or being published. The only remaining work is finishing the PhD thesis which summarises these results.

Related publications

- [1] M. Klausz, et. Al.: *A study of the indirect geometry cold neutron spectrometer, BIFROST, from neutron source position to detector position*, J. Appl. Cryst. Submitted.
- [2] M. Klausz, K. Kanaki, P. Zagyvai, R.J. Hall-Wilton: *Performance evaluation of the Boron Coated Straws detector with Geant4*, Nuclear Inst. and Methods in Physics Research, **A 943**, 162463 (2019)
- [3] K. Kanaki, M. Klausz, et. Al.: *Detector rates for the Small Angle Neutron Scattering instruments at the European Spallation Source*, Journal of Instrumentation, **13:(07)**, P07016 (2018)



II. RESEARCH AND DEVELOPMENT RELATED TO NUCLEAR POWER PLANTS



ACTIVITIES OF EK AS MAIN CONSULTANT OF PAKS NPP

János S. Jánosy, Zsolt Kerner, Tamás Pázmándi, Katalin Kulacsy

Objective

MTA EK, together with NUBIKI (Nuclear Safety Research Institute), has been the main consultant of Paks Nuclear Power Plant (NPP) for over a decade. The main consultant supports the NPP in solving safety-related technical issues and helping with strategic planning. The work is done by the most experienced and highly qualified members of the staff on the basis of yearly work plans. In 2019 MTA EK undertook the following separate tasks, done by different groups of experts:

- determination of the contribution of proton activation products to the activity concentration in and staff dose rates caused by the primary coolant;
- determination of the activity concentration in the secondary circuit and its dose consequences;
- elaboration of a load-follow methodology that preserves the primary circuit (despite Paks NPP does not take part in load-follow for the time being).

Methods

Each task required different method, which can be summarised as follows.

Water and gas samples from the primary circuit were analysed by gamma-spectrometry. Decay curves were fitted to the peak intensities in the measured spectrum series. Total dose rates and gamma-spectra were measured in the water sampling room. Build-up factors were determined by MCNP simulation.

Due to the primary to secondary circuit leakage in the steam generator tubes, radioactive material can emerge in the secondary circuit during normal operation. Activity transport model was established and conservative assumptions were used in model calculations to determine activity concentration values in the secondary circuit.

Smaller changes in reactor power are performed while keeping the steam pressure constant, which allows greater temperature changes in the primary circuit, leading to aging of the structures. In the present work, the cold leg temperature was kept constant despite the broad range of the reactor power, which could be done relatively easily just dedicating different steam pressures for each level of the actual unit power. The strategy was based on implementing load-follow using both turbines and changing the way the steam pressure controller produced its reference signal. The full-scope simulator was used to test the strategy.

Results

The individual results of the tasks were the following.

Three proton activation products were identified in the primary circuit: ^{13}N , ^{18}F and ^{11}C . They are short-lived positron emitters. Their total activity concentration is 10 MBq/kg. The activity concentration of the first two basically depends on the reactor power and is slightly influenced by water purification. The activity concentration of ^{11}C also depends on the boric acid concentration. This indicates that it is primarily formed in reaction $^{11}\text{B}(p,n)^{11}\text{C}$. Proton activation products cause approx. 5% of personnel dose during water sampling.

It was demonstrated with calculations that activity concentration in the secondary circuit could considerably increase due to the decrease of leakage from secondary circuit, but neither dose rates in the plant nor releases of radioactive material to the environment could increase significantly. It was found that activity concentration in secondary circuit depends on the activity concentration in primary circuit, half life of the nuclide and efficiency of water clean-up systems. For tritium also chemistry program has a significant role. Revision of operational limits for activity concentration in secondary circuit was recommended accordingly.

By holding the temperature of the cold leg constant during load follow between 72% and 100% of the nominal reactor power, the average temperature of the primary coolant changed by a maximum of 3.5 °C and the temperature of the hot leg by a maximum of 6.7 °C. This is a more favourable strategy than to hold the steam pressure constant.

Remaining work

The 2019 tasks were finished.

Related publications

- [1] Zs. Kerner, I. Almási, P. Kirchknopf, T. Pázmándi, P. Zagytai: *Proton activation products in the primary circuit*, MTA EK TFO-2019-751-05-01-M0, in Hungarian (2019)
- [2] S. Deme, T. Pázmándi: *Activity concentration in the secondary circuit and evaluation of its radiological consequences*, MTA EK TFO-2019-751-06-01-M0, in Hungarian (2019)
- [3] J.S. Jánosy: *Load follow that preserves the primary circuit*, MTA EK TFO-2019-751-07-01-M0, in Hungarian (2019)

RELEASE OF THE FUROM 2.2 CODE VERSION

János Gadó, Ágnes Griger, Katalin Kulacsy

Objective

The FUROM code was developed in the institute about 20 years ago for the analysis of fuel behaviour in VVER-440 reactors. The code was successively improved using up-to-date results of measurements and state-of-the-art models. As a consequence, several official versions were released over the years. The objective of the present work was to prepare a new advanced version of the code: FUROM 2.2.

The work was financed by MVM Paks NPP Co.

Methods

New models were selected based on extensive review of the literature and the available experimental data. They were then built in and tested. Bug fixes constituted an important part of the work as well. Special attention was given to increase the transparency of the code for future programmers. The code documentations (model description [1], programmer's guide [2], users' guide [3]) were upgraded and the validation was repeated [4].

Results

In 2019 the following works were carried out:

- introduction of a simplified calculation of the radial power and burn-up profiles which greatly reduced computation time,
- introduction of calculations to obtain the radius of each pellet ring,
- inclusion of a new Russian cladding creep model,
- revision of the output files of the code.

The documentation of FUROM 2.2 was released [1], [2], [3], [4].

Remaining work

Feedback from code users will be taken into account in further code development.

Related publications

- [1] J. Gadó, Á. Griger, K. Kulacsy: *Physical models of the FUROM 2.2 code*, MTA EK FRL-2018-713-02-01-M0, in Hungarian (2019)
- [2] J. Gadó, Á. Griger: *Programmers' Guide to the FUROM 2.2 code*, MTA EK FRL-2018-713-02-02-M0, in Hungarian (2019)
- [3] J. Gadó, Á. Griger, K. Kulacsy: *User manual of the FUROM 2.2 code*, MTA EK FRL-2018-713-02-03-M0, in Hungarian (2019)
- [4] J. Gadó, Á. Griger, K. Kulacsy: *Validation of the FUROM 2.2 code* MTA EK FRL-2018-713-02-04-M0, in Hungarian (2019)

SURET CALCULATION OF A NEW TYPE OF FUEL ASSEMBLY HAVING SPACER GRID WITH MIXING VANE

Áron Vécsi, Gábor Házi

Objective

A new type of fuel assembly will be introduced at Paks Nuclear Power Plant in order to improve its fuel economy. The new fuel rods and the claddings are thinner than the ones used now and some of the spacer grids will be supplemented by mixing vanes to intensify the mixing in the assembly. Before starting a fuel cycle with the new design, subchannel calculations have to be carried out to prove that the application of the new fuel will not result in the violation of operational limits during the fuel cycle.

Methods

To simulate the behaviour of mixing vanes we used our SURET (SUBchannel REactor Thermohydraulics) subchannel analysis code, which has been developed based on COBRA 3c. SURET differs from COBRA by the solution of the energy equation and makes possible to locally modify the resistance factors of the spacer grids to model the mixing vanes.

Results

SURET input file has been created to the new fuel design, and benchmark calculations have been carried out to prove that SURET is able to provide reasonably accurate solutions for the new geometry. Calculations were verified by separate effect tests and validated by comparing their results with the ones obtained by Computational fluid Dynamics (CFD) calculations. The difference of temperature maxima based on SURET and CFD calculation are less than 0.15 °C. Also, the distributions of outlet water temperature obtained by SURET fits CFD data reasonably well as it is shown in Figure 1. So, in this stage, we proved that SURET is able to calculate the thermohydraulic parameters of the new fuel design with reasonable accuracy.

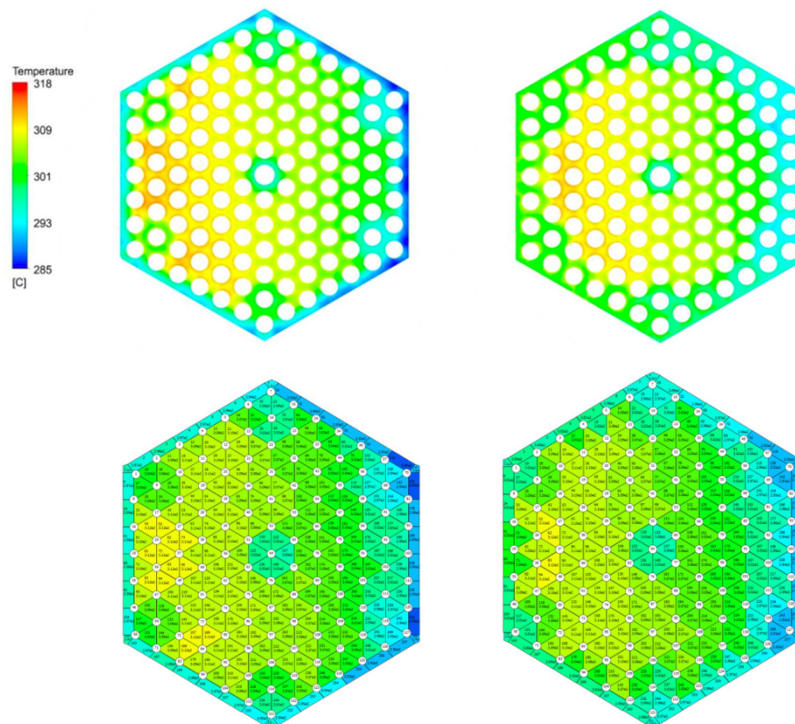


Figure 1: Distributions of outlet water temperature (top: CFD calculation; bottom: SURET calculation; left: without mixing vane; right: with mixing vane)

Remaining work

After a feasibility study, next year we are going to integrate SURET into the VERONA on-line core monitoring system.

Related publications

- [1] Á. Vécsi: Verification test for the new reduced rod diameter fuel assembly, EK-RMSZL-2019-728-01/01, in Hungarian (2019)
- [2] Á. Vécsi: Mixing test in the VVER-440 type reactor's reduced rod diameter fuel assembly by subchannel analysis, EK-RMSZL-2019-728-02/01, in Hungarian (2019)
- [3] Á. Vécsi: Effect of spacer grids with mixing vanes on mixing, EK-RMSZL-2019-726-01/01, in Hungarian (2019)

WORKING FLUIDS

Attila R. Imre

Objective

Energy harvesting from low-temperature heat sources is a more and more important part of sustainable energy production. Although there are several methods to turn low-temperature heat to electricity, at least two major issues should be considered concerning these methods. First, there is no “general” solution for the problem; even two different heat sources with the same temperature values might require two different techniques to utilize their heat content. Second, although technically it is possible to turn low-enthalpy heat to electricity, the efficiency of this conversion is usually very low, while investment and maintenance costs are relatively high, causing feasibility problems. One of the methods might be used for low-temperature energy harvesting is the use of small-to-medium power plants based on Organic Rankine Cycle or ORC (a thermodynamic cycle similar to the traditional water/steam cycle of thermal power plants, but using low-boiling point organic materials instead of water as working fluid). A crucial point to design an economically feasible ORC-based power plant is the proper choice of working fluid. We are already very close to our main objective, namely to establish a proper method for working fluid selection, based on parallel efficiency maximization and cost-minimization.

Methods

Analytical method, special computer codes and some commercial codes and databases (ThermoC, NIST Webbook, Cycle-Tempo) were used for the calculations.

Results

Thermodynamic cycles can be used to convert heat to work; following the cycle, work can be turned to electricity. A crucial step of this conversion is the expansion of the hot, pressurized substance (pure vapour or rarely pure liquid in the initial state); this expanding material can move turbines or other expansion machines. Depending on the working fluid, the expanding material can move through vapour (saturated or overheated) or mixed (vapour and liquid) states. Materials staying in pure vapour phase during expansion are often marked as “dry” fluids, while others, expanding into mixed vapour-liquid phase, are marked as “wet” ones. The exact state of the expanding fluid is crucial for the design of the whole ORC layout, therefore we characterized the possibilities of expansion routes for various classes of working fluids [1].

In the next step, we established a method to distinguish between dry and wet fluids, using basic physical-chemical properties. According to our method, one has to know only the critical temperature and the isochoric molar heat capacity (in a given reduced temperature) of the substance to classify it as wet or dry. In this way, fluids – previously not used as working fluids – can easily be selected or rejected as novel working fluid candidates [2].

Finally, a novel method has been proposed to find the “best expanding” working fluid for a given heat source and heat sink pair. Best expansion route runs in the dry region and terminates very close to the saturation boundary; in this case, the need to use special parts to deal with the problems caused by the potential presence of liquid droplets (like droplet separator or superheater) or with the problems caused by the presence of superheated dry steam (recuperative or regenerative heat exchangers) can be minimized solely by the proper choice of the working fluid [3].

Additionally, two papers related to this topic but containing results already included in the 2018 report have been published in 2019 [4,5].

Remaining work

For the next year(s), we would like to apply these results to design thermodynamic cycles for energy-harvesting of low-temperature heat sources (like the “tertiary” waste heat of a nuclear power plant). Also, we would like to include the effect of internal losses (caused by the expanders, pumps and heat exchangers) to our working fluid selection method.

Related publications

- [1] A. R. Imre, A. Groniewsky: *Various ways of adiabatic expansion in Organic Rankine Cycle (ORC) and in Trilateral Flash Cycle (TFC)*, *Zeitschrift für Physikalische Chemie*, 233 :577–594, (2019)
- [2] G. Györke, A. Groniewsky, A. R. Imre: *A simple method to find new dry and isentropic working fluids for Organic Rankine Cycle*, *Energies*, 12: 480 (2019)
- [3] A. R. Imre, R. Kustán, A. Groniewsky: *Thermodynamic Selection of the Optimal Working Fluid for Organic Rankine Cycles*, *Energies*, 12: 2028 (2019)
- [4] A.R. Imre, A. Groniewsky, G. Györke, A. Katona, D. Velmovszki: *Anomalous Properties of Some Fluids – with High Relevance in Energy Engineering – in Their Pseudo-critical (Widom) Region*, *Periodica Polytechnica Chemical Engineering*, 63: 276-285 (2019)
- [5] G. Györke, A.R. Imre, A.R.: *Physical-chemical Background of the Potential Phase Transitions during Loss of Coolant Accidents in the Supercritical Water Loops of Various Generation IV Nuclear Reactor Types*, *Periodica Polytechnica Chemical Engineering*, 63: 333-339 (2019)

NUMERICAL MODELLING OF FUEL ROD BEHAVIOUR

Eszter Barsy

Objective

This PhD research is aimed to model the azimuthal distribution of oxidation of the Zr-1%Nb cladding. This is a standalone code (numerical model), which simulates the oxidation of a ruptured cladding in steam. This kind of modelling is useful for supporting the planned redefinition of acceptance criteria.

Methods

A model was developed and written into a code to calculate the oxidation of the non-uniformly ballooned fuel rod in steam (Figure 1). The cladding is divided into 32 sections around the circumference and each into 400 laminae radially. First, the diffusion of steam (through the rupture into the gap) is calculated, while the outer cladding oxidation starts. When the steam reaches a section, the oxidation is calculated for the inner side, too. The program calculates the oxidation in two steps: the amount of oxygen that forms the oxide layer is determined according to the new E110 opt oxidation kinetics. In the next step, the radial distribution of that oxygen is calculated using diffusion model.

The F95 program consists of a main part and a subprogram (for steam calculation). Most initial values are taken from input files so they can be changed at any time without having to recompile the program. The code contains three main, nested cycles: one by section, one by time step, and the third by laminae. Oxygen diffusion and oxidation kinetics are calculated according to these loops. The output values are oxygen concentration, oxygen mass, oxide layer thickness, equivalent cladding reacted (ECR).

Results

Oxidation rates for different geometries and scenarios were calculated. Figure 2. shows a typical radial distribution of oxygen in the cladding. The results clearly showed that the degree of local oxidation is significantly different for uniform and non-uniform geometry. The evaluation of the calculated oxide layer thickness corresponded to the experimental results on mechanical load-bearing capacity.

Additional modules can be added in the future, for example calculating transients and extending the model geometry axially.

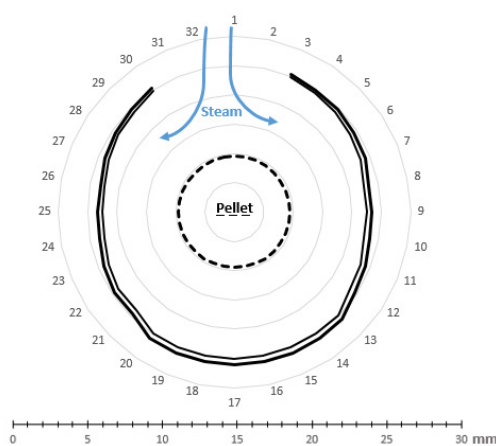


Figure 1: Geometry applied to the model

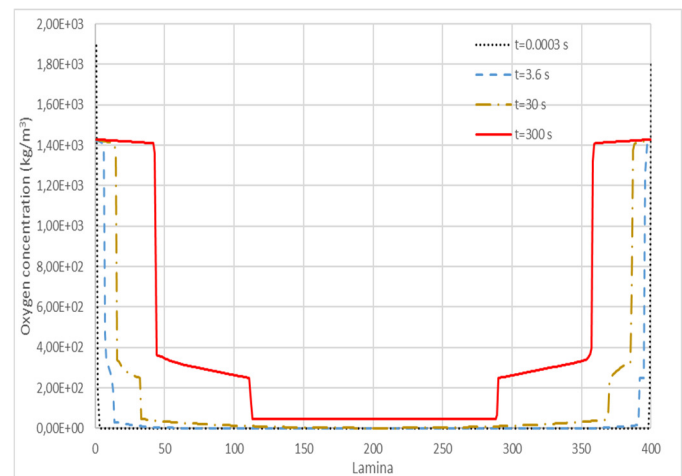


Figure 2: Calculated time evolution of oxygen concentration in the cladding

Remaining work

The project will be continued in 2020.

NUMERICAL SIMULATION OF MANDREL TESTS OF ZIRCONIUM CLADDING SAMPLES WITH DIFFERENT HYDROGEN CONTENTS

Richárd Nagy

Objective

Several measurements were carried out to reveal plastic behaviour of Zr1%Nb cladding (E110 and E110G). Plasticity of these materials depend on the hydrogen content of the samples. Finite element model of mandrel test has been developed in 2017. The purpose of this research was to find appropriate plastic material properties and calculate stress-strain curve from actual measurements. Secondary aim was to calculate higher temperature measurement.

Methods

Finite element method was used to simulate room-temperature and higher temperature mandrel tests on E110 and E110G nuclear cladding materials. In 2017, a mandrel 3D geometry was developed with identical scale. Quad8 elements were used to build tools and samples of mandrel tests. Samples were defined by 7200 elements, such as plastic materials with a Youngs-modulus as 93850 MPa, with a Poisson's-ratio as 0.35. Density was defined as 6.55 gcm⁻³. Effective friction coefficient was found to validate the simulation on pure (as received) samples.

Thermal equations did not give acceptable fitting to the measurements, because all physical parameters depend on the temperature and not all functions are available. To avoid these missing parameter-functions, a constant value was used for these calculations and it led to an unsuccessful simulation.

A reference plastic model curve was used to simulate pure materials and a single parameter transformation, the so called "n"-transformation, was found to calculate different plastic properties of hydrogenized sample.

$$(\sigma, \varepsilon) \rightarrow \left(n\sigma, \frac{\varepsilon^n}{n} \right) \quad (\text{Formula 1.})$$

A relationship between "n" and the amount of occluded hydrogen in the sample was determined by using Formula 1. to fit calculated curves to the measured curves.

Results

A finite element method simulation was successfully developed to calculate mandrel tests. The calculated result was fitted to the E110 and E110G mandrel measurement data. Fitting is seen in the left graph of Figure 1. To handle plastic behaviour an "n" transformation of plastic model stress-strain curve was found. A relationship between "n" parameter and hydrogen content was described with two linear curves (red line on left graph of Figure 1).

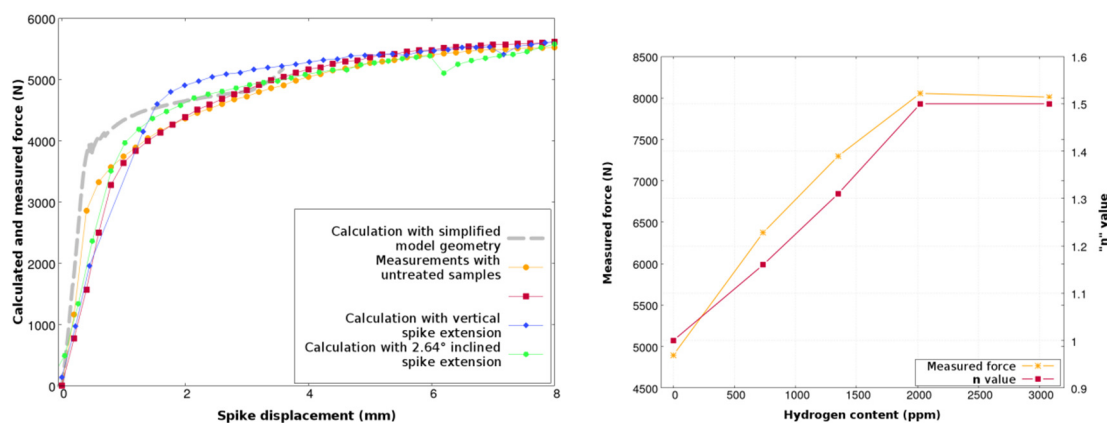


Figure 1: left figure shows calculated and measured stress strain equivalent curves, right figure shows the relationship between the maximum force and the "n" value.

Remaining work

High temperature parameters must be measured to simulate higher temperature mandrel tests on pure samples and the code with proper parameter-functions has to be re-run.

Related publications

- [1] R. Nagy, M. Király: *Finite element simulation of cladding tube mandrel tests*, MTA-EK-FRL-2017-236-1-1-M0, in Hungarian (2017)
- [2] R. Nagy, D. Antók, M. Király, L. Tatár: *Finite element simulation of mandrel tests with pre-hydrogenated samples*, MTA-EK-FRL-2018-236-1-1-M0, in Hungarian (2018)

SOLUTION OF THE VVER-1000 FULL CORE CALCULATION BENCHMARK BY THE KARATE CODE SYSTEM

Emese Temesvári, György Hegyi, Gábor Hordósy, Csaba Maráczy

Objective

The Full Core Benchmark is a two-dimensional (2D) calculation benchmark based on the VVER-1000 reactor core cold state geometry, taking into account the geometry of explicit radial reflector. The main task of this benchmark is to test the pin by pin power distribution in fuel assemblies that are placed mainly at the border of the VVER-1000 core. The test was carried out by the KARATE-1200 code system which is used to analyse the core behaviour of the new VVER-1200 units, so the results are essential for the verification of this calculation tool. The benchmark was specified within the framework of Atomic Energy Research (AER), the organization for scientific cooperation of the VVER user countries.

Methods

In the KARATE-1200 code system the calculation is grouped into levels which are connected to the higher one through parametrized data libraries. Its computational levels are the following:

- The MCNP Monte Carlo code is used to calculate the albedo type boundary conditions at the edge of core reflectors.
- The MULTICELL 2D deterministic neutron transport calculation is applied for an assembly, or an assembly with surroundings. It generates few group constants for higher levels.
- Core calculations are made with the GLOBUS nodal code using the homogenized few group cross sections of assemblies. The result of the core calculations provides flux boundary conditions for the inhomogeneous type fine mesh diffusion calculations.
- The assembly and its vicinity are simulated with the SADR fine mesh code using the homogenized few group cross sections of pin cells.

Results

The fictitious loading of the VVER-1000 has been calculated, which contains unburnt fuel assemblies. The detailed radial reflector treatment is illustrated in Figure 1. The KARATE pin wise normalized power distributions (k_k) were compared to the reference Monte Carlo results. Figure 2 shows the statistical evaluation of the k_k differences. The standard deviation is equal to 0.016. Satisfactory agreement was found.

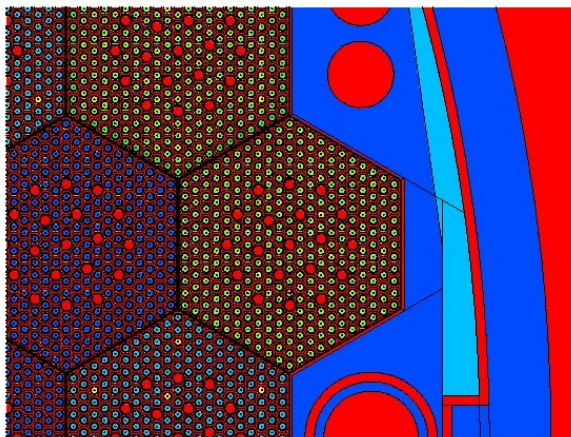


Figure 1: The detailed MCNP model of the VVER-1000 reflector

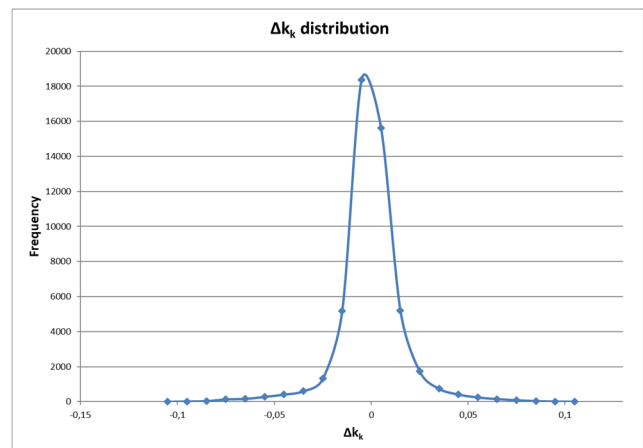


Figure 2: Distribution of k_k differences between KARATE and the reference Monte Carlo calculation

Remaining work

No work remained on this particular test calculation.

Related publication

- [1] E. Temesvári, Gy. Hegyi, G. Hordósy and Cs. Maráczy: *Solution of the VVER-1000 Full Core Calculation Benchmark by the KARATE Code System*, Proceedings of the 29th Symposium of AER, Mochovce, Slovakia, October 14-18, 2019 ISBN 978-963-7351-32-7, pp. 77-87

THE EFFECT OF CHEMICAL COMPOSITION OF CONCRETE ON ITS LONG-TERM PERFORMANCE IN AN IRRADIATED ENVIRONMENT (V4-KOREA RADCON)

László Szentmiklósi, Katalin Gméling, Veronika Szilágyi, Zoltán Kis, Ildikó Harsányi, Boglárka Maróti, Tamás Fekete

Objective

During the construction of the new nuclear power plant (NPP) units of Paks II, the concrete structures will be made preferably from domestic raw materials. For this reason, we have to prepare a suitable recipe for radiation-resistant, durable concrete with low activation susceptibility. The key to achieving that goal is the careful selection of the raw materials (gravel and sand) based upon the compositional data obtained by analytical and petrological methods. Analysis of the chemical composition of the concrete surrounding the reactor vessel is important because it is exposed to high flux gamma and neutron radiation, so the constituents can be substantially activated. Due to the neutron radiation, the high-neutron-capture-cross-section nuclides with short and long half-lives become highly radioactive during the reactor operation time, while isotopes with long half-lives remain radioactive for many years following the reactor shutdown.

Results

(1) Neutron flux characterization and determining the optimum circumstances of irradiation

Neutron fluxes inside the vertical channels of the Budapest Research Reactor are being characterized by irradiating an appropriately chosen set of metal foils. This procedure has to be done for each of the irradiation channels in the beryllium reflector of the BRR, where the parallel irradiations of the concrete blocks are planned to be performed. An analytical calculation procedure of the detailed flux measurements was worked out, while related Monte Carlo calculations have just been started. The temperature is also to be monitored during activation with heat stamps.

(2) Prediction of the neutron-induced sample activity

To predict and plan the activities of samples, irradiation simulations have to be done. Due to neutron irradiation, the samples become structurally damaged and also radioactive. The irradiation will be designed to make possible the subsequent post-irradiation studies. For the calculations, one requires the composition data of the samples from PGAA and NAA measurements, the neutron flux energy distribution and good quality data libraries of possible nuclear reactions. All these are fed into the FISPACT computer code. All necessary inputs are available, and initial calculations gave some agreement with the pilot measurements, but it has to be calibrated and verified again, due to the forthcoming reactor fuel reshuffling, to validate the calculation for future use.

(3) Material characterization studies

To provide input to step (2), we continued the geochemical categorization and characterization of the domestic concrete raw materials (sands, gravels, cement, additives) by our nuclear analytical techniques. We also measured the compositions of all samples provided by our project partners. Prompt gamma activation analysis (PGAA), instrumental neutron activation analysis (NAA) and macro-microscopic petrographic investigations were performed at MTA EK, while the heavy mineral studies were performed by a subcontracted external expert. With the finalizing of the petrographic investigations, the macro-microscopic and heavy mineral studies were completed. The results make up a comprehensive dataset.

Petrographic investigations were done on gravel samples from one remaining region (SW Hungarian). Heavy mineral studies were concluded on separated samples from all the 16 gravel mining sites. Two main regions were compared for sand activation properties: the Mid-Danubian and the NW Hungarian regions (observations in 125–250 μm and 63–125 μm sieve fractions). The heavy mineral assemblages of the two investigated regions show slight differences. The main difference is the lithofragment-content, which is determined by the high limestone-carbonate clast ratio at the NW Hungarian localities, while other (metamorphic) rock types are represented with similar abundances in the two regions. There are much smaller deviations in the NAA spectra of translucent heavy minerals. Opaque minerals, siderite, pyroxenes, and hornblende are more characteristic in Mid-Danubian sediments, while epidote and zoisite-clinozoisite are more common in the NW Hungarian region. It is consistent with the higher activation potential of sand from the Mid-Danubian region compared to sand from the NW Hungarian region.

Neutron-based elemental analysis and activation assessment (NEAAA) was performed on types of cement from different suppliers, additives (hematite, barite, magnetite) and aggregates from Hungarian rock mines, mostly andesite and some basalts (from Recsk, Cserkő-bánya, Tálya, Sárospatak, Bercel, and Szanda).

(4) As an unforeseen field of collaboration, the degradation of shielding concretes of NPPs was studied by dynamic thermal-neutron radiography. Experimental gamma-irradiated recently prepared/hardened cement samples were prepared by the Czech partner using gamma-irradiation in Minsk, Belorussia (in absence of neutrons). Structural damage of cement-based materials due to gamma irradiation was observed by direct measurement of water uptake during imbibition. The process could be correlated with the nano-microscale porosity and absorption capability of the material. The time dependence and dynamics of the water uptake process will be compared with other physical properties (porosity by mercury-intrusion

porosimetry, compressive strength by nanoindentation, etc.).

(5) A specific concrete production procedure, air entrainment, was also studied by thermal neutron tomography. Artificial air void systems (produced by air entraining) enhances the durability of the hardened concrete (especially in freeze-thaw cycles) and increases the workability of the concrete in its plastic state. Using neutron imaging, in collaboration with the Polish project partners, the detailed characterization of the pore system of air-entrained concretes produced with different recipes was possible. Complementary results from X-ray microtomography were done by the Korean partner.

Two project workshops were organized, in Slovakia (11-14 March 2019, Smolenice) and in Poland (25-26 Sept 2019, Warsaw). Our results and their preliminary interpretations were presented by the Hungarian members at these meetings. As a technical aspect of the workshop, the project members discussed the circumstances and technical parameters of the future analytical experiments and the preparation of the test objects. During the first meeting, the Slovakian Bohunice nuclear power plant and the site of the Javys Nuclear Decommissioning Company were visited, while at the IPPT PAN Warsaw meeting, the concrete manufacturing and testing laboratory was visited.

Remaining work

Test irradiations are prepared and will be executed soon, after the BRR fuel rearrangement and FISPACT calibration. The irradiated test specimens are planned to be examined by different physical tests, structural and chemical change analysis and further examinations of the effect of radiation damage, as well as for the residual radioactivity. The closing meeting of the project is planned to be organized in South Korea in 2020. All foreign partners unanimously proposed to expand the project's timespan to four years.

Related publications

- [1] Y. Khmurovska, P. Štemberk, M. Petrik, J. Zak, V. Zacharda, V. Szilágyi, Z. Kis, I. Harsányi: *Equipment for Concrete Irradiation Experiments*, Proc. 24th Internat. Conf. MECHANIKA 2019, 17 May 2019, Kaunas, Lithuania.
- [2] Y. Khmurovska, V. Szilágyi, P. Štemberk, Z. Kis, I. Harsányi, S. Sikorin, Y. Kaladkevich, E. Pavalanski, V. Fatseyeu, *Water absorption test accompanied by dynamic neutron radiography of gamma-irradiated cement samples*, Proc. 12th Brittle Matrix Composites Conf., 211-222, 2019, Warsaw, Poland.
- [3] V. Szilágyi, K. Gméling, Z. Kis, I. Harsányi, L. Szentmiklósi: *Neutron-based methods for the development of concrete*, Proc. 12th Brittle Matrix Composites Conf., 183-194, 2019, Warsaw, Poland.
- [4] J. Dragomirova, M.T. Palou, K. Gmeling, V. Szilágyi, I. Harsányi, L. Szentmiklósi: *Design of heavyweight concrete used in radiation protection based on complete NAA, PGAA and XRF results. Activation and physical properties*. Proc. 12th Brittle Matrix Composites Conf., 195-210, 2019, Warsaw, Poland.
- [5] Y. Khmurovska, P. Štemberk, T. Fekete, T. Eurajoki: *Numerical analysis of VVER-440/213 concrete biological shield under normal operation*, Nucl. Eng. Design, 350, 58-66. (2019)
- [6] L. Szentmiklósi, Z. Kis, B. Maróti, V. Szilágyi, K. Gméling et al: *Tudomány az innováció szolgálatában: Neutronos anyagvizsgálati módszerek ipari alkalmazásai a Budapesti Neutron Centrumban*, Fizikai Szemle **9**, 304-310 (2019)

FLOW REDISTRIBUTION IN UNEQUALLY HEATED PARALLEL CHANNELS

Gusztáv Mayer

Objective

The fuel subassemblies of the ALLEGRO reactor are closed at their periphery. For this reason, the mixing of the coolant between the parallel fuel channels is not possible. Since all the channels connect the upper and lower plenums, the pressure drop is closely identical in each subassembly. The heating power of the assemblies is different due to the radial neutron flux distribution, which unfortunately influences the mass flow rate in the channels to a large extent. In this study two geometrically identical parallel pipes with different heating power is investigated in several steady state conditions. The aim is the identification of the most important factors with special regard to mass flow difference in a helium cooled reactor.

Methods

The French CATHARE thermohydraulic code was used for the analyses. Two main cases were investigated. In the first the parallel channels were aligned vertically (Figure 1a.), in the second horizontally. A mass flow rate boundary condition was used with a helium coolant temperature of 262 °C at the inlet and a pressure boundary condition of 70 bar was applied at the outlet. Both pipes have the same length (1 m) and diameter (10 mm). During the simulations, the first and the second channel were uniformly heated with 200 W and 1200 W power, respectively.

Results

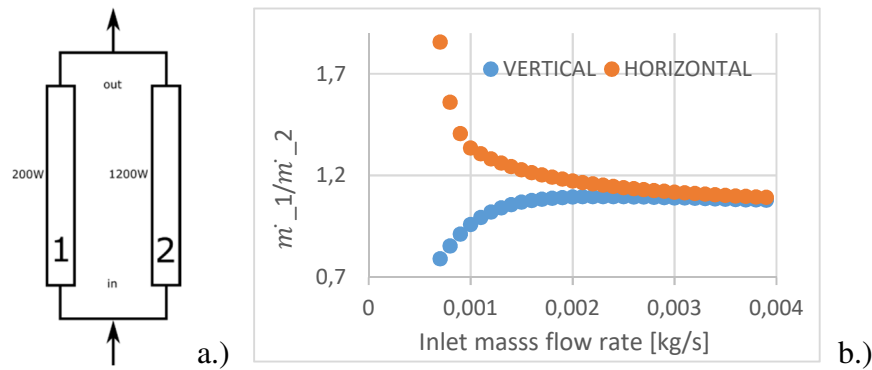


Figure 1: a.) The physical model. b.) The mass flow rate ratio between the two channels in the function of the inlet mass flow rate.

In Figure 1 b the mass flow rate ratio (\dot{m}_1/\dot{m}_2) between the two channels can be seen in the function of the inlet mass flow rate (\dot{m}_{inlet}). Each dot represents a steady state calculation. The sum of the mass flow rates of the two channels ($\dot{m}_{inlet} = \dot{m}_1 + \dot{m}_2$) remains constant in each steady state because of the inlet boundary condition. The velocity of the helium at inlet mass flow rate of 0.001 corresponds to a typical natural circulation scenario in which the inlet velocity is in the order of 1 m/s. A typical example for that is the SBO (Station Blackout) event. The results show that in case of horizontal pipe alignment the mass flow rate significantly decreases in the second channel especially when the inlet mass flow rate is small. This behaviour deteriorates the core cooling, because the second channel – which is heated by higher power – will have smaller mass flow rate.

If the pipes are aligned vertically, the mass flow rate ratio has a maximum value (Figure 1 b). In case of small inlet mass flow rate, the mass flow rate ratio between the two channels becomes even lower than 1.0, which means that the mass flow becomes higher in the second channel. This gravity effect is beneficial at gas cooled fast reactor technology, because it leads to a more balanced outlet temperature at the end of the heated pipes.

As the inlet mass flow rate goes to infinity, the \dot{m}_1/\dot{m}_2 ratio gets closer to the value of 1.0, because the temperature growth caused by the heating will be smaller. It indicates that in case of forced circulation ($\dot{m}_{inlet} > 0.001$ in our case), the mass flow rate difference is less relevant.

To sum up, three main phenomena play significant role in this process. The increased friction due to the velocity rise is important. It is governed by the high temperature and density change throughout the channel. The second phenomena - which has a significant effect at low Reynolds number flows - is the gravity. The third is the high dynamic viscosity growth of the helium coolant due to the temperature rise. The results clearly show that the vertical channel arrangement is beneficial from cooling point of view.

EXTENSION, APPLICATION AND VALIDATION OF THE IN HOUSE KIKO3DMG NODAL CODE FOR FAST REACTOR CORE ANALYSES

Bálint Batki, István Pataki, Martos Tóth, András Keresztúri, István Panka

Objective

The KIKO3DMG nodal code is being developed for the analyses of fast reactor cores. Our main goal is to have a code system which can calculate reactivity transients with thermal feedback. For this purpose, extension of the KIKO3DMG was necessary. A new module has to be developed to simulate the axial expansion of the fuel in three-dimension. Analyses have to be performed for the ALLEGRO reactor using the extended KIKO3DMG code and the Serpent Monte Carlo code. Furthermore, validation of the code and the group constant generation method has been started. Start-up tests of the China Experimental Fast Reactor (CEFR) have to be analysed using the extended KIKO3DMG and the Serpent Monte Carlo code.

Methods

Group constants were generated using the Serpent Monte Carlo code and applied in the KIKO3DMG code. For the fuel region, B1-leakage correction - based on the solution of the B1 equations - was applied which improves the precision of the calculation of power distribution using the KIKO3DMG. Parametrization of group constants was also necessary to perform calculations at any state of the core in the considered parameter range; the parameters are the fuel temperature and the coolant density, among others. A new axial expansion module was developed for the KIKO3DMG, which led to the introduction of mixed nodes. This module is applicable in 3D, when each fuel assembly might have different heights. Simple volume weighting of group constants was applied, which is adequate in our case for small nodes. A formula for the calculation of the mixed diffusion coefficient was derived, which is aiming to keep the neutron current on the boundary of the mixed nodes.

Additionally, full-core models were created, and group constants were generated for the CEFR in Serpent. Core models were also developed in the KIKO3DMG for CEFR. Four start-up tests were analysed by both KIKO3DMG and Serpent codes: first criticality, integral control rod worth, void reactivity and sub-assembly swap reactivity. The temperature coefficient of reactivity and reaction rate distributions were also calculated by using Serpent.

Results

Power distributions and the most important coefficients of reactivity were calculated using the KIKO3DMG code and reference calculation was performed using the Serpent Monte Carlo code for the ALLEGRO. It was pointed out that the KIKO3DMG is a suitable reactor physics calculation tool to investigate fast-spectrum reactors. It was shown that the code is able to calculate reactivity coefficients and the power distribution with excellent accuracy, compared to Serpent. It was found that volume-weighted mixed group constants provide correct fuel temperature coefficient of reactivity, but it is essential to weight the inverse of the diffusion coefficients instead of the diffusion coefficients. Further important coefficients of reactivity were also calculated using the KIKO3DMG code and the differences from the reference Serpent results were found to be small. The radial and axial power distribution was calculated by the KIKO3DMG code with high accuracy. [1]

The Serpent and KIKO3DMG calculation results of the CEFR start-up test show good agreement. The small differences can be explained by the stochastic nature of the Monte Carlo code and the diffusion approximation applied in this study. Furthermore, our applied models and methods were validated by comparison of calculation and measurement results. An example is shown in Fig. 1 for the case of the integral control rod worth.

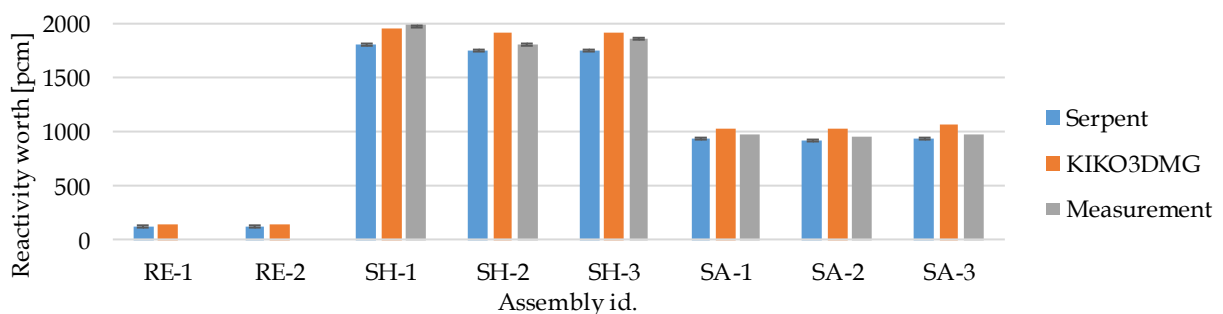


Figure 1: Calculation and measurement results of the regulating (RE), shim (SH) and safety (SA) sub-assembly reactivity worth in the CEFR

Remaining work

The calculation of temperature coefficient of reactivity for the CEFR using the KIKO3DMG is scheduled for next year.

Related publication

- [1] B. Batki, I. Pataki, A. Keresztúri, I. Panka: *Extension and application of the KIKO3DMG nodal code for fast reactor core analyses*, submitted to the Journal *Annals of Nuclear Energy*, under review



III. NUCLEAR SECURITY, DOSIMETRY AND SPACE RESEARCH



NUCLEAR FORENSIC ANALYSIS OF SEALED RADIOACTIVE SOURCES

*Katalin Zsuzsanna Szabó, Tam Nguyen Cong, Zoltán Hlavathy,
Krisztián Roland Soós, Péter Kirchknopf, Éva Kovács-Széles, Péter Völgyesi*

Objective

For a long time nuclear forensics was essentially focused on analysing smuggled nuclear materials to determine their origin and history to support an investigation. In recent years, nuclear terrorism has also targeted other radioactive materials, such as sealed radioactive sources. These, in principle, are easier to acquire, have higher activity and therefore have higher panic, economic and radiation exposure effects in the case of a terror attack. Accordingly, the objective of this study was to determine those parameters (so-called signatures), which can be used for origin identification of sealed neutron sources (e.g. the manufacturer or manufacturing technology).

Methods

Twelve Cf-252 and six PuBe sealed neutron sources from different manufacturers and of different ages were investigated. These sources were analysed mainly by non-destructive methods such as physical characterization, and gamma and neutron emission measurements. For physical characterization, the commonly used techniques were applied, such as camera, optical microscope and a ruler. During gamma-spectrometry, a sensitive planar CANBERRA GL2020 detector was used with a 0.075 keV/channel amplifier setting for the low energy range (<200 keV). In addition, a coaxial ORTEC GEM10P4-70 detector was used with an extended measuring range up to 14 MeV to identify possible prompt-gamma peaks. The gamma spectra were evaluated using ORTEC Maestro, FitzPeaks and MGA++ software. Neutron yield and coincidence measurements were performed by a self-developed device.

Results

An age determination method was developed and validated for the analysed Cf-252 and PuBe sources. This is important because the date on the certificate is often not the same as the chemical separation date, or we do not have this information for unknown material. We found that the counting rate of 177 keV gamma-rays arriving from Cf-251 (selected from several Cf-251 lines) is characteristic for the different Cf-252 sources, so this parameter can be used also for nuclear forensic analysis to determine the origin. We pointed out that the ratio of two, three or more fission products or trace contaminants in Cf-252 sources can be used as a parameter in origin determination (e.g. presence of Eu). Figure 1 shows the counts of the Cs-137, I-132 fission products and the Eu-154 trace contaminant. From their pattern we can group the sources, and hence differentiate between them. All of the determined parameters could be compared with a nuclear forensic library to get the information about the origin.

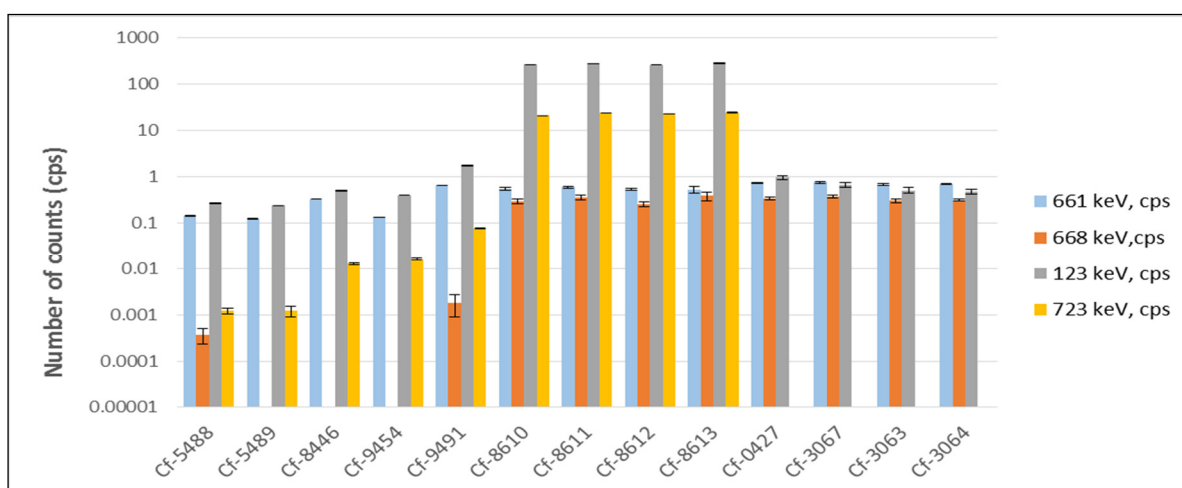


Figure 1: Counts of the Cs-137 (661 keV), I-132 (668 keV) fission products and the Eu-154 (123, 723 and 1274 keV) trace contaminant in the 12 Cf-252 sources (source-detector distance: 80 cm)

Remaining work

Detailed analysis of the neutron sources for the determination of effective and significant signatures for origin assessment is in progress by using several other techniques like X-Ray Fluorescence Spectrometry or X-Ray Radiography.

Related publication

- [1] K. Zs. Szabó, T. N. Cong, Z. Hlavathy, K. R. Soós, É. Kovács-Széles, P. Völgyesi: Analysis of sealed radioactive sources for nuclear forensic purposes (2nd year report). OAH-MMT. EK-SBL-2019-267-01, in Hungarian (2019)

SOURCE-ACTIVITY MEASUREMENTS WITH SCINTILLATION CRYSTAL DETECTORS

Attila Gulyás, Gergely Dósa, Csilla Csöme, Csaba Tóth, Nándor Kaposy,
István Almási, Péter Völgyesi

Objective

A test campaign is being carried out by the Detector Testing Laboratory of the Centre for Energy Research in the frame of a Coordinated Research Project (CRP J02012), supported by the International Atomic Energy Agency (IAEA). The title of the related CRP is „Advancing Radiation Detection Equipment for Detecting Nuclear and Other Radioactive Material out of Regulatory Control”. During the second research year (2019), measurements and analysis of the use of scintillation crystal based Radioisotope Identification Detectors (RID) were our main focus, with the aim to investigate the possibility of source-activity estimation and to develop that possibility with methods, algorithms and specifications.

Methods

The research project includes a number of activities related to nuclear security needs in the area of radioisotope identification and the calibration of the identification equipment. Laboratory test measurements with calibrated sources and analysis of the spectra were carried out with a gamma analysis software called FitzPeaks (developed by Jim Fitzgerald) and a graphing software (Origin) to apply the source-activity measurement method, which is widely used with high resolution gamma-ray detectors (e.g. High Purity Germanium - HPGe - detector), to RID devices as well.

Results

Based on the experiences of the second year test campaign, the RIDs containing LaBr₃ crystals have good capabilities to measure the activity. For RIDs, the basic theory of activity determination can be presented with easy formulas. In the case of an unknown radiation source however, the process of the data evaluation is complex.

Before the measurement, the energy and efficiency calibrations have to be made. In this process, more rationalization and simplification is acceptable (e. g. using simpler fitting functions) to increase accuracy and precision and decrease uncertainty, if the overall loss (e. g. loss of measurable isotopes) is minimal. There are two ways to determine the activity of a nuclide: A_i from one peak and/or $A_{nuclide}$ from a weighted average using several peaks. Both require the count rate of the i 'th gamma peak Cr_i , the probability of the i 'th gamma photon emission $P_{\gamma i}$ (or $I_{\gamma i}$) and the full-energy-peak efficiency of the detector crystal $Eff(E_i)$. The reliability of the measurement can be greatly increased by analyzing several peaks from the identified nuclide (Figure 1): the weighted average formula (for all/top 6/top 3 peaks) smoothly averages out the differences; they are much closer to the conventional true value than the values calculated from the individual peaks. These differences can be seen in percent next to the blue points on the figure. Correction calculations can also be used to improve the accuracy (if necessary). Measurement uncertainties can still be properly calculated and estimated. All in all, the applied measurement performance and this method can be implemented for real field conditions.

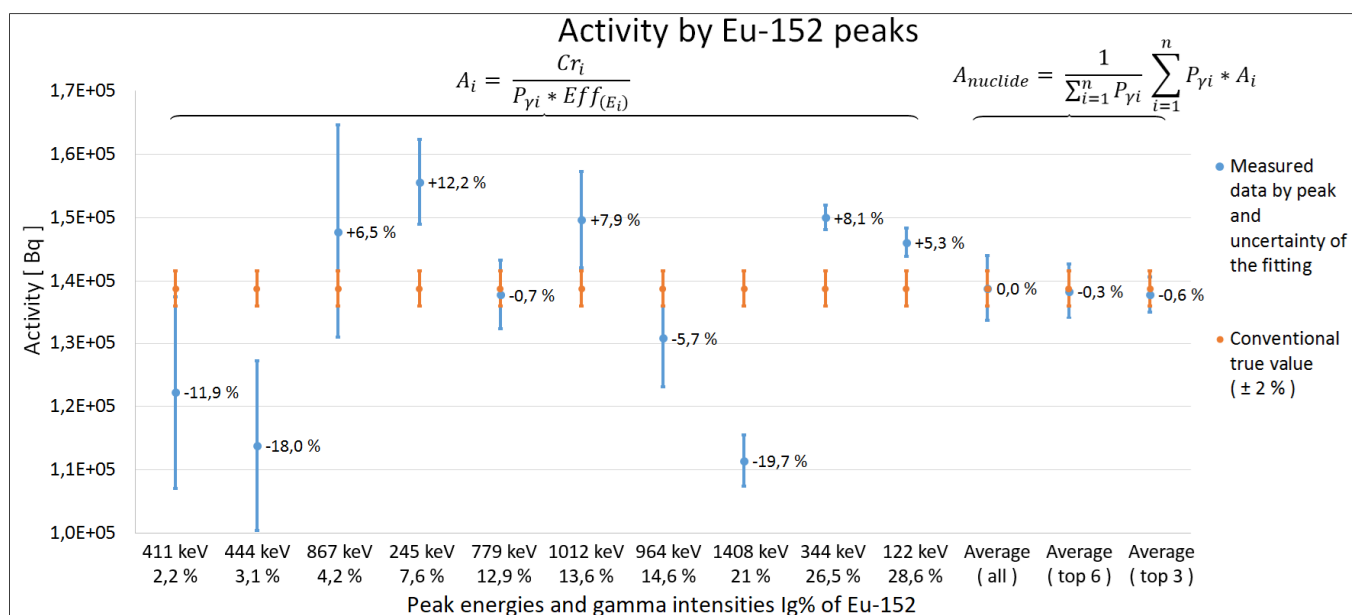


Figure 1: Activities measured/calculated from one or several peaks on the same spectrum with a RID

Remaining work

The project is in progress because it lasts three years. In the third year, this new RID application will be developed with additional components and techniques for field conditions.

IAEA COORDINATED RESEARCH PROJECT: APPLYING NUCLEAR FORENSICS SCIENCE TO RESPOND TO A NUCLEAR SECURITY EVENT

Éva Kovács-Széles

Objective

The International Atomic Energy Agency (IAEA) launched a new 3-year long coordinated research project in which nuclear forensic scientists from different Member States with various capabilities will work together to improve the implementation of nuclear forensics in the context of national laws, and to support investigative needs. This research will yield enhanced methods to document and collect evidence, to rapidly identify nuclear and other radioactive materials that pose a nuclear security threat, and to process traditional forensics evidence contaminated with radionuclides. The project seeks to promote consistent and scientifically defensible implementation of nuclear forensics examinations in line with national laws and international legal instruments. In particular, it seeks to link nuclear science with investigative requirements.

Work at Centre for Energy Research planned for the first year

In the first year of the project, the following work was planned: to start the analysis of several sealed radioactive sources (gamma and neutron) using non-destructive techniques and physical characterization. Also, to start the collection of data from radioactive source producers about production technologies for origin assessment. In parallel, to start to develop a common procedure for Radiological Crime Scene Management, in collaboration with the Hungarian Police. In the program, traditional and nuclear forensics experts have developed a procedure for how to work together at a radiological crime scene and how to collect evidence (radiological, traditional and radiologically contaminated traditional). The next task was to start to develop a small radiation explorer robot and to expand the capability for discovery, detection and sequestration of unknown nuclear or radioactive materials (e.g. the technical Reach-Back functions) at the Centre for Energy Research.

Results

26 neutron sources (Cf-252, AmLi, AmBe, Cm-244) available at the Centre for Energy Research were analysed using the following methods: physical characterization, optical microscopic analysis, gamma-spectrometry, X-ray fluorescence analysis of the source capsule and X-ray radiography. Some promising characteristics (signatures) were found for origin assessment, like physical form/structure, source capsule material, Eu isotope contamination in Russian Cf-252 sources and the Am-241/Cm-245 isotope ratio, as well as the neutron yield in the case of Cm-244 sources.

A common procedure was developed, together with the Hungarian Police, for Radiological Crime Scene Management. A harmonized procedure between law enforcement and radiological experts has been established to preserve the scene, key evidence, radiological materials as evidence and the health of crime scene personnel. A crime scene requires special control, so a police officer must be present from the very first moment of any activity, but the identification of hot spots and radioisotopes, as well as collection of the materials must still be carried out by a radiological experts. This is a unique method, comparable with other procedures available all over the world. The procedure was also tested through several exercises.



Figure 1: The Hungarian protocol for Radiological Crime Scene Management was demonstrated at the IAEA in Vienna

Remaining work

The following tasks are planned for the next year of the project: refinement of the Radiological Crime Scene Management procedure using in-field exercises based on different scenarios; methodological development for in-field and laboratory-based examination of radiologically contaminated traditional forensics evidence; experiments on the contamination of personal protective equipment to find the best practice for packaging, undressing and glove changes; further analysis of sealed neutron and gamma sources focusing on radiography; development of remote detection systems; starting on the development of an on-line data transfer and digital chain-of-custody system.

REVIEW AND ASSESS OF RADIATION PROTECTION IN NUCLEAR INSTALLATIONS - TRAINING COURSE AT THE CENTRE FOR ENERGY RESEARCH

András Kovács, Balázs Madas, Péter Zagyvai

Objective

The purpose of the training course, given to the International Atomic Energy Agency's fellowship holders Saudi Arabian colleagues is to review and assess radiation protection in nuclear installations; to build competence and develop practical skills in the field of radiation protection and safety needed for the regulatory control of radiation protection in nuclear installations; to understand the types, designs and applications of various isotope technologies in Nuclear Power Plants and their influence on radiation protection; to get knowledge of regulatory inspection on radiation protection in nuclear facilities during all stages of process (siting, construction, commissioning, operation and decommissioning).

Methods – Results

The training was carried out at the premises of the Centre for Energy Research and visits were organized to visit the three different types of nuclear reactors in Hungary and radioactive waste disposal site at Püspökszilág.

The training programme contained the following elements:

1. Interactive lectures:

- 1.1. Roles and responsibilities of stakeholders of nuclear facilities with special emphasis on the regulatory body of embarking countries.
- 1.2. Main features of nuclear safety culture, methods, and practices of safety assessment.
- 1.3. Principles and practices of radiation protection with special emphasis on research facilities and radiation sources.
- 1.4. Emergency preparedness and response of nuclear facilities, and radioactive sources.
- 1.5. Issues of radioactive waste management and disposal, decommissioning, exemption and clearance.
- 1.6. Selected Technologically Enhanced Naturally Occurring Radioactive Materials (TENORM) topics.
- 1.7. Lessons learned from events, incidents, and accidents with respect to radiation safety and emergency preparedness and response.

2. Practical problems, case studies, and associated measurements:

- 2.1 Selected case studies from recent experiences: ^{106}Ru -detection in the environment, assessment and treatment of ^{241}Am -caused individual contamination.
- 2.2 Operation of the environmental control service of Budapest Research Reactor (BRR) site (sampling and radioanalytical methods).
- 2.3 Individual dosimetry control.
- 2.4 Assessment of dispersion of radioactivity in the environment.
- 2.5 Methods of neutron and gamma dosimetry at workplaces.
- 2.6 Shielding calculations.

3. Visits to facilities:

- 3.1 Research reactor of the Budapest Neutron Centre (10 MW).
- 3.2 LLW/ILW (Low level waste/ Intermediate level waste) disposal site of Public Limited Company for Radioactive Waste Management (PURAM) at Püspökszilág.
- 3.3 Training reactor of Budapest Technical University (100 kW).
- 3.4 Paks Nuclear Power Plant and its Visitor Centre.

4. Consultation of the covered topics.

5. The visiting scientists:

- Mr. Binshaman Abdulaziz,
- Mr. Alharbi Mohammad,
- Mr. Albishri Ali.

ASSESSMENT OF CAPACITY FOR GAMMA SPECTROMETRIC MEASUREMENT OF ENVIRONMENTAL SAMPLES

Péter Zagvai, Tamás Pázmándi, Gáborné Endrődi, Dorottya Jakab, János Megyeri, Katalin Zsuzsanna Szabó, Péter Völgyesi

Objective

On-site environmental radiation monitoring is one of the basic duties of the Environmental Protection Service (KVSZ) of EK. However, in case of sudden occurrence of extraordinary traces of radioactivity in the environment – due to the rapid reporting obligation, increased sampling frequency and elevated number of samples – the analysis of environmental samples may require the involvement of additional local laboratories. The aim of this work was to assess the compound capacity of EK for gamma spectrometric measurements of environmental samples and to develop their joint usability.

Methods

In order to survey the capacity among the laboratories concerned (KVSZ, NAL, SBL, SVL), a survey was conducted which included questions concerning the technical conditions as well the major aspects of the used gamma spectrometric practices:

- sample types and typical activity concentrations routinely measured with gamma spectrometry,
- number of detectors suitable for measuring environmental samples and their specifications (e.g. manufacturer, type, structure, resolution, relative efficiency and dimensions),
- utilization of low background systems to assess their availability,
- shielding of the systems and their typical background count rates,
- software applied for analysis of gamma-ray spectra,
- methods and frequency of efficiency, energy and peak width calibrations,
- types and properties of the available calibration sources – point and volume sources (e.g. geometry, matrices, nuclides and their activity concentrations, status of certification),
- methods for correction of raw evaluation results (e.g. random and true coincidence summing, self-absorption),
- sample preparation practices and equipment capacity, routinely used sample holder types ,
- typical counting time of low activity samples,
- routine method for background measurements (frequency, counting time, use of blank samples etc.).

The received responses were evaluated and summarized in a database accessible to interested parties. Furthermore, an intercomparison was prepared in order to assess the routinely used gamma spectrometric methods in each laboratory.

Results

As a result of the work, in addition to the assessment of gamma spectrometric practices and the determination of the available capacities, major development requirements for capacity and procedures have also been defined. Concerning the current gamma spectrometric measurements, it was determined that only KVSZ performs environmental measurements on a daily basis, the other laboratories measure environmental (e.g. soils, tailing samples from mines) or other low activity samples only on an ad hoc basis. The samples arrive typically in prepared form, only KVSZ performs regular sample preparations. However, the scope of the other labs' equipment for sample preparation is limited, and to avoid potential contaminations in the need of preparation of samples with elevated activities the range of sample preparation tools should be increased. There are altogether 7 detectors suitable for measuring environmental samples: 1 well detector and 6 coaxial detectors with relative efficiencies from 13% to 60%. The utilization of low background systems is high, and in most cases is continuous. Most laboratories possess certified point sources and perform corrections to convert the measured activity of a volume sample to point source equivalent, whereas KVSZ has several volume sources with the same matrices (water equivalent) with various geometries. These sources may be used to perform adequate efficiency calibration for volume samples for the low background systems. The generally used software for analysis of gamma-ray spectra is the Genie 2000 (Canberra), however it was ascertained that it would be practical to purchase other software with licenses, like GammaVision (ORTEC) and FitzPeaks to use their advanced algorithms for several problems (e.g. precise efficiency corrections for the differences between the sample and source).

Remaining work

A procedure will be developed to be followed when analyzing increased number of samples from sampling during an incident. Extension of the intercomparisons to other measurement geometries and sample types with different material composition is planned. New measurement capacity of KVSZ will also be taken into consideration in these measurements.

Related publication

- [1] J. Salupeto-Dembo, Zs. Szabó-Krausz, P. Völgyesi, Z. Kis and Cs. Szabó: *External radiation exposure of the Angolan population living in adobe houses*, Journal of Radioanalytical and Nuclear Chemistry, 2019. (Accepted for publication)

DETERMINATION OF UNCERTAINTIES AND CHARACTERISTIC LIMITS OF THE ENVIRONMENTAL RADIATION MEASUREMENTS

Tamás Pázmándi, Dorottya Jakab, Péter Zagyvai

Objective

In order to ensure reliable and representative monitoring of environmental radiation levels, it is required to determine the sensitivity as well as the uncertainties of the measurement methods used for environmental radiation monitoring purposes. Thereby their precise quantification and potential reduction is necessary to provide more accurate measurement of low-level environmental radioactivity. The objective of this work was to develop recommendations for the determination procedure of measurement uncertainties and characteristic limits (such as decision threshold, detection limit and confidence interval) for real-time (gamma dose rate measurement, real-time sampling of aerosols and iodine in air), periodic (passive dosimetry) and sampling (air, deposition, soil, vegetation and water sampling) environmental measurement methods.

Methods

The most relevant international and domestic documents published in the areas in question were reviewed. It was recognized that in several cases it would be complicated to put the published methods into practice. Accordingly, our work focused also on the practical adaptability of the evaluation methods. Following their critical review, we have presented a mathematical interpretation of the most commonly used theoretical models in the discipline of uncertainty evaluation (law of propagation of uncertainty, propagation of distributions using Monte Carlo method) and characteristic limit determination (Currie method, method described in the ISO 11929 standards). The conditions for their valid application were also summarized. We have identified potential sources of uncertainty for the examined environmental measurement types and presented also methods to quantify the most significant components in the uncertainty budget. In order to facilitate the practical application, the uncertainty estimation of each investigated measurement type has been presented through example calculations performed with both of the law of propagation of uncertainty and the propagation of distributions using a Monte Carlo method. We determined the contribution of each uncertainty component to the total uncertainty, and analyzed the consequences of neglecting input quantities and uncertainty components. We also have developed recommendations for reporting results to provide sufficient information for their subsequent statistical analysis.

Results

We proved that in most cases the law of propagation of uncertainty can reliably be applied to environmental measurements. The contribution of uncertainty components to the total uncertainty of the measurand was determined for each measurement method. For dosimetry measurements, it has been shown that if the radiation conditions and the dosimeter characteristics are unknown, the requirements for influential quantities (e.g. non-linear dose response, photon energy dependence and deviation due to the angle of incidence) proposed in the relevant standards can be used to estimate the uncertainty of the components affecting the dose or dose rate measurement. The uncertainty of the estimated correction factors can be reduced by providing additional information about the conditions and the measuring device (e.g. expanding the type testing results by performing repeated measurements to reduce statistical uncertainty of the parameters). In case of sampling measurements it was found that the greatest contribution to the uncertainty of the quantity intended to be measured (activity concentration) is due to the statistical uncertainty of counts (typically the background-corrected net peak area) and the uncertainty of detection efficiency. It has also been determined that the effect of neglecting the uncertainty components on the output quantity's combined standard uncertainty may highly depend on the number of input quantities and the relative magnitude of the maximum and minimum contributions to the total uncertainty.

Remaining work

In order to investigate the applicability of the recommendations to domestic environmental control practices, a nationwide survey will be developed and the feasibility of development proposals will also be tested in practice by the on-site environmental monitoring system. Further work will aim to identify ways to reduce the uncertainty and detection limits of environmental radiation measurements and methods to increase their temporal and spatial representativeness.

Related publications

- [1] D. Jakab and T. Pázmándi: *Development of methods to improve precision of the measurement results of environmental radiation monitoring systems: Part 1*, Research report, EK-SVL-2019-270-01-01-01, In Hungarian (2019)
- [2] D. Jakab, I. Apáthy, A. Csóke, S. Deme, G. Endrődi, L. Tósaki and T. Pázmándi, *Comparative analysis of active and passive dosimetry systems used in environmental gamma radiation monitoring*, 5th International Conference on Environmental Radioactivity, Prague, Czech Republic, 2019. (Oral presentation and submitted conference paper)
- [3] D. Jakab, T. Ádámné Sió, G. Endrődi, Zs. Homoki, S. Kapitány, A. Kocsonya, J. Kövendiné Kónyi, A. Lencsés, L. Manga, A. Pántya, T. Pázmándi, K. Radó, P. Rell, P. Turza and P. Zagyvai: *Evaluation of Hungarian monitoring results and source localization of the ¹⁰⁶Ru release in the fall of 2017*, Environmental Monitoring and Assessment, **191**, 431, (2019) <https://doi.org/10.1007/s10661-019-7567-0>

DETERMINATION OF UNCERTAINTIES IN THE ESTIMATION OF INTERNAL EXPOSURE

Annamária Pántya, Tamás Pázmándi, Péter Zagyoai

Objective

In determination of internal radiation exposure, great emphasis should be laid on identifying uncertainties. For the majority of incorporated radionuclides, the internal dose could be estimated in two steps. In the first step the actual activity present in the body is determined by in vivo (e.g. whole or part of body counting) or in vitro (e.g. urine measurement) monitoring methods. In the second step the value of intake and the associated committed dose can be estimated on the basis of measured data considering necessary assumptions on exposure conditions (time and route of intake, chemical form etc.). In recent years we analysed not only the overall uncertainty of thyroid activity measurements in accidental situation and its consequences with dose assessment, but the uncertainties in analysis of urine samples as well. We took part in international projects, participated in numerous national and international intercomparisons and their results were presented for the national and international scientific community. To supplement the work performed in the previous years, three cases of nuclear workers occupationally exposed to uranium were analysed as part of an international intercomparison. Sensitivity analysis was performed based on these data using real measurement results to determine which parameters have the greatest influence on the estimated final results.

Methods

Reference dose calculations were carried out in accordance with recommendations and guidelines from available data of case studies, effects on the effective dose were investigated by selecting and varying the sensitive parameters. Based on the available data of three workers exposed to internal radiation, the reference value of dose estimation was constructed. Key parameters in the hypothesis of dose estimation were: intake data for acute and intake periods for chronic exposures; absorption (transfer) to blood; biokinetic and dosimetric models; software and method for intake assessment; treatment of data below detection limit. During the sensitivity analysis doses were assessed for each worker either by considering reference values for all parameters, or by fixing all parameters but one at the reference values and the selected parameter was set at an alternate value. The reference values for the parameters were arbitrarily chosen as the value that is the most favourable based on our knowledge and the available information. The reference and alternative dose estimations were gathered for each exposed worker.

Results

Table 1. shows that the parameter with the biggest effect for the dose assessment for the three workers is the absorption type, which gives information on the absorption to blood following inhalation or ingestion of different chemical forms of radioisotopes. Therefore, the accurate determination of the absorption type is essential for the appropriate dose estimation. The second most important group of parameters that

Table 1: Mean relative differences in committed effective dose for various parameters

Contributing factors	Worker 1	Worker 2	Worker 3
Treatment of data below detection limit (DL)	-24%	-20%	-75%
Absorption type (Type S - slow, M - moderate and F - fast)	8280%	2202%	15455%
Absorption type without Type S - slow	394%	-37%	905%
Subtraction of dietary contribution	-1%	-2%	-1%
Scattering Factor (SF)	-40%	-42%	-20%
Choice of intake pattern	66%	51%	22%

needs to be determined precisely is the circumstances of the intake. This includes distinguishing between acute and chronic cases, determining the period of chronic exposure or the time of acute exposure. The smallest effect was caused by the subtraction of the alimentary background. The variety of available data also defines the degree of uncertainty in a very diverse way. In many cases, the circumstances of intake are not well defined, thus different assumptions could be applied. It has been shown that the erroneous choice of certain factors may cause significant differences in the estimation of the committed effective dose. It is important for experts to be aware of these sources of uncertainty and to control them.

Our results confirmed that the uncertainty in the estimations and assumptions used in the determination of the effective dose are more significant than the uncertainty of the measured radioanalytical results.

Remaining work

This project has been completed. Publication of the results are in progress.

Related publications

- [1] A. Pántya, E. Blanchardon, E. Davesne, T. Pázmándi: *Investigation of dose estimation uncertainties for uranium exposure*, 3rd International Conference on Dosimetry and Applications, Lisszabon, Portugália, 2019. (Oral presentation)
- [2] A. Andrási, T. Pázmándi, A. Pántya, C. M Castellani, A. Giussani, R. Grareth: *Dosimetry of the Hungarian ²⁴¹Am incorporation into the light of the ICIDOSE results*, 44th Annual Meeting on Radiation Protection, Hajdúszoboszló, Magyarorszá, 2019. (Oral presentation in Hungarian)

- [3] E. Davesne, R. Bull, J. Anderson, D. Bingham, A. Birchall, C.M. Castellani, C. Challeton-de Vathaire, M. L. Fernandez, M. Froning, A. Giomi, A. L. Lebacqz, J. Oško, I. Gomez Parada, A. Pántya, A. G. Rojas, A. Rojo, M. Takahashi, K. Tani, E. Blanchardon: EURADOS Report 2017-03: *Uncertainties in internal dose assessment: Lifetime dose assessment for three example workers occupationally exposed to uranium - Analysing the intercomparison results*, Neuharberg, 2017. ISBN 978-3-943701-16-6
- [4] A. Pántya, T. Pázmándi, P. Zagyvai: *Development of guide for monitoring internal exposure: Part 2*, Research report, EK-SVL-2019-263-03-01-01, in Hungarian (2019)
- [5] A. Pántya, A. András, D. Jakab, T. Pázmándi, P. Zagyvai: *Uncertainty estimation of thyroid activity measurements and its consequences in dose assessment*, 5th European IRPA Congress, The Hague, The Netherlands, 2018 (Oral presentation and conference paper)
- [6] A. Pántya, T. Pázmándi, D. Jakab: *Uncertainties in analysis of urine samples*, PROCORAD Annual Meeting, Ispra, Italy, 2018 (Oral presentation)
- [7] A. Pántya, A. András, T. Pázmándi, P. Zagyvai: *Dose assessment of thyroid in accidental situation*, Sugárvédelem Vol. X., No. 1., in Hungarian (2017)

EFFECTS OF INHALED RADON PROGENY MODELLED AT THE TISSUE LEVEL

Emese Drozsdik, Balázs Madas

Objective

The adverse health effects of inhaled radon progeny are still an important subject for research. It has been shown that alpha particles emitted by inhaled radon progeny result in highly heterogeneous dose distribution in the lungs. It has also been shown that in the highly exposed part of the bronchi increased number of progenitor cells, i.e. progenitor cell hyperplasia, is a potential adaptive response to chronic radon exposure. However, the development of hyperplasia has not been studied so far. The objective of the present study was to develop a time-dependent epithelium model, which can later be used for microdosimetry calculations providing input for mathematical models of biological response.

Methods

The subcellular element method has been applied to model the cells in the bronchial epithelium. In this model, cells are represented as a group of particles, the subcellular elements. The elements' motion is described by stochastic and deterministic interactions, both within the same cell and with elements of neighbouring cells. The biomechanical forces among subcellular elements are described by the generalized Morse potential. In order to describe the thermodynamic fluctuations, a Gaussian-distributed noise is applied. Initially, a few subcellular elements belonging to a single cell are placed close to the basement membrane. At regular times, a new subcellular element is inserted into the centre of mass of the growing cell. If there is already an element close to it, the elements move away from each other due to the intracellular forces. As the number of subcellular elements grows, the probability of cell division increases. This method allows the convenient representation of cell division, differentiation and cell death. These biological processes participate in the development of hyperplasia.

Results

In our epithelium model, progenitor and differentiated cells are distinguished. Basal cells, as progenitor cells have a maximum of 40 elements and they are capable of division, while goblet cells, as differentiated cells had a maximum of 60 elements and they are unable to divide. A cell divides either symmetrically or asymmetrically if its size is large enough (i.e. the number of its subcellular elements reaches half of the maximum element number) and connect to the basement membrane with a minimum element number. The dividing cell is cut in half along the division plane which go through the centre of mass and elements on the right side become part of the new cell (Fig. 1). Once the cells reach the edge of space, the pressure between the cells starts to increase. It leads to extension of cells, i.e. they adhere with fewer elements to the basement membrane, become elongated. Because of that, the elements of a single cell can drift away from each other splitting the cell into two parts. If cells keep growing even at high pressure, some of the cells move away from the basement membrane, resulting in multiple cell layers (Fig. 1.).

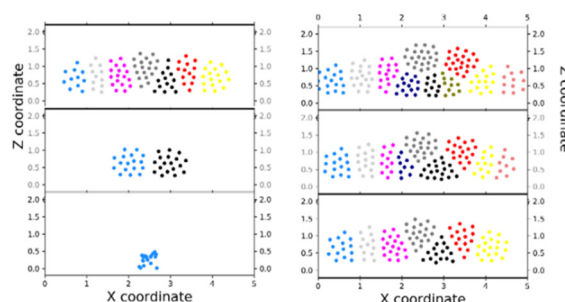


Figure 1: The series of pictures show the development of the epithelial. The elements belonging to the same cell are marked with the same colour. A video can also be found at <https://youtu.be/1VpWZIFWmqA>.

Remaining work

Further development of the epithelium model is required in order to calculate microdosimetric quantities in the bronchial epithelium. In order to protect the integrity of the cells and to determine its boundaries, Voronoi polygons will be assigned to the subcellular elements.

Related publications

- [1] Drozsdik EJ, Madas BG: *Quantitative analysis of the potential role of basal cell hyperplasia in the relationship between clonal expansion and radon concentration*, *Radiation Protection Dosimetry* **183**: 237–241 (2019)
- [2] Drozsdik EJ, Madas BG: *Modelling the bronchial epithelium with the subcellular element method*, 16th International Congress of Radiation Research. 25-29 August, 2019, Manchester, United Kingdom.

ENVIRONMENTAL RADIATION MONITORING WITH DETECTORS IN A NEW GENERATION SCALABLE NETWORK – DOZINET

Attila Hirn, János Volk, István Apáthy, Gáborné Endrődi, András Gerecs, Ákos Horváth, Miklós Szappanos, László Tótsaki, Erika Tunyogi

Objective

The primary objective of the DoziNet project is to demonstrate that the radiation detector system developed by the Space Dosimetry Research Group for sounding rocket experiments can be combined with the communication units and protocol used and developed by the Nanosensor Laboratory for self-organizing scalable networks and that the combined system can be integrated into the network of Geiger-Müller (GM) probes installed and operated by the Environmental Protection Service at the KFKI Campus. The same communication protocol will also be used for transmitting data of the airflow sensors to the server.

Methods

The electrical design of the GM system was adapted to the ZP1220 and ZP1301 GM tubes used in the GM probes of the Environmental Protection Service. The signal is measured on the cathode resistor of the GM tubes. The signal processing unit comprises a pulse shaper (differentiator-integrator unit) and a comparator. At the output of the signal processing unit a monostable multivibrator provides square pulses of fixed amplitude and length. The counter/data processing unit is realized by a Happy Gecko EFM32 type microcontroller unit. The measured count rates, in counts per minute, are transmitted to the server via an RN2483 LoRa® transceiver module. Therefore, as an outdoor gateway, a PDTIOT-ISS00 IoT WInet Station was also installed on top of building 29B with Ethernet connection and protection against rain and lightning. A GPS module was connected to the Happy Gecko developer kit to provide GPS coordinates as metadata for the measurement data. Measurement data are displayed using NodeRed/ThingSpeak and saved into MySQL database. In addition to the GM probe, an airflow meter used at the aerosol stations at the KFKI campus was also connected to the Lora Network for demonstration.

Results

The first breadboard model of the DoziNet system was finished and tested. The prototype of the relocatable GM unit successfully measured the background radiation at the campus and transmitted the measured data to the LoRaWan server. They were successfully processed and displayed on the web-based NodeRed data viewer (Fig. 1).

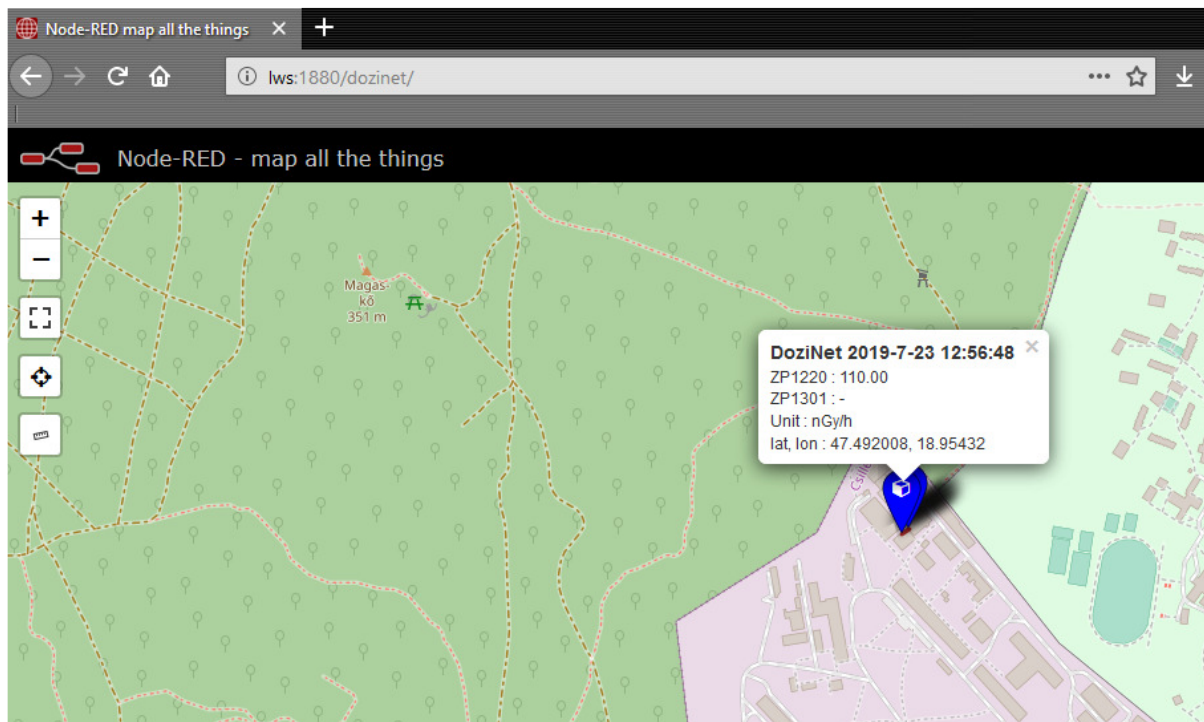


Figure 1: The NodeRed based data viewer of the prototype of the DoziNet system

Remaining work

In the next phase of the project, 3-5 relocatable GM probes connected by the LoRaWan network to the main server will be added to the present network of GM probes. A similar unit will be optimized for use on radiation protection vehicle (DoziMobile).

NUMERICAL MODELLING OF INDIVIDUAL RADIOSENSITIVITY

Árpád Farkas, Péter Fűri

Objective

The main objective of this work was to develop numerical models for the quantification of the differences in terms of radiosensitivity among different members of the general population. The specific aim of the work was to reveal the dosimetric aspects of the inherent anatomical and physiological differences between healthy individuals and chronic obstructive pulmonary disease (COPD) patients related to the inhalation of short-lived alpha-emitting radon progenies.

Methods

The radon concentration considered in this study was characteristic of an average Hungarian home. Spherical inhaled particles with activity median thermodynamic diameter (AMTD) of 0.8 μm were assumed representing the median size of the inhaled unattached radon progenies. The value of the same parameter characterizing the attached progenies was 230 nm. The ^{218}Po , ^{214}Pb and ^{214}Bi activity concentration ratios were 0.58, 0.44 and 0.29, respectively. The applied breathing parameters corresponded to sitting physical activity. Both nose breathing and mouth breathing modes were assumed. The previously developed Stochastic Lung Deposition Model was applied to calculate the deposition fractions of the inhaled radon progenies in different regions of the respiratory tract and in the specific airway generations of the conductive airways. Modification of the primary deposition patterns due to mucociliary clearance was simulated by an in-house clearance model. An alpha particle – epithelial cell interaction model (RADACT) was developed and applied for the calculation of cell nucleus dose distributions.

Results

Our computer simulations revealed the important role of the upper airways in the filtering of harmful inhaled particles. Nose breathing turned out to be more advantageous than mouth breathing when it comes to the radiation burden of the bronchial cells. The dose rates of the inhaled radon progenies in the nuclei of basal and secretory cells of the bronchial epithelium were significantly lower when inhaling through the nose. By the same token, COPD patients received higher bronchial cell nucleus doses than their healthy counterparts. Mucociliary clearance highly influenced the dose distributions of both healthy and diseased individuals. Present results have demonstrated that the individual exposure of the radiosensitive bronchial cells is highly influenced by the individual breathing patterns and airway geometries highlighting the need for personalized radiation dosimetry. Based on the current findings, individual specific dosimetric calculations will lead to a more appropriate estimation of radiation health risks in the future.

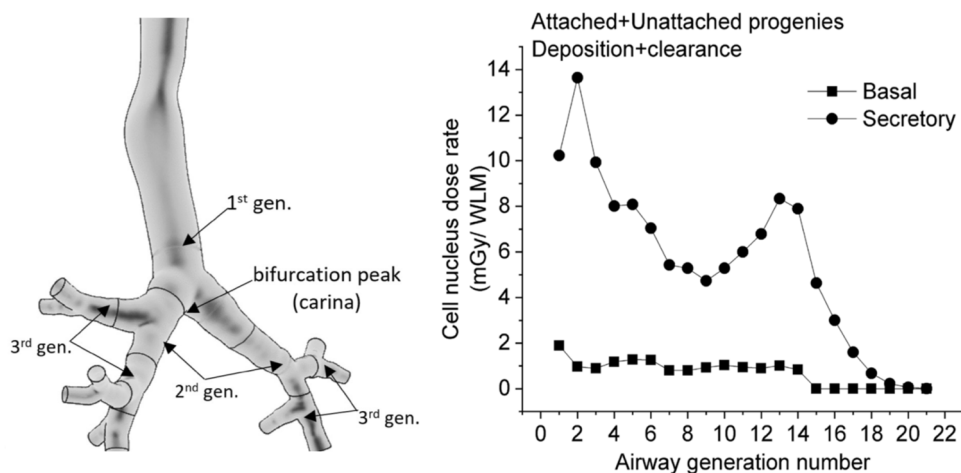


Fig. 1: Segmentation of the airways into airway generations (left panel) and distribution of simulated cell nucleus doses of the attached and unattached radon progenies corresponding to exposure conditions characteristic of homes (right panel, WLM: working level month)

Remaining work

As a continuation of the present work, microdosimetric differences among individuals of different gender, age and with different disease type and degree of disease severity will be assessed.

Related publications

- [1] P. Fűri, Á. Farkas, B. G. Madas, W. Hofmann, R. Winkler-Heil, G. Kudela, I. Balásházy: *The degree of inhomogeneity of the absorbed doses in the bronchial region of the human respiratory tract*. Radiation and Environmental Biophysics doi: 10.1007/s00411-019-00814-0.
- [2] P. Fűri: *Development and application of a customizable numerical lung dosimetry model*. Sugárvédelem (in Hungarian, accepted manuscript).

CHARACTERIZATION OF RADIATION EXPOSURE AND ITS BIOLOGICAL EFFECTS AT DIFFERENT SPATIAL SCALES

Tariq Hailat, Emese Drozsdik, Balázs Madas

Objective

Most experiments in radiation biology are performed to estimate the relationship between biological effects and radiation dose. While the difficulties of measuring the biological effects are well-recognized, less attention is paid to the problems of quantifying radiation dose. It is particularly difficult in case of incorporated alpha-emitting radioisotopes. The objectives of this research were to develop a Monte-Carlo code for specific experiments with alpha-emitting radionuclides, and to measure the dose in order to validate some results of the simulations.

Methods

For this purpose, i) a software was developed to quantify cell nucleus hits and absorbed doses in different exposure geometries, ii) and later CR-39 detectors were applied in order to measure alpha-particle track density at the location of the cells. The number of tracks was counted with an optical microscope. Simulations were performed to estimate the duration of exposure that results in an ideal track density range. However, experiments with longer duration were also performed, in view of the contradiction between the measured DNA double strand break (DSB) number and simulation results on cell nucleus hit distribution.

Results

The hit distributions for cell nuclei with a diameter of 41 μm were highly inconsistent with experimental data on DNA DSB number. These simulation results pointed out to the uncertainty of cell size and predicted that the cells are much smaller what was later confirmed by new experiments. As there was still a significant difference between experimental and simulation data with the new cell size, it was suggested to quantify other input parameters like the thickness of the radiation source.

The measurement of alpha-particle track density with CR-39 detectors showed that the activity distribution in the *in vitro* experiments is highly inhomogeneous. Most probably, this inhomogeneity was responsible for the inconsistency between the simulated number of cell nucleus hits and the measured number of DNA DSBs. In future experiments, it is desired to ensure homogeneous activity distributions. If the track density were homogeneous, then reliable mathematical modelling of cell survival would also become possible in order to estimate the efficacy of radiopharmaceuticals in *in vitro* experiments.

Related publications

- [1] Hailat TF, Drozsdik EJ, Madas BG *Computational cell dosimetry for alpha-particle exposure by Monte-Carlo methods* 7th International Conference on Radiation in Various Fields of Research. 10-14 June, 2019 Herceg Novi, Montenegro, p. 361.

Other publications

- [1] M.M. Eyadeh, K.A. Rabaeh, F.M. Aldweri, M.Y. Al-Shorman, S.M. Alheet, S.I. Awad, T.F. Hailat: *Nuclear magnetic resonance analysis of a chemically cross-linked ferrous-methylthymol blue-polyvinyl alcohol radiochromic gel dosimeter*, Appl. Radiat. Isot. **153**, 108812 (2019)
- [2] T.F. Hailat, M.M. Eyadeh, K.A. Rabaeh, B.G. Madas, F.M. Aldweri: *Dosimetric characterization of Methylthymol blue Fricke gel dosimeters using nuclear magnetic resonance and optical techniques*, 7th International Conference on Radiation in Various Fields of Research. 10-14 June, 2019 Herceg Novi, Montenegro, p. 262.
- [3] T.F. Hailat, B. Al-Bataina, B.G. Madas: *Measurement of radon and thoron concentration levels in Disi soil (in Jordan) using CR-39 detector*, International Conference on Radiation Applications. 16-19 Sept., 2019 Belgrade, Serbia, p. 35

ENVIRONMENTAL AND RADIATION TRANSPORT MODELLING OF SPACE RADIATION TELESCOPES – PHD PROGRESS REPORT

Boglárka Erdős, Attila Hirn

Objective

This document reports on the work of the second and partly the third semester of Boglárka Erdős' PhD studies, which is focused on contaminations and selectivity of silicon charged particle detectors for space weather and space dosimetry measurements. During the reporting period, the work focused on two main projects: the calibration of the RADTEL charged particle telescope for space weather measurements and the environmental modelling of the ESEO student satellite.

Methods

RADTEL is a biaxial silicon detector charged particle telescope for measuring the fluxes and energies of protons, electrons, and heavy ions as a part of the RadMag space weather monitoring system. It will go into a quasi-polar orbit at an altitude of about 500 km around the Earth. One of the telescopes looking into the zenith direction will measure galactic cosmic rays and solar particle events, the other, perpendicular to it, will also measure trapped particles. The ranges of interest in terms of energy are 100 keV–8 MeV for electrons, 1 MeV–1 GeV for protons and 100 MeV/n–1 GeV/n for heavier ions. Both telescopes consist of several detectors connected in coincidence or anticoincidence to determine the energy and to restrict the field of view. The first breadboard model of RADTEL, with only one detector axis, was tested and calibrated at the Proton Irradiation Facility of the Paul Scherrer Institute. The RADTEL1 telescope was placed into proton beams of different energies up to 250 MeV at several angles of incidence, and the data measured were compared to data simulated with the Geant4 Radiation Analysis for Space (GRAS) Monte Carlo simulation code. This toolkit was developed by the European Space Agency (ESA) especially for space applications based on the widely used Geant4 simulation toolkit. The geometries that were required for the simulations were defined in Geometry Description Markup Language (GDML), which were based on STL files created with a Computer-Aided Design (CAD) program. The possible physical processes were analyzed in terms of energy losses of charged particles when travelling through matter. Three straggling functions (Gauss, Vavilov, and Landau) were investigated for fitting measured and simulated spectra. After all data had been processed the calibration curves were fitted [1,2].

The three dimensional silicon detector telescope ESEO-TRITEL, developed at the Centre for Energy Research and adapted for the European Student Earth Orbiter (ESEO) mission of the European Space Agency by the ESEO-TRITEL student team, can measure the absorbed dose and the Linear Energy Transfer (LET) spectra in three orthogonal directions from which the average quality factor of space radiation in orbit and the dose equivalent can be determined. The ESEO satellite was launched on 3 December 2018, but most of the payloads, like TRITEL, have not yet been switched on. Since the original environmental modelling using the obsolete AP8/AE8 trapped proton and electron models has been outdated by now, a new study was made to determine the trapped particle environment and the expected energy deposition spectra with GRAS for a hypothetical mission using the new AP9/AE9 models [3].

Results

For the energy deposition spectra measured by RADTEL1 and simulated with GRAS it was shown that the transition range between Gauss (thick layers) and Landau (thin layers) is well matched by the Vavilov straggling function developed by Vavilov for medium thick layers and it remains accurate in the ranges that can be described with Gauss. Therefore, the Gaussian fitting can be eliminated and only fitting with the Landau and Vavilov functions needs to be performed. Calibration lines of the first two detectors in the RADTEL telescope were fitted.

In the frame of the new ESEO environmental study, the differences between the widely used but older AP8/AE8 and the updated AP9/AE9 trapped energetic particle models were investigated for the ESEO mission. It was found that there are only minor differences in the orbit averaged fluxes. The AP8 overestimates fluxes under 1 MeV and over 50 MeV but underestimates in between these regions compared to AP9. The orbit averaged electron flux provided by AE8 is similar to the one provided by the new model at low energies, but overpredicts above 1 MeV, right in the measuring range of TRITEL and cuts off earlier. This could mean smaller real count rates for electrons. The shape of the South Atlantic Anomaly (SAA) is similar but its overall extent is larger for AP9. Based on the results, a spectrum acquisition time shorter than the present 10 minutes was recommended to obtain a reasonably accurate resolution of the data measured in the SAA and to be able to compare the models with the data to be measured.

Related publications

- [1] B. Erdős, A. Hirn and B. Zábóri: *Úrdozimetriai célú részecsketeleszkópok modellezése Monte Carlo módszerekkel*, Proceedings of the Hungarian Space Research Forum MUF2019-K04 (2019)
- [2] B. Erdős: *Modelling and calibrating charged particle detector telescopes with Monte Carlo simulations*, Proceedings of the PhD workshop of the Physics Doctoral School at the Faculty of Natural Sciences Budapest University of Technology and Economics, Ook Press Ltd. (2019)
- [3] B. Erdős, A. Hirn and B. Zábóri: *Cosmic radiation environment modelling for the ESEO mission*, Proceedings of the 3rd Symposium on Space Educational Activities (2019) (submitted)

SPACE DOSIMETRY FOR HUMAN SPACEFLIGHT

Attila Hirn, István Apáthy, András Gerecs, Andrea Strádi, Julianna Szabó, Balázs Zábori

Objective

Space dosimetry activities of the research centre are concentrated in the Space Dosimetry Research Group. Several dosimeter systems developed by the group operate on board the International Space Station (ISS) with the aim of providing information on the dose distribution at different locations with different shielding conditions and also personal dosimetry. Maintenance, scientific and technical support during operation and upgrade of these systems are key tasks of the group. The activities reported in the present paper are realized in cooperation with the Institute of Biomedical Problems (IBMP), Russian Academy of Sciences and S. P. Korolev Rocket and Space Corporation Energia.

Methods

The Pille space-qualified thermoluminescent (TL) dosimeter system, developed in the institute, provides accurate and high resolution absorbed dose data [1, 2]. Since 2019, the on-board system has consisted of a TL reader unit and 14 TL dosimeter keys equipped with a memory chip containing the identification code and the individual calibration parameters of the given dosimeter. Pille is operated as part of the service dosimetry system of the Russian Segment. For on-board stability analysis, from time to time all dosimeters are placed on panel No. 327 of the Zvezda module for two weeks, and the quasi-homogeneous radiation field at that position is used as a natural calibration radiation source. The correction factors for the individual dosimeters are then calculated from the results of the sensitivity measurements. In the TRITEL experiment a three-axis silicon detector telescope and a set of passive detectors are used to determine the Linear Energy Transfer (LET) spectrum [3].

Results

In year 2019, approx. 6000 measurements were performed with the Pille system, including dosimetry mapping, automatic cyclic measurements and individual dosimetry of the astronauts during extra-vehicular activities. The data obtained were evaluated. Results of monthly read outs of the dosimeters for the first half of 2019 are shown in Fig. 1 as an example. Measured doses differ due to the different shielding configurations around the location of the individual dosimeters.

LET spectra obtained with the TRITEL and its accompanying plastic nuclear track detectors showed good agreement in the overlapping region of 10–100 keV/μm in water, which means that track etch detector data can be used for correction of TRITEL data in the high LET region (>100 keV/μm).

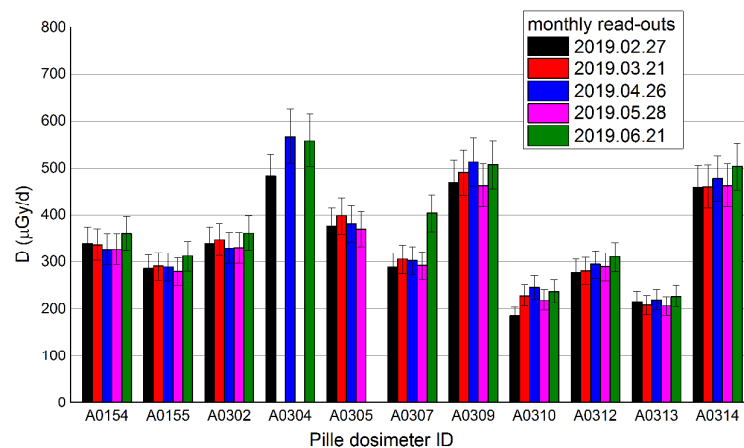


Figure 1: Results of the dosimetry mapping performed with the Pille system in the Russian Segment of the ISS

Remaining work

Evaluation and interpretation of the measurement data produced by the Pille and TRITEL-RS dosimeter systems on board ISS, as well as maintenance of these instruments will be continued.

Acknowledgement

Maintenance and development activities performed in the frame of Russian-Hungarian space cooperation in 2019 were funded by the Government of Hungary through contract number KKM/43047/2019/Adm.

Related publications

- [1] S. Deme, I. Apáthy, A. Csóke and A. Hirn: *40 éves lett a Pille*, Sugárvédelem **12(1)**, 51 (2019)
- [2] A. Hirn, I. Apáthy, A. Csóke, S. Deme: *Pille 40 – egy korszakokon átívelő történet*, Astronautical Almanach **70**, 47 (2019)
- [3] A. Baranyai, A. Hirn, S. Deme, A. Csóke, I. Apáthy, I. Fehér: *212Bi-212Po alpha source for the calibration and functional testing of silicon detectors: Preparation and characterisation*, Appl. Radiat. Isotopes **158**, 109028 (2020)

DOSE DISTRIBUTION INSIDE THE INTERNATIONAL SPACE STATION STATION-3D/DOSIS 3D

Julianna Szabó, Andrea Strádi, Attila Hirn, Balázs Zábóri, József K. Pálfalvi

Objective

The aim of the DOSIS 3D project is the measurement of the radiation environment inside the International Space Station (ISS). The project is organized by the European Space Agency (ESA) under the leadership of the German Aerospace Centre (DLR), with the participation of research groups from all around the world. The Centre for Energy Research (EK) is responsible for the provision of passive radiation detectors for the measurement of the absorbed dose, Linear Energy Transfer (LET) spectra and dose equivalent. These activities are funded in the frame of the ESA PRODEX Experiment Arrangement No. 4000124183. DOSIS 3D had been started in the year 2012 and after several extensions it was prolonged till the remaining lifetime of the ISS. It consists of approximately half-year long exposure cycles (phases). The current report reflects the contribution of EK until the end of 2019, with special attention to the last three phases (12-13-14).

Methods

Thermoluminescent detectors (TLDs) and solid state nuclear track detectors (SSNTDs) are applied by the EK Space Dosimetry Research Group to investigate the dose contribution of the low ($< 10 \text{ keV}/\mu\text{m}$) and the high ($> 10 \text{ keV}/\mu\text{m}$) LET cosmic radiation. The plastic detector boxes contain two SSNTD sheets and six or eight TLD pellets. In each phase there are 10 single boxes and a set of 3 boxes (arranged in 3 normal directions of space) installed inside the European Columbus module. For a better understanding of the properties of the applied radiation detector systems, an extensive ground intercalibration program is applied as an indispensable part of the work with contributions from all participating investigators.

Results

The parameters mostly affecting the radiation environment onboard the ISS are the solar activity, the altitude of the Station and the local shielding. The last three phases of DOSIS 3D took place at the end of solar cycle 25, with very low and almost constant solar activity. The altitude of the ISS was also unchanged. Our results are in accordance with these circumstances. Figures 1. and 2. present the absorbed dose rates measured by TLDs and SSNTDs, respectively, for phases 12, 13 and 14, from December 2017 to June 2019. There is only a slight difference between the consecutive phases. For all three exposure missions we see a similar pattern of absorbed dose rate over the 10 positions in Columbus, for both detector types. The lowest doses are obtained at Boxes 3, 4 and 9, while the highest values at Boxes 2, 6 and 7. The reason for this pattern lies in the different local shielding thicknesses for the 10 positions inside the Columbus Laboratory. Changes in the local shielding configuration mostly influence the contributions to the absorbed dose values due to the low-energy protons of the South Atlantic Anomaly crossings.

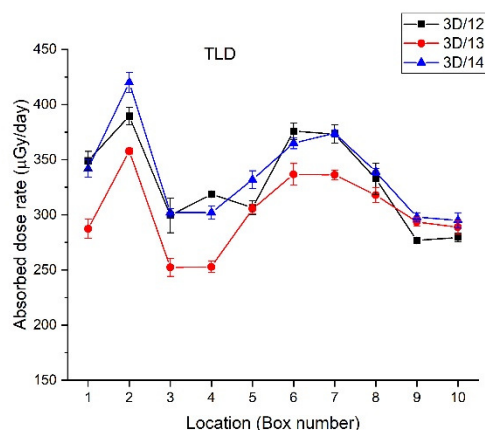


Figure 1: Absorbed dose rates measured by TLDs

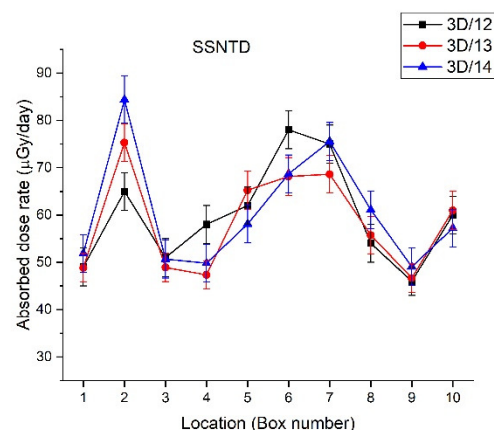


Figure 2: Absorbed dose rates measured by SSNTDs

Remaining work

According to the current plan, the project continues till 2024. The interpretation of the vast amount of data is in progress. An interactive database is going to be built, serving the scientific community and holding essential information for the application of radiation protection standards for manned spaceflight and for any radiation susceptible experiment in space.

Related publication

- [1] T. Berger, ... , J.K. Pálfalvi, J. Szabó, A. Strádi et al.: *DOSIS & DOSIS 3D Onboard the ISS - Status and Science Overview from 2009 - 2019*, 24th Workshop on Radiation Monitoring for the International Space Station, Athens, Greece (2019)

RESEARCH & DEVELOPMENT ACTIVITIES IN SPACE WEATHER

Balázs Zábóri, Boglárka Erdős, Attila Hirn, András Gerecs, István Apáthy

Objective

There is already a heavy dependence of the human civilization on technology, e.g. in the fields of energy and telecommunication systems. A continuous increase in human presence and different space-based infrastructure is in progress in the Near-Earth region. They are seriously affected by changes in space weather, especially during coronal mass ejections and geomagnetic storms. To study space weather and to protect our technology, as a first step, it is necessary to establish and develop an advanced monitoring system to provide scientific data on space radiation intensity and the status of the magnetosphere. Therefore, development of new space weather related instrument technologies got under way in the past years at the Centre for Energy Research, including ground-based measurements and measurements on different suborbital (aircrafts, stratospheric balloons, sounding rockets) and orbital platforms (satellites).

Methods

In the frame of the Space Weather Service Network (SWE) segment of the European Space Agency (ESA) Space Safety programme, ESA requested an operational space weather prediction system with appropriate databases originating from near-real time service provider instruments/payloads. Since the cosmic environment of the Earth is highly influenced by several physical parameters (magnetic field variability, cosmic ray intensity, solar activity, atmosphere, etc.) and mainly due to the complexity of the magnetosphere, a very good spatial and time resolution is required in space weather monitoring. To fulfil this goal ESA defined the Distributed Space Weather Sensor System (D3S) concept utilizing hosted primary and secondary payloads for operational space weather monitoring on board as many platforms as possible. In the framework of the ESA General Support Technology Programme (GSTP) EK has initiated the RADCUBE In-Orbit Demonstration (IOD) mission including the development of a new instrument, called RadMag [1, 2]. The major goal of the RADCUBE mission is to demonstrate the space weather service capabilities of a CubeSat mission to the ESA Space Safety SWE programme segment. However, the development of the RadMag instrument is very much restricted by the technical constraints of a typical CubeSat mission, thus, in parallel, EK initiated a similar development in collaboration with ESA experts, called D3S RadMag or the RadMag (RM) space weather instrument family concept (Fig. 1). The major goal of the development is to provide a market product combining the radiation and magnetic field measurement capabilities into one payload to be directly applicable within the D3S hosted payload concept of ESA. The conceptual approach shall take into account modularity as design driver in order to make it possible to accommodate it to different platforms as a hosted payload. Modularity means that a general, core electrical system is designed (data acquisition and control, power supply and communication), which can handle the sensor systems (silicon detector telescopes, magnetometers and the related boom system) connected. This concept provides a highly variable instrument, which can be fitted to the given hosted mission. Sensor selection will be based on the expected space weather environment and mission constraints, like available volume, mass, power, etc. As a significant optional component, the instrument concept shall feature the capability of providing radiation hardness assurance and monitoring dosimetric quantities, which can be provided as a commercial service for the platform system providers. At the moment, there is no such a complex instrument available on the market or under development as hosted payload candidate which can provide all of the above given needs, has the capability of variable sensor system for the given hosted mission and combines the space radiation and magnetic field monitoring capability.

The intensity of cosmic rays entering the Earth's atmosphere is determined by, and is therefore an indicator of, the level of solar activity. As solar activity approaches a maximum, the importance of monitoring cosmic rays and understanding their effects and the corresponding dose levels increases. When a transient solar event, such as a solar storm, occurs and if it is strong enough, solar cosmic rays can affect electronics and even humans at ground level; this phenomenon is called "Ground Level Enhancement (GLE)". Data from the neutron monitors can be utilized for research on geomagnetic storms, dose effectiveness of cosmic rays and the GLE warning system, predicting changes in cosmic ray intensity and the environmental impact of cosmic rays. Neutron monitor stations are generally used worldwide as basic space weather research and data service systems to monitor the real-time status of the space weather environment of our planet and to provide input data set(s) for operational space weather prediction systems, like in the frame of the ESA Space Safety programme.

Results

The mechanical and electrical parts of the Engineering Qualification Model (EQM) of the RadMag instrument for the RADCUBE mission was successfully manufactured and preassembled. The mechanical and the electrical design of the RadMag Elegant Breadboard Model (EBB) were finished.

A proposal was submitted for the stratospheric research balloon flight opportunity and accepted in the frame of the HEMERA call. HEMERA is a balloon infrastructure project offering balloon flights for research funded by the European Commission within its programme Horizon 2020. A proposal submitted for a sounding rocket flight opportunity is under evaluation. The experiments proposed, with some modification, will be continuation of the experiments performed in the frame of ESA's REXUS/BEXUS (Rocket and Balloon Experiments for University Students) programme in the mid-2010s.

Geographical distribution (height above sea level, geomagnetic rigidity), operating time and availability of measurement data products from the already existing European neutron monitor stations were analysed. It was concluded that the number and availability of neutron monitor stations shall be further increased, especially in Middle-Europe. In Middle-Europe only one station is operated in Slovakia (LMKS station) with less than full operability in time, thus available data set(s) are not complete.

In addition, taking into account the possible geomagnetic environment in Hungary there are only a few stations in Europe with similar geomagnetic shielding environment (~3 GV cut-off rigidity) moreover, they have relatively poor operability in time. Establishment of a neutron monitor station in Hungary will be a benefit for the European neutron monitor network and for the space weather prediction system of ESA, and for Hungary as well.

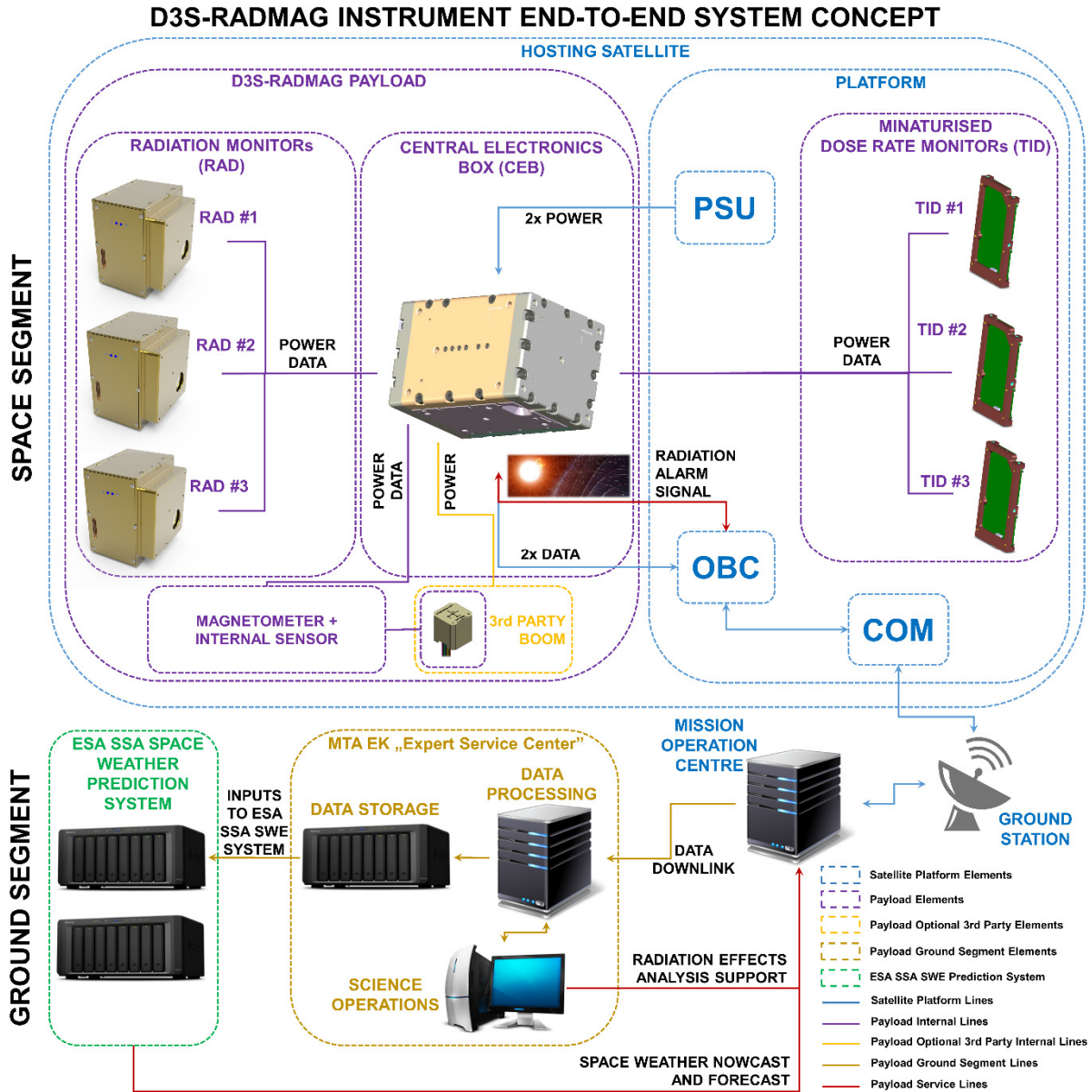


Figure 1: RadMag end-to-end system concept

Remaining work

Due to a change in the model philosophy initiated by the system prime, the EQM of the RadMag instrument for the RADCUBE mission will be made a protoflight model (PFM) in 2020 and tested according to the requirements. The launch of the satellite is expected in 2021 with a minimum of 6 months in-orbit operation for the RadMag instrument. In the case of the D3S-RadMag instrument development, the EBB shall be manufactured and tested in relevant facilities. In parallel, the first IOD flight opportunity for the D3S-RadMag instrument will be identified together with ESA and the related development roadmap shall be investigated. Experiment hardware for the sounding rocket and the stratospheric balloon experiments planned for 2021 and 2022, respectively, will be designed and manufactured. Design of the neutron monitor station will also be performed.

Related publications

- [1] B. Erdős, A. Hirn and B. Zábóri: *Űrdozimetriai célú részecskelevezők modellezése Monte Carlo módszerekkel (in Hungarian)*, Magyar Űrkutatási Fórum 2019 válogatott közleményei, HU ISBN 978-963-7367-22-9, MUF2019-K04 (2019)
- [2] B. Erdős: *Modelling and calibrating charged particle detector telescopes with Monte Carlo simulations*, Proceedings of the PhD workshop of the Physics Doctoral School at the Faculty of Natural Sciences Budapest University of Technology and Economics, Budapest, Hungary: Ook Press Ltd. 76 ISBN: 978-963-421-783-1, Editor: F. Simon (2019)

UPGRADE OF THE SPACE RESEARCH TEST LABORATORY

Attila Hirn, Balázs Zábóri

Objective

A complex space research testing laboratory was solemnly opened at the Centre for Energy Research in 2018. In 2019, upgrade of the facilities was carried out based on European space industry standards (European Cooperation for Space Standardization, ECSS) and frequent customers' requests.

Methods

The central part of the Laboratory is an ISO7 (class 10,000) cleanroom, where space hardware assembling and integration activities can be carried out according to ECSS specifications. The thermal-vacuum (TVAC) facility and the vibration facility, where the essential tests of the space hardware can be performed, are in direct connection with the cleanroom. The Space Research Laboratory also includes electronic development laboratories equipped for space hardware development. Space hardware are tested for high vacuum and extreme temperatures with special equipment in the TVAC facility, whereas launch loads are simulated in the vibration facility with a high-performance vibration test system, which is outstanding in the country. In case of malfunction of the tested instrument, it can easily be returned to the cleanroom for disassembling and error search. This kind of complexity of the laboratory enables that the final integration as well as the essential testing of the flight hardware are performed at the same premises. Significant costs and development time can be saved this way. Nevertheless, some features, such as contactless vibration testing, contamination monitoring, control of the TVAC system and an ECSS conform soldering station were missing from our space equipment testing portfolio. Therefore, possibilities for available extensions to our existing test systems and modifications in the self-developed equipment (e.g. the TVAC chamber) were considered and analysed.

Results

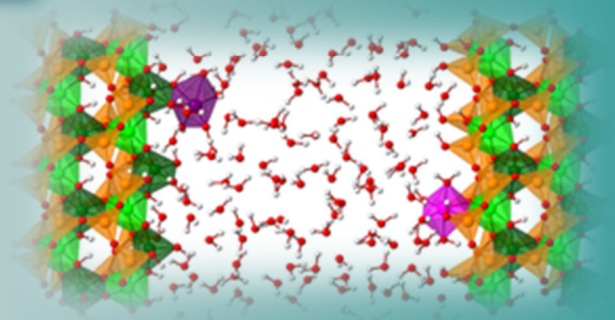
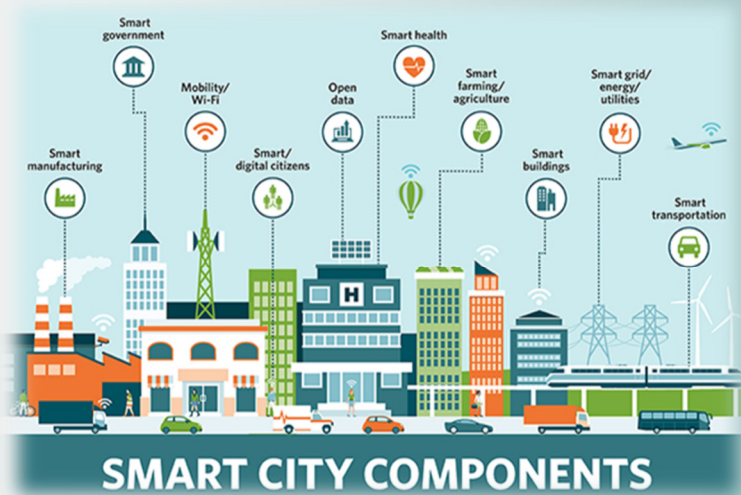
The TVAC system was redesigned to enable contamination control and spectroscopy. Thermoelectric Quartz Crystal Microbalances (TQCM) are used to monitor in real-time the evolution of the amount of volatile condensable materials emitted from the device under test. Mass spectroscopy of the contaminants up to 200 amu is realised with a residual gas analyser. The TVAC system was also modified to enable depressurisation with air of purified N₂ as requested. The vibration facility was extended with a stroboscope system for contactless vibration testing and structural analysis of the device under test. In the ISO7 cleanroom an ECSS conform soldering station was developed, including a stereozoom soldering microscope, a soldering station with temperature control, fume extractor, a digital soldering tip measurement unit, a calibrated portable airborne particle counter and purified N₂ available for cleaning purposes, see below (Fig. 1).



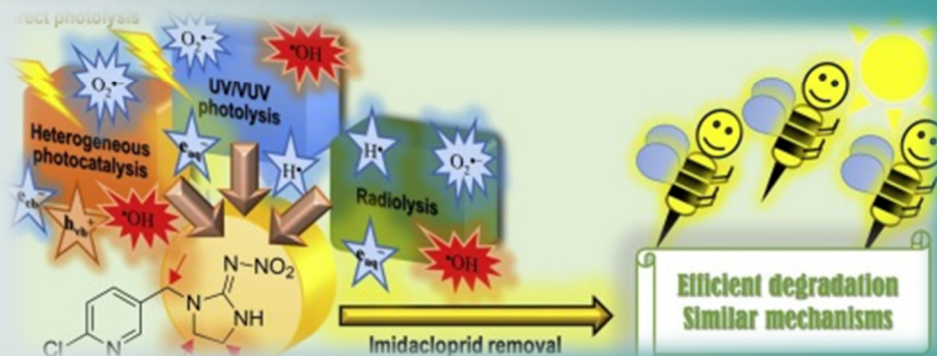
Figure 1: ECSS conform soldering station in the ISO7 cleanroom

Remaining work

Modifications on the thermal-vacuum chamber will be finished in 2020; the rest of the upgrade has been completed. From 2020, the Space Research Laboratory is operated by EK's spin-off company REMRED Technologies Ltd.



IV. ENERGY AND ENVIRONMENTAL STUDIES



UTILIZATION OF CU AND FE COMPLEXES IN WATER OXIDATION

József S. Pap, Dávid Lukács, Tímea Benkó, Krisztina Frey, Sahir M. Al-Zurairi, Tamás Ollár, Zsolt Kerner

Objective

On the basis of our recent success in homogeneous water oxidation electrocatalysis by branched peptides furnishing multiple Cu^{2+} catalytic sites [1], we attempted to extend our research from high pH in phosphate buffer to near-neutral pH in borate buffer. This was expected to result in more stable systems. In parallel, we tested water-insoluble Cu and Fe complexes in order to combine these molecular catalytic units with semiconducting nano-oxides by exploiting hydrophobic interactions. The work is supported by the VEKOP 2.3.2-16-2016-00011 and the NKFIH NN 128841/2018 grants.

Methods

The Cu-peptide complexes were formed by mixing the peptide and $\text{Cu}(\text{ClO}_4)_2$ in aqueous solution. Water-insoluble ligands and their Fe and Cu complexes were synthesized by following known methods. Electrochemical experiments were conducted on a Bio-Logic SP-150 or a GAMRY Reference 3000 potentiostat, in specially designed cells. The working electrode materials included glassy carbon (GC), boron doped diamond (BDD), indium tin oxide (ITO), fluorine-doped tin oxide (FTO), or nanostructured semiconductors like $\alpha\text{-Fe}_2\text{O}_3/\text{Ti}$ (provided by our collaborators). As counter and reference electrodes Pt and Ag/AgCl were used, respectively. The applied electrochemical methods were typically cyclic voltammetry (CV), square wave voltammetry (SWV), or controlled potential electrolysis (CPE). The produced O_2 was detected by an optical probe, or a Shimadzu Tracera 2010 gas chromatograph equipped with a BID detector and a home-made sampling loop. The surfaces of the as-prepared/used electrodes were investigated by X-ray photoelectron spectroscopy (XPS), scanning electron microscopy (SEM), energy dispersive X-ray (EDX) and infrared (IR) spectroscopy. Spectro-electrochemistry was carried out by combining a Cary 60 UV-visible spectrophotometer with an electrochemical cell.

Results

The true electrocatalyst of water oxidation in a number of cases proved to be an *in situ* developed 'CuO' film instead of (or beside) the original Cu complex itself, since metal-ligand interactions may be disrupted under the applied conditions [2]. The decomposition may yield an inexpensive and controllable method to fabricate nanostructured metal oxide coatings. We investigated the Cu-triglycine complex equilibrium system with uniform peptide binding mode throughout the pH range of ~7 to 10 in borate buffer. The development of a 'CuO' nanoparticle coating was observed on oxide working electrodes such as an n-type semiconducting $\alpha\text{-Fe}_2\text{O}_3$ nanoarray, without ruining its morphology (Fig. 1a,b). This coating was a robust electrocatalyst of water oxidation. XPS indicated a mixed $\text{Cu}_2\text{O}/\text{CuO}/\text{Cu}(\text{OH})_2$ surface composition. We identified by spectrophotometry a ' $\text{Cu}^{\text{III}}\text{-O}$ ' intermediate and the interplay of the co-existent borate equilibrium species with the Cu-triglycine system as the key factor to allow control over the deposition.

We compared two selected, water-insoluble Fe^{II} coordination complexes made with the non-symmetric, bidentate ligands, 2-(2'-pyridyl)benzimidazole (PBI) in $[\text{Fe}(\text{PBI})_3](\text{OTf})_2$ (**1**, OTf^- = trifluoromethyl sulfonate) and 2-(2'-pyridyl)benzoxazole (PBO) in $[\text{Fe}(\text{PBO})_2](\text{OTf})_2$ (**2**). CV in water/acetonitrile indicated that only **1** was a homogeneous catalyst. Both complexes were successfully immobilized on an ITO electrode by simple drop-casting of **1** and **2** onto ITO (Fig. 1c). Both **1**/ITO and **2**/ITO showed increased activity in borate buffer at pH 8.3. According to SEM, EDX, XPS and re-dissolution tests, the Fe remained in complex with PBI during electrolysis in the drop-casted, nano-porous films. In contrast, the PBO complex underwent *in situ* decomposition, yielding a mineralized form that was responsible for catalysis.

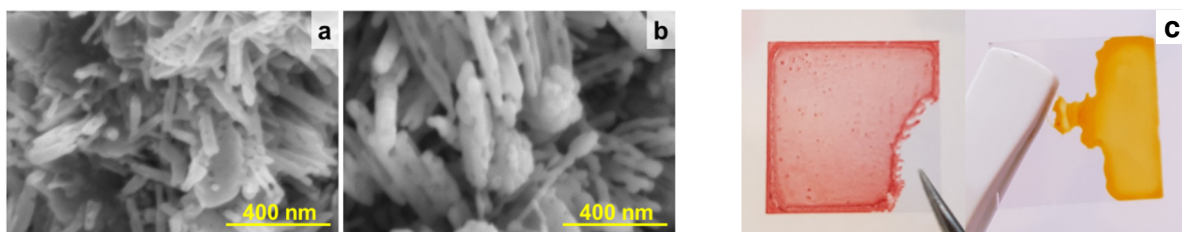


Figure 1: (a) SEM picture ($\times 100,000$) of nano-arrayed $\alpha\text{-Fe}_2\text{O}_3/\text{Ti}$, (b) picture of the same surface after CPE in the presence of $\text{Cu}(\text{II})/\text{H-GGG-OH}$, in sodium borate electrolyte, at pH 9.2 [3] (c) typical drop-casted samples of **1**/ITO (red) and **2**/ITO (orange) [4].

Related publications

- [1] Ł. Szyrwił, D. Lukács, T. Ishikawa, J. Brasun, Ł. Szczukowski, Z. Szewczuk, B. Setner, J. S. Pap: *Electrocatalytic water oxidation influenced by the ratio between Cu^{2+} and a multiply branched peptide ligand*, *Cat. Commun.* **112**, 5-9 (2019)
- [2] D. Lukács, Ł. Szyrwił, J. S. Pap, *Copper Containing Molecular Systems in Electrocatalytic Water Oxidation – Trends and Perspectives*, *Catalysts*, **9**, 83 (2019)
- [3] D. Lukács, M. Németh, Ł. Szyrwił, L. Illés, B. Pécz, S. Shen, J. S. Pap, *Behaviour of a Cu-Peptide complex under water oxidation conditions – Molecular electrocatalyst or precursor to nanostructured CuO films?*, *Sol. Energ. Mater. Sol. C.*, **201**, 110079 (2019)
- [4] S. M. Al-Zurairi, T. Benkó, L. Illés, M. Németh, K. Frey, J. S. Pap, *Utilization of Hydrophobic Ligands for Water-Insoluble Fe(II) Water Oxidation Catalysts - Immobilization and Characterization*, *J. Catal.*, submitted.

METHANE DRY REFORMING OVER NOVEL BIMETALLIC CATALYSTS

Miklós Németh, Andrea Beck, Gergely Nagy, Anita Horváth

Objective

The catalytic dry reforming (DRM) reaction yields valuable synthesis gas, viz. hydrogen and carbon monoxide in an equimolar ratio ($\text{CH}_4 + \text{CO}_2 \rightleftharpoons 2\text{CO} + 2\text{H}_2$) from sources such as, for example, a cleaned biogas. Ni-based bimetallic catalysts supported either on SiO_2 or on $\text{CeO}_2\text{-Al}_2\text{O}_3$ mixed oxide supports were prepared and investigated.

Methods

Catalyst samples containing Ni and Pt or In were synthesized by a wet impregnation (WI) or a deposition precipitation (DP) method using the same $\text{CeO}_2\text{-Al}_2\text{O}_3$ support. The SiO_2 -supported catalysts were already at our disposal. Structural investigations were carried out by the Temperature Programmed Reduction method (TPR), X-ray Photoelectron Spectroscopy (XPS) and Transmission Electron Microscopy (TEM). Diffuse Reflectance Infrared Fourier Transform Spectroscopy (DRIFTS) was applied to detect the surface-adsorbed species in the presence of CO, CO_2 or a dry reforming mixture. Dry reforming catalytic tests were done in a plug flow reactor. Temperature programmed oxidation (TPO) was carried out to quantify the carbon deposited in DRM. CO pulse flow experiments were done to monitor the CO dissociation on Ni and NiIn/SiO_2 .

Results

The recently discovered NiIn/SiO_2 catalyst has beneficial properties in the dry reforming of methane, including inhibited coking. In order to get deeper insights into the coke-free behaviour of this sample, the DRIFTS studies under CO, CO_2 or $\text{CO}_2 + \text{CH}_4$ flow at different temperatures and CO pulse flow experiments at 600 °C followed by mass spectrometry were completed. The lack of bridge and multi-coordinated carbonyls proved the dilution of the nickel surface with indium had taken place, and the band at 2013 cm^{-1} was attributed to CO bonded on Ni atoms surrounded by In neighbours. In the presence of a dry reforming mixture, stable Ni bonded CO species were found on NiIn/SiO_2 suggesting that the metallic sites remained clean during the reaction (unlike on the reference Ni/SiO_2). The pulse CO experiments at 600 °C, tailored to detect the most sensitive surface sites for the Boudouard reaction, proved that CO dissociation on the bimetallic catalyst was markedly hindered, while it caused carbon deposition on the reference sample. Based on all these results, we postulated a picture of the working catalyst that is dispersed ensembles of NiIn-InO_x entities stabilized by SiO_2 .

The new $\text{CeO}_2\text{-Al}_2\text{O}_3$ supported Ni and NiPt catalysts were investigated by infrared spectroscopy (CO chemisorption), and the reduction properties, and the catalytic activity together with the measurement of deposited coke were also determined. According to the TPR data, the samples prepared by the DP method contained nickel-oxide in medium and strong interaction (nickel-aluminate) with the support while WI samples formed only strongly interacting Ni-aluminate after calcination, and most of the platinum seemed to be separated from nickel in both samples. Under the newly set catalytic test conditions, the activity of DP samples was decreasing and significant coke deposits were measured after the reaction. In contrast, Ni and NiPt samples prepared by WI had nice and stable catalytic activity with close to zero coke formation. Based on these results we suggest that the CeO_2 component was very effective in the oxidation of surface coke originating from the activation/dissociation of the reactants, and bulk carbide formation must have been restricted in the impregnated samples (that is the starting point of coke deposition). We suspect that the mixed oxide support structure must have been modified during the deposition precipitation process (when Ni was introduced) resulting in a catalyst that was prone to coke deposition due to the decreased Ni/CeO_x interface and the reduced interaction with the support compared to the very stable impregnated samples.

Remaining work

After some additional measurements (TEM, XRD measurements, long-term catalytic tests) another manuscript will be submitted soon together with the cooperating Italian research group on the $\text{CeO}_2\text{-Al}_2\text{O}_3$ supported samples.

Related publication

- [1] M. Németh, F. Somodi and A. Horváth: *Interaction between CO and a Coke-Resistant NiIn/SiO_2 Methane Dry Reforming Catalyst: A DRIFTS and CO Pulse Study*, doi: 10.1021/acs.jpcc.9b06839, Journal of Physical Chemistry C **123**:(45), 27509-27518 (2019)

BIMETALLIC GOLD CATALYSTS IN AEROBIC SELECTIVE OXIDATION OF ALCOHOLS

Gergely Nagy, Károly Lázár, Zoltán Schay, Miklós Németh, György Sáfrán, Andrea Beck

Objective

The PhD work of Gergely Nagy comprises the investigation of the effect of a second metal (Ag, Ru, Ir) and of various supports (SiO₂, Al₂O₃, MgO, MgAl₂O₃ and hydroxyapatite (HAP)) on the catalytic performance of supported gold catalysts in aerobic oxidation of alcohols. For 2019 the following tasks were planned: (i) several additional measurements to the almost complete experimental work, (ii) submission of two more publications on the subject of the PhD thesis (two papers were published already), (iii) writing the first draft of the thesis.

Methods

In the PhD work the catalysts were prepared by adsorption of pre-formed bimetallic AuAg, AuRu, AuIr and monometallic Au, Ag, Ru sols on the support. Ir/Al₂O₃ was prepared by wet impregnation. Other studied catalysts were prepared by solvated metal atom dispersion (SMAD) deposition by our partners in a bilateral project. Various techniques were used for structural characterisation of the samples: prompt- γ -activation analysis, transmission electron microscopy, UV-vis spectroscopy, X-ray diffraction, X-ray photoelectron spectroscopy, temperature programmed oxidation and reduction, CO adsorption measurements followed by diffuse reflectance Fourier-transform infrared (DRIFT) spectroscopy, temperature programmed CO₂ and NH₃ desorption and in bilateral co-operation, X-ray absorption fine structure (XAFS) spectroscopy. The catalysts were studied in selective liquid phase oxidation of benzyl alcohol with oxygen and in the case of several Au-Ag catalysts also in glycerol selective oxidation (in bilateral co-operation), and also in CO oxidation

Results

The comparison of the effect of various non-redox oxide and hydroxyapatite supports in the benzyl-alcohol oxidation using Au nanoparticles was published with the co-operating Chinese researchers. [1] It was demonstrated that for the interpretation of the obtained data, the roles of active sites on the gold nanoparticles of various dispersion, accessibility of the gold surface and the differing surface partial charge on the gold, as well as the acid-base properties of the various supports should all be considered simultaneously, in various extents, depending on the reaction conditions being used.

The efficiency of titania supported AuAg catalysts with Au/Ag in 1/1 and 4/1 atomic ratio, compared to that of corresponding monometallic samples prepared both by sol immobilization (SOL) and by deposition precipitation by urea (DPU) was investigated in glycerol oxidation in an Italian collaboration, and was published. [2] The presence of bimetallic nanoparticles and the higher resistance of silver to oxidation in the bimetallic systems than in the monometallic one were revealed. Though DPU and SOL techniques created somewhat different structures, both Au-rich AuAg/TiO₂ samples showed a positive synergistic effect enhancing the catalytic behaviour toward the glycerol oxidation, while in the Au/Ag=1/1 composition, the Ag had a detrimental effect on the activity of gold.

An article was submitted on SOL derived, alumina supported, AuRu (Au/Ru=57/43) and AuIr (Au/Ir=77/23) catalysts suggesting the synergetic effect of Ru with Au in both calcined and reduced form and of Ir with Au in a reduced state in benzyl alcohol oxidation carried out with K₂CO₃ addition. [3] This was based on the comparison of their activities with that of monometallic Au and Ru or Ir catalysts related to the same estimated molar amount of surface metal atoms, taking into account the Au/Ru and Au/Ir atomic ratio and the particle sizes/dispersions of active phases, when even distribution of the two metals on the surface and in the bulk was assumed in the bimetallic systems. The synergy is even more expressed if the enrichment of the second metals over the gold on the surface of the bimetallic particles, as was indicated by CO adsorption followed by DRIFT spectroscopy, is also considered.

The first draft of the thesis has been prepared.

Remaining work

The completion of the publication process of the paper on the alumina supported AuRu and AuIr catalysts. Revision of the first draft of the thesis, review of the thesis by external referees, pre-defence, corrections, submission of the thesis.

Related publication

- [1] G. Nagy, A. Beck, Gy. Sáfrán, Z. Schay, S. Liu, T. Li, B. Qiao, J. Wang and K. Lázár: *Nanodisperse gold catalysts in oxidation of benzyl alcohol: comparison of various supports under different conditions*, Reaction Kinetics, Mechanisms and Catalysis **128**, 71-95 (2019) doi: 10.1007/s11144-019-01615-8
- [2] M. Stucchi, A. Jouve, A. Villa, G. Nagy, M. Németh, C. Evangelisti, R. Zanella and L. Prati: *Gold-Silver Catalysts: Ruling Factors for Establishing Synergism*, ChemCatChem **11**, 4043-4053 (2019) doi: 10.1002/cctc.201900591
- [3] G. Nagy, T. Gál, D. F. Srankó, G. Sáfrán, B. Maróti, I. E. Sajó, F.-P. Schmidt and A. Beck: *Selective aerobic oxidation of benzyl alcohol on alumina supported Au-Ru and Au-Ir catalysts*, Molecular Catalysis (2020) doi: 10.1016/j.mcat.2020.110917, in press

CATALYTIC PROPERTIES OF 2D MoSSE DURING ELECTROLYSIS OF WATER

Antal Koós, Tamás Ollár, Zoltán Osváth, Zsolt Kerner, József Sándor Pap, Levente Tapasztó

Objective

Transition metal chalcogenides (TMCs), especially MoS₂, MoSe₂ and MoS₂xSe_(1-2x), are broadly considered promising cost-efficient alternatives to platinum in a hydrogen evolution reaction. Since their activity is limited by the relative inertness of their pristine basal plane, controlled incorporation of defects is of paramount importance. We used several experimental strategies to increase the density of the active sites and improve the efficiency of the samples. We combined the flexibility of Chemical Vapour Deposition (CVD), atomic resolution characterisation, computer simulations and cyclic voltammetry to understand the relationship between the structure and properties of the 2D MoS₂Se samples, and using all these we designed samples with enhanced activity.

Methods

The MoS₂Se samples were produced by the atmospheric pressure CVD method on highly oriented pyrolytic graphite (HOPG). In some cases, Pt nanoparticles were deposited electrochemically. The atomic scale defects in the samples were characterised by scanning tunnelling microscopy and spectroscopy (STM and STS), the surface coverage and layer number was determined by Raman spectroscopy, the Pt nanoparticle distribution was measured by scanning electron microscopy (SEM), atomic force microscopy (AFM) and X-ray photoelectron spectroscopy (XPS), and the electrocatalytic response was investigated by cyclic voltammetry (CV). Calculations were performed in the framework of spin-polarized density functional theory (DFT).

Results

Our experiments showed that the efficiency of monolayer TMCs is higher than the efficiency on double - or multiple-layer samples. Therefore, we used glass-assisted CVD to grow large-area MoS₂Se monolayers. We introduced single- and di-vacancies into the TMC monolayers by adding a hydrogen flow during the deposition, which increases considerably the density of active sites. STM and STS investigations revealed a relatively large (10¹² cm⁻²) concentration of single Mo atom vacancies [1]. Using DFT calculations, we showed that substitution of heteroatoms e.g. S and Se with different electronegativity induces a local redistribution of the charge density. This can create a complex charge density landscape where ions can find their preferred sites for efficient adsorption and charge transfer. The presence of heteroatoms opens subnanometer-wide transverse conduction channels in the direction perpendicular to the sheet [2]. Therefore, we produced a range of MoS₂xSe_(1-2x) samples, tuned the S - Se ratio, optimised the incorporation of heteroatoms and vacancies, and investigated their influence on the catalytic activity of the samples.

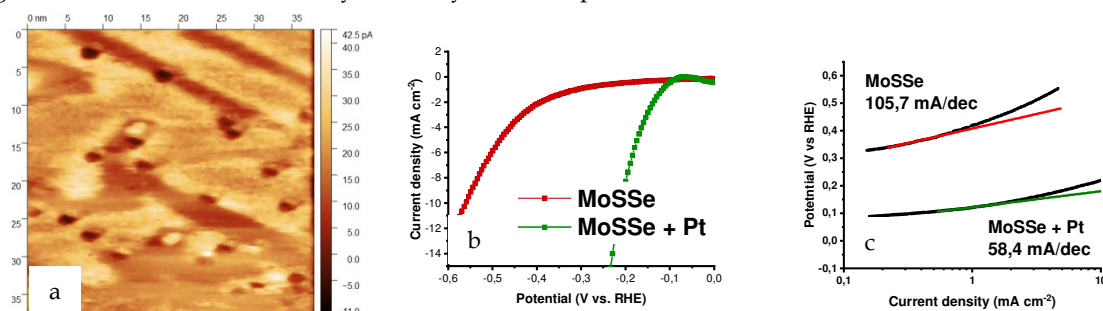


Figure 1: STS map showing S and Se rich regions in a MoS₂Se layer (a). Linear sweep voltammogram curves (b) and corresponding Tafel plots (c) for MoS₂Se and MoS₂Se+Pt samples. In (b) the potential was measured versus a reversible hydrogen electrode – (RHE) reference electrode.

We also deposited platinum nanoparticles on the MoS₂Se surface by an electrochemical method (chronopotentiometry) and we were able to influence the size of the nanoparticles. The catalytic activity of the Pt decorated MoS₂Se in the hydrogen evolution reaction was close to that of a Pt metal electrode, though we used only a very small amount of platinum.

Remaining work

Our results show that it is possible to increase the catalytic activity of MoS₂Se samples by defect engineering and metal nanoparticle deposition. We plan to improve further the efficiency of our catalyst material by increasing the density and homogeneity of active sites like vacancies and substitutional atoms. In addition, we plan to use these defect sites to anchor nm size metal clusters to produce even better cost efficient, high performance catalytic materials.

Related publications

- [1] A. A. Koós, P. Vancsó, M. Szendrő, G. Dobrik, D. Antognini Silva, Z. I. Popov, P. B. Sorokin, L. Henrard, C. Hwang, L. P. Biró and L. Tapasztó: *Influence of Native Defects on the Electronic and Magnetic Properties of CVD Grown MoSe₂ Single Layers*, J. Phys. Chem. C **123**, 24855–24864 (2019)
- [2] P. Vancsó, Z. I. Popov, J. Pető, T. Ollár, G. Dobrik, J. S. Pap, C. Hwang, P.B. Sorokin and L. Tapasztó: *Transition metal chalcogenide single layers as an active platform for single-atom catalysis*, ACS Energy Letters **4**, 1947-1953 (2019)

PREVENTING THE DEVELOPMENT OF ANTIBIOTIC RESISTANCE IN WASTEWATER MATRICES BY HIGH ENERGY IRRADIATION

Renáta Homlok, Krisztina Kovács, Tünde Tóth, Erzsébet Takács, László Wojnárovits, László Szabó

Objective

The objective was to establish the conditions for the high-energy-radiation-induced destruction of antibiotics by following the change in biodegradability and in antimicrobial activity in a synthetic effluent wastewater matrix [1, 2].

Methods

Electron beam (EB) treatment was performed using a vertically mounted Tesla Linac LPR-4 type linear electron accelerator. In order to assess the applicability of this technique for eliminating the subinhibitory effects of antibiotics on the selection of resistant bacteria, a microbiological assay was introduced. The test is based on the dynamics of a mixed (sensitive/resistant) bacterial population in response to the presence of antibiotics in a concentration range well below the minimum inhibitory concentration (MIC) in a synthetic wastewater matrix. Sensitive and resistant subtypes of *Staphylococcus aureus* in a 1:1 ratio are added to the test medium, after an appropriate incubation period. The number of resistant cells on the antibiotic-containing plate and the total number of cells on the control plate without antibiotic were counted. Then the fraction of resistant strains compared to all the colonies (sensitive and resistant) were determined.

Results

Using advanced oxidation treatment, the selective pressure on the bacterial population favoring the predominance of resistant mutants can be eliminated. This is achieved when the fraction of resistant bacteria, to within a statistically insignificant deviation, is the same as in the control sample. In other words, the difference between the control sample and the sample containing the antibiotic (erythromycin or piperacillin) is no longer significant. A synthetic effluent wastewater was designed to be a kinetically appropriate reflection of a real sample while containing the antibiotics at sufficiently high concentration for microbiological assay. We were looking for the absorbed dose that could eliminate the effect of antibiotics on microorganisms in a modeled wastewater, so that we could reduce the resistance to the given antibiotic in the given matrix.

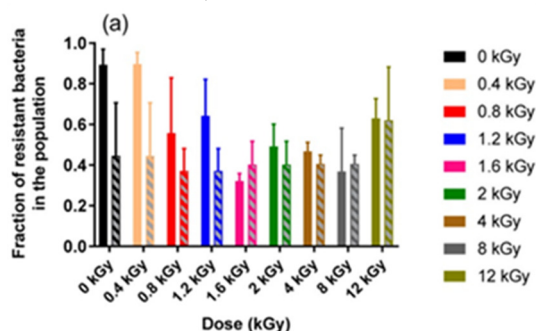


Figure 1: Fraction of resistant *S. aureus* in the bacterial population after incubation for 24 h in samples spiked with treated samples of erythromycin (cross-hatched bars), and in samples without erythromycin (solid color bars).

The fraction of resistant bacteria in the samples after incubation for 24 h is shown in Fig. 1. In the case of erythromycin, a 0.4 kGy dose practically does not have any impact on the elimination of the selective pressure (Fig.1.) At 1.2 kGy, the difference between the control sample and the sample containing the antibiotic is still significant. With 1.6 kGy as a starting point, there is no significant change from the control sample, and it can be stated that the selective pressure has finally been eliminated.

Remaining work

Using this method we plan two series of experiments in the next three years, in one of them wastewater matrix with antibiotic will be used, in the other wastewater-matrix with bacterium. In this case, we will add bacteria to the samples prior to irradiation. The comparison would be to samples of irradiated wastewater matrix without antibiotic and wastewater matrix with antibiotic but without bacterium.

Related publications

- [1] L. Szabó, M. Steinhardt, R. Homlok, K. Kovács, E. Illés, G. Kiskó, Á. Belák, Cs. Mohácsi-Farkas, E. Takács and L. Wojnárovits: *A Microbiological Assay for Assessing the Applicability of Advanced Oxidation Processes for Eliminating the Sublethal Effects of Antibiotics on Selection of Resistant Bacteria*, Environmental Science and Technology Letters **4**, 251 (2017)
- [2] L. Szabó, J. Szabó, E. Illés, A. Kovács, Á. Belák, Cs. Mohácsi-Farkas, E. Takács and L. Wojnárovits: *Electron beam treatment for tackling the escalating problems of antibiotic resistance: Eliminating the antimicrobial activity of wastewater matrices originating from erythromycin*, Chemical Engineering Journal **321**, 314 (2017)
- [3] L. Szabó, T. Tóth, T. Engelhardt, G. Rácz, Cs. Mohácsi-Farkas, E. Takács and L. Wojnárovits: *Change in hydrophilicity of penicillins during advanced oxidation by radiolytically generated OH compromises the elimination of selective pressure on bacterial strains*, Environmental Science and Technology Letters **551–552**, 393 (2016)

HIGH ENERGY IONIZING RADIATION INDUCED DEGRADATION OF AMODIAQUINE IN DILUTE AQUEOUS SOLUTION: RADICAL REACTIONS AND KINETICS

Krisztina Kovács, Tünde Tóth, László Wojnárovits

Objective

The aim of this present study is to demonstrate that the antimalarial drug, amodiaquine (AQ) can be efficiently degraded in one-electron oxidation and reduction reactions.

Methods

The samples in the end-product experiments were irradiated in a panoramic type ^{60}Co - γ irradiation chamber (dose rate = 10 kGy h⁻¹) with doses 0, 0.2, 0.4, 0.6, 0.8, 1, 2.5, 5, 7.5 and 10 kGy under different conditions. The initial AQ concentration was 0.1 mmol dm⁻³. The samples before and after irradiation were characterized by using a JASCO 550 UV-Vis spectrophotometer with a 1 cm cell and applying appropriate dilutions before taking the spectra. The transient intermediates of the degradation reactions were investigated by the pulse radiolysis technique using 4 MeV accelerated electrons with electron pulse length of 800 ns and utilizing kinetic spectrophotometric detection with 1 cm path length cell. In order to identify and quantify the participating free radicals with different reduction potentials, redox titration measurements were conducted. The efficiency of removal was evaluated by using liquid chromatography-mass spectrometry (Agilent 1200 LC and Agilent 6410 MS) devices. The time (dose) dependence of degradation was characterized by chemical oxygen demand (COD) and total organic carbon (TOC) content measurements.

Results

In the radiolysis of dilute aqueous solutions, hydroxyl radicals and hydrated electrons are the main reactive intermediates. The hydroxyl radical reacts with AQ by addition to the aromatic rings and by hydrogen-abstraction ($k = 6 \times 10^9 \text{ mol}^{-1} \text{ dm}^3 \text{ s}^{-1}$). In Figure 1. the suggested mechanisms of AQ degradation in hydroxyl radical induced reactions are shown where the Roman numerals and letters are used for the structural units of AQ and for the forming radicals in the degradation processes, respectively. The hydroxyl radicals were found to add both to the quinoline (~38%) (a) and aminophenol (~50%) (b) parts *via* formation of hydroxycyclohexadienyl radicals, while nitrogen centred radicals may form by H-abstraction or by an electron removal from the tertiary amine part of the molecule (~12%) (c, d). The dihydroxycyclohexadienyl radical formed on the aminophenol part is suggested to transform to aminophenoxy radical. The hydrated electrons ($k = 1.6 \times 10^{10} \text{ mol}^{-1} \text{ dm}^3 \text{ s}^{-1}$) can also effectively contribute to AQ degradation. The efficiency of the decomposition was measured based on the decreases of amodiaquine concentration and the chemical oxygen demand and the total organic carbon content values. In an aerated 0.1 mmol dm⁻³ solution, at 2.5 kGy absorbed dose, AQ was completely demolished.

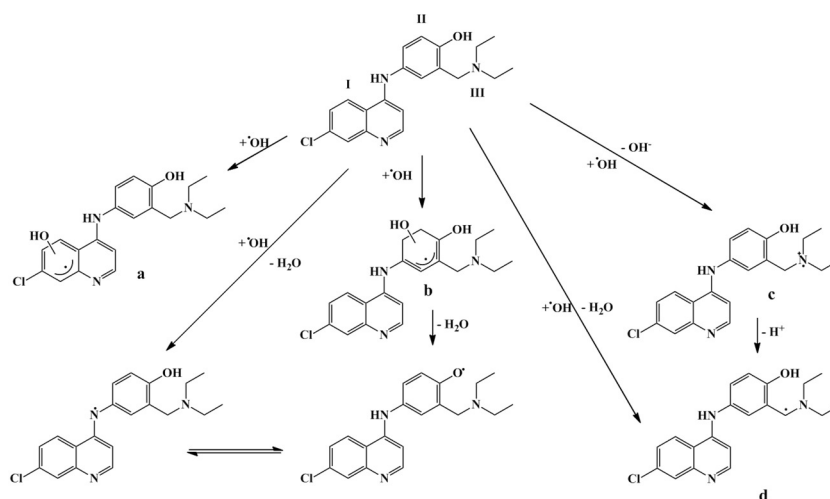


Figure 1: The suggested mechanisms of amodiaquine degradation in hydroxyl radical induced reactions

Remaining work

The separation and identification of degradation products is a very important task from the view of the degradation mechanism of amodiaquine. In order to get a comprehensive picture about the degradation processes we intend to perform mass spectrometric measurements in the future.

OPTIMIZING THE USE OF RENEWABLE ENERGY SOURCES IN THE ENERGY MIX OF HUNGARY

Endre Börcsök, Ágnes Gerse

Objective

This summary reports short-term energy scenarios for the heat and electricity generation in Hungary, considering the recent developments in the overall European and national energy policy framework promoting the use of energy from renewable energy sources. Focusing on the heating and electricity sectors, a methodology for portfolio optimization has been developed in order to identify the optimal energy mix in terms of technology alternatives and energy sources. As a base case, a pure economic assessment was carried out by considering the investment costs, the net present values and the operation and maintenance (O&M) costs. The optimization was extended by involving additional factors in the next steps, taking into account carbon prices and the external costs of the environmental and human health (physiological) impacts to the model. An aggregate approach is applied to reduce complexity; national aggregation was chosen for the electricity sector while building typological groups and local geographical entities were defined for the heating sector. The level of saturation of different technology alternatives in the market is modelled in the proposed methodology, as well. The mathematical formulation of the optimization problem was given as a non-linear case of the distribution problem.

Methods

In our research, we focused on the portfolio optimization of the national renewable energy sources in the heating and electricity sectors. When defining the key optimization problem, we ignored the existing power plant portfolio as a starting point; and considered an ideal energy mix as the target of a potential roadmap. In the calculations underlying the target scenario, we preferred an economic approach, taking into account the specific costs of the individual energy generation alternatives, the levelled-off cost of electricity for the average lifetime. As supplementary calculations, the optimization was also carried out by considering the carbon prices and the external costs of the environmental and human health impacts. Assumptions on realistic investment and O&M costs were made based on the evaluation of benchmark projects. As shown by the project experiences, the costs exhibit a large variation, heavily influenced by the site-specific physical conditions and the closely interrelated number of full load hours. In the mathematical definition of the presented problem, we considered the level of saturation of the market by linear functions; i.e. while all technology alternatives are installed at the most favourable locations and techno-economic conditions at first, they become gradually less competitive as a function of the generation capacity already operating. The mathematical formulation of the optimization problem was provided as a distribution problem with convex, nonlinear objective function.

Results

The purpose of the present work was to develop an optimal national portfolio of the renewable energy sources. We assumed a total gross energy consumption of 760 PJ for Hungary for 2020, 75% of which belongs to the electricity and heating sector. In these sectors, a total energy of 97.5 PJ should be supplied by using renewable energy sources. With respect to the moderate reserves present in the system, several alternatives are limited by the constraints. If only economic aspects are considered, wood and agricultural biomass has a share of 65 PJ in the optimal portfolio because of the large amount and high heat demand of single-family houses and the availability of biomass (Figure 1). The consideration of the external costs does not result in substantial restructuring of the optimal portfolio. The ratios of the energy sources are slightly modified, and there are two new energy sources (hydro, wind) that fully exploit the national potential (Figure 2). The moderately decreasing use of biomass can be explained by the harmful emissions of the individual heating and the closely interrelated, increasingly negative impact on human health. At a pure economic approach, the average energy cost is stabilized at 6.71 c€/kWh and considering the external costs the average energy cost goes up to 8.22 c€/kWh.

Remaining work

There is some potential for further development to perform sensitivity analysis with robust optimization for several variables.

Related publications

- [1] E. Börcsök, Á. Gerse and J Fülöp: *Optimizing the use of renewable energy sources in the energy mix of Hungary*, 17th IEEE World Symposium on Applied Machine Intelligence and Informatics, SAMI 2019, Herlany, Slovakia
- [2] E. Börcsök and Á. Gerse: *Sustainable nuclear-renewable hybrid systems: a case study for Hungary*, International Conference on Climate Change and the Role of Nuclear Power, IAEA 2019, Wien, Austria
- [3] Á. Gerse and E. Börcsök: *Towards a Low-carbon Electricity Supply in Central Eastern Europe: Modelling the Role of Nuclear Power Plants*, International Conference on Climate Change and the Role of Nuclear Power, IAEA 2019, Wien, Austria

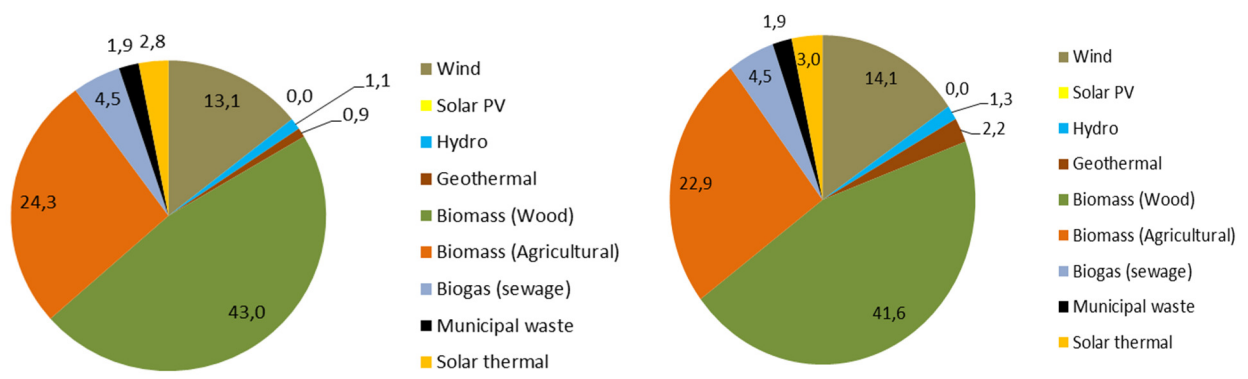


Figure 1: Optimal national portfolio of renewable energy sources with respect to economic impacts only (left) and additionally to human health, environmental and climate impacts (right).

BIOGENIC CARBON CONTENT DETERMINATION OF CATALYTICALLY CONVERTED BIOMASS

Tamás Korányi

Objective

The optimization of direct liquid scintillation counting (LSC) measuring conditions and the development of a sample combustion method of biomass originated samples for the determination of biogenic carbon content of catalytically converted biomass.

Methods

The determination of the biomass content of biocarbon - fossil carbon containing mixtures (cellulose, lignocellulose and lignin derivatives) by radiocarbon (^{14}C) liquid scintillation counting (LSC). This determination depends on the fact that there is no ^{14}C in the fossil-carbon.

- Direct counting: The product mixture was dissolved directly in the scintillation cocktail and its biogenic carbon content was measured in LSC equipment. This method is only applicable using colourless or slightly coloured samples.
- Sample combustion and carbon dioxide trapping: Samples are burned using air in a burning oven and the produced carbon dioxide is trapped in sodium hydroxide and amine solutions. The precipitate is dissolved in the scintillation cocktail and measured in LSC. This method is recently under development; it is not working yet.

Results

Our Dutch partners (Prof. Katalin Barta and Bálint Fridrich, University of Groningen) produced catalytically converted biomass (lignin, cellulose and wood) samples where lignin, etc. are the starting biomass materials. The biomass samples were fully converted to depolymerized oligomeric and monomeric products in a supercritical methanol regime in the presence of a copper containing catalyst. Fossil methanol is both a reactant in the conversion process and a solvent for the final products. The aim of our LSC studies is to reveal the ratio of embedded fossil methanol in the small methylated depolymerized products (aromatics, cyclic alcohols, ethers). Five sample series were analysed by ^{14}C LSC using direct counting. Most samples were slightly yellow coloured, therefore optimization of measuring conditions (counting energy range, storage time) was carried out. Due to the free radicals initially present in the cocktail mixed samples, LSC measurements in the 18-156 keV counting energy region after 8-10 days storage time were suggested. In the last set of experiments the results presented in Table 1 were obtained. As the biogenic carbon content (4th column in Table 1) is very low in each sample, at least 1 g biocarbon content was recommended in every sample for improving the reliability of direct LSC method.

Table 1: Average biocarbon contents and substrate conversions of lignin, cellulose and wood samples measured by direct ^{14}C LSC method

Biomass source material	Mass of Converted Biomass (mg)	Mass of product mixture (mg)	Biogenic carbon (wt%)	Conversion of substrate (%)
Lignin	2 X 200	3011 - 4765	0.003	29
Cellulose	2 X 400	5014 - 5930	0.004	28
Poplar wood	2 X 250	4855 - 5336	0.012	119 (23)

Remaining work

Building of the sample combustion and carbon dioxide trapping experimental setup has been started, but due to the low biocarbon content of the studied samples, burning of larger mass samples is necessary. An incinerator and CO_2 -absorber reactor with larger volume is planned to be built to enhance the precision of ^{14}C detection from biomass samples by LSC.

ELECTRIC POWER GRID FAILURES

Géza Ódor, Bálint Hartmann, Attila Kazsoki

Objective

Power-grids are becoming more and more heterogeneous as renewable (solar, wind, geothermic) small suppliers are connected. Therefore, the danger of failures caused by desynchronization is of a great concern. Failure data of large foreign power-grids have shown blackout size distributions with *power-law (PL) tails*. Previous simulations could explain this using power threshold cascade models, assuming self-organized criticality. In these DC models, the power redistribution, following a line or node cut, is described by a *fixed amount of load*. We have studied the stability of phase and frequency synchronized steady-states of realistic, Hungarian and US high voltage power grids using *dynamical simulations of the swing-equations*, which describe the real power redistribution in AC electric networks. Earlier we have shown that heterogeneities can generate power-law desynchronization duration distributions without the assumption of criticality. As a continuation of the previous research, again the typical time distributions of desynchronization phenomena were in the focus of the work. By adding new elements to the second order Kuramoto model, producers and consumers can be modelled by binary distribution. The effects of directed and undirected graphs, and the network topology connecting producers was to be tested. Other aim of the research was to test the hypothesis that exponent of the distribution of large disturbances can be used to predict faults of power grids.

Methods

We followed the temporal evolution of the phase and frequency synchronization of the second order Kuramoto model, describing AC electric networks on 2D lattices and on real, high voltage (HV) power-grid networks. Equations for the local phases θ_i and frequencies ω_i have been analysed numerically, using the 4th order Runge-Kutta differential solver. We supplemented this algorithm with a power threshold condition, which models overloads and can generate failure cascades, governed by the equation of motion in a natural way. Following an equilibration process we introduced line or node cuts and determined the size of cascades by counting the number of line failures. We compared the effects of Gaussian intrinsic frequency distribution results with exponential ones that may occur in case of wind and solar energy sources.

Typical forms of the Kuramoto model have a significant limitation as all generators and loads are handled with the same distribution, thus all units have the same power. Empirical data are rarely used, which is a large simplification of actual power grid phenomena. In real power systems, all nodes have connection both to generators and loads, thus these parameters have to be considered; during the work, characteristic load states of the Hungarian power system were used. The moment of inertia can be considered as a sum of two contributions: inertia of generators and inertia of consumers. In large power systems the cumulative moment of inertia of power plants exceeds that of the consumers by orders of magnitude, so load inertia is often neglected. In the examined network model, however, there are numerous subsystems, where the power (and thus the inertia) of generators is very low, or even zero, thus this parameter had also to be included as a variable of the Kuramoto model. Finally, empirical values were collected to model transmission capacities (K_i) of the grid.

Results

As the Figs show we obtained roughly *universal PL failure tails*, without tuning to a critical point: i.e. at different thresholds (T), global couplings (K), and self-frequency distributions for the 4941 node US and the 418 node HU HV networks. The fitted exponents agree with those of the HU failure time data and other world-wide measurements. While on the US grid this PL changes to a slower decay in case of exponential self-frequencies, the HU grid seems to be insensitive to it (Fig. 2).

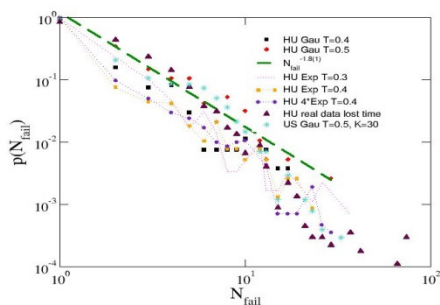


Fig. 1: Comparison of the cascade sizes on HU and US HV grids with Gaussian and exponential self-frequencies and real HU blackout data from HU DSOs.

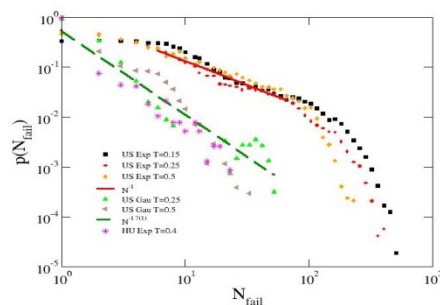


Fig. 2: Comparison of the cascade sizes on HU and US HV grids with Gaussian and exponential self-frequencies.

Remaining work

We would like to understand better the fat-tailed distributions, compare them with 2D lattice results and understand why the available HU energy and consumer loss data show wider distributions. We would like to test the results on larger networks and publish our results in a journal of high impact and at conference talks.

MODELLING DEVELOPMENT OF POWER SYSTEM INFRASTRUCTURE

Bálint Hartmann, Viktória Sugár, Attila Kazsoki

Objective

Topology of power systems shows a great variance, depending on voltage level, assigned tasks or geographical location. Literature dominantly examined only a small portion of this broad area, focusing on topological properties of high-voltage transmission grids, with significant simplifications applied to the modelling approach. Furthermore, most methodologies do not take into consideration that the present infrastructure is the result of an organic development. Aim of our research was to supervise these methods with the use of actual power system infrastructure data, and to create models that are representing certain parts of the infrastructure in a more precise way.

Methods

The literature review has focused on existing models that describe the development of power system infrastructure. Emphasis was given to the few case studies relying on actual data. A comparison of the collected examples was given. To obtain data of the Hungarian power system, large number of historical publications (yearbooks, statistics, maps, etc.) were collected.

Results

All information was merged into a single database, which provides searchability by construction data and voltage level, thus allowing the examination of multiple grids. 70-year history of the Hungarian transmission system infrastructure has given examples of both organic and planned development phases. Centre load and generation areas have varied significantly through the decades, but it had relatively little effect on the present topology. Notable periods have been identified, which have characterized the development (e.g. construction of Paks NPP, long-term grid modernization plan of MVM in the 1990's).

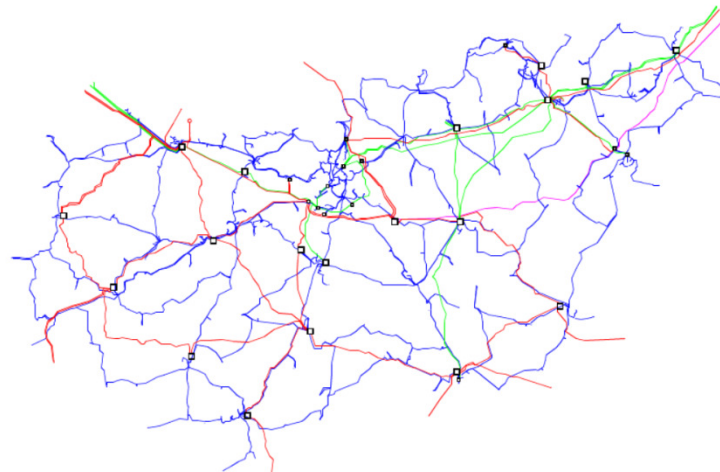


Figure 1: Topology of Hungarian transmission (220, 400, 750 kV) and subtransmission (120 kV) networks:
purple – 750 kV, red - 400 kV, green – 220 kV and blue 120 kV

Remaining work

The authors would like to continue the research in two areas. The first is to examine how CNA (complex network analysis) parameters of the Hungarian power system have changed throughout the years, and how they are related to network development plans. The second area covers municipal networks, where the lack of information is the biggest obstacle to handle.

Related publications

- [1] A. Kazsoki, B. Hartmann: *Data Analysis and Data Generation Techniques for Comparative Examination of Distribution Network Topologies*, International Review of Electrical Engineering **14:(1)**, (2019)
- [2] B. Hartmann, V. Sugár, A. Kazsoki: *Historical development of power system infrastructure*, - under preparation
- [3] B. Hartmann, V. Sugár, A. Kazsoki: *Contextual evaluation of city development and power infrastructure planning*, - under preparation

STUDY OF PUBLIC ENERGY PREFERENCES AND THE VALUATION OF CRITERIA FOR THE UTILIZATION OF MULTI-CRITERIA DECISION WEIGHTED FACTORS

Endre Börcsök, Veronika O. Groma

Objective

Hungary will need new installed electricity generation capacity of 7000 MW in the near future because of the phasing out of old power plants and the measure up to EU expectation to increase the renewable electricity ratio. The opinion of the stakeholders can be taken into account in the weighting of the criteria based on surveys with questionnaires. Our aim was to perform a survey which let us know the opinion of public users about the heating and the electricity production alternatives and the account of remarkable aspects of power supplies. Results are expected to serve the multi-criteria decision (MCD) models connected to power supply.

Methods

A countrywide questionnaire survey was conducted and answered by 1000 people. The sample was representative for age groups, gender, educational level and types of settlements. Criteria and alternatives were selected based on the focus group interviews' results and a complex questionnaire was assembled for 32 indicators and 8 energy alternatives. Beside statistical analysis the numerical evaluation of criteria framework allows us to interpret the main criteria. The survey results showed that the main criteria are non-independent, however, instead of the hierarchical approach of MCD, the analytical network process (ANP) with supermatrix technique is effective. In the developed model one single intermediary cluster (alternatives) projected the weights of the main criteria towards the sub-criteria. The main criterion weights were determined individually by pairwise comparisons, while the other sub-criteria and alternative rankings can be expressed by the result of the limit matrix. Based on individual results sociodemographic analysis was performed with ANOVA (analysis of variance) model.

Results

The developed evaluation model allows mathematical determination of complex criteria or open concepts revealed by focus group discussions of survey. (Table 1.) A further supplementary result of our model is the general ranking of electricity production and heating alternatives. (Figure 1.) Final results on the full dataset showed that greater proportion of public has changed preference towards renewables. Sociodemographic analysis results show that environmentally friendly techniques have surprisingly higher weights for less educated social group. However, economic aspects are more essential for those who have lower income. The criterion of safety was highest for people with average income.

Inexhaustible energy source	Protecting the diversity of life	Air pollution	Human health impacts	Domestic energy source	Climate impact	Local disturbance (noise, odor)	Total waste
100	92	78	62	59	55	52	43

Table 1: Definition of sustainable criterion in the heating sector with ranking

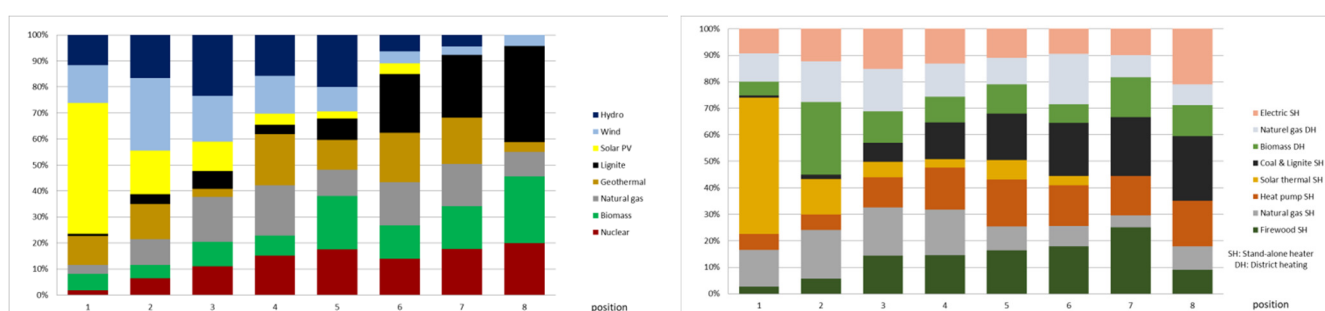


Figure 1: Medal table of electricity production and heating alternatives

Remaining work

The complete set of criteria and rankings provide an opportunity to optimize the domestic energy sector based on MCDA.

Related publications

- [1] E. Börcsök, Á. Gerse, J Fülöp: *Optimizing the use of renewable energy sources in the energy mix of Hungary*, 17th IEEE World Symposium on Applied Machine Intelligence and Informatics, SAMI 2019, Herlany, Slovakia
- [2] E. Börcsök, Z. Ferencz, V. Oláhne Groma, Sz. Török: *Representative social survey on public energy preferences*, 28th International Conference on Nuclear Energy for New Europe, NENE 2019, Portoroz, Slovenia
- [3] E. Börcsök, Á. Gerse: *Sustainable nuclear-renewable hybrid systems: a case study for Hungary*, International Conference on Climate Change and the Role of Nuclear Power, IAEA 2019, Wien, Austria

ATOMIC STRUCTURE AND CHEMICAL DURABILITY OF U-CONTAINING GLASS COMPOSITES

Margit Fábrián, Ottó Czömpöly, János Osán

Objective

The most feasible and presently accepted method for storage of high-level radioactive waste is the vitrification process, where the radioactive elements are melted into a glass form, and then deposited in a deep geological formation. During the past couple of years, we have done systematic experimental work to develop and understand the optimal glassy structure which can act as the host material for radioactive waste storage. Our work focuses on the development of uranium-containing matrix-glasses and to find out the chemical durability of these glasses.

Methods

UO₃-loaded borosilicate glass samples were prepared by the melt-quench technique from reagent grade powders melted in a Pt crucible. The composition of the samples is (100-x)wt% [SiO₂(55)Na₂O(25)B₂O₃(10)BaO(5)ZrO₂(5)](=Matrix)-xwt% UO₃ for x=10,20,30,40; denoted as M10U, M20U, M30U, M40U, respectively. In order to study the short- and intermediate range structural order, neutron diffraction (ND) experiments were performed at the 10 MW Budapest research reactor. Reverse Monte Carlo (RMC) simulation was applied to generate reliable 3-dimensional atomic configurations and to calculate the partial atomic pair correlation functions, coordination number and bond angle distributions. Chemical durability was tested by the ASTM C 1285-02 procedure. Powdered samples of all four Matrix-U glasses were leached statically in pure water over more than 7 days at 90°C. The ASTM C 1285-02 test was applied in order to investigate the glass dissolution and the release of U, representing the radionuclides. Two batches were tested using stainless steel containers. The leaching conditions are shown in Table 1. Elemental analysis was carried out by Inductively Coupled Plasma Optical Emission Spectroscopy (ICP-OES) and Total-reflection X-ray Fluorescence (TXRF) on the leachates.

Table 1: Leaching parameters and conditions

Parameters		
	Test A	Test B
Leaching time	7 days	3, 6, 10 days
Temperature	90 ± 2°C	90 ± 2°C
No. of samples	5	4
Sample mass [g]	1.5	1.5
MQ H ₂ O volume [ml]	15	18

Results

The borosilicate glass samples at UO₃ loading of 10 to 40 wt% were found to be amorphous. The RMC calculation based on ND data show well-defined first neighbour distances for the Si-O of 1.60 Å, B-O of 1.30/1.60 Å, Na-O of 2.10/2.70 Å, Ba-O of 2.70 Å, Zr-O of 1.90 Å, U-O of 1.70 Å and O-O of 2.60 Å. It was established that the basic network structure consists of [4]Si-O-[3]B, [4]Si-O-[4]B bond-linkages and the stable Matrix can incorporate a maximum of 40 wt% UO₃. The concentrations of the elements in the final filtered leachates after tests A and B, normalized to their initial mass fraction in the glass samples (calculated according to the ASTM protocol), are presented in Table 2. For test B, the ICP-OES analyses are on-going.

Table 2: Normalized concentrations in Matrix-U-glass leachates, concentrations in leachates determined by ICP-OES (*TXRF)

Normalized concentration g/l										
Test A, 7 days								Test B, 3 d	Test B, 6 d	Test B, 10 d
	Si	B	Na	Ba	Zr	U	U*	U*	U*	U*
M10U	36.3	20.4	65.1	0.112	0.0555	0.093	0.148	0.004	-	0.004
M20U	22.3	15.2	45.7	0.045	0.0072	0.019	0.025	0.008	0.017	0.014
M30U	26.7	19.7	54.5	0.028	0.0085	0.041	0.055	0.020	0.026	0.037
M40U	7.9	6.5	18.5	0.006	0.0003	0.011	0.014	0.022	0.015	0.010

In case of the Matrix-U glasses, the concentrations in the leachates indicate that the release factors of Si, Na and B are high compared with U, Ba and Zr. The elements are released incongruently; a detailed analysis is needed to have better understanding of these phenomena. The relative error of both methods can be estimated as within 10%. In case of the M30U sample we got higher leaching values than was expected; further studies are needed. During test B, we used one sample for the 3d, 6d and 10d measurements, a small aliquot of the leachate being removed at the end of 3d, 6d and 10d periods for the chemical analysis. These are preliminary results, more details will be available in the near future.

Remaining work

The evaluation of the chemical-physical and corrosion properties is in progress.

Related publication

- [1] G. Boguszlavszkij, M. Fabian: *Investigation of structural and chemical stability of uranium-containing borosilicate compounds*, Scientific Student Conference; presentation, 12 November 2019, Budapest

CHARACTERIZATION OF IRON ADSORPTION ON CLAY MINERALS

Annamária Kéri, János Osán

Objective

In the safety assessment of high-level radioactive waste (HLW) disposal, the study of the iron redox cycle is indispensable since a large amount of Fe^{2+} will be dissolved in the pore water due to the anoxic corrosion of the steel casks. Iron is known as one of the most abundant redox active elements, which effects the fate of radiocontaminants (e.g. UO_2^{2+}). The argillaceous host rock and the bentonite buffer in the HLW repository contain large amounts of Fe-bearing clay minerals, which may control the sorption mechanism of redox sensitive elements (e.g. $\text{Fe}^{2+}/\text{Fe}^{3+}$). The atomistic-level understanding of iron complexation and the probable oxidative behaviour of iron in clay minerals is fundamental for the accurate prediction of the geochemical evolution at the HLW disposal site. Despite their importance in the iron redox cycle and contaminant immobilization, the exact sorption mechanism of iron on clay minerals remains unclear. In this project, a detailed investigation on the Fe sorption stability and the formed iron complexes on the edge sites of clay minerals was performed.

Methods

A combination of *ab initio* simulations and X-ray absorption spectroscopy (XAS) was used in this study. The structure relaxations and the molecular dynamics simulations were performed based on the density functional theory (DFT) using the Gaussian plane wave method as it is implemented in the QUICKSTEP module of the CP2K code. The XAS spectra were calculated based on molecular configurations derived from *ab initio* structure optimizations. Real space multiple scattering theory was applied for extended X-ray absorption fine structure (EXAFS) as it is implemented in the FEFF 8.40 software, while X-ray absorption near edge structure (XANES) spectra were obtained using the density functional theory with the local spin-density approximation (DFT-LSDA) as it is implemented in the FDMNES code. Experimental EXAFS and XANES spectra were measured on samples consisting of a synthetic iron free montmorillonite equilibrated for 1 week with different Fe^{2+} concentrations at pH 7 in 0.1 M NaCl.

Results

A large-scale *ab initio* molecular dynamics simulation was successfully used to reveal the structure and the stability of the edge surfaces of montmorillonite, the main constituent clay mineral in bentonite. The molecular configurations from the simulations were used to obtain reference XAS spectra for distinct Fe inner-sphere complexes on the edge sites of montmorillonite. The quantitative interpretation of the experimental XAS spectra measured on samples with different Fe loadings was based on the theoretically calculated (atomistic modelling-based) ones. The results indicated a particularly complex behaviour of iron. Although, iron is mostly present in Fe^{3+} form, the proportion of this form decreases at increasing Fe loadings [1]. The combination of *ab initio* simulations and XAS demonstrated that not only the oxidation state of Fe determines the speciation, but *strong-/weak-site* complexation (Fig. 1) has different characteristics.

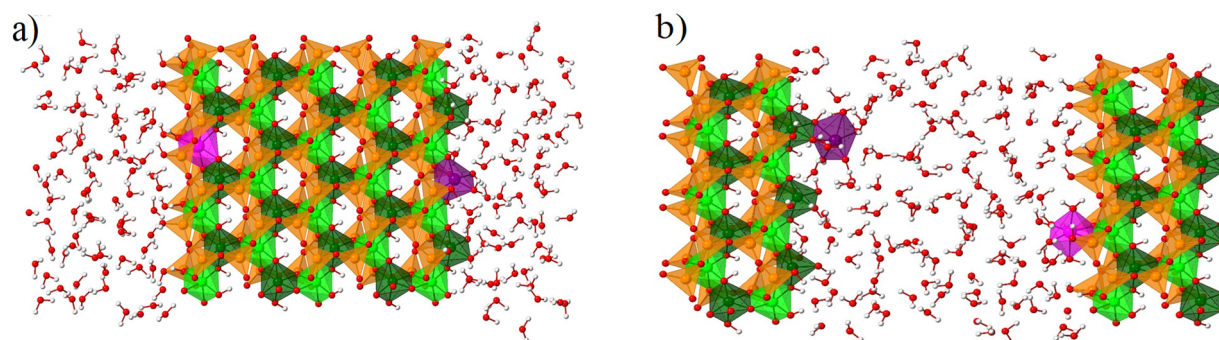


Figure 1: Views of inner-sphere sorption complexation models. The complex referred to as “strong-site” is shown in panel a, while the structure shown in panel b represents the “weak-site” complex. Alumina octahedra are shown in green, silica tetrahedra are orange, iron is marked with pink colour, while red and grey colours correspond to oxygen and hydrogen atoms, respectively. The different octahedral occupational sites can be distinguished by the different relative position of hydroxyl (OH^-) groups (cis-site is marked with lighter, while trans-site is shown with darker colours).

Remaining work

The atomistic-level understanding of the radiocontaminant sorption complexes is also essential in the long-term safety assessment of the HLW repository. Structural iron in Fe-bearing clay minerals might not only influence the surface uptake of ferrous iron but also other transitional metal (e.g. uranyl) ions. Theoretical and experimental investigations will be performed and compared to determine the preferred uptake mechanism of uranyl ion.

Related publication

[1] A. Kéri, R. Dähn, M. M. Fernandes, A. Scheinost, M. Krack, S. V. Churakov: *Iron adsorption on clays inferred from atomistic simulations and XAS spectroscopy*, Environmental Science & Technology, doi.org/10.1021/acs.est.9b07962

PREPARATION AND CHARACTERIZATION OF NANOPARTICLE SYSTEMS CONSIDERED FOR PLANT NUTRITION EXPERIMENTS

Zoltán Klencsár, Sándor Stichleutner, Viktória Kovácsné Kis

Objective

Preparation and characterization of nanoparticle systems to investigate the metal uptake and iron metabolism of plants.

Methods

Samples were prepared by a hydrothermal process by Gy. Tolnai. ^{57}Fe Mössbauer spectroscopy (MS), transmission electron microscopy (TEM) and temperature dependent magnetization measurements were used for sample characterization. Magnetization measurements were performed by L. Kiss at the Wigner Research Centre for Physics (Wigner RCP).

Results

Magnetization measurements have been performed on three different suspensions of ferrihydrite/ $\text{Fe}_2\text{O}_3 \cdot n\text{H}_2\text{O}$ nanoparticles, prepared by using different surfactant materials, as well as on an iron-oxide-hydroxide nanocolloid-suspension sample containing iron enriched in ^{57}Fe . Field Cooling (FC) and Zero Field Cooling (ZFC) magnetization measurements confirmed the presence of nanoparticles in the ferrihydrite/ $\text{Fe}_2\text{O}_3 \cdot n\text{H}_2\text{O}$ suspension samples by revealing superparamagnetic blocking at $T_b \approx 20$ K. However, paramagnetic behaviour was observed for the sample with iron enriched in ^{57}Fe even at the lowest temperatures used (~ 5 K), which confirmed our previous results regarding the incomplete formation of nanoparticles in that sample. $M(H)$ curves of the samples recorded at 5 K revealed an effective magnetic moment of the individual magnetic units that was in the order of the magnetic moment of a single Fe^{3+} ion, suggesting that iron ions in the nanoparticles of the ferrihydrite/ $\text{Fe}_2\text{O}_3 \cdot n\text{H}_2\text{O}$ samples are mainly antiferromagnetically coupled, leading to a strong reduction of the overall magnetic moment of the individual particles.

The iron-oxide-hydroxide nanocolloid-suspension sample prepared by the use of a precursor enriched in ^{57}Fe was reprocessed in order to achieve a higher concentration of nanoparticles compared to the original sample. The reprocessed sample was studied by ^{57}Fe MS (in a frozen state at ~ 80 K) and TEM. The ^{57}Fe Mössbauer spectrum clearly reflected a change in the sample composition as a result of reprocessing by showing that ferrihydrite was the main phase of the sample, incorporating ca. 75% of all iron atoms. Roughly 25% of the spectrum area was taken up by a minority sextet component, which could refer to various $\text{Fe}_2\text{O}_3 \cdot n\text{H}_2\text{O}$ phases with higher crystallinity and particle size. TEM measurements confirmed the presence of nanoparticles in the sample with a characteristic particle size being in the order of ~ 10 nm and smaller, with the decisive fraction of nanoparticles being ferrihydrite particles with a diameter of 2-7 nm. Consistent with the results of ^{57}Fe MS, according to the TEM images, a fraction of the particles have slightly larger (~ 4 -12 nm) particle size and may also be aggregates of smaller crystallites of $\text{Fe}_2\text{O}_3 \cdot n\text{H}_2\text{O}$. Overall, the successful preparation of the ^{57}Fe -enriched iron-oxide-hydroxide nanocolloid-suspension sample was confirmed.

A new magnetite nanoparticle powder sample has been prepared in considerable quantities (5 g) following a procedure that aimed to avoid oxidation of the particles to maghemite. Investigation of the sample by ^{57}Fe Mössbauer spectroscopy revealed spectral components that can be identified with magnetite, with a considerable amount of the spectral area associated with intermediate ($\sim \text{Fe}^{2.5+}$) valence iron ions, reflecting fast electron hopping between Fe^{2+} and Fe^{3+} ions at the octahedral site of the spinel structure. This latter is a typical trait of magnetite at room temperature and shows that Fe^{2+} was abundantly preserved in the sample, confirming that the preparation was essentially successful. In addition to magnetite, a new pair of ZnFe_2O_4 nanoparticle samples have also been prepared in order to investigate the effect of preparation conditions on the crystallinity of the particles. ^{57}Fe Mössbauer spectroscopy measurements carried out at room temperature suggests that the difference in crystallinity detected between the two formerly investigated ZnFe_2O_4 nanoparticle samples was successfully reproduced in the case of the new samples as well, despite the different preparation conditions used in the latter case.

A corresponding pair of $\text{Mn}_{0.05}\text{Zn}_{0.95}\text{Fe}_2\text{O}_4$ nanoparticle samples have also been prepared in order to investigate how a slight alteration of the stoichiometry influences the crystallinity difference detected in the ZnFe_2O_4 samples. Room-temperature ^{57}Fe Mössbauer spectroscopy measurements suggested that the crystallinity difference found in the ZnFe_2O_4 samples exists in the $\text{Mn}_{0.05}\text{Zn}_{0.95}\text{Fe}_2\text{O}_4$ nanoparticle samples as well.

Remaining work

Further X-ray diffractometry and TEM studies are needed in order to elucidate the structural and morphological features of the prepared magnetite, ZnFe_2O_4 and $\text{Mn}_{0.05}\text{Zn}_{0.95}\text{Fe}_2\text{O}_4$ nanoparticle samples.

Related publications

- [1] Z. Klencsár, A. Ábrahám, L. Szabó, E.Gy. Szabó, S. Stichleutner, E. Kuzmann, Z. Homonnay, Gy. Tolnai: *The effect of preparation conditions on magnetite nanoparticles obtained via chemical co-precipitation*, Mater. Chem. Phys. **223** (2019) 122.
- [2] Z. Klencsár, K.V. Kovács, S. Stichleutner, Z. May, E. Kuzmann, L.K. Varga, L.F. Kiss, D.L. Nagy, Gy. Tolnai: *ZnFe₂O₄ Nanoparticles With Different Crystallinity: A Comparative Study*, ICAME 2019, 01-06 September, 2019, Dalian, China Chinaerence Program p. 148 (Abstract).

EXPLORING THE IMPACT OF NANOPARTICLES ON PRODUCTIVITY, METAL UPTAKE AND IRON METABOLISM OF PLANTS

Zoltán Klencsár, Sándor Stichleutner, Viktória Kovácsné Kis

Objective

Characterization of nanoparticle systems, and their application in studies investigating the metal uptake and iron metabolism of plants.

Methods

Nanoparticle samples were either prepared via a hydrothermal process by Gy. Tolnai, or were purchased commercially from *Nanografi Nanotechnology Co. Ltd.* Plant fluid samples from earlier studies were received from F. Fodor at the Eötvös Loránd University (ELTE). ^{57}Fe Mössbauer spectroscopy (MS), transmission electron microscopy (TEM), powder X-ray diffractometry (PXRD), electron magnetic resonance (EMR) spectroscopy and inductively coupled plasma optical emission spectrometry (ICP-OES) were used for characterization of the various samples. The ICP-OES measurements were performed by Z. May at the Research Centre for Natural Sciences. The PXRD experiments were performed in cooperation with L.K. Varga at the Wigner Research Centre for Physics (Wigner FK). The low-temperature ^{57}Fe MS measurements were performed at ELTE ($T \approx 20\text{K}$) and Wigner FK ($T \approx 4.3\text{K}$) in cooperation with E. Kuzmann and D.L. Nagy, respectively.

Results

^{57}Fe MS measurements were carried out at temperatures of $\sim 20\text{K}$ and $\sim 4.3\text{K}$ on the ZnFe_2O_4 samples ZF-001 and ZF-002. In contrast with the 20 K measurements, which show paramagnetic or superparamagnetic behaviour of the samples, at 4.3 K a sextet feature is observed for both samples, with the absorption peaks being clearly more broadened in the case of ZF-002. At this temperature the broadening may be related to a distribution of hyperfine parameters due to a disordered occupation of tetrahedral and octahedral sites of the spinel by the Fe^{3+} and Zn^{2+} ions. The analysis of the spectra were performed by assuming that the overall stoichiometry of the samples is well approximated by the formula $(\text{Zn}_x\text{Fe}_{1-x})_{\text{T}}(\text{Fe}_{1+x}\text{Zn}_{1-x})_{\text{O}}\text{O}_4$ where $(\text{ })_{\text{T}}$ and $(\text{ })_{\text{O}}$ designate ions at tetrahedral and octahedral sites, respectively. Assuming, furthermore, that the Fe^{3+} and Zn^{2+} ions are randomly distributed at tetrahedral sites, and the hyperfine parameters of Fe^{3+} ions at neighbouring octahedral sites depend linearly on the number of their Zn^{2+} neighbours, we obtained the compositions of $(\text{Zn}_{0.37}\text{Fe}_{0.63})_{\text{T}}(\text{Fe}_{1.37}\text{Zn}_{0.63})_{\text{O}}\text{O}_4$ and $(\text{Zn}_{0.26}\text{Fe}_{0.74})_{\text{T}}(\text{Fe}_{1.26}\text{Zn}_{0.74})_{\text{O}}\text{O}_4$ for ZF-001 and ZF-002, respectively, suggesting that during formation Zn^{2+} and Fe^{3+} ions built up the spinel structure by taking the tetrahedral and octahedral positions in a quasi-random manner, in proportion to their occurrence.

Commercially purchased nanoparticle powders of Al_2O_3 (three samples with different characteristic particle size) and ZnO (two samples with different characteristic particle size) were investigated by PXRD in order to determine their suitability for experiments aimed at the elucidation of the possible effects of the particle size on plant-nanoparticle interactions. Two of the Al_2O_3 powders were identified as having cubic (spinel) crystal structure, and could therefore be classified as being $\gamma\text{-Al}_2\text{O}_3$ with a lattice parameter of $a \approx 7.9\text{Å}$ and a crystallite size of $\sim 5\text{nm}$ in both cases. The third sample was identified as having hexagonal crystal structure with $a = 4.8\text{Å}$ and $c = 13\text{Å}$, along with an average crystallite size of $\sim 27\text{nm}$, which are indicative of $\alpha\text{-Al}_2\text{O}_3$. The diffractograms of the ZnO samples both reflect hexagonal crystal structure with lattice parameters of $a = 3.25\text{Å}$ and $c = 5.2\text{Å}$, typical for ZnO . The crystallite sizes of the two ZnO samples were found to differ considerably: for one of the samples the crystallite size was 30 nm, whereas for the other 240 nm was obtained. Overall, the differences found in the crystallite sizes appear to make the nanopowders suitable for the experiments, though the particle sizes still need to be confirmed by subsequent measurements.

Xylem fluid of cucumber plants were collected from plants that were grown either under normal or under iron deficient conditions and subjected to the nanoparticle colloid suspension of $\text{Mn}_{0.25}\text{Zn}_{0.75}\text{Fe}_2\text{O}_4$ for one hour. The fluids were investigated by EMR spectroscopy, which detected the signals of Fe^{3+} (at $g \approx 4.3$) and Mn^{2+} (at around $g \approx 2$) complex species in the samples. Interestingly, the EMR spectra of the xylem fluid collected from the plants grown under iron deficient conditions displayed a more intense Fe^{3+} signal than that corresponding to the normal conditions. The situation was reversed for the case of the Mn^{2+} signal, which had a higher amplitude in the case of the plants grown under normal conditions. In contrast, ICP-OES measurements of the xylem fluids revealed that the sample associated with the iron deficient conditions has a total iron concentration that is roughly half of that present in the sample associated with the normal conditions. The discrepancy between the EMR and ICP-OES results may indicate the presence of EMR-silent iron complex species (such as antiferromagnetically coupled Fe^{3+} dimers or Fe^{2+} species) in the samples.

Remaining work

Subsequent work is needed to confirm the particle size of the purchased Al_2O_3 and ZnO nanopowders, and to interpret the EMR spectra of plant xylem fluids.

Related publications

- [1] Z. Klencsár, A. Ábrahám, L. Szabó, E.Gy. Szabó, S. Stichleutner, E. Kuzmann, Z. Homonnay, Gy. Tolnai: *The effect of preparation conditions on magnetite nanoparticles obtained via chemical co-precipitation*, Mater. Chem. Phys. **223**, 122 (2019)
- [2] Z. Klencsár, K.V. Kovács, S. Stichleutner, Z. May, E. Kuzmann, L.K. Varga, L.F. Kiss, D.L. Nagy, Gy. Tolnai: *ZnFe₂O₄ Nanoparticles With Different Crystallinity: A Comparative Study*, ICAME 2019, 01-06 September, 2019, Dalian, China Conference Program p. 148 (Abstract).

STRUCTURE OF OXY-HALIDE COMPOSITIONS FOR SOLID STATE BATTERIES

Margit Fábrián, István Tolnai, Viktória Kovács Kis

Objective

Discovering new chemistry and materials to enable rechargeable batteries to higher capacity and energy density is our priority. The novel inorganic and thermally stable oxides are potential substitutes for the toxic and flammable organic liquid electrolytes that are used in the Li-ion batteries. The oxy-halide solids are derived from the precursors of crystalline antiperovskites of metal hydroxides and have the highest reported Li^+ and Na^+ conductivity, $\sigma > 10^{-2} \text{ S cm}^{-1}$ at room temperature (25°C).

Methods

Here we study Li- and Na-ion based oxides, with nominal composition: $A_xM_{1-x}O_{1+y}Cl_{1-2y}$ (where $A=\text{Li, Na}$; $M=\text{Ba, Ca}$), which were prepared from commercial precursors: NaCl, LiCl, NaOH and $\text{Ba}(\text{OH})_2$, having applied multi-step heat treatments. The structure characterization is challenging, first of all we intend to understand the atomic structure of the new materials. Neutron diffraction experiments were carried out at the 10 MW Budapest Research Reactor using the PSD (Position Sensitive Detector) diffractometer, $\lambda_0 = 1,069 \text{ \AA}$. Since electrode materials are inherently nano-scale stuffs, local observation of these materials at high resolutions can be helpful to understand the microscopic processes that occur inside nano-particles and their interfaces with the electrolyte. TEM and HRTEM microscopy coupled with energy dispersive X-ray spectroscopy was applied to understand the morphology and chemical composition of the samples.

Results

Neutron diffraction showed that both Li and Na based compositions have well-defined, but different structural properties:

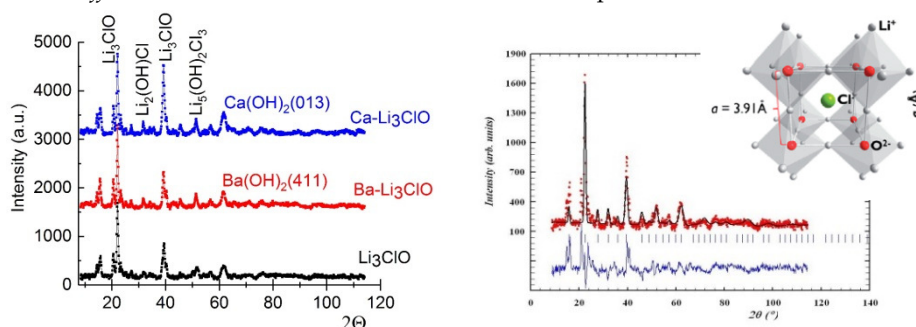


Figure 1: Neutron diffraction results for Li_3ClO -based samples

Space group: $Pm-3m$, $a=3.91\text{ \AA}$. There is evidence of a small amount of hydroxide phase, but the presence of crystalline Li_3ClO is still clear. Micro-crystalline phases were identified in both (Li- and Na-based) series. The two sample series based on Li and Na have different structures, but seems to be in different phases.

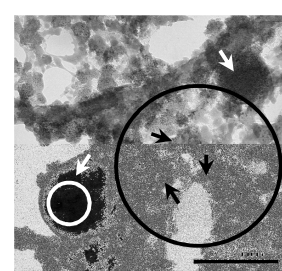


Figure 2: TEM measurements of $\text{Ba-Li}_3\text{ClO}$ sample

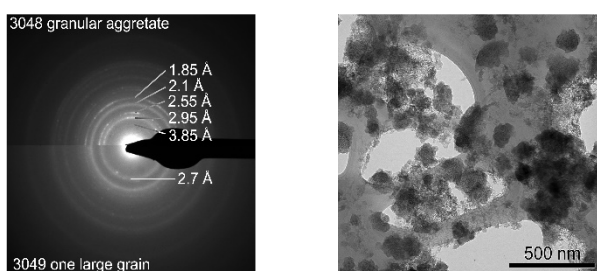


Figure 3: TEM measurements of $\text{Ca-Li}_3\text{ClO}$ sample

During the HRTEM measurements, the sample proved to be extremely sensitive to the radiation, so we worked with very low intensity (ca. 0.06 nA screen current and 150-200 $\text{e}/\text{\AA}^2\text{s}$). The morphology of $\text{Ba-Li}_3\text{ClO}$ sample consists of nanograins, based on the low magnification HRTEM and Fourier transform, the nanocrystalline structure of $\text{Ca-Li}_3\text{ClO}$ sample is proven, the size of the nanograins is $< 10 \text{ nm}$. The nano-domains were verified by high-resolution transmission electron microscopy.

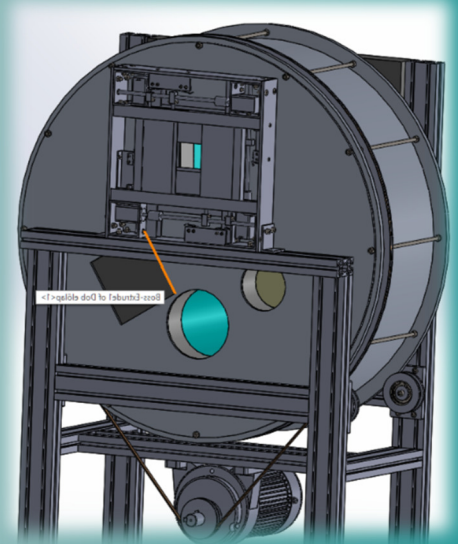
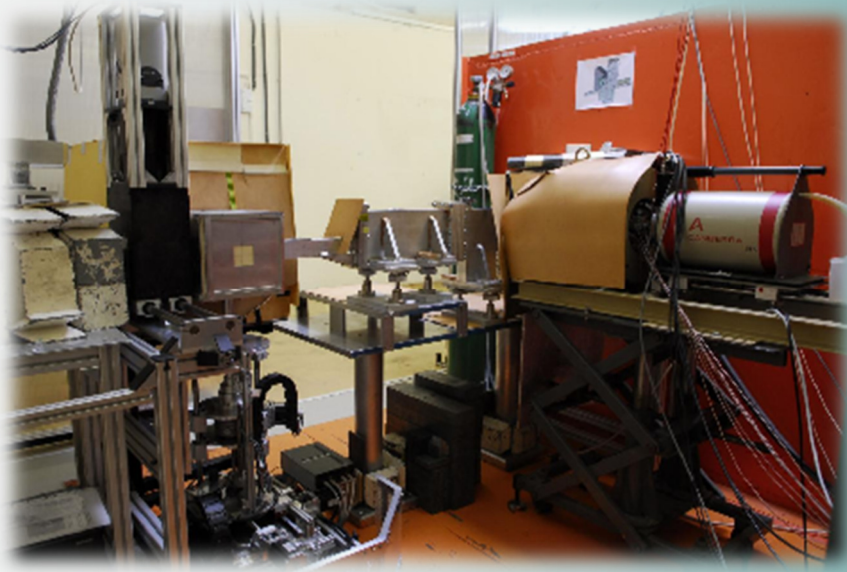
This work was supported by the NKFIH, Nr. 2017-2.3.7-TÉT-IN-2017-00023.

Remaining work

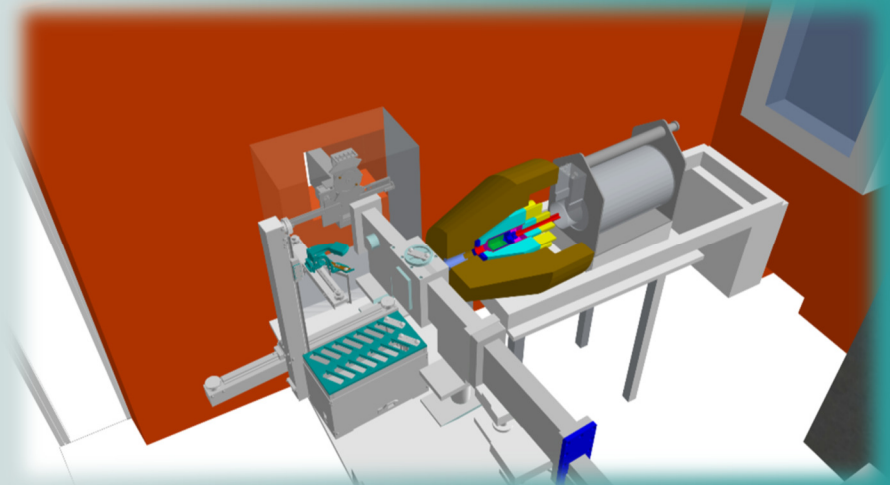
This is the first year of a three-year project; we continue the well-prepared TÉT schedule.

Related publications

- [1] M. Fabian, I. Tolnai: Structure of oxy-halide compositions for solid state batteries, VII European Conference on Neutron Scattering, poster presentation, 30 June-5 July 2019, Saint-Petersburg
- [2] M. Fabian, I. Tolnai, V.K. Kis: Structure of oxy-halide glasses for solid state batteries, American Crystallographic Association Annual Meeting, lecture, 19-25 July 2019, Cincinnati



V. NUCLEAR ANALYSIS AND CHEMISTRY



RAPID SEPARATION OF ACTINIDES FROM SOIL AND SEDIMENT MATRICES BY EXTRACTION CHROMATOGRAPHY

Márton Zagyvai, Nóra Vajda (Radanal Ltd.), László Szentmiklósi

Objective and scope

Our aim is to develop a rapid method to determine actinides in soil and sediment samples. Soil and sediment samples were digested by the time-consuming conventional acid destruction and also by the rapid alkaline fusion. Both sample preparation techniques were combined with the extraction chromatographic separation of actinides using Diglycolamide (DGA)[®] resin. The two methods were tested and compared regarding productivity and chemical recoveries.

Methods

DGA is a commercially available resin that contains N,N,N',N'-tetra-n-octyldiglycolamide on an inert support. Am, U, Pu and Th are sequentially separated by extraction chromatography based on DGA resin. A previously developed method for radioactive wastes [1,2] and human urine samples, was modified by applying two different digestion procedures and omitting the preconcentration step before the DGA resin separation. Tracers were added to the sample before the chromatography step.

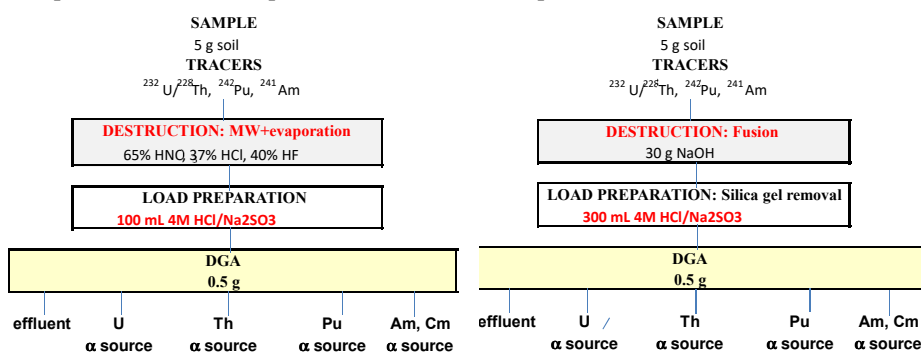


Figure 1: Method 1: acid destruction

Figure 2: Method 2: fusion

In the first procedure, soil and sediment samples were digested by the conventional method (Fig. 1) using microwave digestion combined with evaporation of SiF₄ before column separation. In the second procedure, samples were digested by fusion with NaOH, followed by the removal of silica gel by centrifugation and filtration before column separation (Fig. 2). No preconcentration step was involved in the procedure.

Results

IAEA standard reference soil (375, 326) and sediment (300, 367) samples were used to test the whole method. Chemical recoveries are shown in Table 1.

Pu and Am recoveries were acceptably high except for sample 367 which was a coral consisting of practically pure limestone (CaCO₃). Calcium interference has, therefore, gained our attention. Th and U recoveries varied; sometimes they were poor. We found that both methods were slow. The method with acid destruction took 3 days due to the long evaporation. The fusion itself took 1 hour but the whole procedure took about 2 days due to the slow filtering out of silica gel.

Table 1: Results of analysis of IAEA SRM soils and sediments

Sample code	Sample weight g	Load volume mL	Chemical recovery %			
			U	Th	Pu	Am
Acid destruction						
375	4	80	66	85	75	91
326	4	80	57	71	81	88
300	4	90	5	100	73	85
367	4	80	87	11	8	34
Fusion						
375	5	300	45	72	35	90
326	5	300	81	78	48	71
300	5	300	74	34	61	84

Remaining work

- We will continue to develop rapid digestion methods based on fusion (with NaOH and Na₂CO₃) for different matrices (soil, sediment).
- Pre-concentration probably cannot be omitted. We will develop (a) procedure(s) to separate the possible interferences (silica, calcium, iron, aluminum).
- Separation of actinides will be further examined for soil and sediment samples by extraction chromatography based on DGA resin.
- We plan to extend the method to concrete samples for decommissioning.

Related publications

- [1] J. Groska, N. Vajda, Zs. Molnár, E. Bokori, P. Szeredy, and M. Zagyvai: *Determination of actinides in radioactive waste after separation on a single DGA resin column*, J. Radioanal Nucl Chem **309**, 1145–1158 (2016)
- [2] M. Zagyvai, N. Vajda, J. Groska, Zs. Molnár, E. Bokori, and P. Szeredy: *Assay of actinides in human urine by rapid method*, J. Radioanal Nucl Chem **314**, 49–58 (2017)

APPLICATIONS OF NUCLEAR ANALYTICAL TECHNIQUES

Zsolt Kasztovszky, László Szentmiklósi, Boglárka Maróti, Ildikó Harsányi, Zoltán Kis, Veronika Szilágyi, Katalin Gméling

Objective

We determined the elemental compositions of various kinds of samples using PGAA, PGAI, NAA, and portable XRF methods. The data obtained are very useful in studies in catalysis, material science, geochemistry, paleontology and heritage science.

Methods

- Prompt Gamma Activation Analysis (PGAA) – to determine the bulk elemental composition, mostly for major components, and some trace elements with high neutron absorption cross-section
- Prompt Gamma Activation Imaging (PGAI) – to determine the elemental distribution within a large heterogeneous sample
- Neutron Activation Analysis (NAA) – to determine the elemental composition of a sample taken from a larger object, mostly for trace elements
- Portable X-ray Fluorescence Analytical instrument (pXRF) – to determine the elemental composition of a near-surface region of an object

Results

Selective functionalization of alkanes has been studied by in-situ PGAA, in co-operation with the ETH Zürich. We found that the product-distribution in direct alkane functionalization by oxyhalogenation strongly depends on the halogen of choice and the superior selectivity of an iron phosphate catalyst in oxychlorination is the consequence of a surface-confined reaction mechanism. By contrast, in oxybromination reaction the alkane activation follows a gas-phase radical-chain mechanism and yields a mixture of alkyl bromide, cracking, and combustion products [1].

In the field of Cultural Heritage, the elemental compositions of chipped and polished stone archaeological objects from Neolithic sites (e.g. Polgár-Csőszhalom) have been determined by PGAA. Based on the composition of the archaeological object and geological references, the possible raw material sources can be determined. [2-5]

An overview paper was published about the provenance research on obsidian archaeological objects found in today's Romania. Sources for 72 archaeological pieces have been identified based on fingerprint-like components (mostly B, Cl, and Ti) measured by PGAA [6].

Between 27 and 29 May 2019, we took part in the organization of the International Obsidian Conference (IOC 2019), where oral and poster communications were presented [7].

Within the "Lendület" project led by the Archaeological Institute of the Hungarian Academy of Sciences, Bronze Age limb spirals have been studied by PGAA and neutron imaging. Based on the experiments, three main groups of the objects were separated. The big pieces were made by the lost-wax technique, the small ones with cold working and hammering, while the medium ones were made by the combination of the above techniques. No correlation between the size and the composition of the objects was found [8-9].

Under the supervision of the Nuclear Physics Division of the European Physical Society, we published a review paper "Nuclear physics for cultural heritage" [10].

We analysed the compositions and geometrical shapes of Miocene sea urchin fossils. The initial results were reported in two oral presentations [11-12] at the prestigious European Geochemical Congress (EGU 2019), generating highly positive feedbacks.

We also took part in the celebration of the 60th anniversary of the Budapest Research Reactor's first criticality, for which a booklet was compiled [13]. We disseminated our industry-related R&D results arising from multiple projects in the form of Hungarian-language popular science papers [14-15].

Remaining work

Applications of PGAA and other elemental compositional measurements will be continued according to the current applications from various groups of users and ongoing projects

Related publications

- [1] G. Zichittella, M. Scharfe, B. Puértolas, V. Paunović, P. Hemberger, A. Bodi, L. Szentmiklósi, N. López, J. Pérez-Ramírez: *Halogen-Dependent Surface Confinement Governs Selective Alkane Functionalization to Olefins*, *J. Angewandte Chemie Int. Ed.* **58**, 18 (2019).
- [2] F. Bernardini, A. De Min, D. Lenaz, Zs. Kasztovszky, V. Lughi, V. Modesti, C. Tuniz, U. Tecchiati: *Polished stone axes from Varna/Nössingbühel and Castelrotto/Grondlboden, South Tyrol (Italy)*, *Archaeological and Anthropological Sciences* **11**:(4), (2019)
- [3] Zs. Bendő, Gy. Szakmány, Zs. Kasztovszky, K. T. Biró, I. Oláh, A. Osztás, I. Harsányi, V. Szilágyi: *High pressure metaophiolite polished stone implements found in Hungary*, *Archaeological and Anthropological Sciences*, **11**:(5), (2019).
- [4] B. Vácz, Gy. Szakmány, E. Starnini, Zs. Kasztovszky, Zs. Bendő, F. A. Nebiacolombo, R. Giustetto, R. Compagnoni: *High-pressure meta-ophiolite boulders and cobbles from northern Italy as possible raw-material sources for "greenstone" prehistoric tools: petrography and archaeological assessment*, *European Journal of Mineralogy*, in press, DOI: 10.1127/ejm/2019/0031-2859
- [5] Zs. Kasztovszky, K. T. Biró, I. Nagy-Korodi, S. J. Sztáncsuj, A. Hágó, V. Szilágyi, B. Maróti, B. Constantinescu, S. Berecki, P. Mirea: *Provenance study on prehistoric obsidian objects found in Romania (Eastern Carpathian Basin and its neighbouring regions) using Prompt Gamma Activation Analysis*, *Quaternary International* **510**, (2019)
- [6] M.I. Diasa, A.L. Rodrigues, Imre Kovács, Zoltán Szőkefalvi-Nagy, M.I. Prudêncio, Zsolt Kasztovszky, Boglárka Maróti, R. Marques, P. Flor, G. Cardoso: *Chronological assessment of della Robbia sculptures by using PIXE, neutrons and luminescence techniques*, *Nuclear Inst. and Methods in Physics Research B* (2019, in print)
- [7] Zs. Kasztovszky, A. Přichystal: *An overview of the analytical techniques applied to Study the Carpathian obsidians*, *Archeometriai Műhely* **15**(3), (2018)
- [8] G. Szabó, P. Barkóczy, S. Gyöngyösi, Zs. Kasztovszky, Gy. Káli, Z. Kis, B. Maróti, V. Kiss: *The possibilities and limitations of modern scientific analysis of Bronze Age artefacts in Hungary*, *Archeometriai Műhely* **16** (1), (2019)
- [9] I. Szathmári, B. Maróti, J. G. Tarbay, V. Kiss: *A Magyar Nemzeti Múzeum gyűjteményéből származó bronzkori arany hajkarika leletek vizsgálata (in Hungarian)*, In: *Mikroszkóppal, feltárásokkal, mintavételezéssel, kutatásokkal az archeometria, a geoarcheológia és a régészet szolgálatában*; Bartosiewicz, L., T. Biró, K., Sümegi, P., Töröcsik, T., Eds.; GeoLitera: Szeged, (2019)
- [10] A. Mackova, J. Kucera, J. Kamenik, V. Havranek, Z. Smit, L. Giuntini, Zs. Kasztovszky: *Nuclear physics for cultural heritage*, *Il Nuovo Cimento C* **42** (2-3), (2019)
- [11] B. Maróti, B. Polonkai, V. Szilágyi, Z. Kis, Z. Kasztovszky, L. Szentmiklósi, B. Székely: *Geophys. Res. Abstr.* 2019, 21, EGU2019-17493.
- [12] B. Székely, B. Polonkai, B. Maróti, Z. Kasztovszky, V. Szilágyi, Z. Kis and L. Szentmiklósi: *In Geophysical Research Abstracts; 2019; Vol. 21, pp EGU2019-12213.*
- [13] Budapest Research Reactor - 60 years of research and innovation
https://www.bnc.hu/sites/default/files/BRR_60_Web_preview_190328.pdf
- [14] L. Szentmiklósi, Z. Kis, B. Maróti, V. Szilágyi, K. Gmél, A. Len, L. Rosta, T. Kun, R. Baranyai, M. Fábán, L. Bottyán, J. Janik: *Tudomány az innováció szolgálatában: neutronos anyagvizsgáló módszerek ipari alkalmazásai a Budapesti Neutron Centrumban*, *Fizikai Szemle* **69**: 304-310 (2019)
- [15] L. Rosta, Z. Kis, F. Mezei, L. Szentmiklósi: *Anyagvizsgálat neutronbesugárással – új lehetőségek*, *Anyagvizsgálók Lapja* 2019/III. 9-20 http://avilap.hu/data/uploads/2019/avilap_2019iii.pdf

DEVELOPMENT OF NUCLEAR ANALYTICAL TECHNIQUES, NUCLEAR DATA MEASUREMENTS & DISSEMINATION ACTIVITIES

Tamás Belgya, Boglárka Maróti, Zoltán Kis, László Szentmiklósi

Objective

To develop our analytical capabilities and know-how in Prompt-Gamma Activation Analysis, to accurately determine related nuclear data, and to provide training and education for guest researchers and students

Methods

(n, γ) measurements, evaluation of nuclear data and comparison to literature, computer programming, teaching.

Results

Data from two of last year's nuclear physics experiments were processed and papers were published in Phys. Rev. C [1-2]. The radiative capture cross section of ^{242}Pu , required for innovative Mixed Oxide (MOX) fuel reactor designs, was measured to resolve the disagreement of up to 20% between existing experimental data at the thermal point and the keV region. The measurement we carried out used the same thin targets of a previous measurement at CERN's n_TOF-EAR1 [3], containing 30 mg of 99.995% pure ^{242}Pu . The combined analysis of the full prompt γ -ray spectrum and the ^{243}Pu decay has led to three compatible values for the thermal cross section, as shown in Fig.1. Their average value, 18.9(9) b, has an improved accuracy compared to other recent measurements [4].

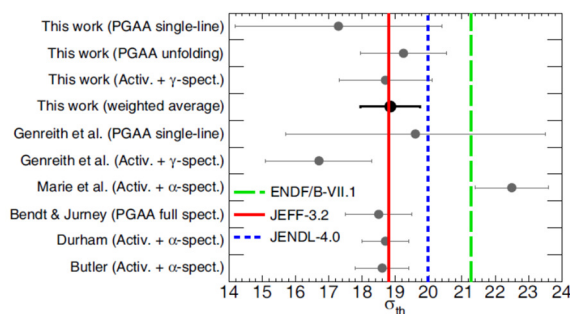


Figure 1: The literature data for cross-section of ^{243}Pu

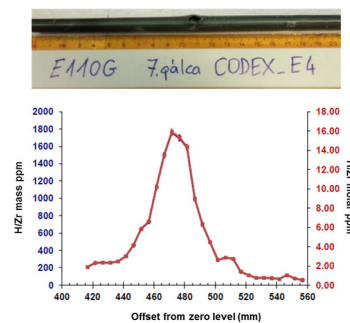


Figure 2: The longitudinal hydrogen profile of a Zr fuel cladding

Contributions were made to the most recent edition of the IAEA Photonuclear Data Library [5]. The result of the position-dependent hydrogen-measurements by Prompt-gamma Activation Imaging – Neutron Tomography (PGAI-NT), completed within the Zirconium Material Studies (CAK) project, was published in the domestic journal Nukleon [6], showing a clear correspondence of elevated local hydrogen content and Loss of Coolant Accident (LOCA) damage position (Fig. 2).

Education and dissemination activities

- PhD course at Eötvös University, 'Nuclear Analytical Methods and their Application in Earth Sciences and Archaeometry I-II.'
- Central European Training School on Neutron Techniques: A revised, extended second edition of the Handbook [7]
- PGAA laboratory training for University of Debrecen, BME and ELTE students

Related publications

- [1] T. Belgya, S.B. Borzakov, M. Jentschel, B. Maróti, Y.N. Pokotilovski, L. Szentmiklósi, Phys. Rev. C **99**, 044001 (2019)
- [2] A. M. Hurst, A. Ureche, B.L. Goldblum, R.B. Firestone, M.S. Basunia, L.A. Bernstein, Zs. Révay, L. Szentmiklósi, T. Belgya, J. E. Escher, I. Harsányi, M. Krčicka, B.W. Sleaford, and J. Vujic, Phys. Rev. C **99**, 024310 (2019)
- [3] J. Lerendegui-Marco, C. Guerrero et al., Phys. Rev. C **97**, 024605 (2018).
- [4] J. Lerendegui-Marco, C. Guerrero, T. Belgya, B. Maróti, K. Eberhardt, Ch.E. Düllmann, A.R. Junghans, C. Mokry, J.M. Quesada, J. Runkle, P. Thörle-Pospiech, Eur. Phys. J. A **55**, (2019)
- [5] T. Kawano et al. IAEA Photonuclear Data Library, (2019) Nuclear Data Sheets **163** (2020) 109-162 arXiv preprint arXiv:1908.00471
- [6] Kis Zoltán, Maróti Boglárka, Szentmiklósi László, Nukleon **6**, 26-31 (2019)
- [7] Z. Kis, L. Szentmiklósi: Neutron imaging; L. Szentmiklósi, K. Gméling: Neutron activation analysis; L. Szentmiklósi, Zs. Kasztovszky: Prompt gamma activation analysis. In: Research Instruments at the Budapest Neutron Centre, Handbook of the Central European Training School on Neutron Techniques. Budapest Neutron Centre (2019) ISBN 978-615-00-5068-3

PHASE ANALYSIS AND ACTIVITY OF IRON AND GOLD PARTICLES PROBED BY MÖSSBAUER SPECTROSCOPY AND OTHER METHODS

Sándor Stichleutner, Zoltán Klencsár, Károly Lázár

Objective

Iron is an important constituent in various systems and identification of its phases and valence states is essential for interpreting the observed properties. Recently, iron based fly ash zeolites, suitable for catalytic oxidation of volatile organic compounds and for CO₂ adsorption, as well as the formation and stabilization of various iron alloys and compounds during electric explosion of wires in liquid media were studied. Also, continuing our previous studies, the catalytic activity and selectivity of monodisperse gold nanoparticles deposited on various supports in the oxidation of benzyl alcohol to benzaldehyde were also studied.

Methods

⁵⁷Fe transmission Mössbauer spectroscopy was mainly used, along with other appropriate techniques.

Results

Fly ash zeolites (FAZ) of NaX accompanied by ferrous oxides or Fe²⁺ and Fe³⁺ ions incorporated in the zeolite matrix were prepared by alkaline conversion of coal ash residue collected from the electrostatic precipitator of the "AES Galabovo" thermal power plant which was supplied with lignite coal from the "Maritza-East" basin in Bulgaria. The zeolite crystallites were of uniform size (1-2 μm) and exhibited a micro-mesoporous composite structure with relatively high specific surface area (220-500 m²/g). FAZ showed a high capacity for CO₂ adsorption, depending on the content and state of iron in the zeolite structure. Cobalt-modified Co-FAZ was also prepared with 6 wt.% cobalt loading. Addition of cobalt leads to a significant increase of the catalytic activity for degradation of various volatile organic compounds (VOC). These initial and modified FAZ are promising candidates for a dual adsorption/catalytic system for CO₂ elimination and VOC oxidation [1].

The method of electric explosion of wires (EEW) in water was used to produce nanosized particles from melt quenched iron containing crystalline Fe₅₀Co₅₀, as well as from amorphous Fe₄₅Co₄₅Zr₇B₃ (HITPERM) and Fe_{73.5}Si_{15.5}B₇Nb₃Cu (FINEMET) ribbons. Formation of metallic globules in various size distributions (fine and coarse) with partial or almost total transformation of the initial crystalline structure present in the ribbons is observed. Mössbauer spectra of initially crystalline Fe₅₀Co₅₀ samples show the formation of recrystallized particles along with iron oxides (wüstite) due to reaction with water. HITPERM samples exhibit the loss of the initial amorphous state due to crystallization during EEW, while FINEMET samples partly retain the amorphous state (~15%) accompanied by the occurrence of various Si-containing crystalline phases (Fig. 1) [2].

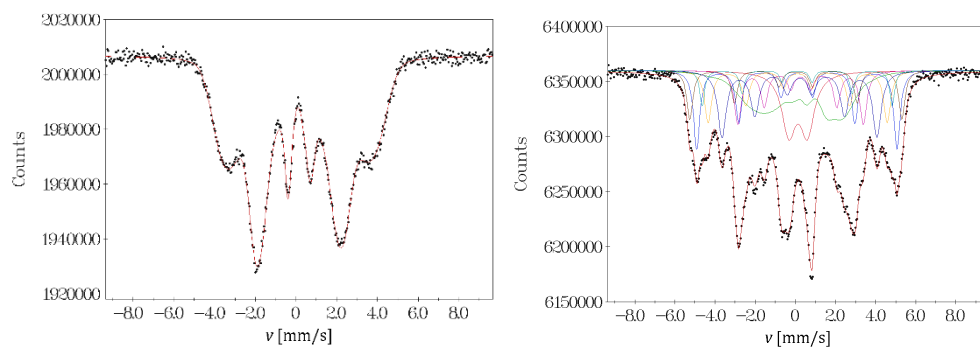


*Figure 1:
⁵⁷Fe Mössbauer spectrum of
amorphous Fe_{73.5}Si_{15.5}B₇Nb₃Cu
(FINEMET) alloy before (left)
and after (right) EEW in water.*

Previously we have studied the stabilization of gold nanoparticles with ¹⁹⁷Au Mössbauer spectroscopy. This year, in the framework of a Chinese-Hungarian bilateral TÉT project, catalytic activity of monodisperse gold nanoparticles (~2 nm) deposited on various supports was studied in the oxidation of benzyl alcohol (BzOH = C₆H₅CH₂OH). Initial stages of the oxidation process were determined from 60 °C measurements in xylene solvent under atmospheric oxygen pressure. Addition of K₂CO₃ resulted in a significant activity increase with benzaldehyde (BzO = C₆H₅CHO) selectivity of >75% at around 70% conversion. Extents of conversion and selectivity for BzO formation were determined in solvent-free experiments performed at elevated temperature and pressure (150 °C, 5 bar O₂) for 5 h. The selectivity of the investigated samples to produce BZO at >85% conversion was significantly smaller as compared to other catalysts, which exhibit much lower extents of BzOH conversion [3].

Related publications

- [1] M. Popova, S. Boycheva, H. Lazarova, D. Zgureva, K. Lázár, Á. Szegedi: VOC oxidation and CO₂ adsorption on dual adsorption/catalytic system based on fly ash zeolites, *Catalysis Today*, <https://doi.org/10.1016/j.cattod.2019.06.070>
- [2] K. Lázár, L.K. Varga, S. Stichleutner, V. K. Kis, T. Fekete, Z. Klencsár: *Electric explosion of metallic ribbons in water*, International Conference on the Applications of the Mossbauer Effect (ICAME 2019), 01-06 September, 2019, Dalian, China, Conference Program p. 102 (Abstract)
- [3] G. Nagy, A. Beck, Gy. Sáfrán, Z. Schay, Sh. Liu, T. Li, B. Qiao, J. Wang, K. Lázár: *Nanodisperse gold catalysts in oxidation of benzyl alcohol: comparison of various supports under different conditions*, *Reaction Kinetics, Mechanisms and Catalysis*, **128**, 71 (2019)

NANOSTRUCTURE RESEARCH BY SMALL ANGLE NEUTRON SCATTERING

Adél Len

Objective

The objective of the Small Angle Neutron Scattering (SANS) measurements has been to characterize the nanostructure of various systems: photoluminescent porous aerogel monoliths containing ZnEu-complex, Rh(III) chromonic-like coordination complexes, and organically modified silica. SANS has also been used to study archaeologically related ceramic samples. For this latter purpose the HWXY two-dimensional SANS data evaluation software has been developed. The study of construction materials by SANS and other complementary methods has been started.

Results

SANS measurements have been performed on silica-based aerogels modified with Zn-Eu heterometallic complexes. The incorporation of the heterometallic complexes resulted in low nuclear homogeneity at the mesoscopic range. The presence of several interrelated structural levels in the scattering system has been identified. Gyration radii of the primary particles and fractal dimensions connected to the interfacial characteristics have been obtained. The aerogels demonstrated strong luminescence upon excitation with UV light.

Two types of rhodium complexes have been synthesized and structurally characterized. Using SANS, the form factor changes, the changes of the structure factor peaks with temperature, the interaction between objects, and the formation of columnar structures have been identified. The class of transition metal coordination complexes with the ability of self-assembly in water into ordered supramolecular architectures is important in understanding the self-assembly mechanism in nature, and to obtain advanced functional materials for applications in medicine or electro-optics.

Mesoporous silica particles have been prepared with functionalized precursors either by in situ co-condensation or by post-synthesis grafting. SANS has been used to evaluate the effects of various recipes on the structural properties of the composite materials. Ordered mesoporous structures have been obtained for most of the synthesis conditions. The fine tuning of the structures will further be used for design of materials for drug loading or pollutant adsorption applications [1].

The acid catalysed one-pot sol-gel method has been used to obtain crystalline iron-oxide nanoparticles in a silica matrix. SANS revealed a two-level structure consisting of primary units and their agglomerates which is generally present in dry xerogel materials. The presence of finite size nanoparticles of average sizes of 20 nm – 30 nm has been demonstrated. The same materials have successfully been used for cadmium removal from aqueous solutions [2].

SANS has been used for identifying a correlation between the fractal-like behaviour of nano-inclusions present in the pottery matrix and the firing temperature of control clay samples with different origin. Some first conclusions about an existing correlation have been drawn. The direct identification of the ways in which ancient pottery vessels were formed remains largely dependent on the observation of preserved macroscopic surface features or, less commonly, the preferred orientation of inclusions. SANS has been used to differentiate between pottery forming techniques by comparison to a series of modern fine-ware vessels made under controlled conditions. The first results are very promising.

Destructive and non-destructive methods have been used for the analysis and condition assessment of historic masonry structures. The improvement of the reliability of the techniques used and the finding of better correlations between the destructive and non-destructive test results and the mechanical properties of masonry have proven to be of great importance [3].

Rising damp is a common problem of many buildings worldwide. However, often the desired sealing success does not occur. With the aid of neutron tomography it was possible to provide a three-dimensional representation of the distribution of an injection agent in a mineral building material and to make statements on the quality of the performed seal [4].

Remaining work

Discussing and comparing the SANS results made on Rh complexes with crystallographic data is to be done. The measurements on cement and pottery samples need to be completed, and conclusions to be drawn. Some measurements had to be postponed due to technical reasons and will be realized in 2020.

Related publications

- [1] A. Putz, L. Almásy, A. Len, C. Ianasi: *Functionalized silica materials synthesized via co-condensation and post-grafting methods*, Fullerenes, nanotubes and carbon nanostructures, **27(4)**, 323 (2019)
- [2] C. Ianasi, M. Piciorus, R. Nicola, M. Ciopec, A. Negrea, D. Niznansky, A. Len, A. Almásy, A. Putz: *Removal of cadmium from aqueous solutions using inorganic porous nanocomposites*, Korean J. Chem. Eng. **36(5)**, 688-700 (2019)
- [3] B. Balla, Z. Orbán, A. Len: *Assessing the reliability of single and combines diagnostic tools for testing the mechanical properties of historic masonry structures*, Pollack Periodica, **14(3)**, 31-42 (2019)
- [2] A. Walter, H. Wenzmer, A. Len, Z. Kis: *The use of neutron methods in the research of building materials – quality management of a sealing by illustrating the distribution of an injection agent in building materials*, In: H. Wenzmer: *Bautenschutz II Nachweismethoden und Anwendungen*, Edition Bautenschutz, 1-19 (2019)

RADIOGRAPHY AND TOMOGRAPHY AT BRR

Zoltán Kis, László Horváth, László Szentmiklósi

Objective

To develop and use imaging instrumentation and methodology at the Budapest Research Reactor (BRR).

Methods

New developments in techniques and instrumentation can broaden the scope of amenable materials for these techniques and allow performing better experiments. A systematic investigation of powder metallurgical structure and corrosion defects for objects, and the systematic study of porous materials were carried out by obtaining and evaluating tomographic datasets.

Results

A multifunction neutron beam filter and shaper device (Fig.1 a) was designed for the radial beamline No.2 of the BRR, the RAD station. The filter would provide the possibility of choosing the most suitable energy range of the neutron beam for experiments. It would host a beam limiter, a prefilter, and a rotating drum with a set of filters to provide thermal, epithermal and fast beams. The project for its realization (CERIC ARCHE) was not funded.

At the NORMA station, in collaboration with the Paul Scherrer Institute (PSI), Switzerland, measurements were carried out to increase the spatial resolution, and test the developed scattering correction method for the first time outside of the PSI. We changed the lens and the scintillation screen and also moved the plane of the scintillator screen closer to the sample. The line pattern was used to determine the pixel size to be 33 μm . Plotting the averaged profiles from the line patterns showed that spatial frequencies in the order of 80 μm can already be resolved (Fig.1 b), giving a significant improvement over that of the present setup (220 μm). We also made 3D tomograms with 600 projections, plus the reference scans required for an advanced scattering correction with black bodies. As a practical application, we did 3D neutron imaging to determine the maximum sample thickness for identifying cracks and follow the self-healing process within a broken bitumen sample. This indicated that it is possible to use a cylindrical bitumen sample with a diameter of 6 mm. From the time series study - made with golden-ratio rotation technique - (Fig. 1 c), we found out how fast the data acquisition must be performed to avoid motion artefacts.

In the field of cultural heritage studies, we carried out position-sensitive PGAI-NR to better understand the post-excavation corrosion of copper alloys. Results showed that the Cl/Cu ratio and hence chloride concentration, varied across the surface of the coins. Incremental analysis confirmed high chloride levels where this corrosion product was visible (Fig. 1 d).

Using neutron imaging we verified finite element simulations for cemented carbide cutting tools fabricated by slightly different powder metallurgical techniques. A detailed evaluation of the 3D datasets for the first time provided the local density values of the cutting inserts (Fig. 1 e). The results confirm that the influence from the pressing speed on the density gradient is significantly more important than the holding time. The local density variations can thus be used for inverse modelling.

In porous material research one of the main topics was to characterize the system of pores and air voids in concrete using neutron radiography and tomography (NR/NT) to give a quantitative description of pore size and connectivity. A detailed evaluation of the 3D datasets provided the void distribution of three air-entrained concrete samples (Fig. 1 f). A statistical evaluation of the pore volume distributions and shape analysis was completed. The fundamental differences in the pore/void system could be clearly visualized and partly quantified. However, comparing our results to those from more conventional physical methods, e.g. mercury intrusion porosimetry or micro X-ray imaging, an underestimation of the porosity was observed due to the lower spatial resolution and the consequent segmentation limitations of neutron imaging.

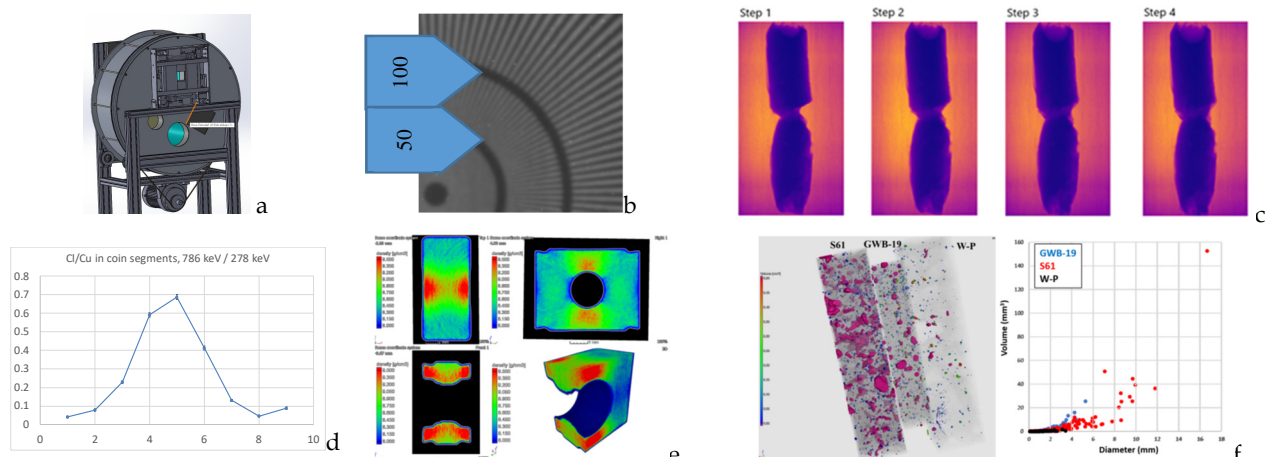


Figure 1: Neutron imaging results: see text for further information

Related publications

- [1] H. Staf, Z. Kis, L. Szentmiklósi, B. Kaplan, E. Olsson, and P.-L. Larsson: *Determining the density distribution in cemented carbide powder compacts using 3D neutron imaging*, Powder Technol., **354**, 584–590 (2019)
- [2] R. Zboray, R. Adams, M. Morgano, and Z. Kis: *Qualification and development of fast neutron imaging scintillator screens*, Nucl. Instruments Methods A, **930**, 142–150 (2019)

NON-DESTRUCTIVE, SPATIALLY-RESOLVED ELEMENT ANALYSIS OF STRUCTURED SAMPLES (OTKA K124068)

László Szentmiklósi, Boglárka Maróti, Zoltán Kis

Objective

To develop Prompt-Gamma Activation Imaging (PGAI), and apply it to non-homogeneous and irregularly-shaped samples

Methods

Linear attenuation coefficient measurements via neutron imaging, composition measurements by Prompt-Gamma Activation Imaging – Neutron tomography (PGAI-NT), computer programming, Monte Carlo modelling.

Results

Within the OTKA Grant No. K124068 project, we continued the work with the empirical determination of neutron attenuation coefficients of different materials with various thicknesses at the RAD and NIPS-NORMA imaging facilities. By measuring a series of homogeneous samples with identical density but different thicknesses, the change in the linear attenuation coefficient can be determined (Fig. 1). These functions will be used in the proper self-shielding correction of bulky materials.

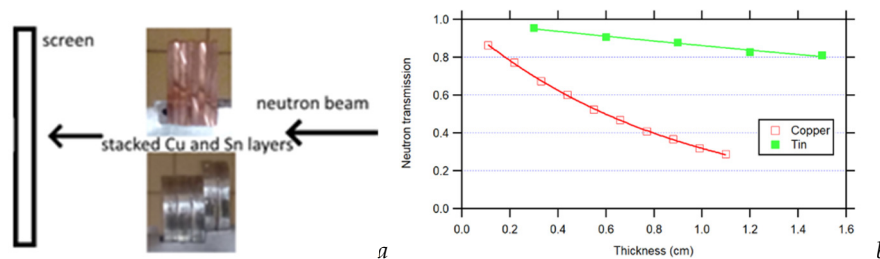


Figure 1: Arrangement of the Cu- and Sn-layers (a) and the determined neutron attenuations at different thicknesses (b)

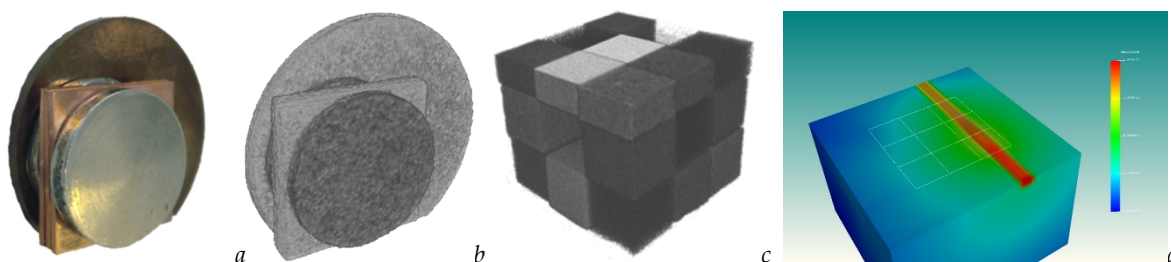


Figure 2: Photo (a) and neutron tomogram (b) of pure copper and tin, as well as a bronze reference material. Thermal-neutron tomogram of a multi-material magic cube (c), and the related MCNP6 Monte Carlo calculation (d)

Neutron tomography of a sample stack of pieces of pure copper, pure tin and bronze was made for image segmentation (Fig. 2. a and b). Based on the neutron attenuation, all three materials were easily distinguishable. Knowing the bulk composition of the bronze based on the PGAA results, the neutron attenuation of bronze (Sn-Cu mixture) was calculated. This value was in good agreement with the neutron attenuation obtained based on the neutron tomography.

A magic cube assembled of 7-mm unit blocks of lead, tin, copper, iron, aluminum, PTFE, graphite, sandstone, and tile was characterized by 3D imaging and local PGAA analysis, as well as by MNCP6.2 simulations to study the matrix effect and the influence of neutron scattering. The data processing is ongoing.

Related publications

- [1] L. Szentmiklósi, B. Maróti, Z. Kis, J. Janik, L.Z. Horváth: *Use of 3D mesh geometries and additive manufacturing in neutron beam experiments*, J. Radioanal. Nucl. Chem. **320**, 451-457 (2019)
- [2] L. Szentmiklósi, Z. Kis, B. Maróti, V. Szilágyi, K. Gméling, A. Len, L. Rosta, T. Kun, R. Baranyai, M. Fábrián, L. Bottyán, J. Janik: *Tudomány az innováció szolgálatában: neutronos anyagvizsgálati módszerek ipari alkalmazásai a Budapesti Neutron Centrumban*, Fizikai Szemle **69**, 304-310 (2019)
- [3] 2 oral presentations, SAAGAS (27th Seminar on Activation Anal. and Gamma Spectrometry) (2019. Feb. 24-27. Garching)
- [4] One invited and one regular oral presentations, RANC (2nd International Conference on Radioanalytical and Nuclear Chemistry), 2019. May 5-10, Budapest)

IAEA COORDINATED RESEARCH PROJECT ON PHOTONUCLEAR DATA AND PHOTON STRENGTH FUNCTIONS

Tamás Belgya and László Szentmiklósi

Objective

The main goals of the IAEA Coordinated Research Project (CRP) are to update the Photonuclear Data Library (1999) and to generate a Reference Database for Photon Strength Functions (PSF). Also, to further develop the methods of uncertainty calculations, both for experimental spectra and modelled spectra

Methods

The development of uncertainty calculations was concentrated on working out ways to subtract the beam-background, impurity spectra and decay spectra by minimizing the area of the corresponding peaks, while at the same time minimizing background above the highest energy of the investigated and impurities' peak energies. The most challenging task is to estimate the propagation of calculated branching ratio uncertainties while carrying out the numerous subtractions of response functions since they have a strong correlation through their normalisation to 1. Another difficulty is that the probability distribution of the individual gamma decay probability is strongly changing as a function of energy due to the Porter-Thomas (first-order Chi-square) distribution.

Results

To calculate the uncertainty of the unwanted contribution of the beam-background, impurities and decay spectra from the experimental isotopic spectrum requires careful peak identifications, then the determination of normalization factors for each spectrum to be subtracted and the setting up of regions to be minimized by the least-square method. Since every subtracted spectrum contains the beam-background, it is a non-trivial task. After the minimization, the total uncertainty can be calculated easily by adding up the squares of constituent uncertainties.

As already mentioned, the estimation of the branching ratio uncertainties depends on the Porter-Thomas distribution $x^{-1/2} \exp\left(-\frac{x}{2}\right)$ where $x = \frac{\Gamma_\gamma}{\Gamma_\gamma}$ and Γ_γ is the gamma-decay width. The average of this function is 1 and its variance is 2. The gamma-decay branching ratios are defined as $b_{i,k} = \Gamma_{\gamma,i,k} / \sum_{m=1}^{i-1} \Gamma_{\gamma,i,m}$. Their correlated uncertainties were calculated analytically. The variance was then used in the program BITS (Bin Type Statistical simulation). The result of calculations for ^{243}Pu is shown in Fig. 1 using the uncertainty estimates in the BITS model and the unfolded background corrected spectrum.

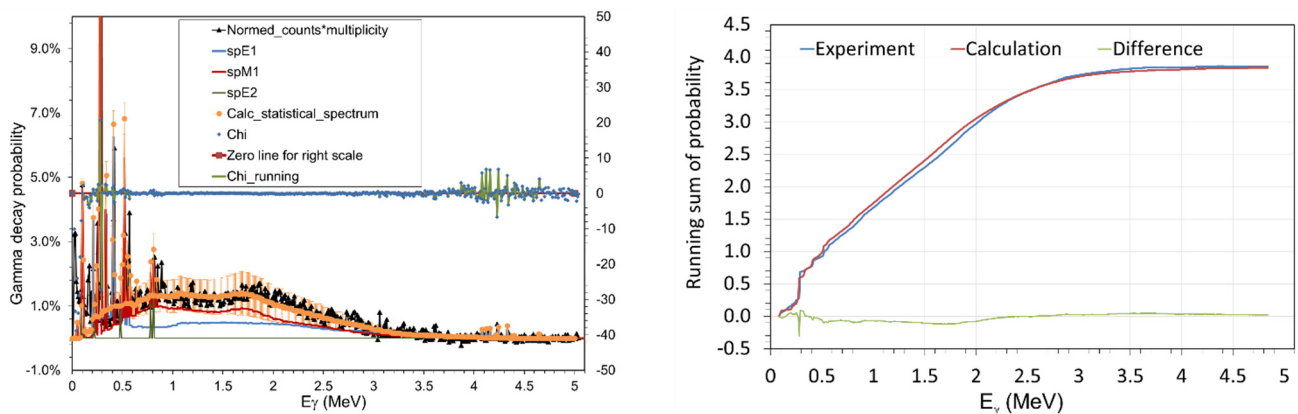


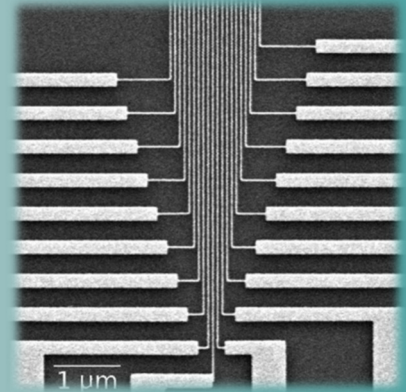
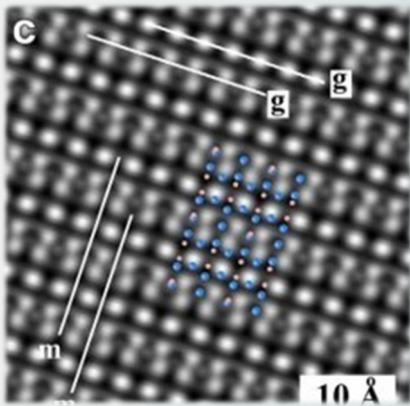
Figure 1: The simulation of the ^{243}Pu radiative capture gamma-ray spectrum using 1DM-QRPA theoretical photon strength function with fitted parameters. The experimental spectrum is shown with black triangles. The error bars of the statistical spectrum presented as a band around circles. The left panel shows the simulation results in orange with its full uncertainties, while the right panel presents the running sum of the measured gamma decay probabilities that results in the gamma multiplicity at the high end of the curve. The electric E1 and magnetic M1 contributions to the calculated statistical spectrum are also shown.

Remaining work

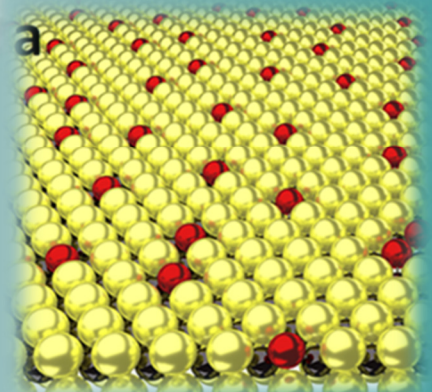
Preparing publications on the modelling of unfolded radiative neutron capture spectra.

Related publications

- [1] S. Goriely, P. Dimitriou, M. Wiedeking, T. Belgya, R. Firestone, J. Kopecky, M. Krťicka, V. Plujko, R. Schwengner, S. Siem, H. Utsunomiya, H. S. P'eru, Y.S. Cho, D.M. Filipescu, N. Iwamoto, T. Kawano, V. Varlamov, R. Xu: *Reference database for photon strength functions*, Eur. Phys. J. A. **55**, 172-224 (2019) doi:10.1140/epja/i2019-12840-1.



VI. RESEARCH AND DEVELOPMENT IN INSTITUTE OF TECHNICAL PHYSICS AND MATERIAL SCIENCES



NON-DESTRUCTIVE EVALUATION (NDE) SYSTEM FOR THE INSPECTION OF OPERATION-INDUCED MATERIAL DEGRADATION IN NUCLEAR POWER PLANTS

EU H2020 NFRP-2016-2017-1 -755330 „NOMAD“

A. Gasparics and G. Vértesy

The long-term operation (LTO) of existing nuclear power plants (NPPs) has already been accepted in many countries as a strategic objective to ensure adequate supply of electricity over the coming decades. In order to estimate the remaining useful lifetime of NPP components, LTO requires reliable tools. The objective of NOMAD project is the development, demonstration and validation of a non-destructive evaluation (NDE) tool for the local and volumetric characterization of the embrittlement in operational reactor pressure vessels (RPVs). In order to address these objectives, the following steps should be taken: Development and demonstration of an NDE tool for the characterization of RPV embrittlement; Extension of the existing database of RPV material degradation by adding correlations of mechanical, microstructural and NDE parameters; and application of the developed tool to Charpy geometry samples and also to clad material resembling the actual RPV inspection scenario.

The MFA contributes to the NOMAD project with own micromagnetic testing method: so called Magnetic Adaptive Testing (MAT). MAT is a recently developed method for non-destructive characterization of ferromagnetic materials, which is based on systematic measurement and evaluation of minor magnetic hysteresis loops. This method is being tested and evaluated regarding its applicability for the determination of the material changes and the variation of the material properties during exposure to neutron irradiation. As shown in our several previous research activities, MAT provides more sensitivity for material degradation than the major hysteresis loop and has an improved feature of measurement error suppression. An additional significant advantage of this method is that there is no need for magnetic saturation of the measured samples, which eases the practical application.

MAT measurements were performed on reactor steel material before and after neutron irradiation and the non-destructively determined magnetic parameters were compared with the destructively measured ductile-to-brittle transition temperature (DBTT) values. Standard Charpy specimens from 22NiMoCr37 type base and from 18MND5 type weld materials were measured. These steel grades are members of the typical RPV steel groups: Mn-Ni-Mo steels (western RPV design). The samples were prepared, irradiated and measured at the Belgian Nuclear Research Centre (SCK•CEN). The samples were irradiated there in the BR2 reactor at 260 °C temperature by $E > 1$ MeV energy fast neutrons with total neutron fluence in the range of 4.02×10^{19} – 8.95×10^{19} n/cm². Since irradiated samples are radioactive, they can be measured only in hot cell laboratories. A special sample holder was designed and built for this purpose. Charpy impact testing (ASTM-23-16b) was used to determine the 41 Joule transition temperature (T_{41J}). The transition temperature shift ($\Delta DBTT$) is the difference between the neutron irradiated T_{41J} and the as-received (base-line) T_{41J} which is a measure for the embrittlement of the material. In the following figures the correlation between optimally chosen MAT descriptors and the transition temperature shift are shown for the two types of Charpy specimens. MAT descriptors are normalized by the corresponding parameter of the reference (not irradiated) sample. Those parameters were chosen from the calculated big datapool, which characterize most sensitively and at the same time most reliable the material degradation (optimally chosen MAT descriptors).

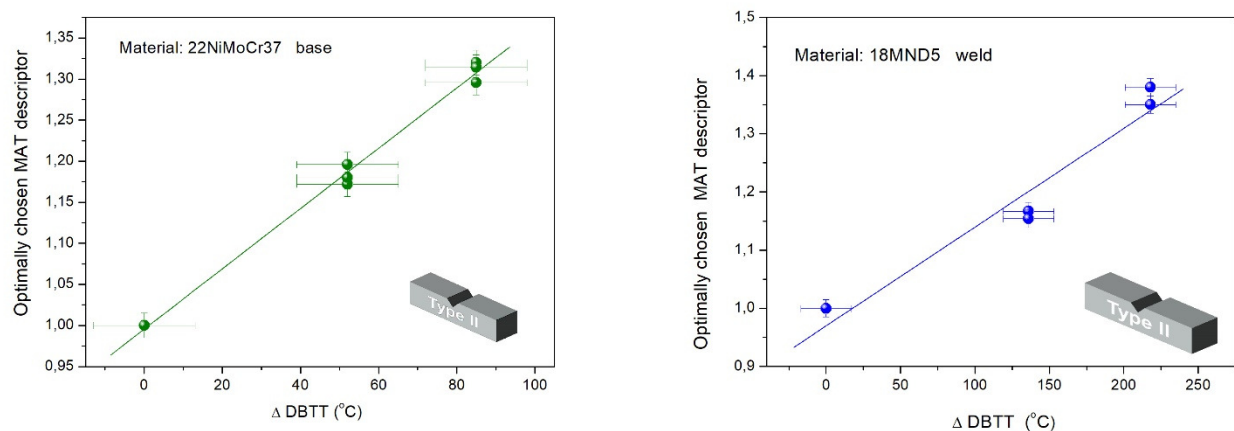


Figure 1: (left) Optimally chosen normalized MAT descriptor as a function of the transition temperature shift for a 22NiMoCr37 type base material and (right) for a 18MND5 type weld material, measured on Charpy samples.

A linear correlation was found between magnetic parameter and neutron fluence. About 30% increase at 3% error level of the MAT descriptor was detected due to 6×10^{19} n/cm² neutron fluence in case of the base material, compared with the not irradiated sample; and close to 40% increase at 5% error level due to 8.5×10^{19} n/cm² neutron fluence in case of the weld material. The influence of neutron irradiation is reflected on the shift of transition temperature, as shown in Fig. 1. The linear

fit on the measured points is to lead the eye to reflect more visible the character of the correlation. It does not reflect a strict mathematical fitting, because of the limited number of measured points.

In another series of experiments clad and underclad block specimens made of 15H2NMFA material were measured. Blocks were cut from the forged ring as shown in Fig. 2. The size of blocks was 115mm x 50mm x 50mm. Cladding (7-10 mm thick) was on the top of the blocks. The clad surface of the real pressure vessels is usually made by submerged strip welding (a special way of the submerged arc welding) in three layers. The surface is either grinded, or roughly machined to provide coupling for the ultrasonic testing. The samples were aged by thermal treatments using a special step cooling technology (details are not given here) used for accelerated evaluation of thermal ageing sensitivity. The main consideration at the selection of the thermal treatment was to produce similar microstructural changes of which occurs at irradiation.

Two types of step cooling were performed, which resulted different material degradations controlled by transition temperature determination. MAT measurements were performed on the clad and underclad blocks. Both sides of the blocks were measured. Regular loops with large amplitude were experienced on base (highly ferromagnetic) material. The situation is different on the top side, which is covered by cladding. Cladding is an austenitic, almost paramagnetic material, which means practically a large air gap between magnetizing yoke and ferromagnetic part of sample. Because of this, a very weak magnetic signal was found.

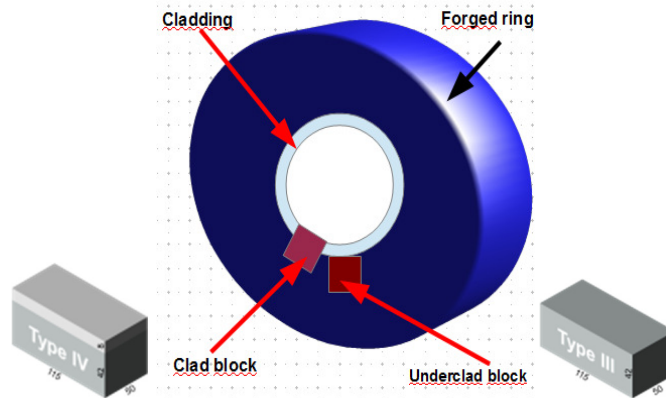


Figure 2: Cutting of clad and unclad blocks from forged ring

The correlation between MAT parameters and transition temperature in case of blocks is shown in Fig. 3. Again excellent, almost perfect linear correlation was found between MAT parameters and transition temperature even if the measurement is performed through the cladding.

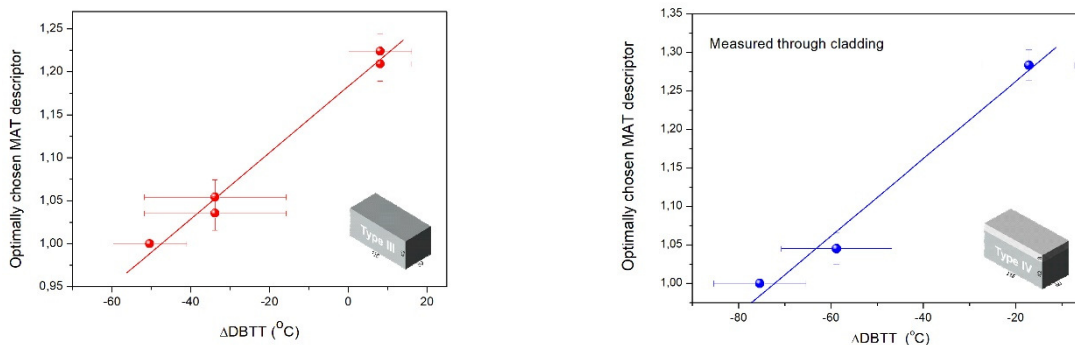


Figure 3: Correlation between normalized MAT parameters and transition temperature, measured directly on base material (left) and on cladding (right)

An important and novel result of the present work is, that the ferromagnetic base material can be inspected even through the relatively thick cladding, and the measurement through the cladding result the same correlation between magnetic parameters and independent variable as obtained by direct measurement of base material. This fact proves the unique applicability of MAT in non-destructive inspection of degradation of nuclear pressure vessel material.

Another fact, worth of mentioning is, that the error of magnetic measurement is significantly lower than the error of destructive Charpy measurement, which is clearly seen on the above graphs. So magnetic measurement is not only non-destructive, but – perhaps – it provides even more precise value about material degradation, than Charpy impact test.

TRANSITION METAL CHALCOGENIDE SINGLE LAYERS AS AN ACTIVE PLATFORM FOR SINGLE-ATOM CATALYSIS

680263-NanoFab2D-ERC-2015-STG, LP2014-14 Lendület, LP2017-9 Lendület, OTKA KH130413, VEKOP-2.3.2-16-2016-00011, Korea-Hungary Joint Laboratory

P. Vancsó, Z. I. Popov (MISiS), J. Pető, T. Ollár, G. Dobrik, J. S. Pap, C. Hwang (KRISS), P. Sorokin (MISiS), L. Tapasztó

Among the main appeals of single-atom catalysts are the ultimate efficiency of material utilization and the well-defined nature of the active sites, holding the promise of rational catalyst design. A major challenge is the stable decoration of various substrates with a high density of individually dispersed and uniformly active monatomic sites. Transition metal chalcogenides (TMCs) are broadly investigated catalysts, limited by the relative inertness of their pristine basal plane. In this work we proposed that TMC single layers modified by substitutional heteroatoms can harvest the synergistic benefits of stably anchored single-atom catalysts and activated TMC basal planes. These solid-solution TMC catalysts offer advantages such as simple and versatile synthesis, unmatched active site density, and a stable and well-defined single-atom active site chemical environment. Furthermore, 2D crystal substrates are highly convenient, as they can be easily investigated by direct atomic resolution imaging techniques such as high-resolution transmission electron microscopy or scanning tunnelling microscopy (STM). Fig. 1 shows an example of resolving the individual heteroatom (oxygen) sites embedded into MoS₂ single layer revealed by STM. The sample has been prepared by annealing the exfoliated single layer at 130°C in air for a week.

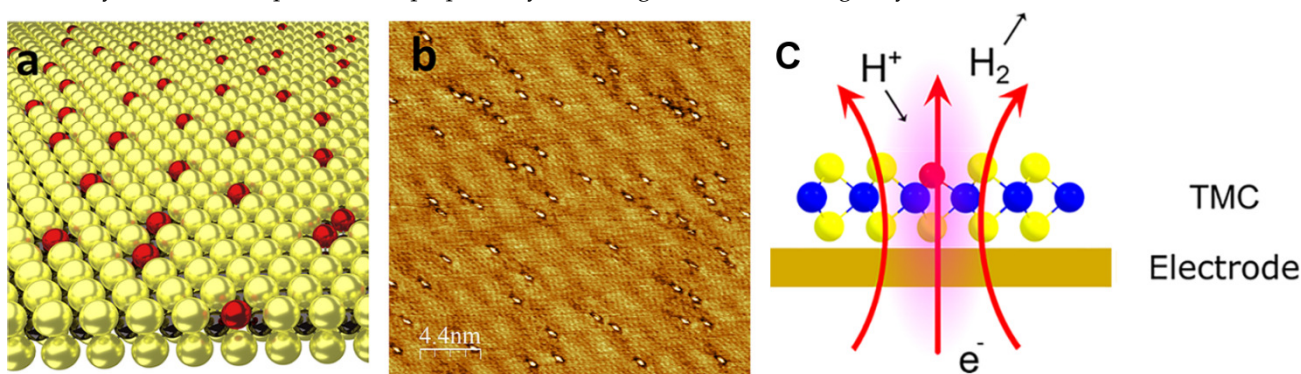


Figure 1: (a) Schematic model of individually dispersed heteroatoms substituting chalcogenide atoms of 2D transition metal chalcogenide crystals. (b) The practical realization of such structures evidenced by atomic resolution STM images of oxygen-atom-doped MoS₂. (c) Schematic model of the hydrogen evolution reaction in the presence of the heteroatom.

In order to understand the potential mechanisms responsible for the increased catalytic activity of heteroatoms incorporated by substitution in various TMC crystals (Fig. 1c), we performed Density Function Theory (DFT) calculations for different TMC single layers (2H- MoS₂, MoSe₂, MoTe₂, WS₂, WSe₂, WTe₂) and investigated the role of oxygen heteroatoms in catalysing the hydrogen evolution reaction. We observed several common properties related to the catalytic activity of the different TMC single layers.

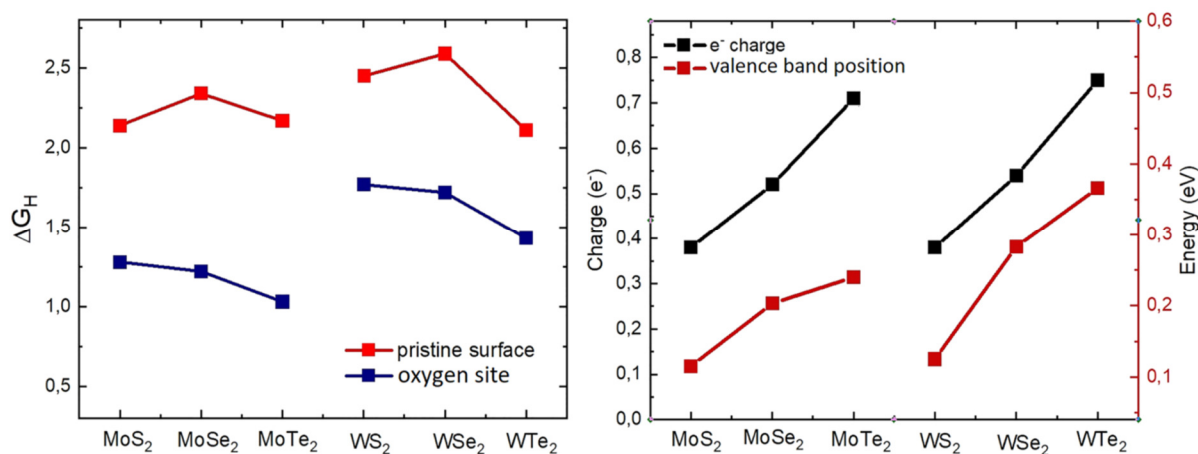


Figure 2: (left) Hydrogen adsorption Gibbs free energy on the basal plane chalcogen sites (red) and O substitution sites (blue). (right) Electron charge surplus on the O sites relative to pristine chalcogen atom sites and the position of the valence band at the Γ point of the Brillouin zone relative to Fermi level for various 2D TMC crystals with O substitution sites.

First, decreased hydrogen adsorption potential on the oxygen atoms (Fig. 2 left) has been calculated from the change of the H atom adsorption Gibbs free energy (ΔG_{H}), which is a widely used descriptor for the catalytic activity. Second, negatively charged oxygen atoms has been obtained from Bader charge analysis (Fig. 2 right), where such negative charges can provide an additional attractive interaction for the positively charged H species, facilitating their adsorption. Finally, increased transversal conductivity around the oxygen atom was revealed resulting an efficient transverse electron transfer for the catalytic process. In the latter case, we found that the presence of oxygen atoms locally enhances the z-like character of the atomic orbitals around the Fermi-level, as it can be seen in the local density of states (LDOS) iso-surface plot (Fig. 3). This induces an enhanced overlapping of the O, S, and Mo orbitals, opening sub-nanometer wide transverse conduction channels in the direction perpendicular to the sheet.

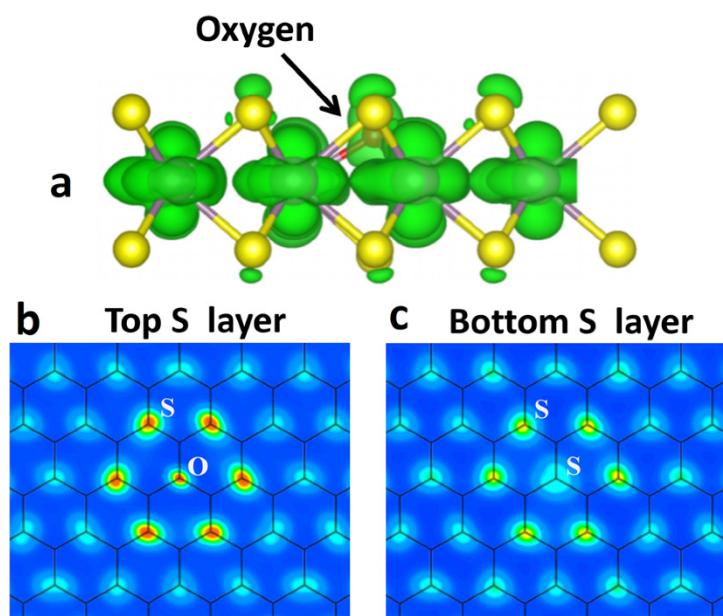


Figure 3: Electronic density of states redistribution near the O substitution site in MoS₂ single layer. In-plane view of the S layers highlighting increased electron density on the nearest neighbor S atoms.

In conclusion, 2D solid solution TMCs with identical active sites emerge as an excellent platform for single-atom catalysis, where the fully characterized atomic and electronic structure are also expected to provide a new model system for understanding single-atom catalysis.

VISIBLE-FREQUENCY GRAPHENE PLASMONS IN EXTREMELY NANOCORRUGATED GRAPHENE SHEETS

680263-NanoFab2D-ERC-2015-STG, LP2014-14 Lendület, LP2017-9 Lendület

G.Dobrik, P. Nemes-Incze, P. Süle, P. Vancsó, G. Piszter, L. Tapasztó

Graphene plasmons – hybrids of Dirac fermions and photons – are particularly appealing due to their unmatched mode volume confinement, long lifetime and easy tunability. To fully exploit these unique properties, visible-frequency graphene plasmons are desirable, given that our most efficient optical techniques are available for visible light. However, tuning up the resonance frequency from native THz values into the visible range turned out particularly challenging. It has been proposed that graphene structures below 10 nm characteristic size, can scale up plasmon frequencies into the visible. However, this approach is strongly limited by the detrimental effects of edges on plasmon resonances. We have demonstrated the realization of visible graphene plasmons through their edge-free lateral confinement into sub-5 nm graphene nanocorrugations with particularly high aspect ratios. Such graphene sheets with strong nanoscale corrugations were prepared by cyclic thermal annealing between Room Temperature (RT) and $\sim 400^\circ\text{C}$. The Root mean square (RMS) value characterizing the surface roughness is about 0.5 nm, which is almost the double of the RMS value measured in graphene on SiO_2 (0.27 - 0.35 nm).

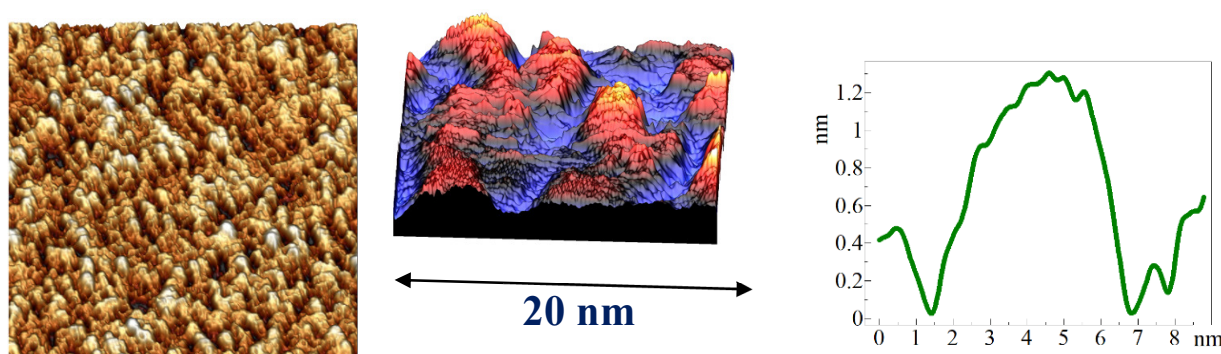


Figure 1: The structure of nanobuckled graphene sheets. STM images of graphene sheets prepared by cyclic thermal annealing displaying a particularly strong nanoscale corrugation, with lateral size below 10 nm, and nanometer height. Line cut displaying a typical graphene nanocorrugation geometry with an aspect ratio of $h_{\text{max}}/R \sim 0.5$.

Graphene corrugations with aspect ratios (h_{max}/R) as high as 0.5 could be easily found. These numbers clearly highlight the extreme nature of the nanoscale deformation (corrugation). The most striking findings were observed when measuring the Raman spectra of corrugated graphene sheets with 633 nm excitation wavelength. Such measurements revealed a huge Raman signal, only by exposing the samples to laboratory air (Fig.2.b). Detecting Raman peaks with 20 times higher intensity than the G peak of graphene by only air exposure is truly remarkable, and indicates a strong and robust underlying phenomenon. The huge Raman signal picked up from air, was identified as the fingerprint of copper phthalocyanine (CuPc) molecules. As expected, exposing quasi-flat graphene sheets to the same conditions (i.e. air) does not result in any detectable CuPc signal in the Raman spectra.

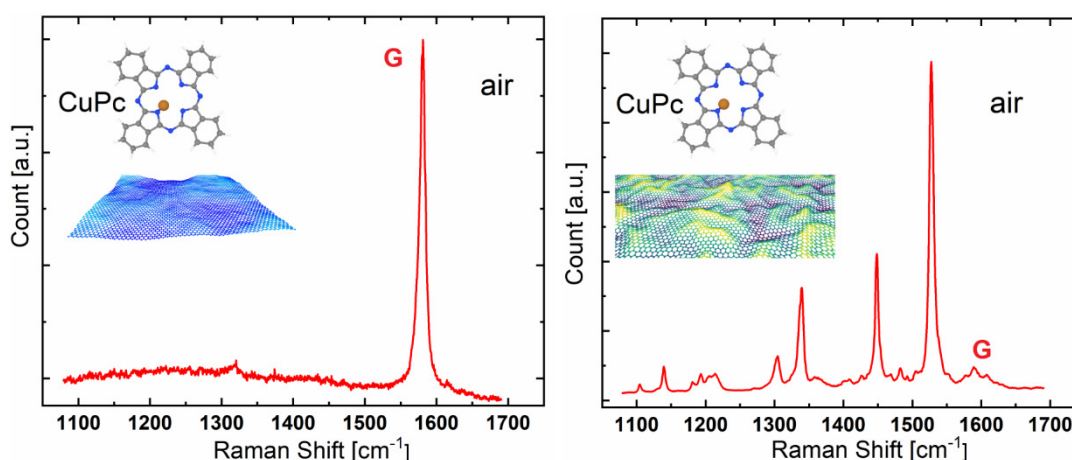


Figure 2: (right) Huge Raman enhancement on nanocorrugated graphene sheets. Detection of CuPc molecules from “clean” air by nanocorrugated graphene sheets. (left) The Raman spectrum of quasi-flat graphene subjected to the same conditions is shown for reference.

To gain insight into the origin of the increased optical response, we have calculated the electron energy loss spectrum of nanocorrugated graphene that directly reveals plasmon peaks. As apparent in Fig. 3, several peaks appear in the calculated Electron Energy Loss Spectrometry (EELS) spectra that can be associated with plasmons or quasi-plasmons of energies in the visible range.

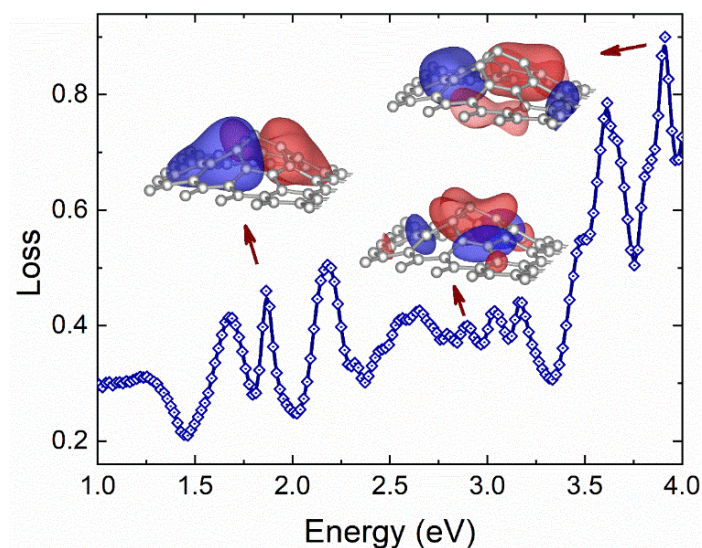


Figure 3: Plasmonic excitations in nanocorrugated graphene. Calculated EELS spectrum of a model graphene nanocorrugation, revealing several loss peaks in the visible range. The insets display the charge distributions of optical excitations corresponding to different loss peaks.

We have demonstrated the realization of visible graphene plasmons through their edge-free lateral confinement into sub-5 nm graphene nanocorrugations. The emerging strong near-fields of localized visible graphene plasmons provide such exceptional Raman enhancements that enable the detection of specific molecules even from “clean” air. This enormously enhanced interaction of molecules adsorbed on nanocorrugated graphene with visible light opens the way towards highly efficient and tunable Surface Enhanced Raman Spectroscopy (SERS) substrates and quantum emitters.

ULTRA-FLAT TWISTED SUPERLATTICES IN 2D HETEROSTRUCTURES

680263-NanoFab2D-ERC-2015-STG, LP2014-14 Lendület, LP2017-9 Lendület

M. Szendrő, P. Süle, G. Dobrik, L. Tapasztó

When 2D materials are layered on top of each other an interference pattern called the Moiré-pattern is formed due to the lattice mismatch and relative rotation between the layers. Moiré-patterns already host a large variety of exciting physical phenomena e.g. secondary Dirac cones, Hofstadter's butterfly, superconductivity. However, the corrugation stemming from the pattern is still a largely unexplored field and is lacking a comprehensive theoretical description. The way 2D heterostructures relax strain through out-of-plane deformation can highly influence the properties of such systems. The commonly accepted picture is that the corrugation is a monotonically decreasing function of the twist angle.

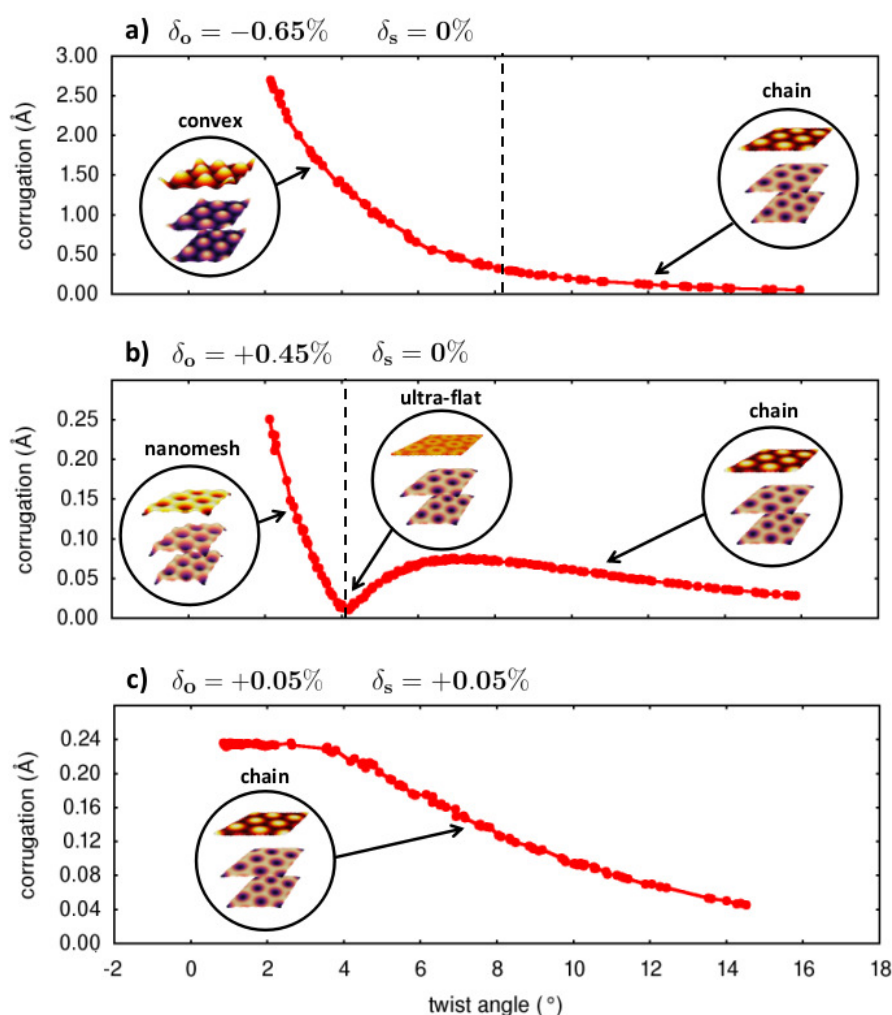


Figure 1: Moiré-superlattice corrugations of the top rotated graphene layer for three differently strained 5-layer graphene systems from molecular mechanics simulations. a) The overlayer is externally compressed with $\sim 0.65\%$ which leads to a convex phase for angles below 8.2° and a chain phase for angles above. b) The overlayer is stretched with $\sim 0.45\%$ strain, inducing a nanomesh phase for angles below 4° , and a chain phase above. Near the phase transition (dashed line), the corrugation vanishes and an ultra-flat phase appears. c) Both overlayer and substrate are stretched with 0.05% . In the range of $0-4^\circ$ The corrugation is closely constant (plateau-effect).

Here we found by lattice relaxation of around 8000 different Moiré-superstructures using high scale Classical Molecular Simulations combined with analytical calculations, that even a small amount of strain can substantially change this picture, giving rise to more complex behaviour of superlattice corrugation as a function of twist angle. One of the most surprising findings is the emergence of an ultra-flat phase that can be present for arbitrary small twist angles having a much lower corrugation level than the decoupled phase at large angles. A possible experimental realization of the ultra-flat state is revealed by Scanning Tunnelling Microscopy (STM) investigations of the graphene/graphite system.

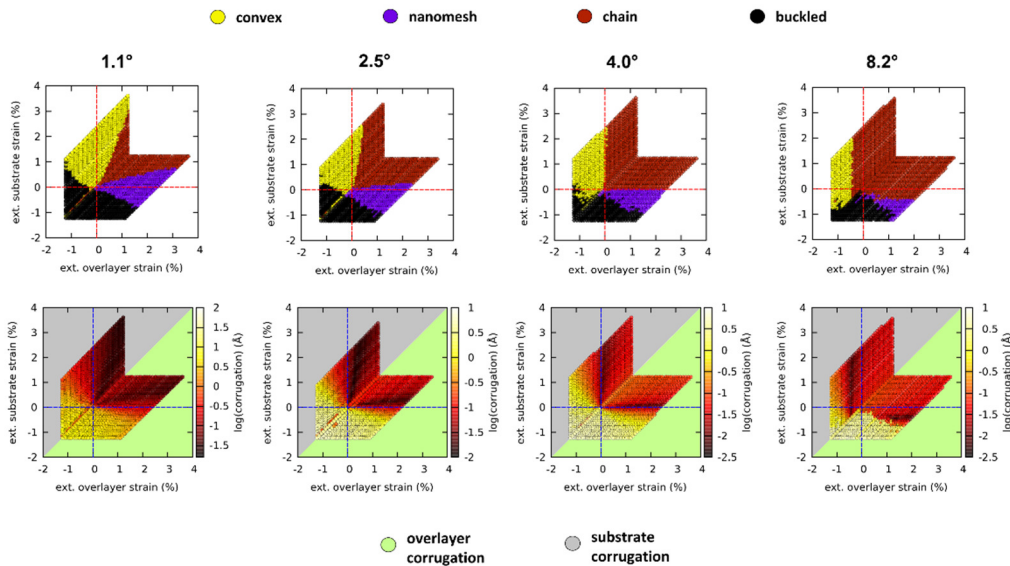


Figure 3: Top row: Moiré-phases of the twisted trilayer graphene system for different twist angles in the space of externally applied homogeneous strains (phase-maps). The corresponding Moiré-phases are indicated with different colours (yellow - convex, purple - nanomesh, red - chain). Bottom row: The same phase-maps but coloured by the corrugation of the relaxed Moiré-superlattices. The dark areas show the ultra-flat states around the phase boundaries.

We have prepared and analysed graphene layers deposited at various rotation angles on graphite substrates. We measured the rotation angle, Moiré-periodicity, as well as the Moiré amplitude for various rotation angles. We were able to find a graphene flake where the corrugation was very low, almost undetectable at an intermediate (9°) rotation angle. Consequently, the graphene flake displayed in Fig. 3.b) can be regarded as an experimental realization of an ultra-flat state predicted theoretically, although the exact parameters (heterostrain values) could not be directly inferred.

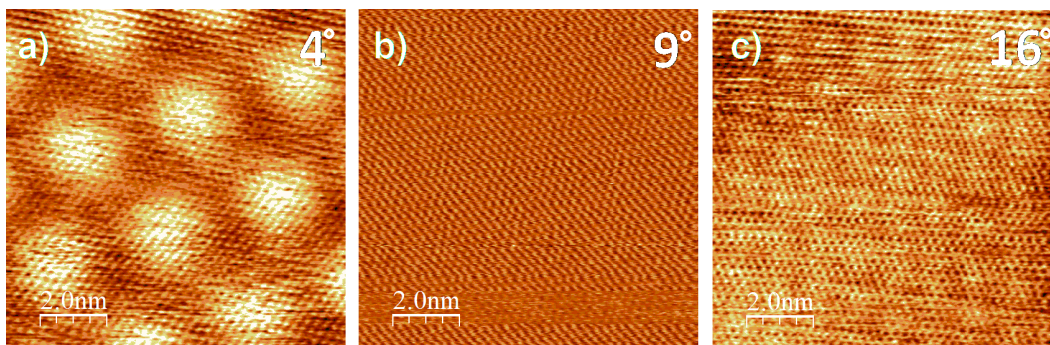


Figure 3: Topographic scanning tunnelling microscope images of graphene layers deposited on top of a graphite substrate for various relative rotation angles. The STM image in panel (b) reveals an ultra-flat state, much smoother than observed even for high rotation angles (c). The experimental conditions for image acquisition ($I_{tunnel} = 1nA$, $U_{bias} = 200mV$), data processing, and graphic display parameters are the same for all panels.

ANISOTROPIC STRAIN EFFECTS IN SMALL-TWIST-ANGLE GRAPHENE ON GRAPHITE

OTKA K119532, OTKA KH129587, Korea-Hungary Joint Laboratory

M. Szendrő, A. Pálinkás, P.Süle, Z.Osváth

Graphene and other two-dimensional (2D) materials are intensively studied from the perspective of building new van der Waals heterostructures by stacking one layer on top of the other. The interaction between stacked 2D layers affects the resulting electronic properties. Already the interaction between two superimposed graphene layers implies rich physics. Moiré patterns can appear when two similar crystalline layers are superimposed, with a spatial period depending on the misfit and the rotation angle between the lattice parameters of the two layers. This moiré superstructure introduces not only a slight geometric corrugation in graphene, but also modulates the local density of states (LDOS). Graphene layers superimposed with small twist angle ($\sim 1^\circ$) are of peculiar interest due to the decreased Fermi velocity, charge localization, the emergence of flat electronic bands, electron-electron interaction, and also due to the appearance of unconventional superconductivity and correlated insulator behaviour.

We have investigated a small-twist-angle (0.64°) graphene on highly oriented pyrolytic graphite (HOPG) by scanning tunnelling microscopy (STM) and show that the measured moiré superstructure reflects a locally strained graphene with anisotropic variations of the lattice parameter (Fig. 1.).

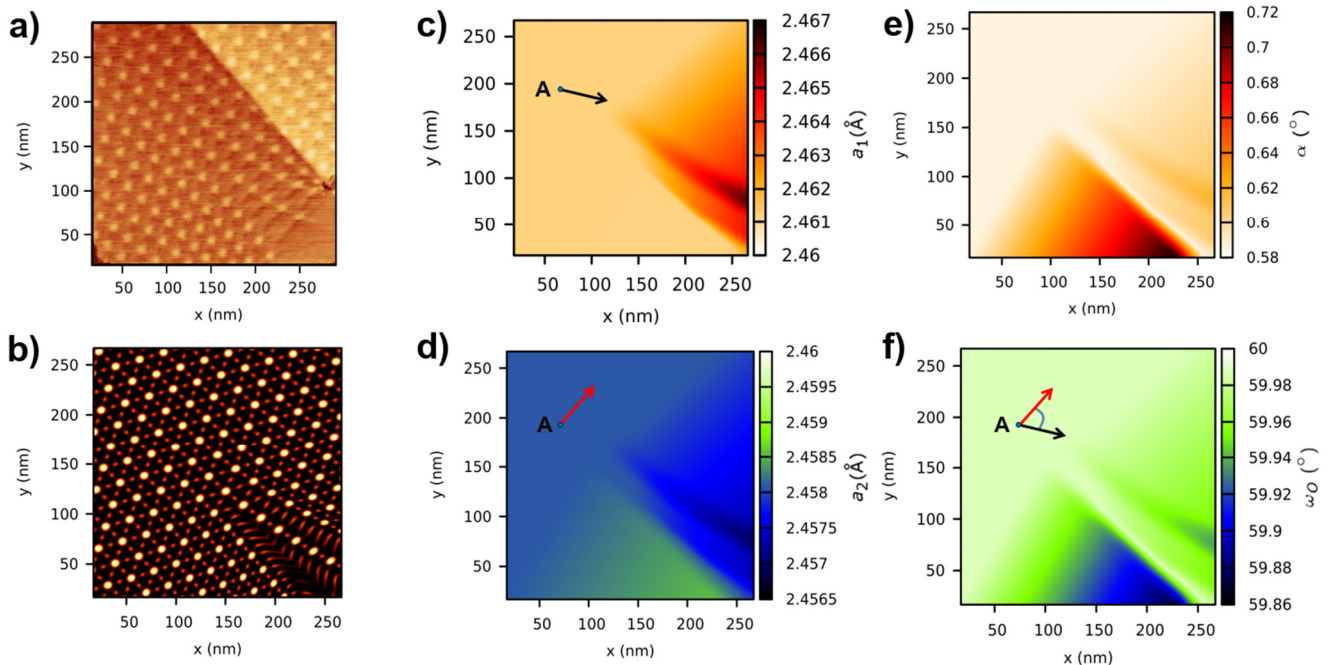


Figure 1: a) STM image of the moiré pattern. b) Simulated moiré pattern. c)-f) Spatial distributions of the following parameters: c) length of a_1 lattice parameter, d) length of a_2 lattice parameter, e) the twist angle α between the graphene and the HOPG, f) the angle between a_1 and a_2 , ω_0 . The directions of a_1 and a_2 are marked in point A by black and red vectors, respectively.

The observed moiré pattern was reproduced by simulation using a rigid lattice Fourier method. The dI/dU spectra obtained from Scanning Tunnelling Spectroscopy (STS) measurements (Fig. 2.a) show a slightly p -doped graphene with the Dirac point at $U_D \cong 50$ mV, as observed from the spectrum measured in a moiré valley (black line). In contrast, the dI/dU measured on moiré hills reveal significantly higher LDOS near the Dirac point.

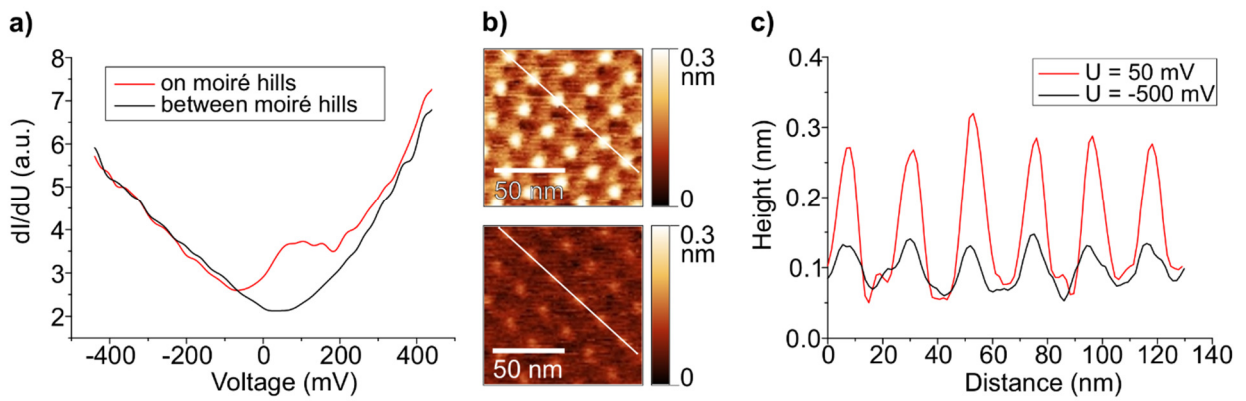


Figure 2: (a) dI/dU spectra measured on moiré hills (red curve) and moiré valleys (black curve). (b) STM images of the same moiré pattern measured with bias voltages of $U = 50$ mV (top panel) and $U = -500$ mV (bottom panel). (c) Height profiles taken at $U = 50$ mV (red) and $U = -500$ mV (black) along the same moiré hills, marked with white lines in b).

In order to understand in more detail the observed LDOS peak, DFT calculations have been carried out for trilayer graphene (TLG) supercells with AAB and ABA stackings (pre-optimized by classical molecular dynamics - CMD simulations), which take into account also the uppermost two layers of the HOPG substrate. Full self-consistency calculations performed on AAB-TLG supercell resulted in a band structure as shown in Fig. 2.12.b. The corresponding DOS calculations (Fig. 3.a, red) show a double-peak feature near the Dirac point. Note that the DOS of ABA-TLG is featureless near the Fermi energy (Fig. 3.a, black). These results capture very well the peak localization in the AA stacked regions and are in good agreement with the measurements, although the peak splitting is not well resolved by room temperature STS. In addition, we performed also a constrained, Harris-functional-like DFT calculation for the full CMD pre-optimized, moiré commensurate bilayer (MCB) supercell, including 33076 atoms at 0.63 twist angle. No peak splitting occurs in the obtained DOS (Fig. 3.a, dotted) due to the mixed effect of differently stacked regions.

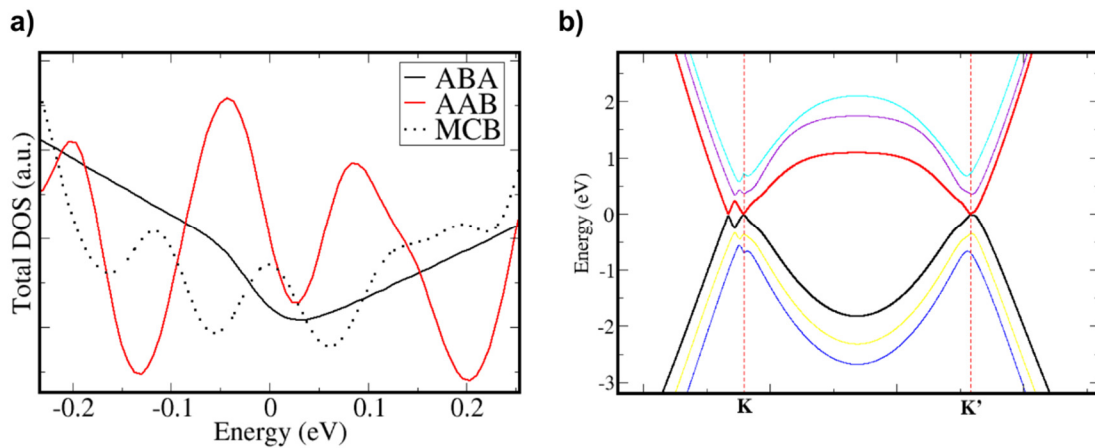


Figure 3: (a) DFT calculations of total DOS for ABA-TLG (black), AAB-TLG (red), and MCB supercell (dotted) at twist angle of 0.63. (b) Calculated band structure for AAB-TLG.

OPTICAL DETECTION OF VAPOUR MIXTURES USING STRUCTURALLY COLOURED BUTTERFLY AND MOTH WINGS

OTKA K111741, OTKA K115724

G. Piszter, K. Kertész, Zs. Bálint, and L. P. Biró

The efficient detection of volatile organic compounds in current applications is highly needed as monitoring air quality in the living environment is becoming increasingly important. The multivariate sensors, based on the photonic nanostructures of butterfly wings, are excellent candidates for this task as their optical readout is relatively easy and their response time is short, while they can operate in ambient air without high operating temperature or vacuum conditions. The sensing process is based on the capillary condensation of the vapours, which results in the conformal change of the chitin-air nanostructures and leads to substance-specific colour change signal.

We investigated the optical responses of structurally coloured wings of five butterfly and moth species when mixtures of volatile vapours were applied to the surrounding atmosphere. Fig. 1 depicts the responses for acetone + ethanol mixtures.

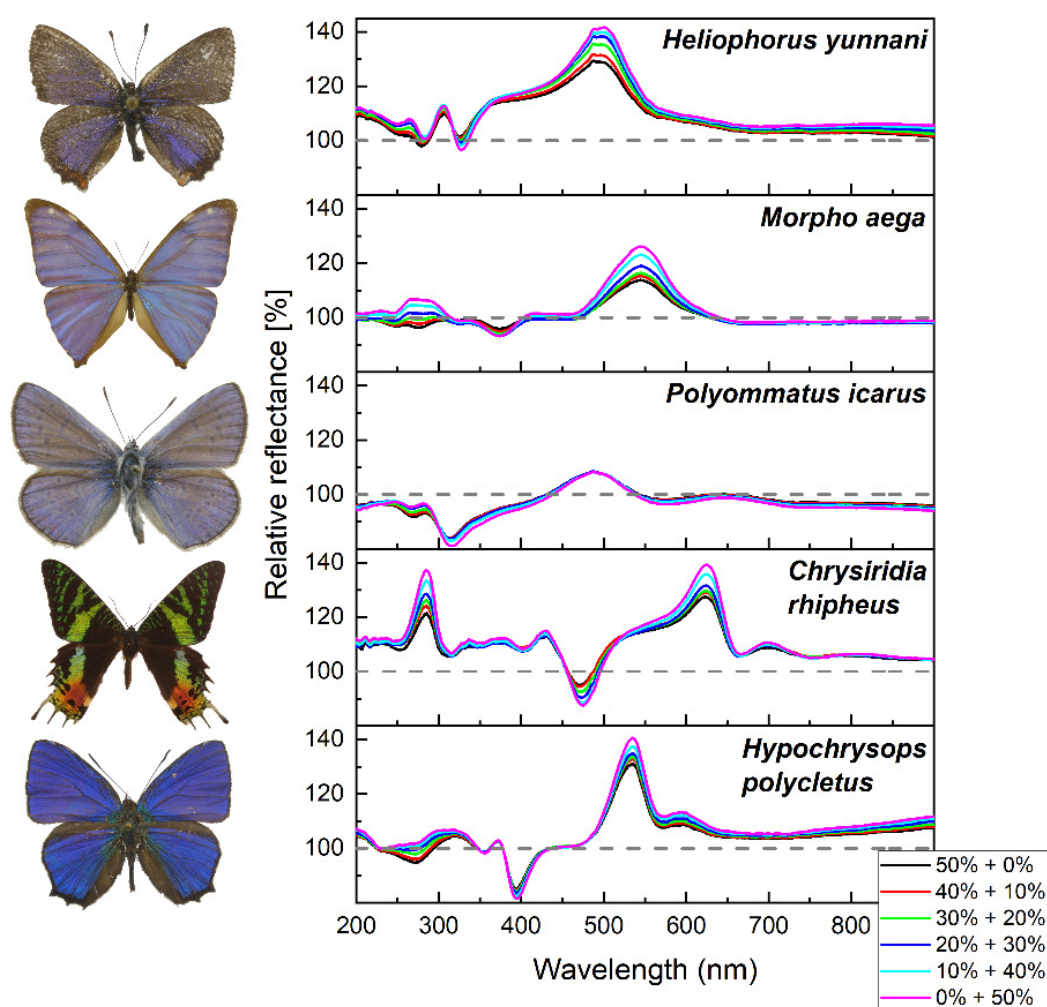


Figure 1: Optical responses of the wings of five species were investigated when mixtures of acetone + ethanol vapour mixtures were applied. All showed similar colour change behaviour: the optical responses of the mixtures fell between the colour change signals of the pure solvents. The broken lines show the initial relative reflectance spectra used as a reference (100%).

The changes in the structural colours caused by the different acetone + ethanol vapour mixtures fell between the optical responses generated by the two pure substances in a consecutive order. Therefore, the optical response from a certain vapour mixture consists of the linear combination of the optical responses caused by the vapour components separately. This shows that the photonic nanostructures occurring in the wing scales are capable of chemically selective sensing of vapour mixtures.

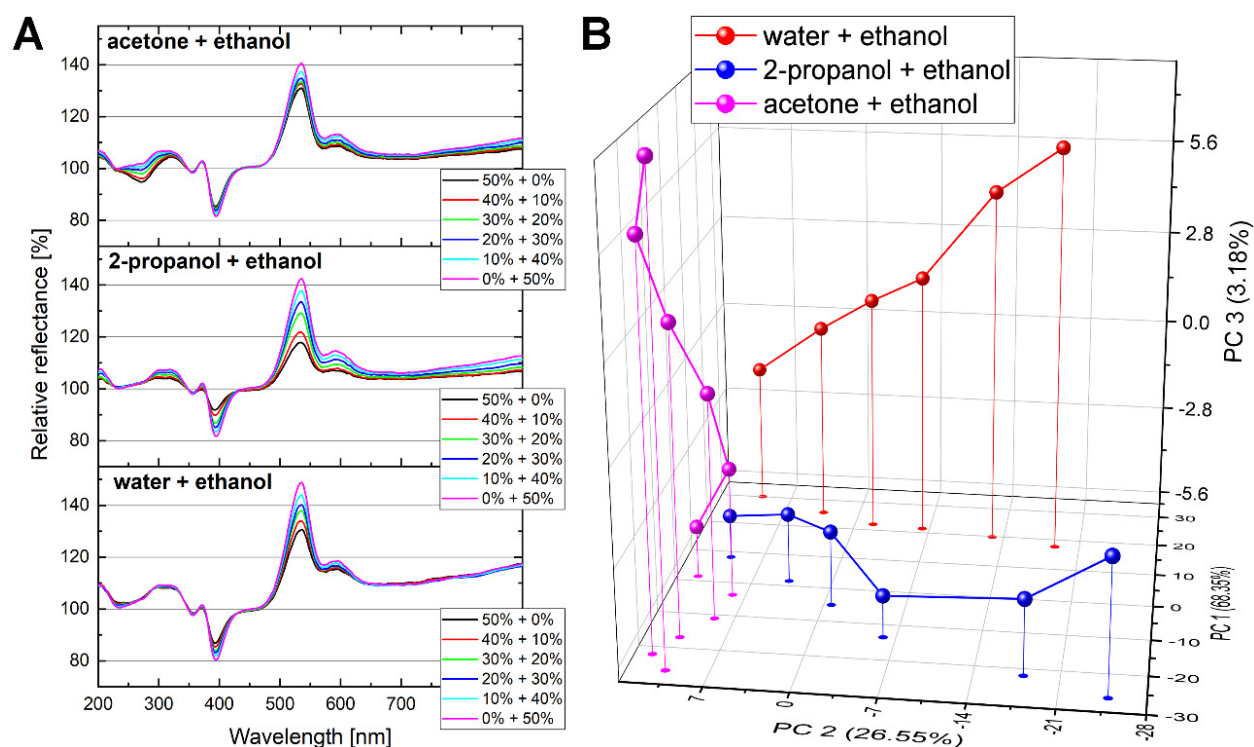


Figure 2: Different vapour mixtures generated different optical responses of the wing of a *H. polyctetus* male specimen. (A) The optical responses (relative reflectances) of the three mixtures are characteristically different from each other. (B) The PCA scores plot shows the characteristic trajectories of the three mixtures. The three points close to each other on the left side are the points of the pure ethanol vapour from which the trajectories spread apart.

To investigate the chemically selective behaviour of the butterfly wings in detail, a *Hypochrysops polyctetus* specimen with bright blue structural colour was used in the vapour sensing experiment and three different vapour mixtures were applied. The measured optical responses, i.e., the colour changes of the wing in the case of acetone + ethanol, 2-propanol + ethanol, and water + ethanol vapour mixtures were recorded, and the results are depicted in Fig. 2.A. All vapour mixtures showed similar behaviour, as described earlier, as the optical responses of the mixtures fell between the pure substances.

To analyse the vapour-specific behaviour, the measured data were evaluated with principal component analysis (PCA). Figure 2.B provides the PC scores plot, which contains the vapour sensing trajectories of the three different vapour mixtures. The three data points on the left that are close to each other, from which the trajectories originate, are the points of the pure ethanol vapour spectrum. Away from this, the curves spread apart, as the compositions of the mixtures shift to their other component. These results demonstrate that butterfly wing-based sensor materials can discriminate between different vapour mixtures very efficiently, as the optical responses of these biological photonic nanostructures are highly substance-specific.

REPRODUCIBLE PHENOTYPE ALTERATION DUE TO PROLONGED COOLING OF THE PUPAE OF *POLYOMMATUS ICARUS* BUTTERFLIES

OTKA K111741, OTKA K115724

G. Piszter, K. Kertész, Z. E. Horváth, Zs. Bálint, and L. P. Biró

The phenotypic changes induced by prolonged cooling (2 – 12 weeks at 5 °C in the dark) of freshly formed *Polyommatus icarus* pupae were investigated. We used more than 200 pupae in our laboratory. Cooling halted the imaginal development of pupae collected shortly after transformation from the larval stage. After cooling, the pupae were allowed to continue their developmental cycle. The wings of the eclosed specimens were investigated by optical microscopy, scanning and cross-sectional transmission electron microscopy, UV-VIS spectroscopy and microspectroscopy. The eclosed adults presented phenotypic alterations that reproduced results that we published previously for smaller groups of individuals remarkably well (see Fig. 1); these changes included i) a linear increase in the magnitude of quantified deviation from normal ventral wing patterns with increasing cooling time; ii) slight alteration of the blue coloration of males; and iii) an increasing number of blue scales on the dorsal wing surface of females with increasing cooling time. Several independent factors, including disordering of regular scale rows in males, the number of blue scales in females, eclosion probability and the probability of defect-free eclosion, showed that the cooling time can be divided into three periods: 0 – 4 weeks, 4 – 8 weeks, and 8 – 12 weeks, each of which is characterized by specific changes. The shift from brown female scales to first blue scales with a female-specific shape and then to blue scales with a male-specific shape with longer cooling times suggests slow decomposition of a substance governing scale formation.

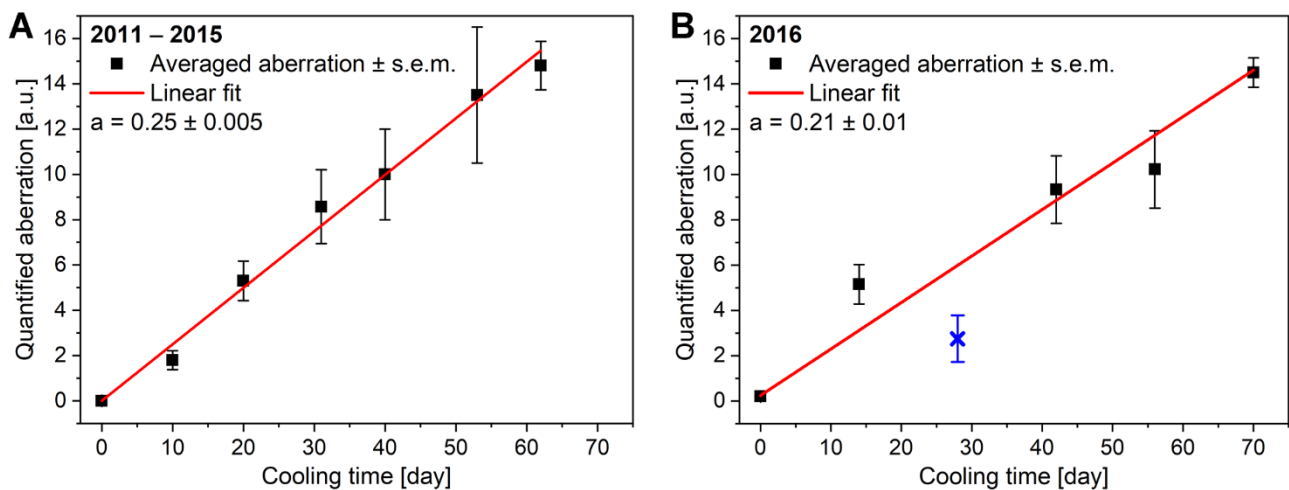


Figure 1: Quantification of the aberration of the pigment-based pattern on the ventral wing surfaces of *P. icarus* butterflies. (A) Previously reported results; (B) results of the set of cooling experiments conducted to check reproducibility. (s.e.m. = standard error of the mean)

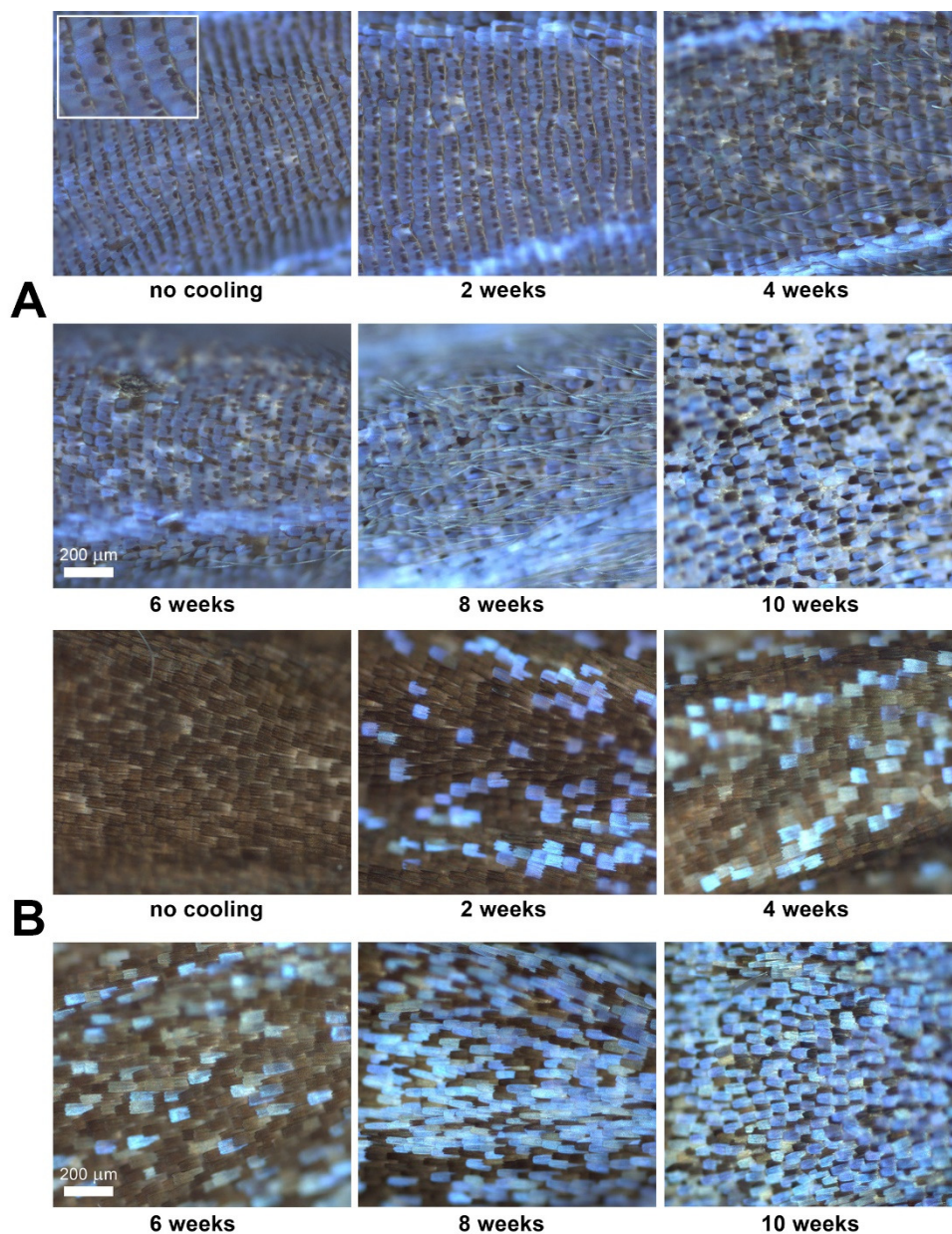


Figure 2: Changes in the dorsal wing scales of *P. icarus* specimens with increasing cooling times, as seen under an optical microscope. Male (A) and female (B) specimens. The inset in the top left corner of (A) shows the androconia separating the regular rows of the cover scales of the males.

The normally brown females developed an increasing number of blue scales as the cooling time was increased (see Fig. 2.) and exhibited greater deviation in the spectral position of the blue reflectance peak associated with blue scales than males. We attribute this difference to the fact that the genes regulating the production of the blue-generating nanoarchitecture of females are not subjected to reproductive selection, in contrast to those of the males, as the production of their blue scales is induced only under special conditions.

COMBINATORIAL INVESTIGATION OF WO_3 - MoO_3 MIXED LAYERS BY SPECTROSCOPIC ELLIPSOMETRY USING DIFFERENT OPTICAL MODELS

M-ERA.NET Transnational Call 2018 VOC-DETECT, OTKA NN131269, OTKA K129009

R. Bogar, Z. Labadi, Z. E. Horvath, Z. Zolnai, M. Fried

Protection against heat waves through the glass windows, the electrochromic film as a smart window is the most useful tool to reduce heat in buildings. This type of glass consists of a layer of electrochromic film bounded by metal oxide layers able to change their transparency under DC bias. Typical materials for this purpose are MoO_3 and WO_3 but relatively little attention is paid for the applicability of their mixed oxides. In our work we investigated mixed oxides deposited by combinatorial reactive sputtering. Metal oxides were deposited onto glass substrates by using Argon-Oxygen plasma for sputtering metallic targets, while combinatorial method meant that substrates were in cyclic movement under two different plasma streams.

W- and Mo-targets were placed separately into the sputtering chamber and 30x30 cm glass substrates were slowly moved under the two separated targets. Two possible arrangements of the targets can be seen in Fig. 1. In the first arrangement, the two targets were placed at 35 cm, in the second arrangement they were placed at 70 cm distance from each other. According to the measurements, in the first arrangement the two „material streams” overlapped around the centre position, while in the second arrangement the two „material streams” were separated.

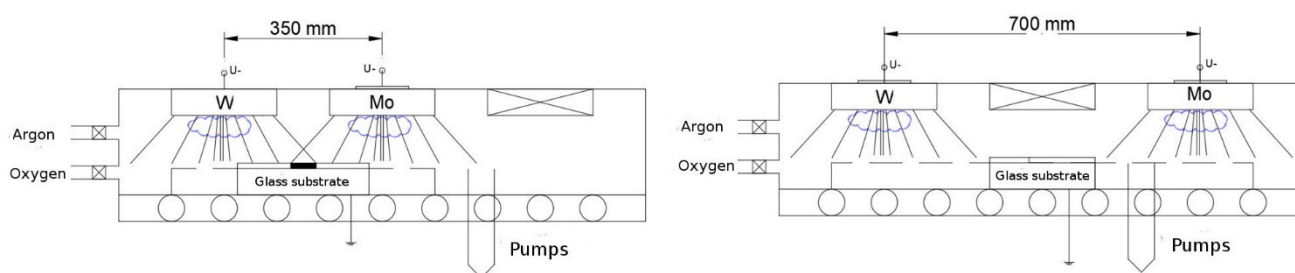


Figure 1: Two arrangements of the targets: a) the two targets in closer position (35 cm from each other) b) the two targets in distant position (70 cm from each other).

Reactive sputtered mixed oxide layers were investigated and mapped by Spectroscopic Ellipsometry (SE). We used different (oscillator- and Effective Medium Approximation, EMA-based) optical models to obtain the thickness and composition map of the sample layer relatively quickly, and in a cheap and contactless way. In a set of experiments, we changed the position of the sputtering targets, the speed and cycle number of the substrate motion. Our aim was to compare the “goodness” of the different optical models depending upon the sample preparation conditions.

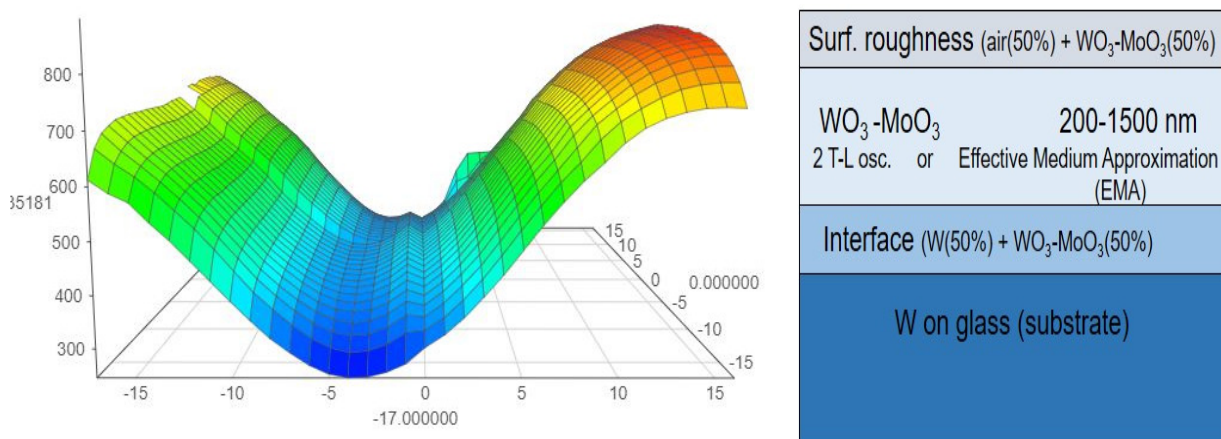


Figure 2: Thickness-map based on Tauc-Lorentz oscillator model

Figure 2 shows a typical SE map of the deposited layer (together with the schematic optical model). We have also used Rutherford Backscattering Spectrometry (RBS) to check the SE results (see Fig. 3). We showed that we were able to produce mixed oxide layers using the combinatorial approach in a magnetron sputtering system. These samples can be mapped (thickness and composition maps, too) by fast and non-destructive manner by Spectroscopic Ellipsometry. We can choose

between appropriate optical models (2-Tauc-Lorentz-oscillator model versus the Bruggeman Effective Medium Approximation, BEMA) depending on the process parameters.

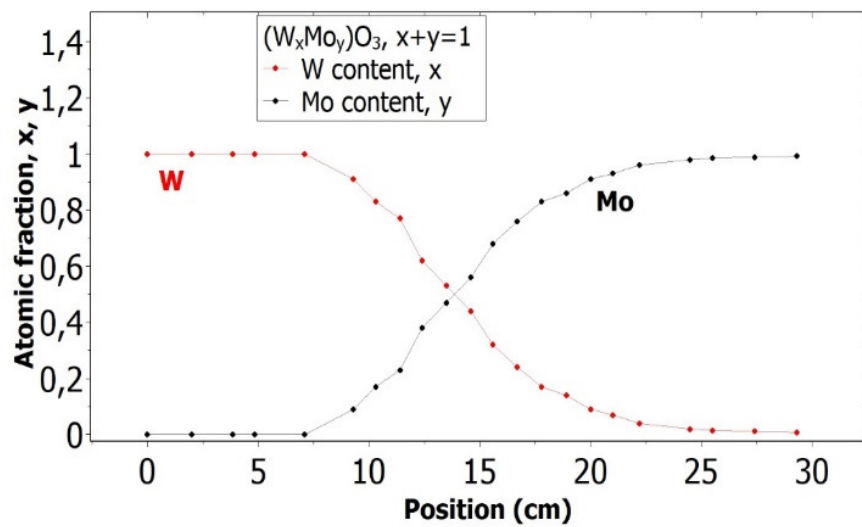


Figure 3: Composition-map along a line by Rutherford Backscattering Spectrometry

Our further aim is to investigate the goodness of $\text{WO}_3\text{-MoO}_3$ mixed layers as electrochromic materials for „smart“ windows (transparency ratio, switching speed, coloration efficiency).

SENSING LAYER FOR NI DETECTION IN WATER CREATED BY IMMOBILIZATION OF BIO-ENGINEERED FLAGELLAR NANOTUBES ON GOLD SURFACES

OTKA NN117847, OTKA NN117849, OTKA K131515,
INFRANANOCHEM - Nr. 19/01.03.2009

Z. Labadi, B. Kalas, A. Saftics, L. Illes, H. Jankovics, É. Bereczk-Tompa,
A. Sebestyén, É. Tóth, B. Kakasi, C. Moldovan, B. Firtat, M. Gartner,
M. Gheorghe, F. Vonderviszt, M. Fried, P. Petrik

Environmental monitoring of Ni is needed around the WHO threshold limit of 0.34 μM . This sensitivity target can usually only be met by time consuming and expensive laboratory measurements. There is a need for cheap field-applicable methods, even if it is only used for signalling the necessity of a more accurate laboratory investigation.

In this work bio-engineered bacterial Ni-binding flagellin variants were fabricated and their applicability in capture layers was tested. Nanotubes of mutant flagellins were built by *in vitro* polymerization (Fig. 1.).

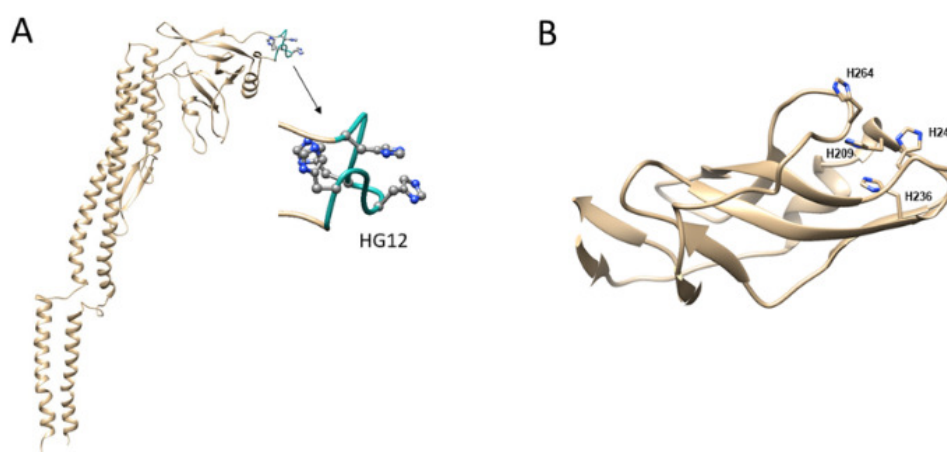


Figure 1: Construction of Ni-binding flagellin variants. (A) The D3 domain of *Salmonella* flagellin was replaced by a Ni-binding motif. (B) The Ca backbone trace of the D3 domain of flagellin is displayed showing residues mutated for histidine.

A large surface density of the nanotubes on the sensor surface was achieved by covalent immobilization chemistry based on an optimized dithiobis(succinidyl propionate) (DSP) crosslinking. Surface coverage was monitored by using *in situ* plasmon enhanced spectroscopic ellipsometry (Fig. 2.).

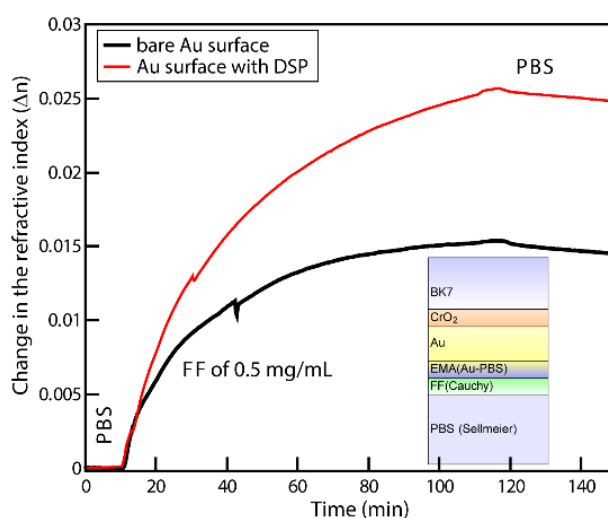


Figure 2: Increase of refractive index (at the wavelength of 633 nm) in the layer modelling the filaments at the interface during adsorption to gold surface with (red line) and without (black line) a DSP layer for covalent bonding. The change of refractive index corresponds to surface densities of 391 ng/cm^2 and 184 ng/cm^2 , for DSP-covered and non-covered surfaces, respectively.

Nickel detecting capability of the filament layers was tested by cyclic voltammetry (CV) using added NiSO_4 in different concentrations. Fig. 3 left shows that a cathodic peak associated with the Ni^{2+} ion reduction appears in the potential range around -250 mV, and the peak intensity monotonously increases with the Ni^{2+} concentration, up to saturation. Regeneration of the samples was also successfully realized (Fig 3 right).

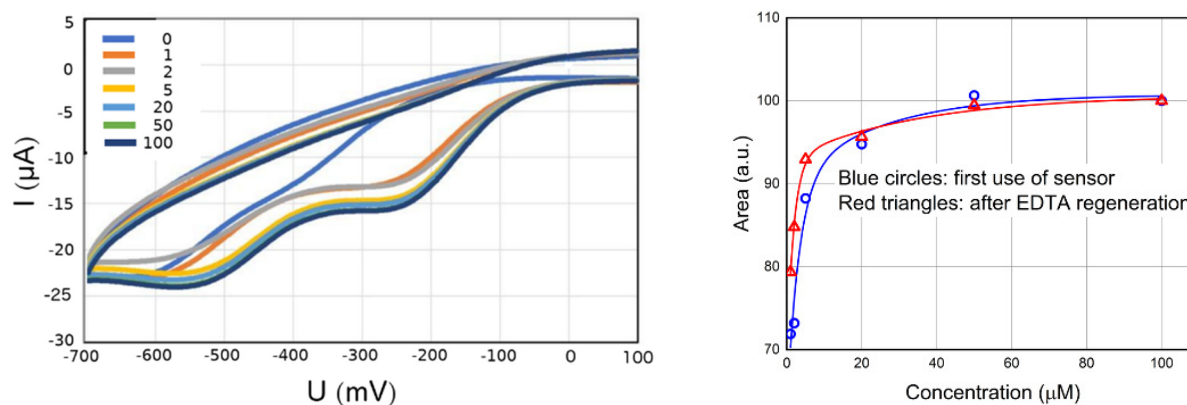


Figure 3: (left) Set of CV curves measured in the presence of $\text{Ni}(\text{II})$ on flagellar nanotubes. (right) Ni peak areas are represented for first use (blue) and for regenerated (red) samples.

Our work demonstrates [1] that mutant flagellar filaments have the potential to form protein-based Ni sensing layers on a Si substrate which can be employed in low-cost portable electrochemical biosensors to fulfil the requirements for sensing Ni in water at concentration as low as the WHO health threshold limit.

Related publication

- [1] Z. Labadi, B. Kalas, A. Saftics, L. Illes, H. Jankovics, É. Bereczk-Tompa, A. Sebestyén, É. Tóth, B. Kakasi, C. Moldovan, B. Firtat, M. Gartner, M. Gheorghe, F. Vonderviszt, M. Fried, P. Petrik: *Sensing layer for Ni detection in water created by immobilization of bio-engineered flagellar nanotubes on gold surfaces*, accepted in ACS Biomaterials Science & Engineering.

OPTICAL PROPERTIES OF HYDROGENATED AMORPHOUS $\text{Si}_{1-x}\text{Ge}_x$ FOR THE ENTIRE RANGE OF COMPOSITIONS

OTKA K131515, OTKA K129009 and M-ERA.NET Transnational Call 2018 VOC-DETECT

B. Kalas, Z. Zolnai, G. Sáfrán, M. Serenyi, E. Agocs, T. Lohner, A. Nemeth, M. Fried, and P. Petrik

The optical parameters of hydrogenated amorphous $a\text{-Si}_{1-x}\text{Ge}_x\text{:H}$ layers were measured with focused beam mapping ellipsometry for photon energies from 0.7 to 6.5 eV. The applied single-sample micro-combinatorial technique enables the preparation of $a\text{-Si}_{1-x}\text{Ge}_x\text{:H}$ with full range composition spread. Linearly variable composition profile was revealed along the 20 mm long gradient part of the sample by Rutherford backscattering spectrometry and elastic recoil detection analysis. The Cody-Lorentz approach was identified as the best model to describe the optical dispersion of the alloy. The effect of incorporated hydrogen on the optical absorption is explained by the lowering of the density of localized states in the mobility gap. It is shown that in the low-dispersion near infrared range the refractive index of the $a\text{-Si}_{1-x}\text{Ge}_x$ alloy can be comprehended as a linear combination of the optical parameters of the components [1].

The micro-combinatorial sample preparation with mapping ellipsometry is not only suitable for the fabrication of samples with controlled lateral distribution of the concentrations, but also opens new prospects in creating databases of compounds for optical and optoelectronic applications.

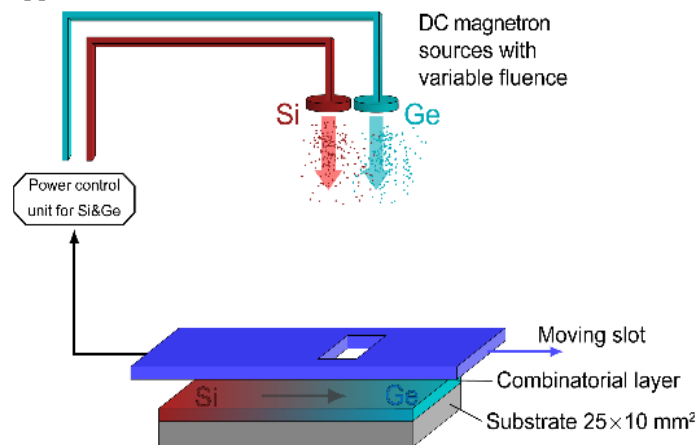


Figure 1: Setup used for the "single-sample concept" combinatorial deposition

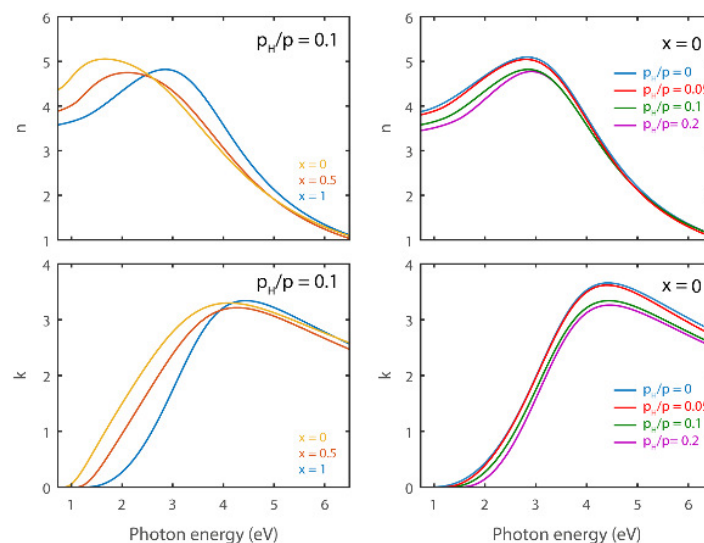


Figure 2: Real and imaginary parts of the complex refractive indices of $a\text{-Si}_{1-x}\text{Ge}_x\text{:H}$ with $p_H/p=0.1$ for different compositions (left-hand side) and for different H contents for $x=0$ given as p_H/p values written next to the corresponding curves (right-hand side).

Related publication

- [1] B. Kalas, Z. Zolnai, G. Safran, M. Serenyi, E. Agocs, T. Lohner, A. Nemeth, M. Fried, P. Petrik: Micro-combinatorial sampling of the optical properties of hydrogenated amorphous $\text{Si}_{1-x}\text{Ge}_x$ for the entire range of compositions towards a database for optoelectronics, under publication in Scientific Reports.

DETERMINATION OF COMPLEX DIELECTRIC FUNCTION OF ION-IMPLANTED AMORPHOUS GERMANIUM BY SPECTROSCOPIC ELLIPSOMETRY

OTKA K131515, OTKA K129009

T. Lohner, E. Szilágyi, Zs. Zolnai, A. Németh, Zs. Fogarassy, L. Illés, E. Kótai, P. Petrik, M. Fried

Accurate reference dielectric functions play important role in the research and development of optical materials. Libraries of such data are required in a broad range of applications from integrated optics to photovoltaics. Amorphous semiconductors are gaining increasing interest in optoelectronics and many other applications. Measuring with a spectroscopic ellipsometer (SE) in the wavelength range from 210 to 1690 nm we determined the complex dielectric function of fully amorphized Ge (a-Ge) layer produced by a two-step implantation (120 and 300 keV) of Al ions into single-crystalline Ge. The reason for selecting a relatively light mass projectile (Al) was to avoid void formation in case of implantation of heavy mass ions. The evaluation of ellipsometric spectra at multiple angles of incidence was performed using a two-layer optical model: an a-Ge layer with a GeO₂ surface layer. The complex dielectric function of a-Ge was modelled using the Tauc-Lorentz or the Cody-Lorentz dispersion relations (Fig. 1.). The thickness of the a-Ge layer was determined by Rutherford backscattering spectrometry (RBS) in combination with channelling and by cross-sectional transmission electron microscopy (XTEM). The thickness values evaluated from SE, RBS and XTEM measurements agree within the experimental limits of accuracy. The complementary investigations revealed a high-quality amorphous layer, suitable for providing optical reference data [Ref.].

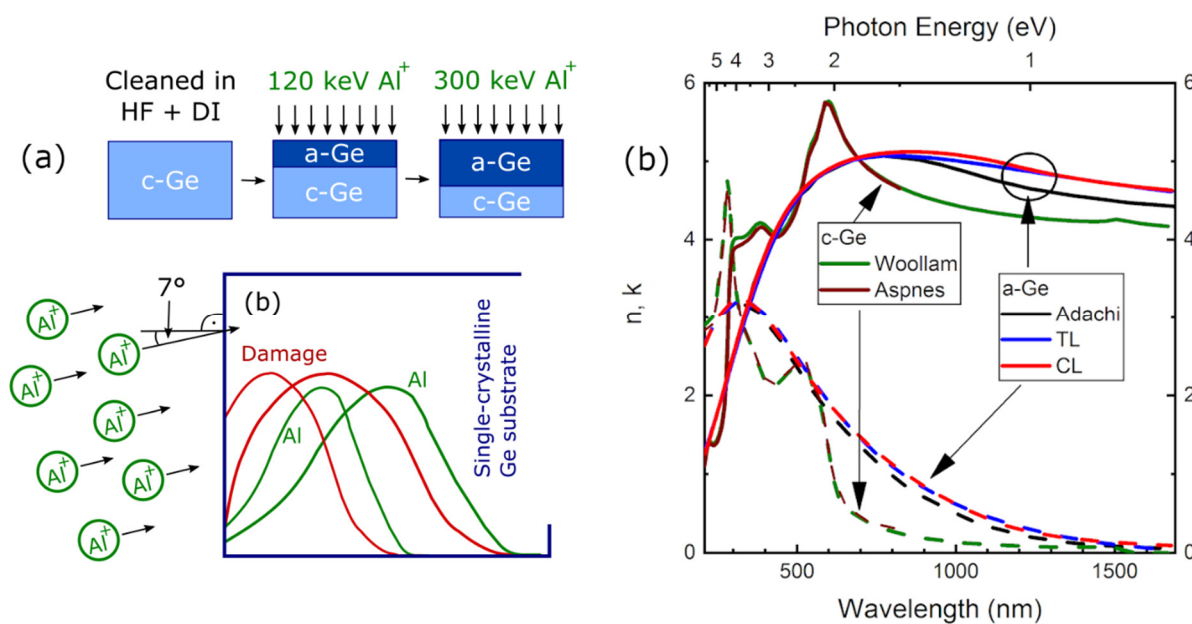


Figure 1: (a) Dual-energy ion implantation to create amorphous Ge. (b) Refractive index (n , solid lines) and extinction coefficient (k , dashed lines) spectra measured by ellipsometry using the Cody-Lorentz (CL) and the Tauc-Lorentz (TL) dispersions. For comparison, the data of c-Ge and evaporated a-Ge (Adachi) are also presented.

Related publication

- [1] T. Lohner, E. Szilágyi, Z. Zolnai, A. Németh, Z. Fogarassy, L. Illés, E. Kótai, P. Petrik, M. Fried: *Determination of the Complex Dielectric Function of Ion-Implanted Amorphous Germanium by Spectroscopic Ellipsometry*, *Coatings*. **10**, 480 (2020) <https://doi.org/10.3390/coatings10050480>

OPTICAL SPECTROSCOPY STUDIES ON NANOPARTICLES

OTKA FK128327, OTKA KH129578, 2018-2.1.13-TÉT-FR-2018-00002

D.P. Szekrényes, D. Zámbo, A. Deák

Our earlier works on gold nanoparticle heterodimers have shown that it is possible to site-selectively surface modify gold nanorods with specific molecules that in turn enables the region-selective assembly of nanosphere/nanorod heterodimers [1,2]. We also demonstrated that the assembly process of such patchy colloids can be captured in-situ in the aqueous environment even at the single particle level by relying on the scattering spectrum measurement of individual heterodimers [3].

In our recent work we push these studies one step further by systematically investigating the polarization resolved scattering spectra of sphere/rod heterodimers with the aim to conclude on the relative spatial arrangement on the particles more precisely [Ref.4.]. For the measurements we use a custom developed dark-field microscopy-based setup, which allows the measurement of the scattering spectrum of individual nanoparticles via a high sensitivity imaging spectrometer. As we use gold nanoparticles for the experiments, their localised plasmon resonance determined scattering spectrum will drastically change upon binding of a second particle due to plasmon coupling. The scattering spectrum of such a particle dimer contains rich details when the dimer is formed by a sphere and a rod. One prominent feature is the Fano resonance arising due to the destructive interference of the spatially and energetically overlapping rod and sphere plasmon modes. Polarization resolved scattering measurements performed on individual heterodimers reveals, however, that apparently identical scattering spectra of sphere/rod heterodimers belonging to different relative particle arrangements (namely top or bottom arranged in term of the spheres' position with respect to the nanorod), show markedly different behaviour as an analyser is placed at different azimuthal angles in the beam path (Fig.1.).

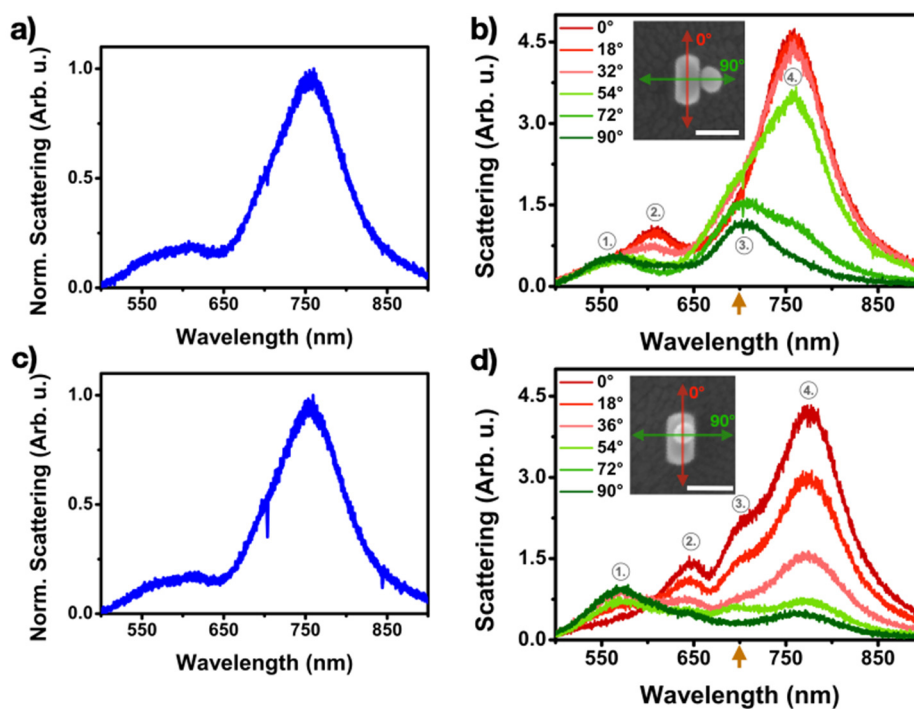


Figure 1: White light scattering spectra obtained for sphere/rod heterodimers featuring different nanosphere arrangements (side: a, top: c). The scattering spectrum of the same heterodimers obtained using a linear analyser at different angles with respect to the rod longitudinal axis (b,d).

It has to be stressed that in the polarisation resolved spectra there is a peak (marked '3' in Fig. 1.b, 1.d) that behaves markedly differently for the two arrangements. This peak – supported by optical simulations on the structures – can be attributed to the coupled sphere dipole/rod transversal mode. The different intensity modulation of this mode with the analyser angle can be expected as the coupling axis is different for the two arrangements. For the side arranged case the peak is fairly pronounced at 90°, as in this case the coupling axis is parallel to the analyser direction and the coupled dipole radiates effectively towards the collecting optical system. For the top arranged case, however, its intensity remains fairly low and constant at all angles, as the coupling axis is vertical and radiation from this coupled mode propagates largely towards the sides. This implies that the polarisation dependence of this coupled mode can be used to conclude on the relative arrangement of the particles in the direction perpendicular to the substrate (side or top arranged). We successfully exploited this strategy to investigate the formation of individual heterodimers in aqueous environment and their eventual rearrangement upon drying the very same structure. We provided evidence for the structural rearrangement of such a rod/sphere heterodimer based on correlative spectroscopic / scanning electron microscopic investigations [4].

Another direction of the research is centred on the controlled preparation of nanosphere dimers at solid/liquid interface with the specific aim to investigate their arrangement and surface separation in-situ in the aqueous environment by optical microspectroscopic measurements. As the coupled spectrum of such dimers is well known change sensitively with the surface-to-surface separation, it could provide a platform to study in the (attractive) interaction between nanoparticles featuring dissimilar surface molecular coatings. We prepared colloidal systems from gold nanoparticles that are individually stable, but have high affinity towards each other owing to their opposite surface charge. One of these attractive particle types are PEGylated to provide an additional steric repulsion. Polyethylene Glycol (PEG) is used as a benchmark molecule in bio-related fields as it can significantly improve the stealth capability of nanosized materials introduced into the body. The goal will be to correlate the effective particle separations with the relevant colloidal interactions, including the steric repulsion due to the presence of the PEG chains. At the preliminary stage of this work the model systems have been prepared and their assembly potential verified based on bulk spectroscopy measurement (Fig. 2). In the next phase of the work these systems will be used to carry out the single particle (dimer) spectroscopy measurements.

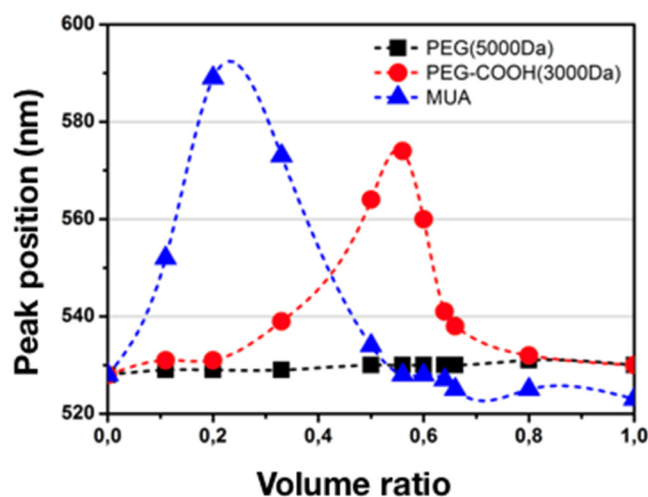


Figure 2: Spectral peak position changes upon mixing positively charged ((11-Mercaptoundecyl)-N,N,N-trimethyl-ammonium bromide coated) gold nanoparticles with negatively charged ones (carboxy-PEG; 3000 Da and 11-mercaptoundecanoic acid coated). As a reference only PEG covered particles (5000 Da) are used where no changes in the optical spectrum are observed, underlining the role of the electric double layer attraction in the assembly process.

In the framework of a bilateral project we also work with a French partner, Doru Constantin from the Laboratoire de Physique des Solides (Orsay) on the detailed small angle x-ray scattering (SAXS) investigation of our PEGylated gold nanoparticles, that we used earlier successfully demonstrate the ionic strength and temperature triggered clustering of the particles [5]. We successfully repeated our earlier experiments and amended the characterization with the SAXS data, from which the equilibrium distance between the particles within the clusters was obtained. We compare this to theoretical calculations on the soft-sphere type interaction between the nanoparticles. The results are planned to be published next year.

Related publications

- [1] D. P. Szekrenyes, S. Pothorszky, D. Zambo, Z. Osváth, A. Deák: *Investigation of Patchiness on Tip-Selectively Surface Modified Gold Nanorods*, J. Phys. Chem. C **122**:(3), 1706–1710 (2018) <https://doi.org/10.1021/acs.jpcc.7b11211>.
- [2] Sz. Pothorszky, D. Zámbo, T. Deák, A. Deák: *Assembling Patchy Nanorods with Spheres: Limitations Imposed by Colloidal Interactions*, Nanoscale **8**:(6), 3523–3529 (2016) <https://doi.org/10.1039/C5NR08014B>
- [3] S. Pothorszky, D. Zámbo, D. Szekrényes, Z. Hajnal, A. Deák: *Detecting Patchy Nanoparticle Assembly at the Single-Particle Level*. Nanoscale, **9**:(29), 10344–10349 (2017) <https://doi.org/10.1039/C7NR02623D>
- [4] D. P. Szekrényes, S. Pothorszky, D. Zámbo, A. Deák: *Detecting Spatial Rearrangement of Individual Gold Nanoparticle Heterodimers*, Phys. Chem. Chem. Phys. **21**:(19), 10146–10151 (2019) <https://doi.org/10.1039/C9CP01541H>
- [5] D. Zámbo, G. Z. Radnóczy, A. Deák: *Preparation of Compact Nanoparticle Clusters from Polyethylene Glycol-Coated Gold Nanoparticles by Fine-Tuning Colloidal Interactions*, Langmuir **31**:(9), 2662–2668 (2015) <https://doi.org/10.1021/la504600j>

ROBUST CONTACT ANGLE DETERMINATION FOR SESSILE DROPS WITHOUT APEX

OTKA FK128901

E. Albert, B. Tegze, Z. Hajnal, D. Zámbo, D. P. Szekrényes, A. Deák, Z. Hórvölgyi, N. Nagy

The polynomial fitting to the profile of a sessile drop is widely used in those cases when the drop apex is not visible. The major disadvantage of this approach is that the resulted contact angle is highly sensitive to the applied polynomial order and the number of pixels to which the polynomial was fitted. In order to overcome these uncertainties, an easily implementable method was introduced.

Circumcircles are constructed independently for the left and right unperturbed parts of the profile. Polynomial is fitted to the vertical difference between the circumcircle and the profile, see Fig. 1.

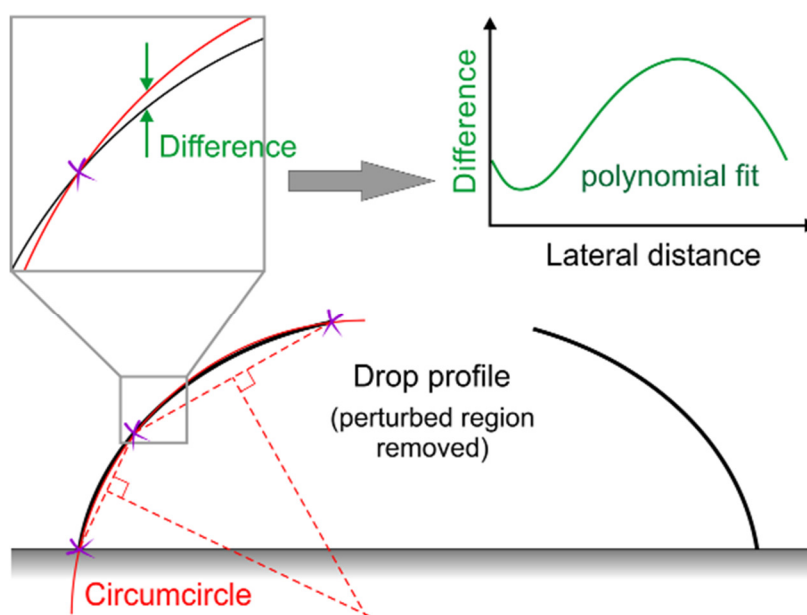


Figure 1: Schematics of the circumcircle and difference fitting method are shown. That region of the profile is intentionally omitted, which is affected by the needle. Three points are selected from each resulted arc: the endpoints and the point at the half of maximum height. Circumscribed circles that pass through these points are constructed independently and polynomial is fitted to the difference between the circle and the profile as a function of the lateral distance from the contact point.

The contact angle is calculated from the sum of the slope of the circumscribed circle and the polynomial curve at the three-phase contact point for each side. The derivative of the circumcircle at the contact point can be calculated analytically. The slope of the polynomial curve at the contact point does not change significantly with the contact angle or with the drop volume.

The method was validated in the contact angle range of 20° – 150° with two different image resolutions (1280×1024 and 750×600 pixels) by comparing the results to the values calculated by the Young-Laplace fit (Fig. 2). The accuracy of the method was found to be $\leq 0.6^\circ$ and it does not show significant dependence on the actual contact angle and on the resolution of the captured image. In comparison, the accuracy of the most sophisticated polynomial method is $\geq 1^\circ$.

Needle-in-drop measurements were carried out on a thermal SiO_2 surface for demonstration the capability of the present method (Fig. 3). Two syringes were applied with different needle diameter and the determined contact angles were in good agreement considering their standard deviation. The results obtained using the small-diameter needle were a bit closer to the values resulted from the Young-Laplace fit [1].

The method improves the accuracy of the evaluation of the needle-in-drop measurements in sessile drop, captive bubble, electrowetting, and electrodedewetting experiments and it might be useful also for tilted plate measurements as well.

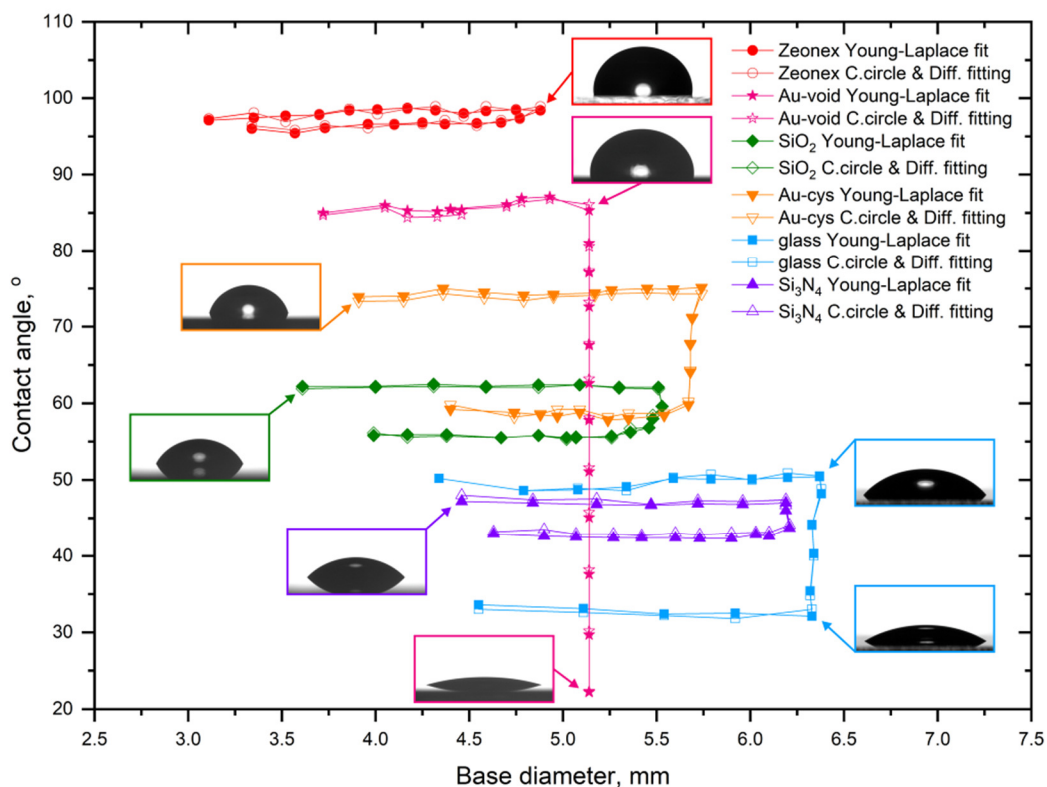


Figure 2: Contact angles as a function of the drop's base diameter. The values determined by the Young-Laplace fit are shown by filled markers. The hollow markers designate the values determined by the proposed circumcircle and differential fitting. The insets show droplet images corresponding to the marked points. The contact line pinning on the gold nanovoid surface is obvious.

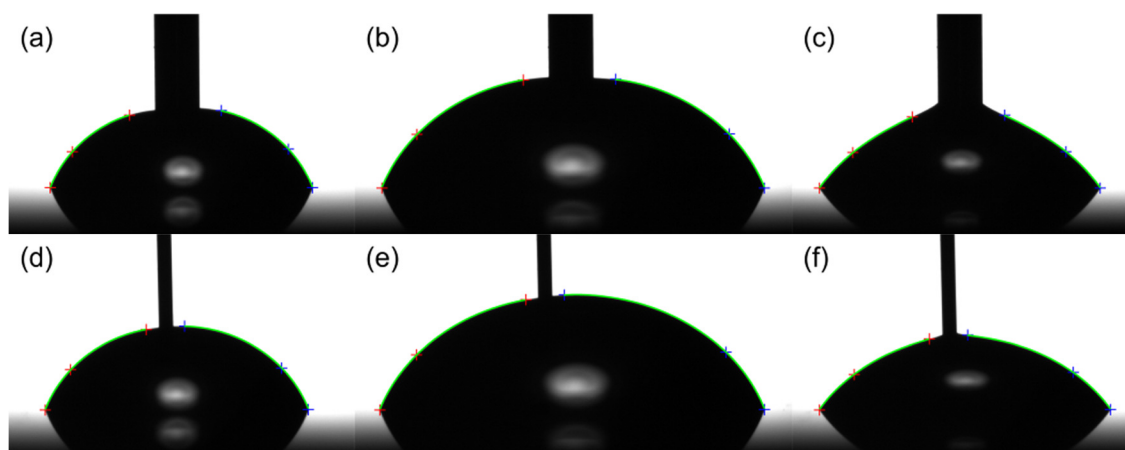


Figure 3: Evaluated images of water droplets with the volume of $10 \mu\text{L}$ (a,c,d,f) and $30 \mu\text{L}$ (b,e) captured in the advancing (a,b,d,e) and the receding phase (c,f). The measurements were carried out on the SiO_2 sample using two different needles with the diameter of 0.718 mm (a-c) and 0.235 mm (d-f). The red and blue crosses designate the points for the circumcircle construction, the green curves show the resulted profile after difference fitting.

Related publication

- [1] E. Albert, B. Tegze, Z. Hajnal, D. Zámbo, D. P. Szekrényes, A. Deák, Z. Hórvölgyi, N. Nagy: *Robust Contact Angle Determination for Needle-in-Drop Type Measurements*, ACS Omega **4**:(19), 18465-18471 (2019)

CONTACT ANGLE DETERMINATION ON SUPER HYDROPHILIC SURFACES BY USING CAPILLARY BRIDGES

OTKA FK 128901

N. Nagy

Measurement of low contact angles is challenging. The developed indirect Capillary Bridge Probe method combines the accuracy of the Wilhelmy method and the general usability of the sessile drop method without their limitations.

The method is based on the use of a liquid bridge as a probe: the capillary bridge of the test liquid is stretched between the rim of the base of a cylinder and the investigated surface under equilibrium conditions. The advancing contact angle on the sample can be measured during the stepwise decrease of the bridge length. The receding contact angle is determined during the retraction of the cylinder. The contact angle is calculated from Delaunay's analytical solution, while the necessary parameters are obtained from the measured capillary force and from the automated analysis of the captured image of the liquid bridge. The bridge is formed from a pendant drop. This unique feature ensures that the advancing contact line finds dry (not prewetted) surface.

A new effect was observed during the measurements on freshly acid-cleaned glass surfaces, *i.e.* in complete wetting situations. The receding contact line starts to advance again during the increase of the bridge length, see Figure 1.

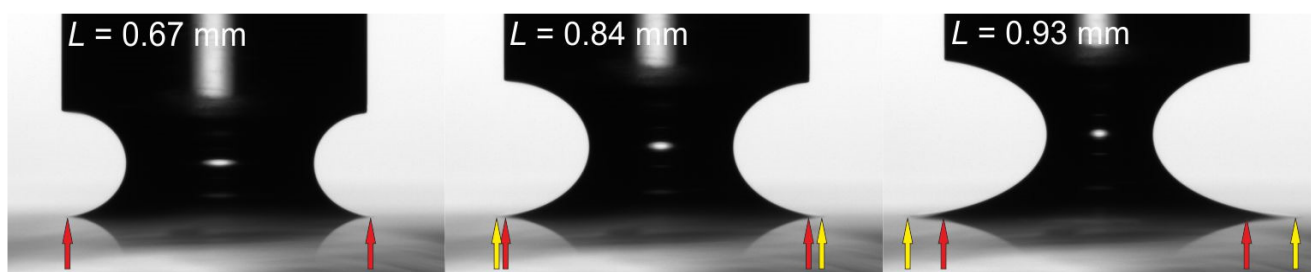


Figure 1: Images of a water capillary bridge taken during the retraction of the cylinder. The receding contact line starts to advance again after a given bridge length (L). The capillary bridge was formed on a glass slide treated freshly in sulphuric acid. Note that images show equilibrium states, not snapshots of a dynamic process.

The measured capillary force does not exhibit hysteresis. The contact radius started to increase in the retraction phase, around the bridge length corresponding to bridge formation (Fig. 2.a). It can be observed in Fig. 2.b that the advancing and receding contact angles are equal within their standard deviation: $4.7^\circ \pm 0.3^\circ$ and $4.5^\circ \pm 0.3^\circ$, respectively. The measured contact angle in the readvancing phase, *i.e.* the readvancing contact angle is much lower, its value is $1.0^\circ \pm 0.1^\circ$. When the receding contact line starts to advance again, it finds prewetted surface, therefore the resulted contact angle is much smaller.

As a demonstration of the capability of capillary bridge probe method, lightly corroded glass slides were investigated: how does the water contact angle change as a function of the exposure time to air. Microscope glass slides were cleaned and soaked in 3:1 Piranha-solution. The glass slides were rinsed thoroughly in hot ultrapure water. The measurement was started directly after the cleaning process on a glass slide, while other samples were soaked for four days at room temperature. Before the samples were inserted into the chamber they were dried thoroughly under filtered nitrogen flow. The samples were measured periodically in different positions, and they were left in the humid atmosphere (94%) of the sample chamber between the measurements.

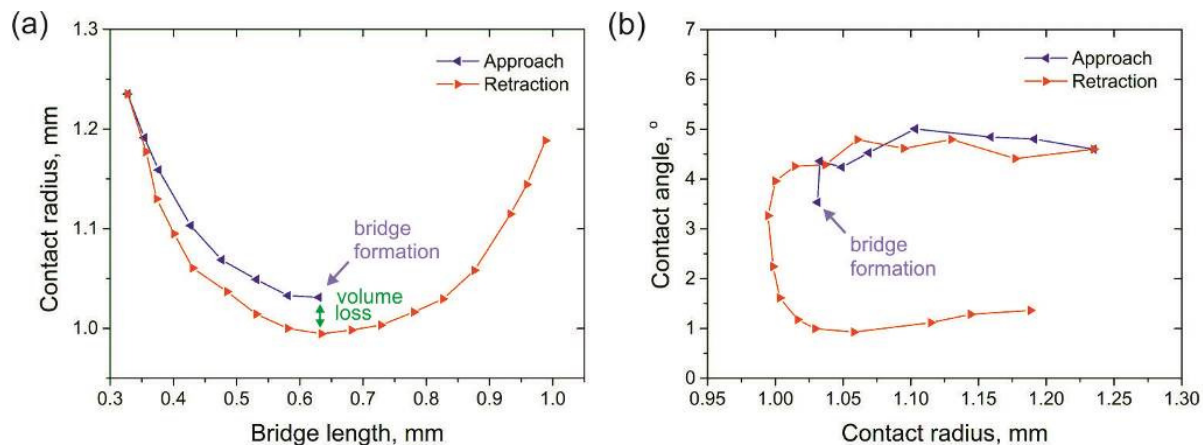


Figure 2: (a) Contact radius as a function of the bridge length measured on a glass surface treated in concentrated sulfuric acid. The contact radius increases after a given point during the increase of the bridge length. The small difference between the approaching and retraction phase refers to small volume loss. (b) Contact angle on the glass surface versus the contact radius. Advancing and receding contact angles are equal, while the readvancing contact angle is lower, because the readvancing contact line finds prewetted surface. The volume of the liquid bridge was $1.17 \mu\text{L}$.

The advancing and receding contact angles were determined to be equal ($3.6^\circ \pm 0.1^\circ$ and $3.6^\circ \pm 0.4^\circ$, respectively) by the first measurement. Their values remain equal for ca. 150 min, and finally significant hysteresis can be observed, while the readvancing phase disappears. The increased standard deviations of the last measurement can be connected to the increasing amount of surface inhomogeneity, while the surface hydroxyl group density decreases. On the contrary, the advancing, receding, and readvancing contact angles on the soaked sample remain almost unchanged, although the increase of the amount of surface contamination can be similar to the previous sample. The advancing and receding contact angles were measured to be $3.8^\circ \pm 0.1^\circ$ and $3.6^\circ \pm 0.2^\circ$ in the first position. A slight increase of ca. 1° can be observed for both after 260 min [1].

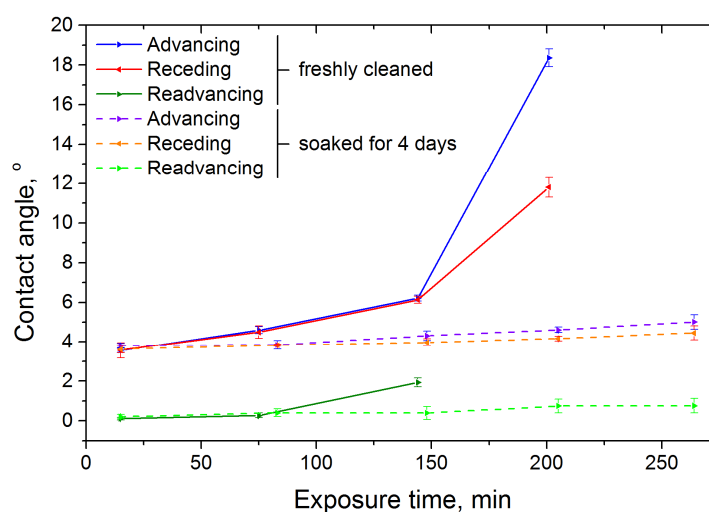


Figure 3: Advancing, receding, and readvancing contact angles on glass slides as a function of exposure time to humid air (94%) of the sample chamber. The capillary bridge probe measurements were performed directly after the cleaning process (continuous lines), and after soaking the sample in ultrapure water for four days (dashed lines). The super-hydrophilic character and the readvancing phase of the directly measured surface disappear, while the alteration zone formed by corrosion preserves the super-hydrophilicity

Related publication

- [1] N. Nagy: Contact Angle Determination on Hydrophilic and Superhydrophilic Surfaces by Using r - θ -Type Capillary Bridges, *Langmuir*, **35**:(15) 5202-5212 (2019)

MAKYOH TOPOGRAPHY

F. Riesz

Makyoh topography is an optical tool for the qualitative flatness testing of specular surfaces, based on the defocused detection of a collimated light beam reflected from the tested surface. By inserting a square grid into the path of the illuminated beam, the height map can be calculated by integrating the gradients obtained from the distortion of the grid's reflected image (quantitative extension).

In the past year, activities were concentrated both on methodology and applications as follows.

The effect of the global sample curvature on the qualitative-mode Makyoh imaging was analysed based on a geometrical optical model. It was shown that the global curvature can be taken into account by establishing an equivalent screen-to-sample distance formula containing the global curvature radius. The different regimes of the imaging were analysed in detail [Ref.].

The swirl defects in *p*-type Si wafers were studied (see Fig. 1). White-light interference microscopy confirmed the existence of the circular-structure relief pattern of the wafers. The geometrical optical origin of the swirl-like pattern in the Makyoh image was proven. In addition, a visual swirl pattern in the rough backside was observed in certain wafers, not always correlated with the front swirl pattern.

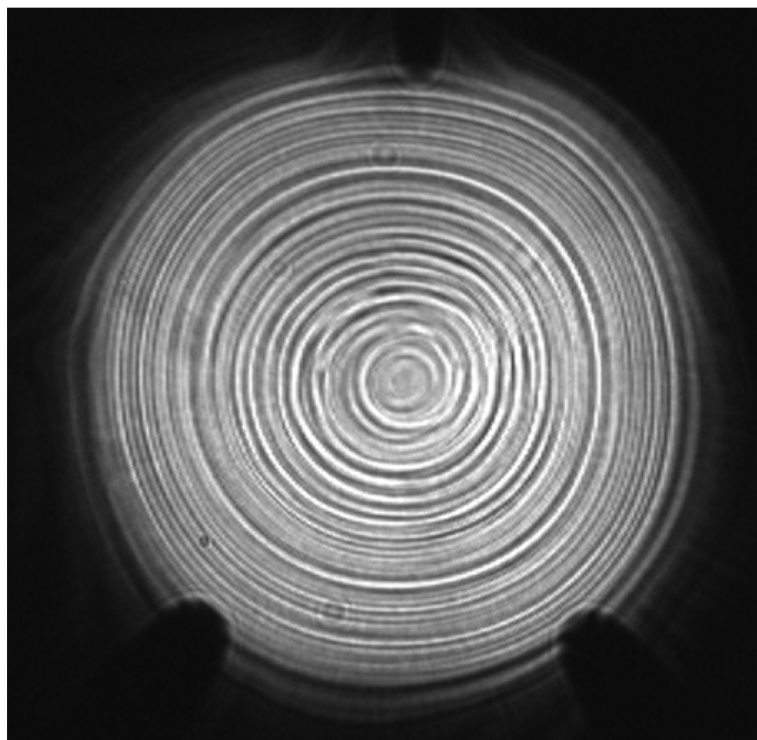


Figure1: Typical Makyoh-topography image of a swirl defect in a *p*-type Si wafer

Related publication

- [1] F. Riesz: *The effects of the global surface curvature on Makyoh-topography imaging*, Photonics Letters of Poland, **11**:(1) 4-6 (2019)

OPTIMIZATION OF CO-SPUTTERED $\text{Cr}_x\text{Al}_{1-x}\text{N}$ THIN FILMS FOR PIEZOELECTRIC MEMS DEVICES

NVKP_16-1-2016-0018 "KoFAH"

S. Soleimani, Z. E. Horváth, Zs. Zolnai, Zs. Czigány, and J. Volk

CrAlN alloys can play an important role in the improvement of next generation piezoelectric MEMS devices. However, enhanced piezoelectric constants require high degree of uniaxial orientation in the polycrystalline thin film. In this work $\text{Cr}_x\text{Al}_{1-x}\text{N}$ thin films of varying compositions were deposited at different substrate temperatures by reactive DC co-sputtering technique and compared with respect to their microstructure and optical properties. The relationship between the atomic composition of the layers and the plasma powers over the Al and Cr targets during co-sputtering was revealed accurately by Rutherford Backscattering Spectrometry (RBS). As it was revealed by X-ray and selective area electron diffraction methods, thin films in the range of $x=0-0.23$ show hexagonal wurzite-type phase, which changes to cubic rock-salt-type structure between $0.23 < x < 0.31$. At lower Cr cation concentration, like $x=0.12$ the wurzite type polycrystalline film indicates uniaxial texture, whereas it is almost randomly oriented at $x=0.23$. Among the compared compositions $\text{Cr}_{0.12}\text{Al}_{0.88}\text{N}$ showed the strongest c-axis orientation, whereas the optimal substrate temperature was found to be $T=350^\circ\text{C}$. While the refractive index measured by ellipsometry monotonously increases increasing Cr from 2.07 to 2.64 with cation concentration in the range of $x=0-0.31$, the optical band gap shrinks from 2.65 to 2.23 eV. These optical data can serve as reference in future contactless wafer-scale optical monitoring process.

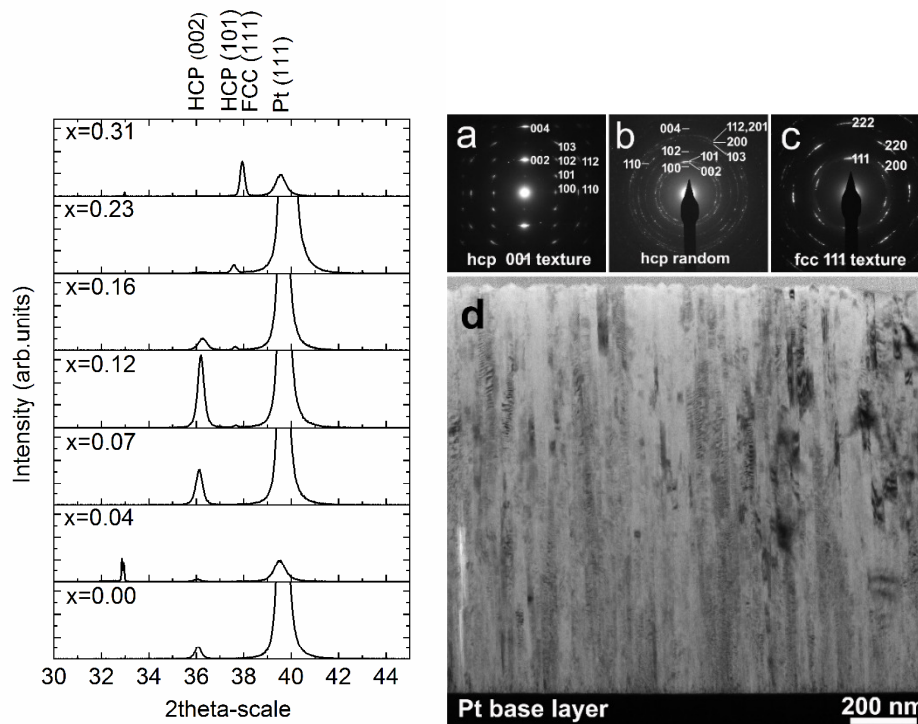


Figure 1: XRD spectra of $\text{Cr}_x\text{Al}_{1-x}\text{N}$ films ($x = 0.04, 0.07, 0.12, 0.16, 0.23$, and 0.31) (left); Selected area electron diffraction (SAED) pattern of $\text{Cr}_x\text{Al}_{1-x}\text{N}$ films at $x=0.12$ (a) $x=0.23$ (b), and $x=0.31$ (c) cation ratios showing a changing crystal structure (textured hcp, random hcp, and textured fcc, respectively). d) TEM overview image of $\text{Cr}_{0.12}\text{Al}_{0.88}\text{N}$ cross section

ENERGY HARVESTER POWERED VIBRATION ANALYSER

NVKP_16-1-2016-0018 "KoFAH"

M. Szappanos, J. Volk

We continued to work on our vibration analyser – or *VibrAn* for short – and improved 1) the measurement range, 2) the energy management system, 3) the wireless transmitter module and 4) introduced the device to the internet, effectively making it an Internet of Things (IoT) application with a well-defined infrastructure. This device (or rather system) can be used to monitor the vibrations, while the embedded Fourier-transform algorithms provide real-time analyzation features. The device is powered by energy harvesting (piezoelectric, thermoelectric, photovoltaic).

1) The device by now is capable to measure vibrations ranging up to 1.6 kHz with an average precision of 1 mg. This was achieved with a dual accelerometer topology: one of the accelerometers has ultra-low power consumption and can measure up to 200 Hz, while another accelerometer may provide frequency range up to 1.6 kHz albeit with higher energy consumption.

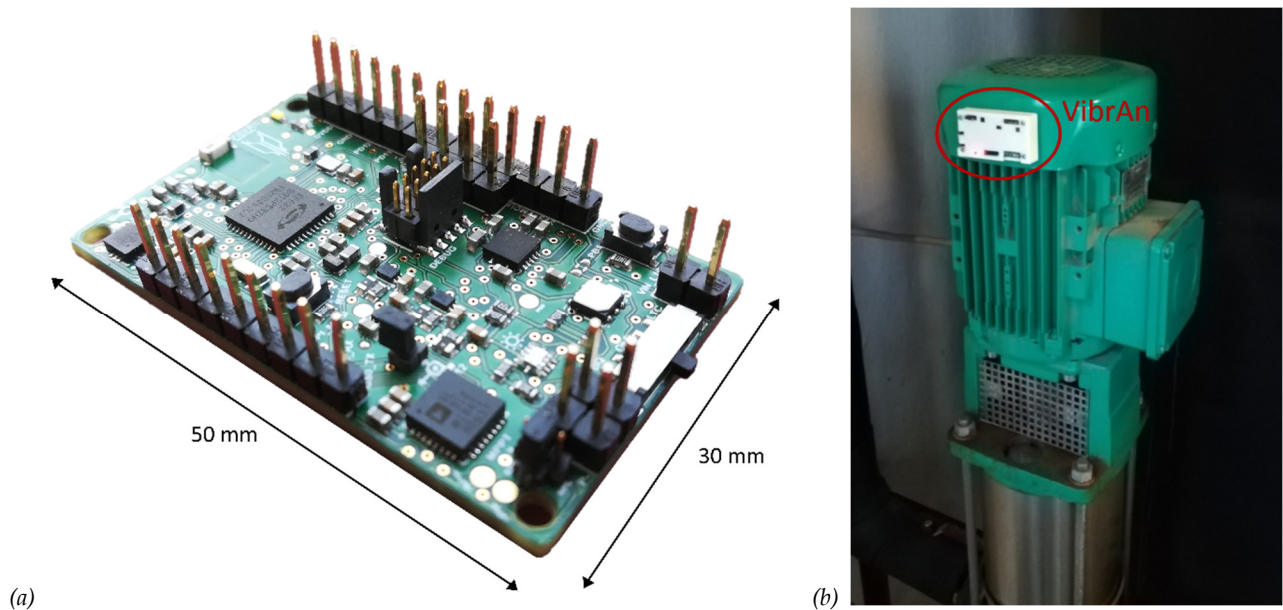


Figure 1: (a) The vibration analyser circuit board and (b) measurement setup in the engine room of building 29/B attached to an air-ventilation pump

2) With the upgraded energy management system, it is now possible to harvest energy from three different sources simultaneously, for example connecting a piezoelectric cantilever, a solar cell and a thermoelectric generator to the device will all charge the same on-board super capacitor. Furthermore, both low impedance (thermoelectric generator) and high impedance (piezoelectric cantilever, solar cell) sources are applicable. These features are achieved by having two energy management integrated circuits, one for low and another for high impedance sources.

3) We designed our own radio frequency protocol and transceivers with the help of partners Bonn Hungary Electronics and Datalist Ltd. The protocol operates using the principle of time-to-digital conversion (TDC), thus by creating a radiofrequency transmission with a very low duty-cycle (<1%) of the transmitter radio signal. This short active time makes this an ideal protocol for energy harvesting applications, where low-power operation is critical.

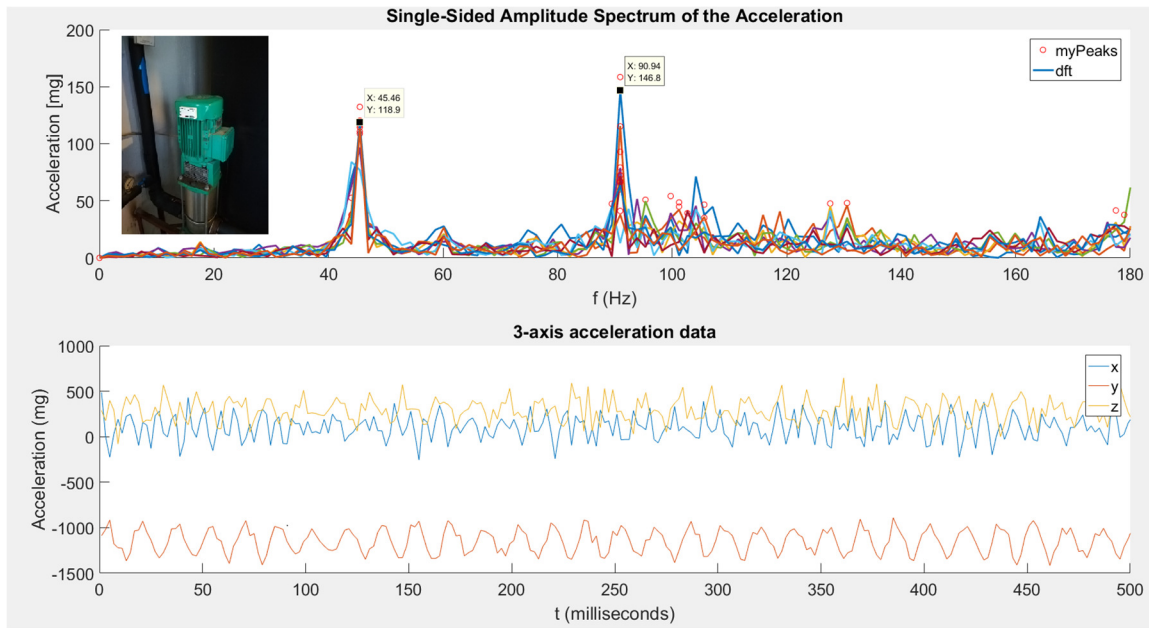


Figure 2: Vibration analyser measurement results on an air-ventilation pump, these results are essential to tune a piezoelectric cantilever for energy harvesting

4.) The device seen in Fig. 1. represents a sensor node in our system. These sensor nodes operate from energy harvesting and they transmit the vibration analysis results to a radio receiver unit. A radio receiver unit can collect data from up to 32 numbers of devices. All the measurement results then get transmitted to a database and can be loaded and further inspected from this (see Fig. 3.).

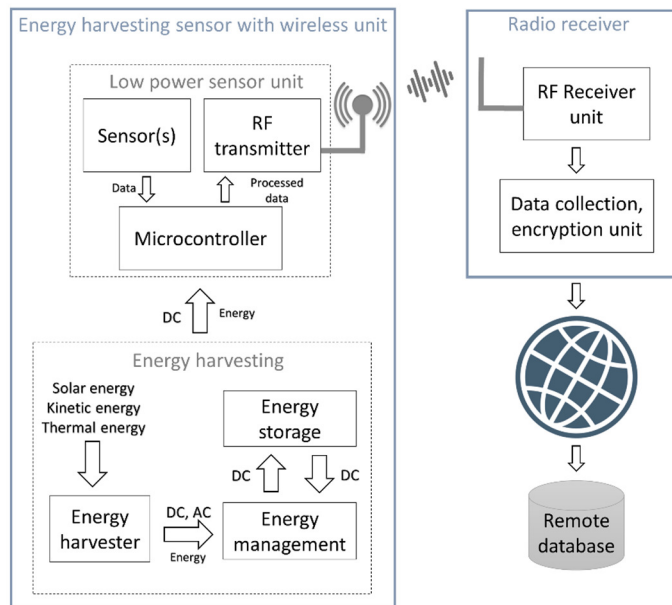


Figure 3: Block diagram of a sensor node with the receiver unit and the connection to the database on the internet. The system was already tested in a few live demonstrations (the latest at the PowerMEMS 2019 conference during December 2-6) and currently the utilization of this system in a real application is pursued.

WIRELESS ENVIRONMENTAL RADIATION MONITORING SYSTEM - DOZINET

NVKP_16-1-2016-0018 "KoFAH"

E. Tunyogi, M. Szappanos, J. Volk

The primary objective of the DoziNet project is to demonstrate that the radiation detector system, developed by the Space Dosimetry Research Group for rocket experiments, can be combined with the communication units and protocol used and developed by the Nanosensor Laboratory for scalable networks. The targeted system can be integrated into the network of Geiger-Müller (GM) probes installed and operated by the Environmental Protection Service at the KFKI Campus. The same communication protocol will also be used for transmitting data of the airflow sensors to the server.

The electrical design of the GM system was adapted to the ZP1220 and ZP1301 GM tubes used in the GM probes of the Environmental Protection Service. The signal is measured on the cathode resistor of the GM tubes. The signal processing unit comprises a pulse shaper (differentiator-integrator unit) and a comparator. At the output of the signal processing unit a monostable multi-vibrator provides square pulses of fixed amplitude and length. The counter/data processing unit is realized by a Happy Gecko EFM32 type microcontroller unit. The measured count rates, in counts per minute, are transmitted to the server via an RN2483 LoRa® transceiver module. Therefore, as an outdoor gateway, a PDTIOT-ISS00 IoT Wernet Station was also installed on rooftop of building 29B with Ethernet connection and protection against rain and lightning. A GPS module was connected to the Happy Gecko developer kit to provide GPS coordinates as metadata. Measurement data are displayed using NodeRed/ThingSpeak and saved into mysql database. In addition, for demonstration purposes an airflow meter used at the aerosol stations at the KFKI campus was also connected to the Lora Network.

The first breadboard model of the DoziNet system was completed and tested. The prototype of the relocatable GM unit successfully measured the background radiation at the campus and transmitted the measured data to the LoRaWan server. Data were successfully processed and displayed on the web-based NodeRed data viewer (Fig. 1).

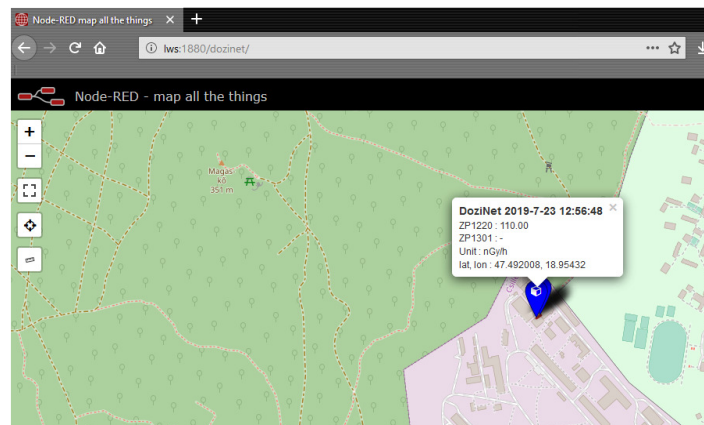


Figure 1: The NodeRed based data viewer of the prototype of the DoziNet system

In the next phase of the project, 3-5 relocatable GM probes, connected by the LoRaWan network to the main server will be added to the present network of GM probes. A similar unit will be optimized for use on radiation protection vehicle (DoziMobile).

BICYCLE TRAFFIC MONITORING SYSTEM

NVKP_16-1-2016-0018 “KoFAH”

A. Nagy, M. Szappanos, E. Tunyogi, T. Csukás, J. Volk

We designed and built a sensor strip (approximately 1 m long, see Fig. 1.), which not only provides bicycle counting and shows the direction with calculated speed of the biker in the traffic, but with a 2-3 cm precision detects the accurate position where the cyclist crossed the sensor strip.



Figure 1: Sensor strip (covered with red adhesive tape) across a bicycle lane



Figure 2: “I Bike Budapest” (2019.04.28.) bicycle parade with our 6 m long sensor strip (with green adhesive tape)

The project fits well with KOF AH project (NVKP-16-1-2016-0018) as in order to transmit the measured bicycle traffic data we need a network. The network used here is called LoRaWAN, which is a wide area network aimed for low power applications and the transmission distance can reach tens of kilometres. We tested this system near Margaret Bridge during a 10 day period (Fig. 1.), when the data (time, direction, speed, section) of almost 40.000 cyclists were collected. We also installed the sensor during a big bicycle event (Fig. 2.) and successfully covered a 6 m wide road surface. The project results are by now matured enough to move to fabrication by the newly established spin-off company LogLine Sensing Kft.

NANOMETER-SCALE RESISTIVE SWITCHES

OTKA K128534

L. Pósa, I. E. Lukács

Resistive switching phenomena were detected recently in a wide range of material systems. In proper device geometries these materials exhibit a reversible change of their resistance as voltage is applied. Our studies mainly focus on the fabrication of resistive switches below the resolution of current lithography techniques and the demonstration of complex operation on single or a few devices utilizing their multiple physical timescales. This year the following device constructions were realized studied using our nanofabrication facilities.

Sub-10 nm sized graphene-SiO_x-graphene resistive switch was investigated regarding electrical noise in steady state and during the switching process. The ultra-small active region was formed in graphene nanogap created by controlled electrical breakdown of a 200 nm wide graphene nanoribbon (Fig. 1.a-b). The noise spectra were already studied during the graphene breakdown process offering information about the origin of the large resistance fluctuation in graphene nanogap systems. Since the SiO_x resistive switch has several physical timescales, time resolved noise measurements were carried out to gain information about the evolution of the mechanisms in conduction and switching. The SiO_x memristive system was also investigated in nanofabricated Nb-SiO_x-Nb structure. In this case few nanometer size active regions could not be generated by the electromigration of an initially continuous nanowire due to the formation of NbO_x. To exclude the formation of NbO_x, the Nb electrodes were placed 24-34 nm far from each other by electron-beam lithography. Compare to the devices with graphene electrodes, all relevant parameters were similar, however the switching stability and the device-to-device variations were poorer. We demonstrated the multi-level programming capability and also the 1/f type electrical noise was investigated. In the near future, owing to the superconductive behaviour of Nb, Andreev spectroscopy will be performed to reveal the conduction channels of the resistive switch.

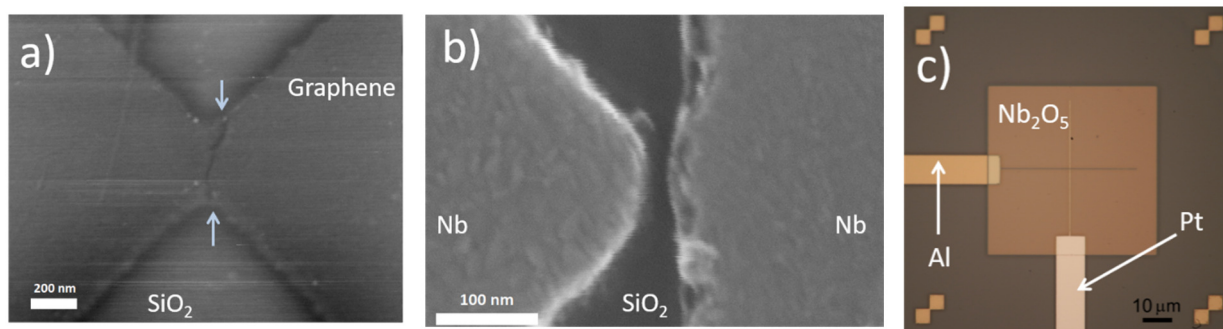


Figure 1: SEM image of graphene constriction after electrical breakdown and electroformation of SiO₂ at the nanogap region. The gap in the graphene is visible as a thin line, marked with arrows. b) A SEM image of the Nb-SiO_x-Nb resistive switch after the sample preparation. The gap between the two Nb electrodes is 24 nm. c) Optical image of Pt/Nb₂O₅/Al vertical resistive switch.

Resistive switching memories can also be created from atomic-sized contact, in which the switching mechanism is attributed to voltage induced reversible movement of a single atom. Such devices can be realized in many systems: electromigrated nanowire, notched wire Mechanically Controlled Break Junctions (MCBJ) or STM, however these arrangements either do not have high enough mechanical stability, or a new contact cannot be defined again after complete rupture of the wire. Nanofabricated suspended silver nanowire can combine the advantages of these arrangements, it has high stability and the contact can be pushed several times. The structure lies on a spring steel substrate covered by polyimide providing smooth surface for the nanofabricated structure. During the mechanical rupture we could observe conduction quantization at room temperature and the resistive switching of atomic sized contact was also demonstrated.

The switching behaviour of Nb₂O₅ is attributed to the valence change effect, in which the conductive filament is built up by local enrichment of oxygen vacancies. Typically, one of the contacts serves as an oxygen reservoir in forming oxides, while the other one is inert (i.e. Pt). This year three different device structures were fabricated in vertical arrangement, where two metal wires cross each other perpendicularly (Fig. 1.c). Widths of the metal wires were varied between 100 nm and 5 μm. The inert electrode was 50 nm thick Pt for all types of devices (bottom electrode), while the other electrode was either aluminium or titanium (top electrode). Between the two metal electrodes an about 16 nm thick Nb₂O₅ layer was deposited by reactive sputtering. In case of one set of devices with aluminium top electrode the Nb₂O₅ layer was exposed to argon plasma for 2 min, which typically aids the electroforming process, when the insulator layer transforms into switchable state. The devices with Ti top electrode did not show robust switching effect, only weak resistance changes: less than 1.5 switching ratio could be observed for 100 cycles. In case of Al top electrode we could induce stable resistive switching independently of the plasma treatment and the wire width. The electroforming voltage for the plasma etched devices was lower; it decreased from 2.8 V to 2.3 V. We could switch these devices more than 10 thousand times under ambient condition for 5 months. We demonstrated signal detection in a noisy background using only single device and we also studied their 1/f type electrical noise.

The work was done in collaboration with Physics Department at BME.

OPTIMIZATION OF VO₂ THIN FILMS FOR MEMRISTORS

OTKA K128534

Gy. Molnár, L. Pósa

The metal-insulator transition phenomenon accompanied by a rapid reversible phase transition in vanadium dioxide (VO₂) has attracted great attention both from scientific and from technological point of view due to the various potential applications. Vanadium dioxide thin films are prepared by different physical and chemical vapour deposition methods.

During our experiments, thin vanadium oxide films were prepared by electron gun evaporation of vanadium metal in a high vacuum environment followed by the annealing in the presence of air. According to the available literature, initially, glass plates were used as substrates. It was shown, that in contrast to the literature the expected VO₂ phase was not present in the layers. The detailed x-ray diffraction measurements revealed that the sodium content of the glass substrates interacted with the layer, and three different sodium-vanadium-oxygen phases were formed (NaV₃O₈, Na_{0.76}V₆O₁₅, Na₅V₁₂O₃₂) instead. The replacement of the glass substrates by SiO₂ covered Si wafers resulted in the appearance of the desired VO₂ phase. The substrates were: (a) 100 nm SiO₂ covered Si wafers, and (b) 1.3 μm SiO₂ covered Si wafers. 200 nm vanadium metal was evaporated by electron gun onto the substrates in a high vacuum environment. The heat treatment was carried out in a tube furnace at temperatures of 350-500°C. The annealing times ranged 1 - 4 hours. Initially, the samples were inserted into the hot furnace, and removed at the end of heat treatment. Later, slow temperature ramping and slow cooling processes were applied, too. X-ray diffraction measurement confirmed the presence of the VO₂ phase in the layers. For temperature dependent resistivity measurements, 1 mm diameter Cr/Au contacts were evaporated onto the vanadium oxide through a contact mask. According to the electric measurements the metal-insulator transition could be detected in some samples. The best results were achieved in case of 400°C and 3 hours annealing, the resistance change almost reached two orders of magnitude. In some cases, the heat treatment caused the appearance of bubbles in the layers. The quantity of bubbles depended on the temperature and time of the annealing, and on the thickness of the SiO₂ layer of the substrates too. The work was done in collaboration with Physics Department at BME.

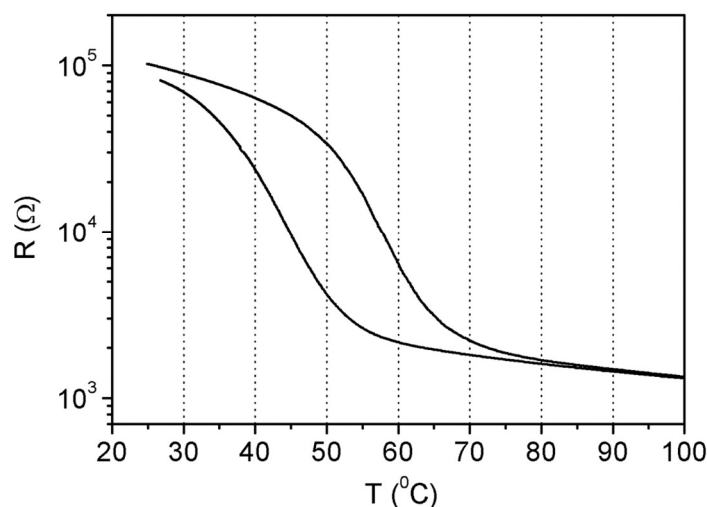


Figure 1: Temperature dependence of electrical resistance of a VO_x film on SiO₂/Si substrates after annealing at 400°C for 3 hour

OPTIMIZATION OF SUPERCONDUCTING MICROWAVE RESONATORS AND HIGH SPATIAL RESOLUTION BOTTOM GATES

National Quantum Technology Program (HunQuTech)

I. Lukács, M. Sütő

In 2019, we continued our cooperation with the consortium of the National Quantum Technology Program in the field of generating, sharing, and developing quantum information networks. Low dimensional nanosystems and quantum nanocircuits were implemented by our group whereas the consortium partners are responsible for theoretical models and measurements. The charge density in InAs nanowires can be well manipulated by an electrical potential on high resolution gate electrodes resulting in quantum dots of adjustable width and depth. Topological phases of matter are accompanied by protected surface states or exotic degenerate excitations such as Majorana modes or Haldane's localized spinons as well as Weyl degeneracies. According to the literature, the high-frequency modulation of the potential of quantum dots rotates the quantum bit through spin-orbit coupling. The coupling of quantum circuits to superconducting resonators enables faster characterization of quantum circuits, for example by reading the charge and spin quantum bits.

NbTiN layer on intrinsic silicon wafer is a good choice to prepare superconducting resonator due to its chemical stability, higher critical temperature and simplicity to be produced by reactive sputtering. We used an AJA UHV system for deposition at a DC sputtering power of 150W on a 3 inch diameter Nb(60%)Ti(40%) source. The applied Argon flow rate was 10 sccm and the gate valve of turbomolecular pump (TMP) was fixed at a chamber pressure of 2.5 mTorr. In order to optimize the NbTiN layer we deposited 14 samples at several nitrogen flow rates. In some cases we also used additional radio frequency (RF) bias plasma at a power of 5 W on the sample holder.

The designed resonators with several geometries were formed by electron beam lithography and reactive ion etching of NbTiN on sample S_2.4_RF (Fig. 1.a). From geometry (Fig. 1.b) and transmission measurements (Fig. 2.) of the coplanar transmission line (CTL) the inner and coupling quality factors, the specific capacity, the magnetic inductance, the effective dielectric constant, the kinetic inductance and the square kinetic inductance of the system (Table 4.2) can be determined.

Sample name	N ₂ flow rate	Bias plasma	T _c (K)
S_2.0	2.0	Off	12.8±0.3
S_2.2	2.2	Off	13±0.3
S_2.4	2.4	Off	12.8±0.3
S_2.6	2.6	Off	12.8±0.1
S_2.8	2.8	Off	12.1±0.1
S_3.2	3.2	Off	11.2±0.5
S_3.6	3.6	Off	10±0.8
S_4.0	4.0	Off	10.1±0.3
S_6.0	6.0	Off	6±0.1
S_8.0	8.0	Off	<5
S_2.2_RF	2.2	On	14±1
S_2.4_RF	2.4	On	14.6±0.5
S_2.6_RF	2.6	On	14±1
S_2.8_RF	2.8	On	10.1±0.3

Table 1: Deposited layers with its critical temperatures

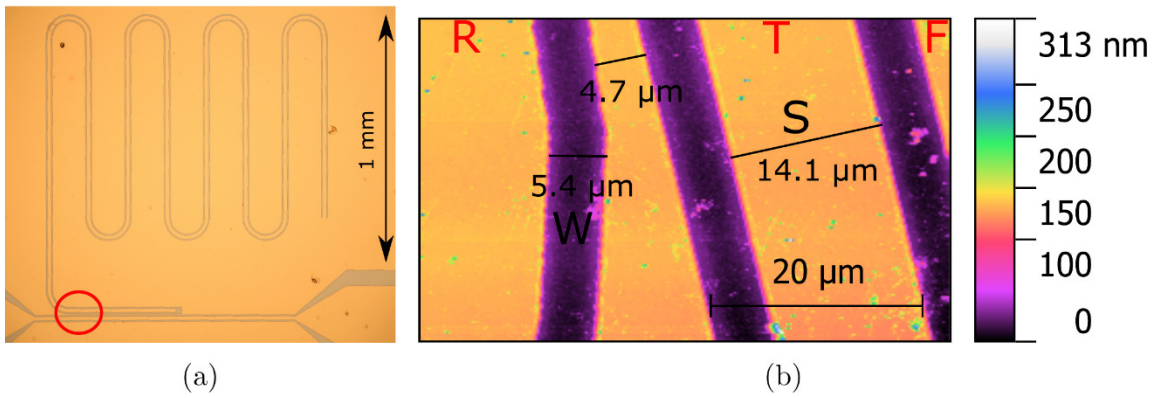


Figure 1: (a) Optical microscope image of a superconductor resonator and (b) AFM image with the relevant geometric data

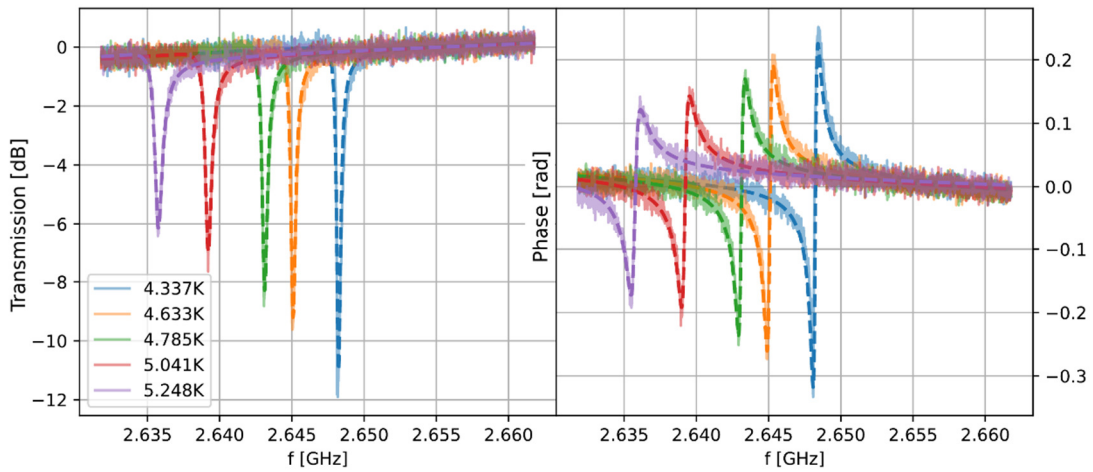


Figure 2: Transmission measurements of the resonator shown in Figure 1 at various temperatures

Q_i	Q_c	C pF/m	ϵ_{eff}	L (nH/m)	L_m (nH/m)	L_k (nH/m)	L_k^{\square} (pH/ \square)
7787	14972	186	12.12	727	380	347	4.4

Table 2: The calculated characteristic values of the shown CTL

In order to increase the resolution of electron transmission measurements through tuneable quantum dot system in InAs nanowire, it is necessary to decrease the spatial period of the gate electrodes. Previously gate electrodes were fabricated from Ti/Au vaporized on silica layer by lift-off technology. By reducing the distance between the Ti/Au gate electrodes, gold can easily migrate on the surface of the chip at low temperature, causing an open or short circuit in the electrode system. By substituting the gold to platinum and optimizing the sample preparation processes, we can reduce the spatial resolution of bottom gates from 80 nm to 50 nm (Fig. 3).

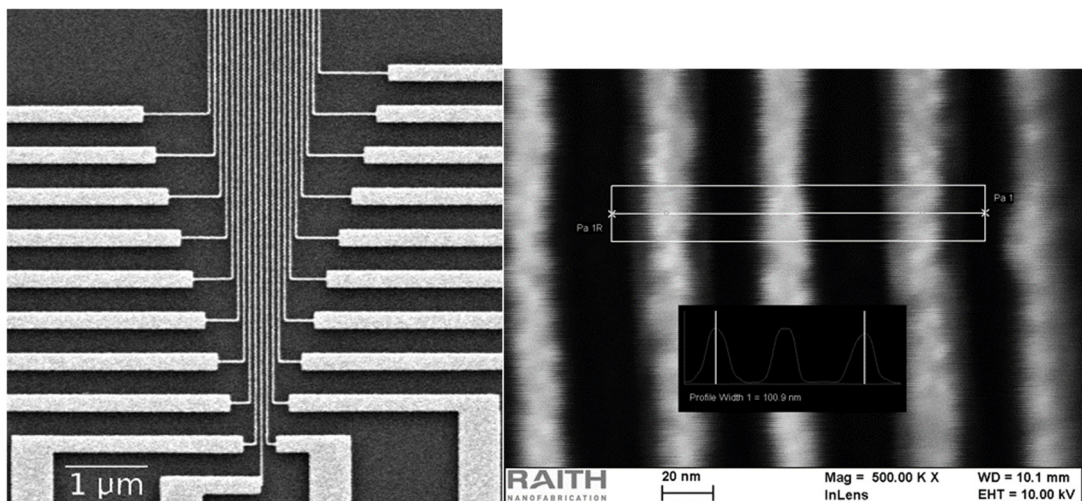


Figure 3: SEM images of high spatial resolution Ti/Pt bottom gates on SiO₂

ATOMIC LAYER DEPOSITION AND CHARACTERISATION OF Ga_2O_3 FILMS

OTKA PD116579

Zs. Baji, I. Cora, Z. Szabó, Zs. E. Horváth, E. Agócs

Gallium oxide (Ga_2O_3) is a wide bandgap (4,7-4,9 eV) semiconducting material with a number of crucial applications in sensorics, optoelectronics and catalysis. Due to its UV transparency and its absorption of deep-UV, it may find important applications in photonics and as a deep ultraviolet (DUV) photo-detector. The present work focuses on the atomic layer deposition and annealing of Ga_2O_3 prepared with $\text{Ga}_2(\text{NMe}_2)_6$, which promises some advantages over the other often used chemicals, such as a lower deposition temperature. The Ga_2O_3 films in this work were prepared at deposition temperatures between 100°C and 300°C. Although it has been shown to be possible to grow such films in a temperature range of 100°C to 300°C, the precursor source had to be heated to 130°C to achieve sufficient vapour pressure. At temperatures exceeding 270°C, the precursor decomposes resulting in growth of inhomogeneous rough CVD-like film. The growth rate within the Atomic Layer Deposition (ALD) window is 0.4 - 0.8 Å/cycle at 130°C - 270°C. The films prepared with these optimised parameters are homogeneous, and as can be seen in Fig. 1., their roughness is below 1nm. All the as deposited films are amorphous.

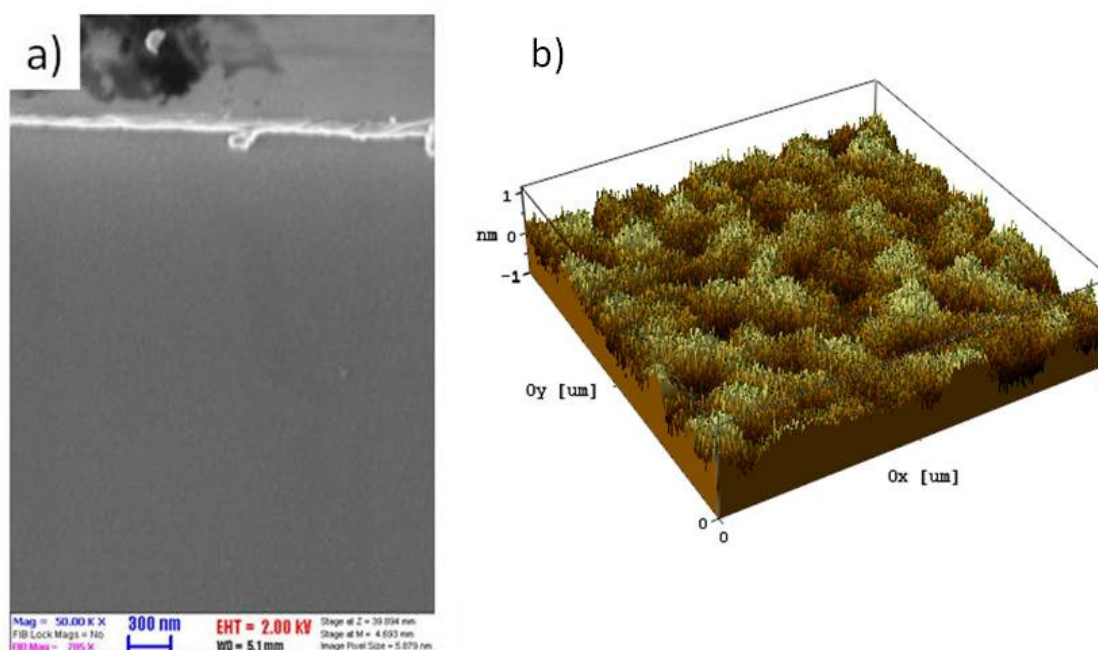


Figure 1: The morphology of the Ga_2O_3 layer deposited at 130°C

To induce a crystallisation in the ALD Ga_2O_3 films, different annealing procedures were tested. 3 hour long heat treatments at 900°C were required to achieve crystalline films. Fig 2a shows that in the film annealed in nitrogen atmosphere a crystallisation started, but according to XRD measurements, these films remained still mainly amorphous. On the other hand, annealing in oxygen resulted in crystalline β - Ga_2O_3 films with large crystallites on the surface, as it is shown in fig. 2.b and c. The films are textured and oriented mainly in the (-204) direction.

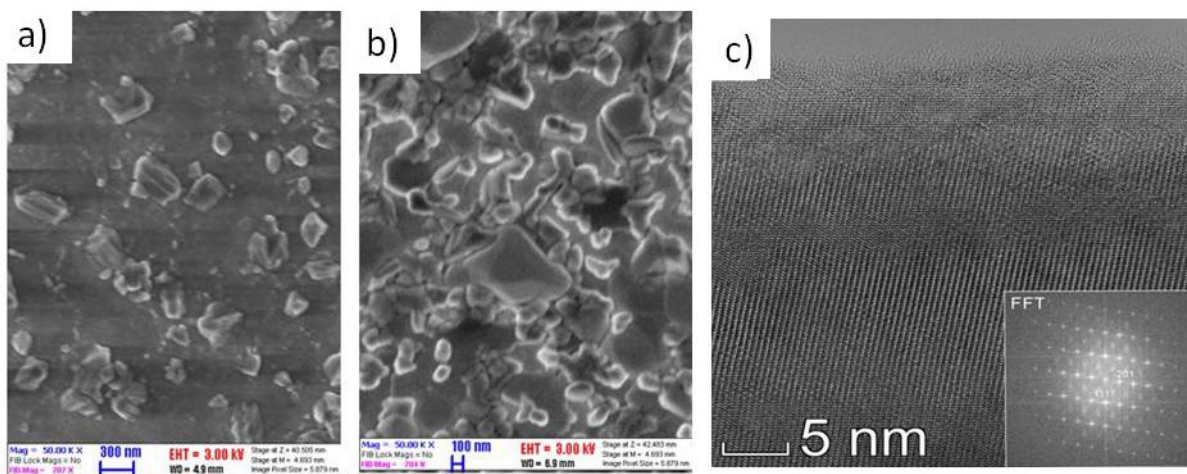


Figure 2: SEM image of the film after annealing in nitrogen (a), and oxygen (b) at 900°C for 3 hours, and the TEM image of the latter one

To determine the electrical parameters of the layers, spectroscopic ellipsometric measurements were conducted. As it is shown in Fig. 3., the bandgaps of all deposited layers were within the regime predicted by the literature: between 4eV and 4.8 eV. The deposition temperature also affected the bandgap of the films; the ones deposited at 130°C had the widest bandgap. The dielectric constants are between 3.2 and 3.5, i.e. this property was not significantly influenced by the deposition temperature. The annealing reduced the dielectric constants of the layers significantly.

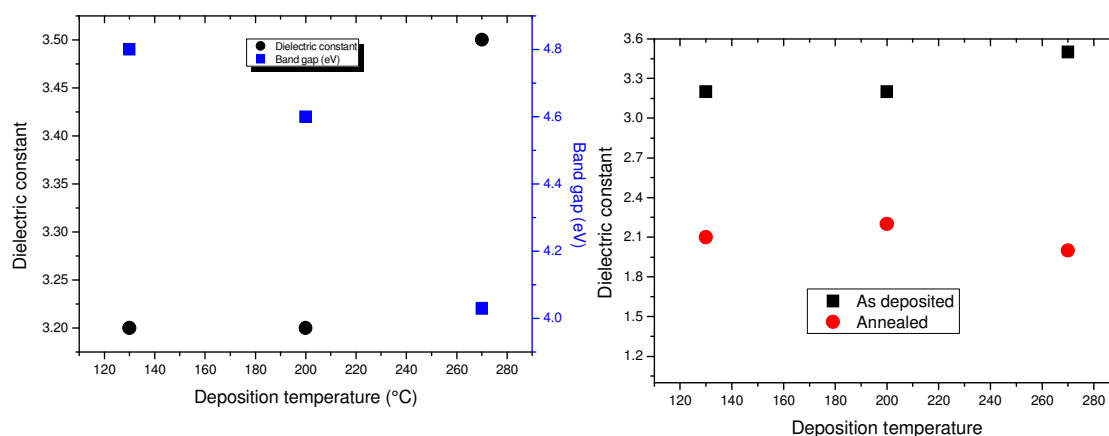


Figure 3: Dielectric constants and bandgaps of the as deposited and annealed films as determined by spectroscopic ellipsometry

RADIATIVE DAMPING OF SURFACE PLASMON RESONANCE IN GOLD NANOPARTICLES: THE INFLUENCE OF SHAPE, SIZE, AND SUBSTRATE MATERIAL

Z. Zolnai, D. Zámbo, D. P. Szekrényes, and A. Deák

In the surface plasmon resonance (SPR) of metal nanoparticles (NPs) the linewidth and spectral intensity – besides the shape and size of the particles – is determined by radiative and non-radiative damping terms. So far mainly the role of surface/chemical interface damping term was investigated in the detection of different ligand molecules bound to the surface of the NPs, and less attention was paid to the role of radiation damping (Γ_{Rad}) in plasmonic NPs. Nevertheless, to evaluate the intensity and the overall damping, i.e., full width at half maximum of the SPR spectra a reliable estimation of Γ_{Rad} is also required. The value of Γ_{Rad} and thus spectral intensity depends on the local environment of NPs, that is, the substrate material and the dielectric function of the surrounding media. In case of polarizable substrates supporting plasmonic NPs the dipole moment of the NP is coupled to the dipole moment induced by the mirror charge appearing in the substrate (or, in the NP shell for core-shell NPs).

In this work we investigated the effect of the underlying material on the radiation damping for gold nanospheres (NS) and nanorods (NR) with dark-field single-particle scattering spectroscopy correlated with scanning electron microscopy analysis. Besides spectrum shape, the relative intensities of the optical spectra were also considered as the detector system is corrected for spectral intensity vs. the excitation wavelength. Au NPs on glass, Si, and SiC, i.e., on substrates with significantly different refractive indices were analysed. The effect of the anisotropic environment was taken into account through an effective dielectric constant, which is extracted from the resonance frequency of SPR.

Through the correlation of the optical scattering spectra with the NP size extracted from SEM analysis, significantly higher relative spectral intensity and radiation damping was found for nanospheres deposited on Si and SiC as compared to the nanospheres deposited on glass. For nanorods an opposite effect was observed, i.e., higher relative intensity, but lower radiation damping was observed for NRs on glass as compared to NRs on Si. These findings can be explained by a dipole oscillator model that relates the spectral intensity with the net polarization of the system, the SPR frequency, and the effective dielectric constant of the NP environment. For spheres (rods), the substrate mirror charge induced polarization is parallel (opposite) to the transversal (longitudinal) polarization of the Au NPs induced by the excitation light source. As the induced polarization of the substrate is higher for higher refractive index, the observed trends in Γ_{Rad} and intensity can be understood considering the net polarization of the different systems. We note that besides the oscillator model, possible influence due to reflectance of the incident light and the NPs dipole radiation on the substrate surface and the spectral transmittance of the substrate/air interface on the detected intensity were estimated.

This work can pave the way toward the detection of ligand molecules and local dielectric environment through the parameters of the SPR resonance of metal nanoparticles.

INVESTIGATION OF ATOMIC OR MOLECULAR PROCESSES INDUCED BY ULTRASHORT LASER AND/OR ELECTRON PULSES

2018-1.2.1-NKP-2018-00010

G. Battistig

The collaboration of the three institutions (University of Pécs, Faculty of Sciences, Institute of Physics, Institute for Nuclear Research and MFA) of complementary competencies develops a new tool able to study atomic and molecular processes triggered by the combined action of photons and electrons. The ultra-short pulses of electrons needed for the process will be produced by terahertz radiation. The new scientific tool is planned to be setup and operate at ELI-ALP.

The task of MFA in the project is aimed at producing micro- and nano-sized structures and devices in which the terahertz electromagnetic space can accelerate electron packets with great efficiency. For the production and processing of semiconductor and dielectric structures in the required micrometer size range, only the MFA Microtechnology Laboratories provide the appropriate technology and expertise.

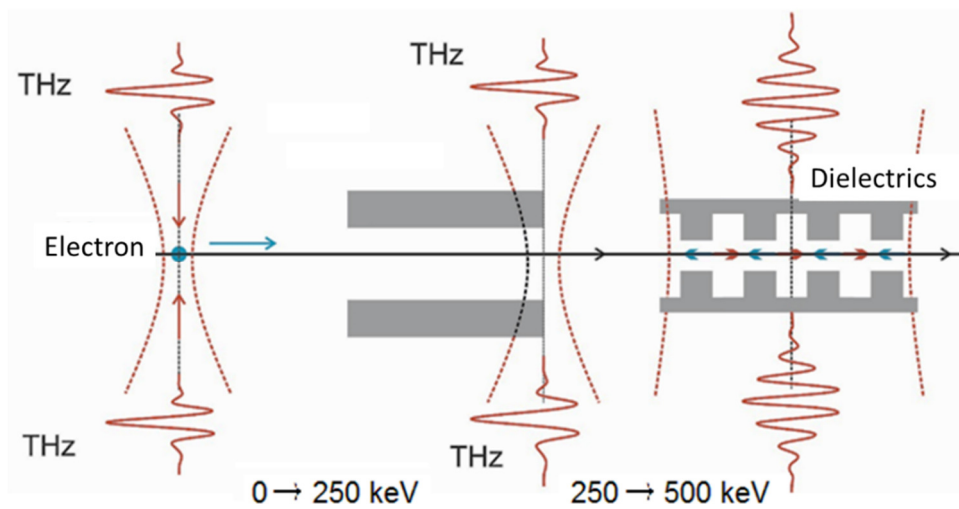


Figure 1: Principle of electron acceleration by electromagnetic field of THz radiation

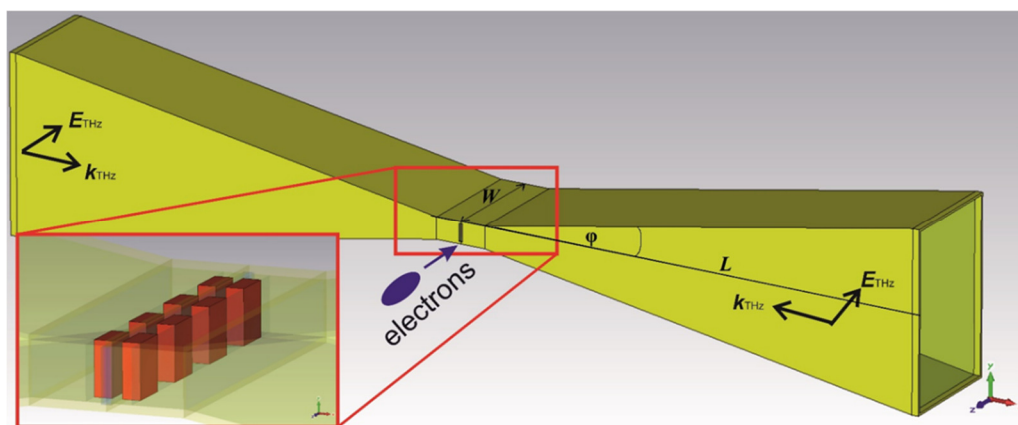


Figure 2: The planned setup: THz illumination of the dielectric microstructure (inset) through the waveguides. The electromagnetic field across the structure accelerates the electron packets flying through the microstructure.

LOW POWER CONSUMPTION-TYPE NANO-SENSORS FOR GAS DETECTION IN HARSH ENVIRONMENT

Hungarian-Russian Collaborative Research Program 2017-2.3.4-TéT-RU-2017-00006

F. Bíró, Z. Hajnal, I. Bársony, Cs. Dücső

The ultimate goal of the project is to develop a novel calorimetric gas sensor family what is able to detect CH₄, NH₃ and CO up to their lower explosion limits (LEL), i.e. 5, 15 and 12.5%, respectively. The sensors can be operated in harsh environment without any risk of ignition even over LEL concentrations. Beside the optical and electrochemical approaches and the corresponding systems, sensors operate with catalytic-calorimetric principle are still among the dominant devices in safety systems.

The catalytic device is expected to detect lower gas concentration and exhibit better sensitivity, than the heat-conductivity type device which is simpler and still in use in practice. Still a more sophisticated device applies both sensors, thereby extending the detection range and improves the detection reliability.

Another advantage is the commonly used filament or micro-hotplate structure. Therefore, to develop a micro-hotplate meets all the mechanical, electrical and chemical requirements is essential for a reliable and commercialized device.

The activity of the Microsystems Lab can be described in 2 sections (1) Development and testing of the final micro-hotplate structure optimized for high temperature thermal-catalytic sensing processes and (2) Joint decision making on the selection of the final structures, components of the device for the demonstration at the end of the project; and the construction of heat conductivity type sensing device.

The optimum layer structure of the full membrane micro-hotplate was elaborated and finalized. The vertical structure was set to parallel provide minimum stress (~100MPa, but definitely below 200MPa), protection of the filaments from the environment - and vice-versa! - as well as appropriate thermal and electrical isolation. Nevertheless, the geometry of the filament is determining both in terms of lifetime and sensor response. The catalysis requires operation at elevated temperature. Depending on the catalyst applied it must be 500-700°C. There are two substantial issues; the temperature and its gradient along the filament as well as along the heated area of the hotplate must be kept as low as possible, thereby the temperature of the active hotplate surface must be uniform. Having concluded the deterioration mechanisms we designed and processed alternative filament geometries. Thereby we tuned the geometry of the filament to exhibit better uniformity, smaller gradient but still having large cross sections to withstand migration related deterioration.

Using the high resolution visible pyrometry method we analysed the latest structures and found very good temperature uniformity. The heated area exhibits less than ±5 °C temperature difference at 550°C for the appropriately tailored heater structure. This structure will be used for testing catalyst and also in the demo devices. The targeted operation temperature is 550°C or below, which can be achieved with max. 27mW/element. We have been testing the long time performance of micro-hotplates. After 6 months continuous operation at 600 °C the resistance change of the filament is around 1.1-1.2%, therefore we conclude that in a Wheatstone-bridge configuration the resistance drift will be much less than the required 1%/year.

As the heat conductivity mode is also feasible for hydrogen or higher concentration methane detection, we constructed chips for testing this operation. One of the hotplates of chips presented above was encapsulated with a dome like Si element and vacuum-sealed around the cover and also around the bottom of the chip. Fig. 1. shows the structure.

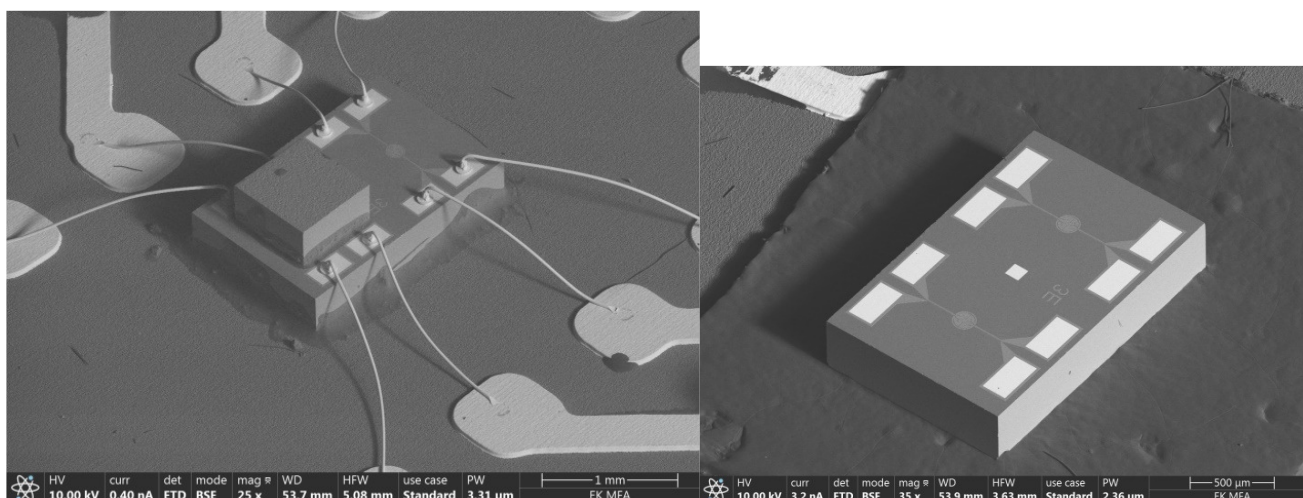


Figure 1: Construction of the heat conductivity sensor. The two identical micro-hotplates (left) and one of the hotplates are vacuum-sealed(right). The chip is mounted on a small PCB for testing.

Thermal conductivity sensors formed from micro-heaters were tested in synthetic air-methane gas mixture. Before test every filament was heated in synthetic air for at least 3 hours by 21 mW. Active and reference element were connected in Wheatstone-bridge arrangement and supplied by constant voltage.

Related publications

- [1] F. Bíró, Z. Hajnal, I. Bársony and Cs. Dücsó: *MEMS microhotplate constraints*, open access book *Advances in Microelectronics: Reviews*, Vol. 2, Book Series, published by IFSA Publishing, S.L. February, 2019
- [2] N. Samotaev, A. Pisljakov, A. Gorshkova, I. Bársony, Cs. Dücsó, F. Bíró: *Al₂O₃ Nanostructured Gas Sensitive Material for Silicon Based Low Power Thermocatalytic Sensor*, International Scientific Conference "Materials Science: Composites, Alloys and Materials Chemistry" (MS-CAMC-2019, Nov 20-21), Szentpétervár, Oroszország

DESIGN AND DEVELOPMENT OF A 3D FLEX-TO-RIGID COMPATIBLE FORCE SENSOR

H2020-ECSEL-2017-2-783132 "POSITION-II", 2018-2.1.6-NEMZ-ECSEL-2018-00001

J. Radó, P. Asztalos, Z. Hajnal, P. Földesy, Gy. Molnár, P. Fürjes, Cs. Dücső

The main objective of the POSITION-II project is the realization of a pilot line for the fabrication of the next generation of smart medical instruments. This second generation of smart medical instruments offers improved performance through better sensors and transducers combined with an improved manufacturability and lower cost. The task of our research group is to develop and demonstrate the applicability of a capacitive force sensor integrable in the tip of an electrophysiological catheter.

The F2R compatible 3D force sensors exploit the capacitive read-out; thereby three capacitors positioned symmetrically on a deforming membrane are needed to resolve the vector components of the loading force. The Partners agreed upon the basic structure, i.e. a force transferring and amplifying rod will be formed from the handle layer of the Silicon On Insulator (SOI) wafer, whereas the deforming membrane will be the 40 μ m thick device layer with isolated capacitors on top. Two types of surface micro-machined capacitors will be investigated; the cavity/oxide dielectric capacitor presented by Philips in the Capacitive micromachined ultrasonic transducer (CMUT) device and an alternative structure having an oxide/compressible Polydimethylsiloxane (PDMS) dielectric (Fig.1). The Laboratory has to develop the PDMS base sensor and also to adapt the CMUT like chip to force sensing purposes.

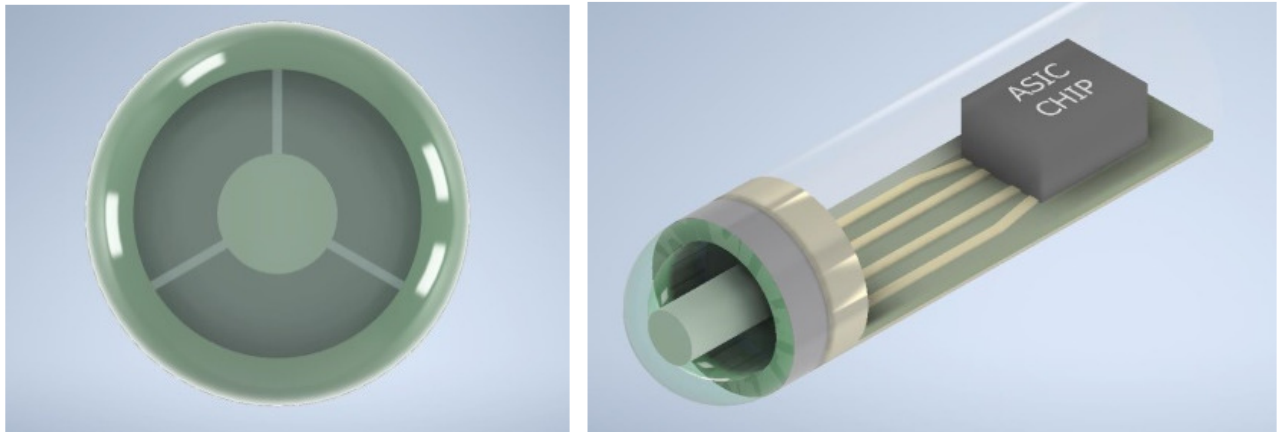


Figure 1: Schematic cross section of the catheter head with the fixed sensor at the tip (left). The front view of the tip symbolises the position of the 3 capacitors (right). (The diameter of the catheter is in the mm range.)

On the basis of general geometric requirements Finite element method (FEM) models were set to predict functional properties of the deforming capacitor. The simplified model is applied to see the geometric changes of the capacitors under load. In the first step the deformation vs. applied force was modelled. Following the deformation the change of capacitance was calculated. Typical C-F responses were found to be around 0.5-1.0 pF/N. As in this specific task, the thin film membrane "sandwich" structure cannot be neglected. Nevertheless, its aspect ratio (lateral dimensions vs. thickness of individual components) is in several orders of magnitude, their mechanical behaviour was only simulated at a moderate level of applied forces (~0.2 N). The elastic response of the membrane becomes more and more non-linear above that load, which would require enormous extension of the mesh-refinement for mathematically convergent results. However, the mechanical "real-life" behaviour can probably be considered linear at a much broader range of forces.

Parallel with modelling, the additional thin film compatible elastic PDMS processing steps were elaborated. Due to the lateral size limitations of the capacitors the thickness of the elastic dielectric must be definitely below 1 μ m to exhibit capacitance in the pF range. Test structures were manufactured on SOI wafer to verify model calculations and determine geometric constraints. The diameter of the sensor is varied between 300-2500 μ m. Due to the assembly issues and the construction of force sensing measurement setup the 2 x 2cm² test chips contain 9 sensor elements of the above lateral sizes. Force transferring rods are formed in the handle wafer whereas the capacitors (3/sensor) and wire contacts on the device layer. In order to limit the deformation in the PDMS layer a solid backside Si element was bonded on the device layer side (Fig. 2.).

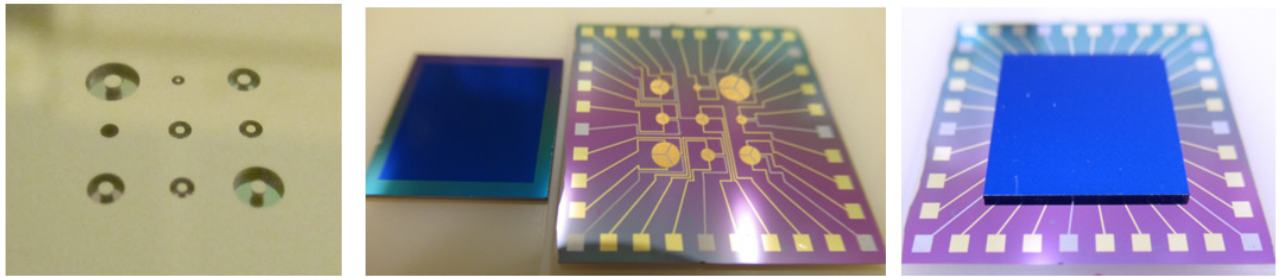


Figure 2: Processed test chip with nine force sensors of different lateral geometry. Force transferring rods in the handle wafer (left), 9x3 capacitors on the device layer and the supplementary Si chip with a 1µm frame to prevent membrane deformation (centre) and test chip with back-side bonded deformation limiting Si element (right).

The test chips were mounted on rigid Printed Circuit Board (PCB) elements and measured by a manual 3D loading and force sensing setup. The on-going measurements have proven the validity of the concept (Fig. 3.) however the actual signal level is still below 1pF. It has to be increased in order to improve the signal/noise ratio and minimize the effect of parasitic capacitances. We found measurable signals up to 100fF / sensing elements for up to 2N load but resolving load directions is still to be improved. Due to the low signal/noise ratio on site filtering will be a must in the final device.

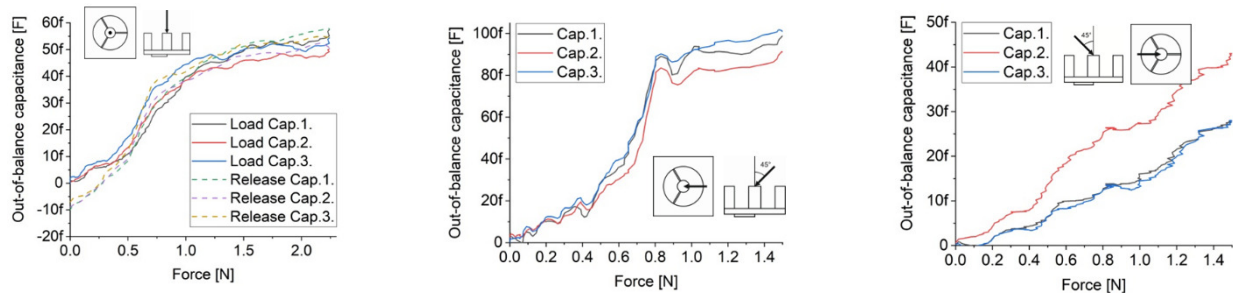


Figure 3: Responses of the three elements for the three characteristic directions as indicated with the insets.

MANUFACTURING IMPLANTABLE MICROELECTRODE ARRAYS

OTKA K120143, 2017-1.2.1-NKP-2017-00002 „Nemzeti Agykutatási Program 2.0”

A. Zátonyi, Á. Horváth, A. Pongrácz, A. Nagy, R. Hodován, Z. Fekete

The PPKE “Implantable microsystems” group contributed to the development of an implantable microelectrode array, which is able to change its Youngs-modulus from 2 GPa to 300 MPa if being exposed to physiological temperature (see Fig. 1.). Besides the micromachining of the thiolene-acrylate based microdevice, packaging of the system was optimized to meet the demands of long-term operation in the living body. After successful electrochemical aging tests involving thiolene-acrylate neural probes, acute in vivo recordings have been carried out and repeated from the rat hippocampus several times.

As spatial resolution tests through Parylene HT based ECoG devices using fluorescent two-photon imaging provided promising data, the focus of experiments moved to application of the microsystem in living subjects instead of in vitro cultures. The concurrent use of high-density electrophysiology and Ca imaging was presented in awake mice and the dataset in both the optical and electrical domain is being evaluated. Besides the preparation of in vivo experiments, our group made further efforts to confirm the mechanical and electrochemical stability of these Parylene HT/ITO devices (see Fig. 2.).

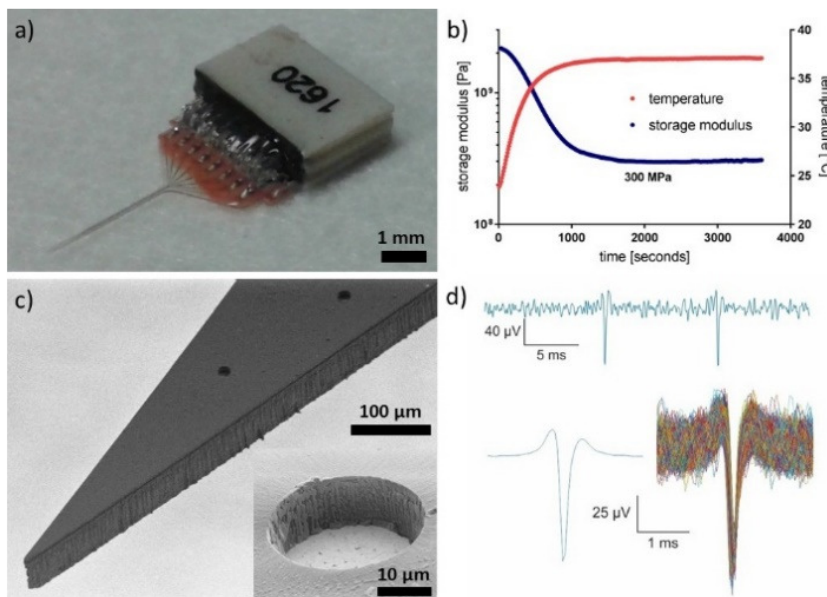


Figure 1: (a) Ready-to-use neural probe for hippocampus recording. (b) Scanning electron microscopy view on the sidewall profile (b) on a reference recording site (c) Softening of a polymer sample upon immersion into room temperature saline solution and heating to 37 °C. (d) Representative filtered waveform of action potentials in vivo.

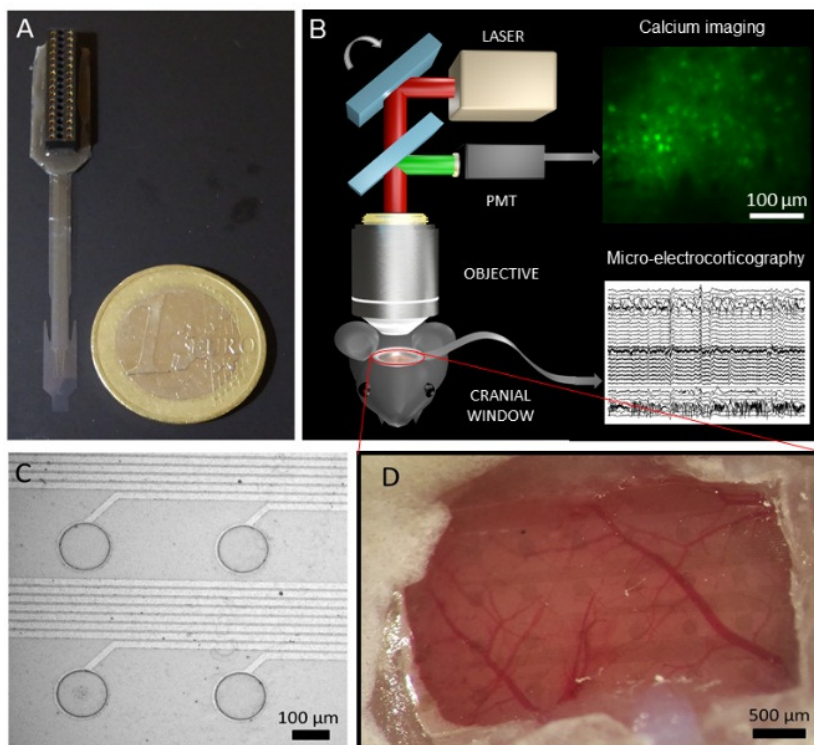


Figure 2: (A) transparent microECoG array made of low-autofluorescent Parylene HT substrate. (B) Schematic figure representing the experimental design for simultaneous Ca²⁺ imaging and electrophysiology in vivo. (C) Close view of recording sites and wires made of sputter-deposited indium-tin-oxide. (D) Epidurally implanted microECoG array prepared for two-photon imaging in freely moving mouse.

The group contributed to the in vitro and in vivo demonstration of a multimodal implantable actuator (Fig. 3.), which comprises of monolithically integrated infrared waveguide, a temperature sensor and electrophysiological recording sites. A coupled mechanical – optical-thermal model has been created and validated to estimate the surrounding temperature in the deep neural tissue. During the first in vivo experiments, controlled elevation of the background temperature using the integrated device resulted in reversible excitation or inhibition of cellular activity depending on the targeted brain region and cell type. [1, 2, 3]

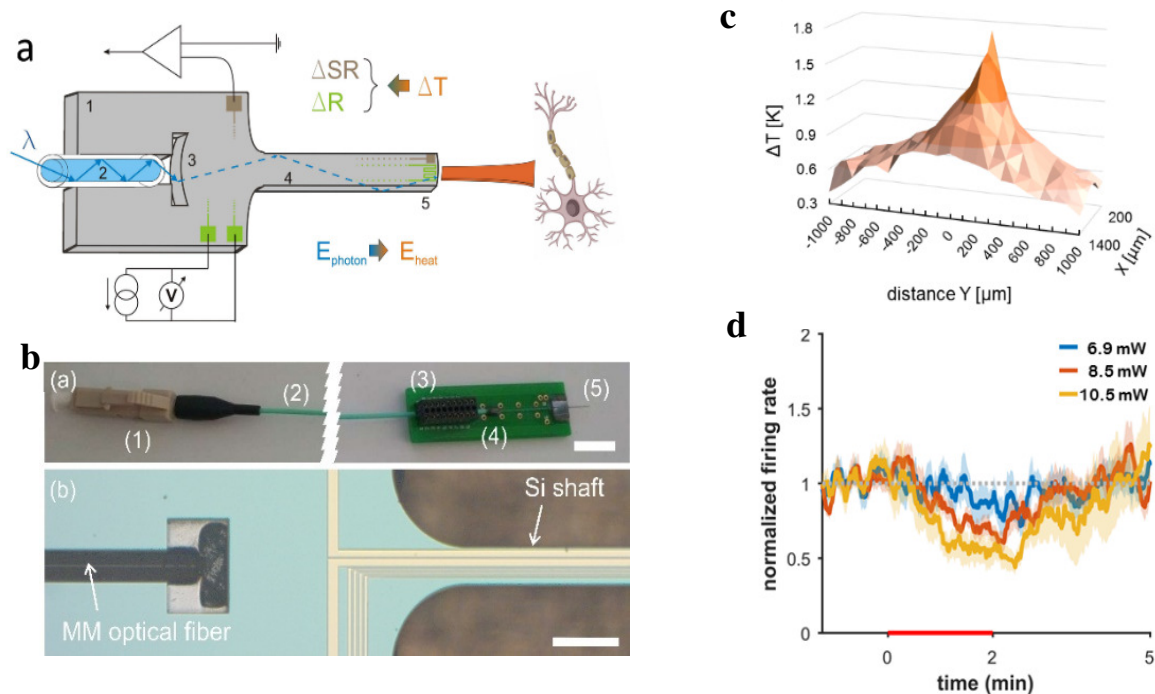


Figure 3: (a) Operation of the multifunctional probe chip designed to deliver infrared light into the neural tissue and monitor electrophysiology concurrently. (b) Photo on the ready-to-use device (top) and microscopy image of coupling region of the chip (bottom). Denoted parts: (1) optical connector, (2) optical fiber, (3) electrical connector, (4) PCB, (5) silicon chip. (c) Measured spatial distribution of temperature change evoked by the absorbed IR light around the probe shaft. (d) Representative cellular response in the cortex to IR stimulation at various input optical power.

Related publications

- [1] A Zátanyi, G. Orbán, R. Modi, G. Márton, D. Meszéna, I. Ulbert, A. Pongrácz, M. Ecker, W.E. Voit, A. Joshi-Imre, Z. Fekete: *A softening laminar electrode for recording single unit activity from the rat hippocampus*, *Scientific Reports* **9**, 37237 (2019)
- [2] A. Zátanyi, M. Madarász, Á. Szabó, T. Lőrincz, R. Hodován, B. Rózsa, Z. Fekete: *Transparent, low-autofluorescence microECoG device for simultaneous Ca^{2+} imaging and cortical electrophysiology in vivo*, *Journal of Neural Engineering*, in press (2020), DOI: 10.1088/1741-2552/ab603f
- [3] M. Csernai, S. Borbély, K. Kocsis, D. Burka, Z. Fekete, V. Balogh, S Káli, Z Emri, P. Barthó: *Dynamics of sleep oscillations is coupled to brain temperature on multiple scales*, *The Journal of Neurophysiology* **597**, 4069-4086 (2019)
- [4] Ö. C. Boros, Á. C. Horváth, S. Beleznai, Ö. Sepsi, D. Csósz, Z. Fekete, P. Koppa: *Optimization of an optrode microdevice for infrared neural stimulation*, *Applied Optics* **58**, 3870-3876 (2019)

POLYMER BASED AUTONOMOUS MICROFLUIDIC SYSTEMS FOR MEDICAL DIAGNOSTICS

GINOP-2.3.2-15 „Stratégiai K+F műhelyek kiválósága - Chiptechnológia alkalmazása a humán in vitro fertilizáció eredményességének javításában”

O. Hakkel, A. Füredi, P. Hermann, L. Bató, L. Illés, P. Fürjes

Precise and fast Point of Care (PoC) monitoring of marker molecules or bacteria levels in body fluids or cell culture media could be crucial in effective diagnostics and choosing therapies. Due to the specific tools and novel microtechnology processes the cost-effective, complex but miniaturised analytical systems, such as Lab-on-a-Chip (LoC) and microfluidic devices have become available and applicable for implementing the overall sample analysis from the preparation to the molecular detection. The microfluidic system has to transport the sample and the washing buffer to the active area of the chip meanwhile mix and incubate the sample with the reagents. As the incubation and read-out needs a specified time, precise sample handling and flow control are crucial. The perspective of our work is to develop a polymer based microfluidic cartridge suitable to autonomously controlled sample transport or preparation for integrated bioanalytical device.

In a previous project (Multiparaméteres Point of Care in vitro diagnosztikai rendszerek fejlesztése, KTIA VKSZ_14-1-2015-0004) an autonomous microfluidic system was designed and manufactured for transporting blood or plasma by precisely controlled sample rate. These autonomous sample transport systems were integrated into Point-of-Care Lab-on-a-Chip based diagnostic devices. The developed systems are to be applied for detection cardiovascular diseases in cooperation with 77 Elektronika Ltd. Based on these results we are developing Lab-on-a-Chip based diagnostic device for a specific project of the University of Pécs dedicated to support human in-vitro fertilisation with the 77 Elektronika Ltd. In the actual period the geometry of the microfluidic systems was modified according to the additional requirements of the optical detection method and the real sample. Accordingly a new, actualised microfluidic structure was designed (see Fig. 1.) to be compatible with the applied bioanalytical specifications (targeted detection limits, surface blocking, etc.):



Figure 1: The autonomous microfluidic cartridge proposed for transport culture media applied in human in-vitro fertilisation (left) and its microstructure (SEM image).

The material composition of the pre-industrial / laboratory stage cartridge was optimised according to the required sample flow rate, the optical and mechanical properties. The embedding protocol of PDMS-PEO molecules was optimised considering the applied molecular weight, concentration and the physical parameters of the PDMS polymerisation process (temperature, time, surface treatments of the molding master). The long term stability of the modification is continuously verified. According to the project requirements the geometry and the fabrication protocol will be able to be improved.

MICROFLUIDIC SAMPLE PREPARATION SYSTEM FOR RAPID URINE BACTERIA ANALYSIS

VEKOP-2.2.1-16-2017-00001

A. Bányai, O. Hakkel, P. Hermann, Zs. B. Sik, Z. Hajnal, P. Fürjes

The goal was to develop a single-channel microfluidic cartridge for certain subtasks of sample preparation and handling, which then can be integrated into a measuring instrument. During the optical measurements of bioanalytical tests, the sample handling is solved in an integrated Lab-on-a-Chip cartridge. The cartridge includes transport and filtration of the liquid sample, positioning of bacteria in the detection chamber over the sensing layer, and a microfluidic component for storage of used sample. Accordingly, we focused our attention to develop a passive hydrodynamic unit that is capable of filtering larger elements ($>6\mu\text{m}$) in urine samples and positioning permeated bacteria laterally. In order to achieve this goal, we designed and characterized such units. Simultaneously, single-channel cuvettes were made to test the optical system with the sample solution.

1. The previously designed DLD (deterministic lateral displacement) structures were modified, manufactured and analysed their flow profile with finite element method in COMSOL Multiphysics.
2. A so-called crossflow type filtration system was designed and implemented that is more advantageous regarding high-speed fluid handling. This system provides a continuous mechanical filtration in a microfluidic environment due to its longitudinal arrangement. Conclusions were based on the efficiency of each of the separation geometry.
3. The lateral focusing of the bacteria was accomplished by a hydrodynamic method. The focusing depends on the particle to channel size ratio, which was investigated in an asymmetric fluidic system with variable parameters and special geometry.
4. Single-channel cuvettes were made to optimize the optical measurements. The design advanced over several iterations in order to sufficiently detect the bacteria in the sample solution. The flow profiles were analysed with finite element method and experimentally.

Size dependent sorting of components is essential for effective sample preparation in Lab-on-a-Chip systems. Our goal is to achieve separation of bacteria from residues of urine having diverse sizes, shapes. DLD microchannels were fabricated by soft lithography with six pillar cross-sections: circle, square and triangles with various orientations to test the separation efficiency depending on their shape and arrangement (Fig. 1).

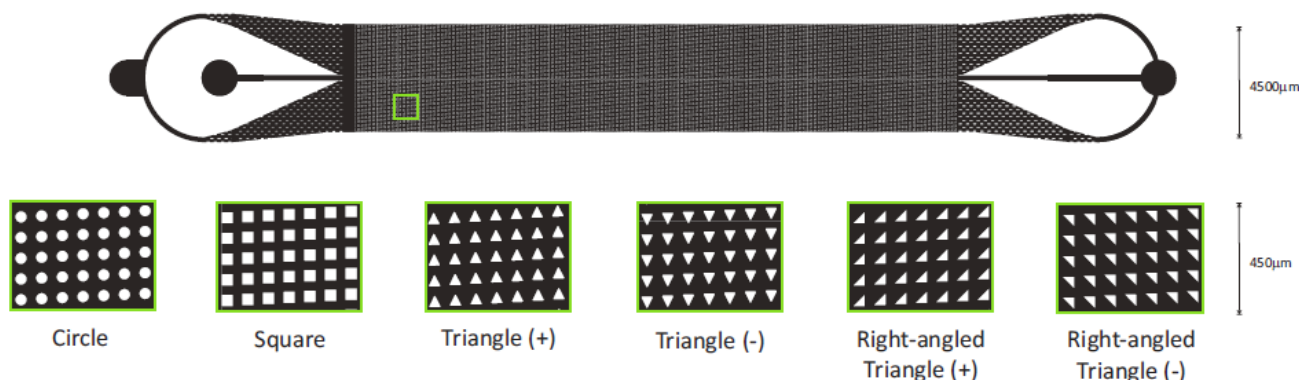


Figure 1: Layout and pillar types of the proposed DLD structure

A suspension of fluorescently labelled microbeads (with 16.5 and 20.4 μm diameters) and Human Serum Albumin (FITC-HSA) were focused between buffer fluids in the device. The separation efficiencies of the individual structures were quantified by the range of bead-deflection from the centred flow. Molecular diffusion was captured by recording the concentration of the diluted FITC-HSA along the channel. Pillars' shape and configuration strongly influence not only the DLD effect, but the concentration profiles determined mainly by diffusion in laminar flow. Deflection of particles and spreading of focused sample stream were explained by FEM simulation considering the pressure distribution and transversal flow generated by inhomogeneous hydrodynamic resistance due to asymmetries as presented in Fig. 2.

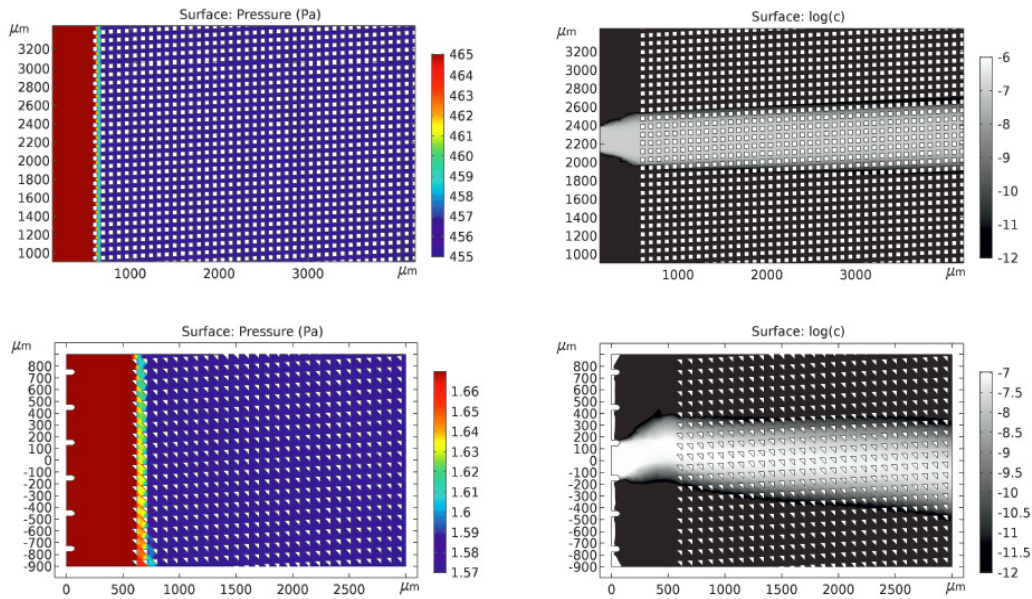


Figure 2: FEM simulation of the flow characteristics in different DLD separation systems

The effects of pillar geometry in microfluidic DLD systems were analysed experimentally and simulated by FEM regarding their separation efficiency. Deflection of particles and spreading of the focused sample stream were recorded and explained by theoretical considerations.

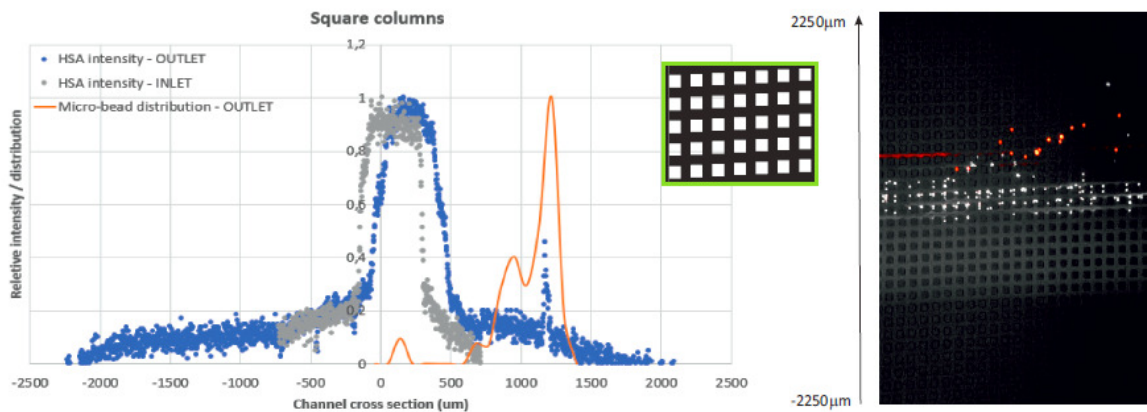


Figure 3: Experimental characterisation of the separation efficiency of the square shaped pillar based DLD microfluidic structure. Bead diameter: 16.5μm (white) / 20.4μm (red) (in the right fluorescent picture)

In order to handle the liquid sample with high-speed in the corresponding volume, the application of crossflow type separation / filtration system proved to be beneficial. The crossflow system achieves a continuous mechanical filtration within a microfluidic environment. The size of the permeable particles determines the geometry of the microchannels, which then filters any particle that is larger in size. Moreover, the longitudinal arrangement allows larger sample volumes without clogging. We tested several geometrically variant separation structures with fluorescent microbeads (diameter ranging from 4.8 μm to 15.8 μm) and different flow velocities.

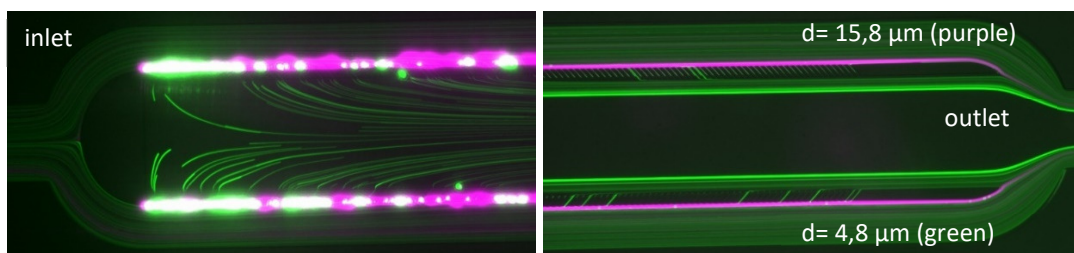


Figure 4: Size dependent filtration of different fluorescent beads in cross-flow type microfluidic separation system (at 3μL/s flow rate)

More efficient filtration achieved at lower flow velocities in the structures, where the surface of the filter is parallel to the flow direction. While the filter surface is less prone to clogging, and bubble trapping. Similar efficiency can be achieved at higher flow velocities in structures, where the surface of the filter is perpendicular to the flow direction. The system is less sensitive to bubble formation; however, clogging is strongly dependent on the particle concentration and saturation is quick.

After filtering every larger component of the urine sample, the permeated bacteria must be vertically and possibly laterally focused in the detection chamber in order to achieve high trapping efficiency on the functionalized surface. The lateral focusing was achieved by a hydrodynamic method. The efficiency of the hydrodynamic focusing depends mainly on the characteristics of the fluidic system and on the particle to channel size ratio. The position of the particle within the flow profile is determined by forces acting on the particle in the fluidic system. The focusing was carried out in an asymmetric microfluidic system with alternating geometric parameters. Fluorescent beads were used in order to mimic the size range of the *E. coli* bacteria. The efficiency of the focusing increased with both the flow velocity and the growing inhomogeneity of the alternating geometric structure (Fig. 5). The behaviour of the microfluidic systems was characterized by finite element methods as well (Fig. 6). [1, 2, 3]

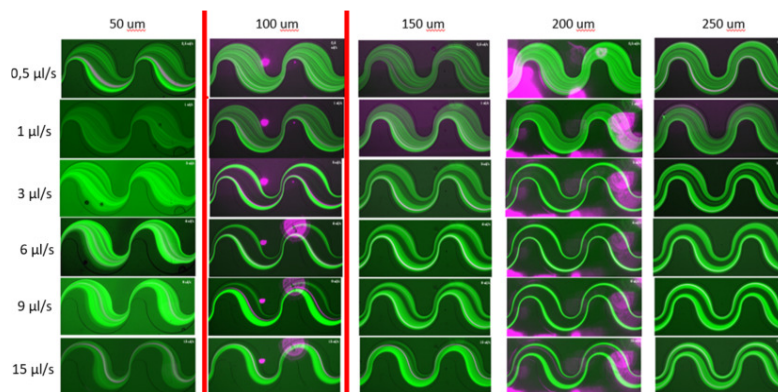


Figure 5: Lateral focusing of fluorescent microbeads ($d = 4.8\mu\text{m}$) in asymmetrically altering microfluidic channels affected by the flow rate and asymmetry parameter (lateral size of the constrains of the channel)

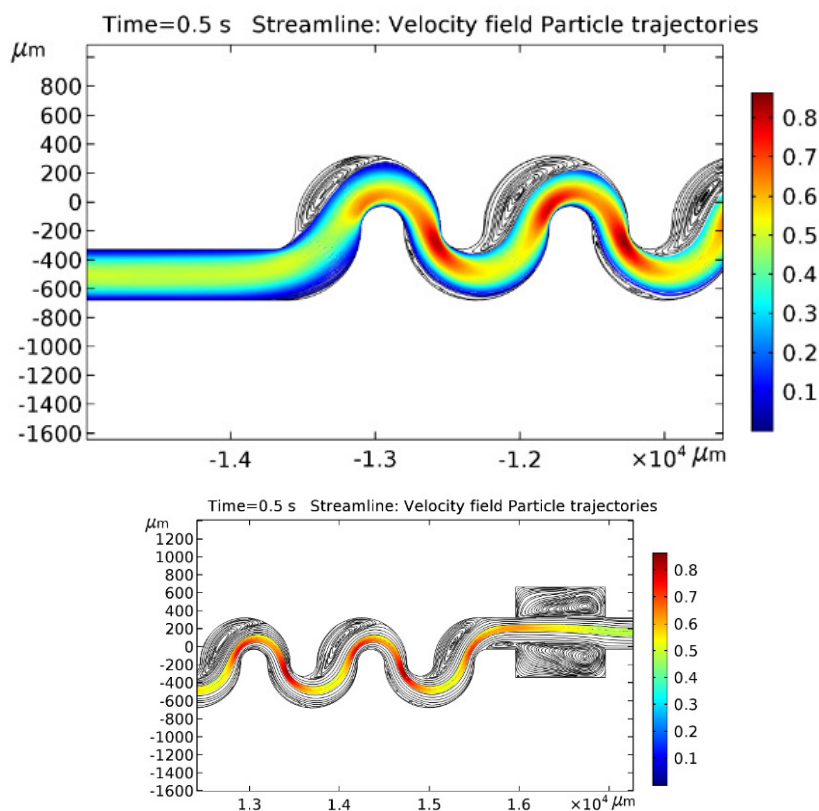


Figure 6: Streamlines and particle trajectories in the focusing microfluidic system at the inlet (left) and the outlet (right) of the 250/1000 μm channel

Related publications

- [1] D. Petrovszki, S. Valkai, E. Gora, M. Tanner, A. Bányai, P. Fürjes, A. Dér: *Dielectrophoretically enhanced detection of E. coli cells by an integrated optical biosensor system*, 45th Int. Conference on Micro & Nanoengineering, Rh odes, Greece, 2019
- [2] D. Petrovszki, S. Valkai, E. Gora, M. Tanner, A. Bányai, P. Fürjes, A. Dér: *E. coli sejtek dielektroforetikusán erősített detektálása integrált optikai bioszenzorral*, a Magyar Biofizikai Társaság XXVII. Kongresszusa, Debrecen, Magyaro. 2019
- [3] A. Bányai, P. Hermann, O. Hakkel, Z. Hajnal, P. Fürjes: *Shape design dependent performance of DLD (deterministic lateral displacement) based particle separation systems - FEM modelling and validation*, Lab-on-a-Chip Europe Conference, Rotterdam, The Netherlands, 2019

MICROFLUIDICALLY INTEGRATED SERS ACTIVE CELL TRAP ARRAY FOR ANALYSIS RED BLOOD CELLS

O. Hakkel, R. Öcsi, Zs. Zolnai, I. Rigó (Wigner FKK), M. Veres (Wigner FKK), P. Fürjes

Surface Enhanced Raman Scattering (SERS) is applied to enhance the Raman signal by several orders of magnitude and significantly improve the sensitivity of the ordinary scattering method. As a result of the electromagnetic enhancement emerging in the vicinity of metallic nanostructures the sensitivity of molecule detection can achieve attomolar concentrations. Thus by using this method efficient detection method can be developed for the analysis of low concentration biological samples assuming that sample transport and preparation system is also integrable. In our case the 3D SERS active structure is simultaneously forming the cell trapping array of the microfluidic system, in line with the concept presented previously.

According to our approach a perforated membrane of tailored size and shape was prepared to be applicable for cell entrapment and highly sensitive detection of molecular components also. Arrays of periodic inverse pyramids were prepared in the 5 μm thick device layer of SOI (silicon-on-insulator) wafers. The 3D structure was shaped by alkaline etching after development of appropriate masking pattern. By the definition of the initial pattern and the device layer thickness the geometry of the truncated pyramids could be fitted to the estimated cell size. Vertical microchannels were revealed by etching away the back-side handler silicon and buried oxide and coated with a 50nm thick evaporated layer of gold. The resulted structure was used as an array of particle traps and SERS substrate simultaneously. Additional sample injection microfluidic channels were formed over the SERS substrate to support the blood transport to the sensing area. Normal blood sample was diluted and injected onto the 3D structure and red blood cells (RBCs) were captured on its surface and in the perforated inverse pyramids. The lateral distribution of the cells was characterized by bright field microscopy and later by scanning electron microscopy (SEM) as presented in Fig. 1.

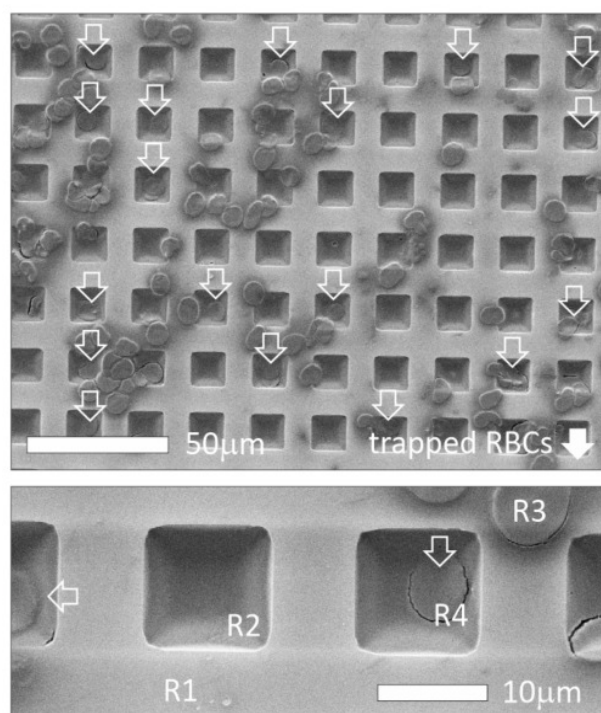


Figure 1: SEM image of the entrapped RBCs on the SERS substrate. The empty wells are filled by plasma. Note, that the structure was covered with a 50nm Au layer before SEM microscopy.

Trapped RBCs and blood plasma were also analysed on the flat gold surface and in the inverse pyramid structures by Raman spectroscopy. Centrifuged blood plasma was also analysed on a specific SERS substrate, where the hierarchically combined micro- and nanostructures achieve significant SERS enhancement. The SERS spectra of the RBC and blood plasma were compared. The differential spectrum is demonstrated and the most relevant molecular components of the Red Blood Cells are indicated in Fig. 2. The primary component of the RBCs is the hemoglobin molecule which has significant resonant peaks at: 570 cm^{-1} (FeO_2), 670 cm^{-1} and 750 cm^{-1} (pyrrole), 820 cm^{-1} and 1550 cm^{-1} (tyrosine and phenylalanine), 1227 cm^{-1} (CH group of hemoglobin). These peaks refer to the major molecular components of the RBCs, as membrane lipids, hemoglobin, etc. The applicability of special perforated periodic 3D SERS structure was demonstrated for simultaneous cell trapping and sensitive Surface-Enhanced Raman Spectroscopy based detection of characteristic molecular vibrations of the blood and red blood cell components. [1, 2]

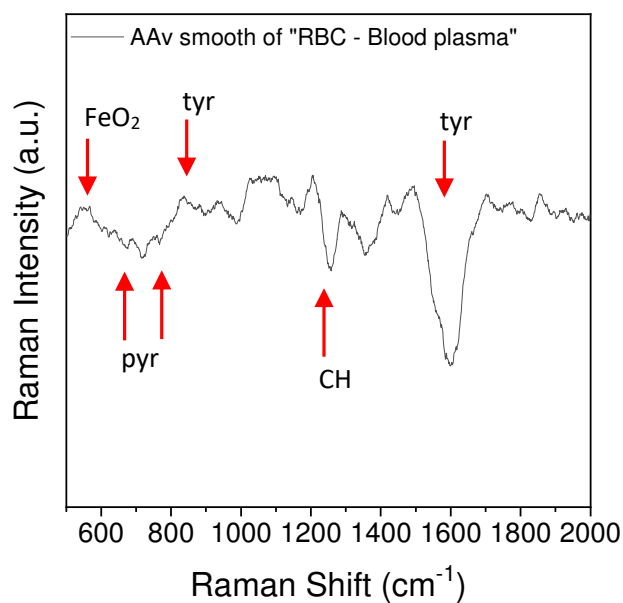


Figure 2: Differential SERS spectrum of the RBC and plasma, obtained by subtraction of normalized plasma SERS spectrum from RBC SERS spectrum. Peaks at: 570cm^{-1} (FeO_2), 670cm^{-1} and 750cm^{-1} (pyrrole - pyr), 820cm^{-1} and 1550cm^{-1} (tyrosine - tyr and phenylalanine), 1227cm^{-1} (CH group of hemoglobin).

Related publications

- [1] I. Rigó, M. Veres, T. Váczi, E. Holczer, O. Hakkel, A. Deák, P. Fürjes: *Preparation and Characterization of Perforated SERS Active Array for Particle Trapping and Sensitive Molecular Analysis*, *Biosensors* **9:3** Paper:93, 9 (2019)
- [2] O. Hakkel, I. Rigó, M. Veres, P. Fürjes: *Microfluidically Integrated SERS Active Cell Trap Array for Sensitive Analysis of Red Blood Cells Transducers & Eurosensors*, 2019 Conferences, Berlin, Germany, 2019

MODELLING AND ANALYSING OF FLUID DYNAMIC PHENOMENA IN TWO-PHASE MICROFLUIDIC SYSTEMS

Zs. Szomor, Z. Hajnal, P. Fürjes

We are facing many problems that necessitate moving, manipulating, sorting, counting or analysing localised cells and particles with commensurate dimensions. The response of the individual cells to physical and chemical effects can be precisely analysed in the cell-size scale micro-environment. Two-phase microfluidic systems can create such a specific environment by generating monodisperse microemulsions as cell traps. The long-term goal of our research is to design and create a microfluidic system that generates a specific chemical environment in cell-size trapping in containers. However, understanding and designing physical processes on the microscale is quite challenging, thus deeper characterisation of the behaviour of the fluids in such environment is crucial. During the work, we have investigated the design, preparation and analysis of two-phased microfluidic devices, being able to generate controlled microdroplets and change the chemical environment within them.

Two-phase microfluidic systems have been manufactured by soft lithography technology in Polydimethylsiloxane (PDMS) polymer. A stable emulsion of an oil and water phase was prepared in the devices and the influence of the hydrodynamic and geometric parameters on the droplet sizes was determined.

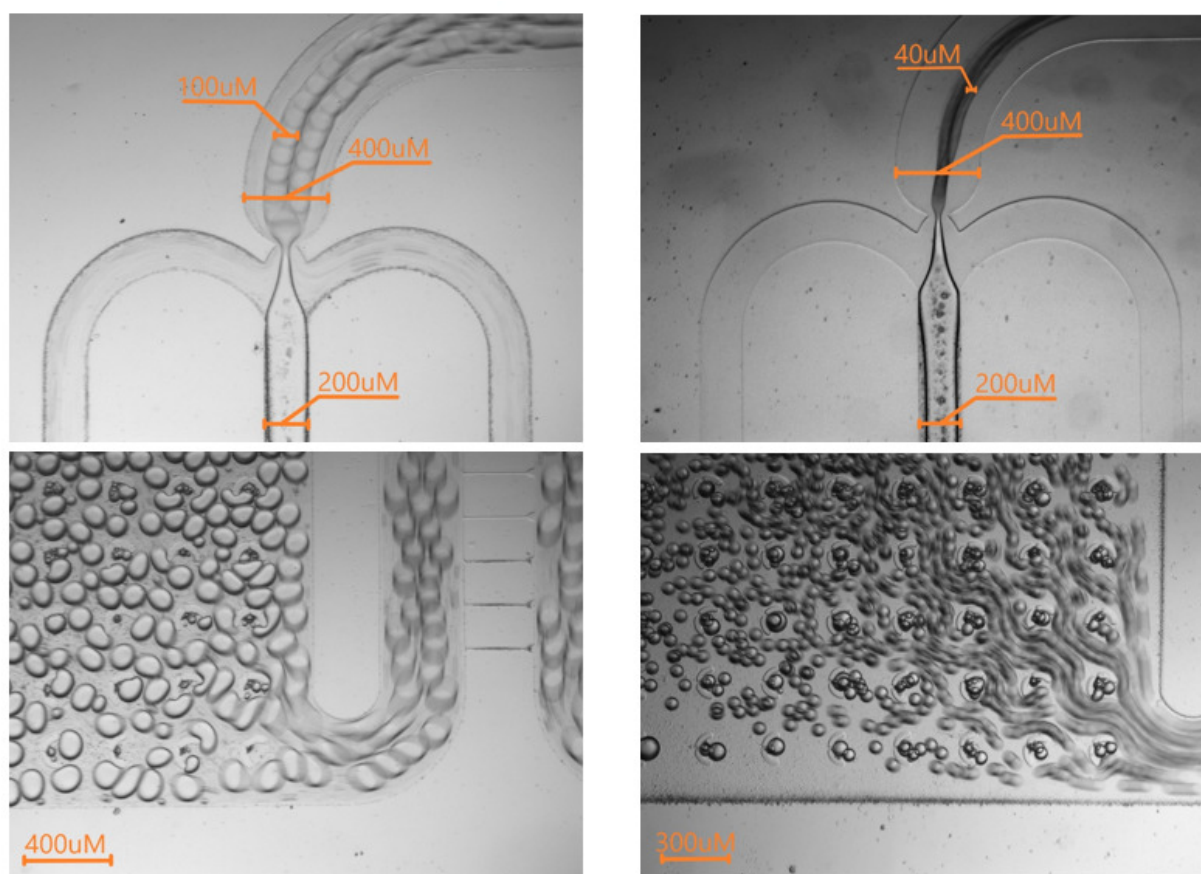


Figure 1: Droplet generation in junction type two-phase microfluidic system in case different flow rates of the dispersed (water) and continuous (oil) phase. The applied flow rates are: water – $0.1\mu\text{l/s}$ / oil – $0.3\mu\text{l/s}$ (left) and $0.4\mu\text{l/s}$ (right).

The key parameters of the droplet formation have also been studied by finite element modelling (FEM) and simulations, using available standard methods of multiphase dynamics in Comsol Multiphysics. The influence of volume flow ratio at the inlets, viscosity of the fluids, and interface tension were determined in successive parametric sweep simulations as presented in Fig. 2. The advantages and disadvantages of the different design geometries have been revealed also. [1]

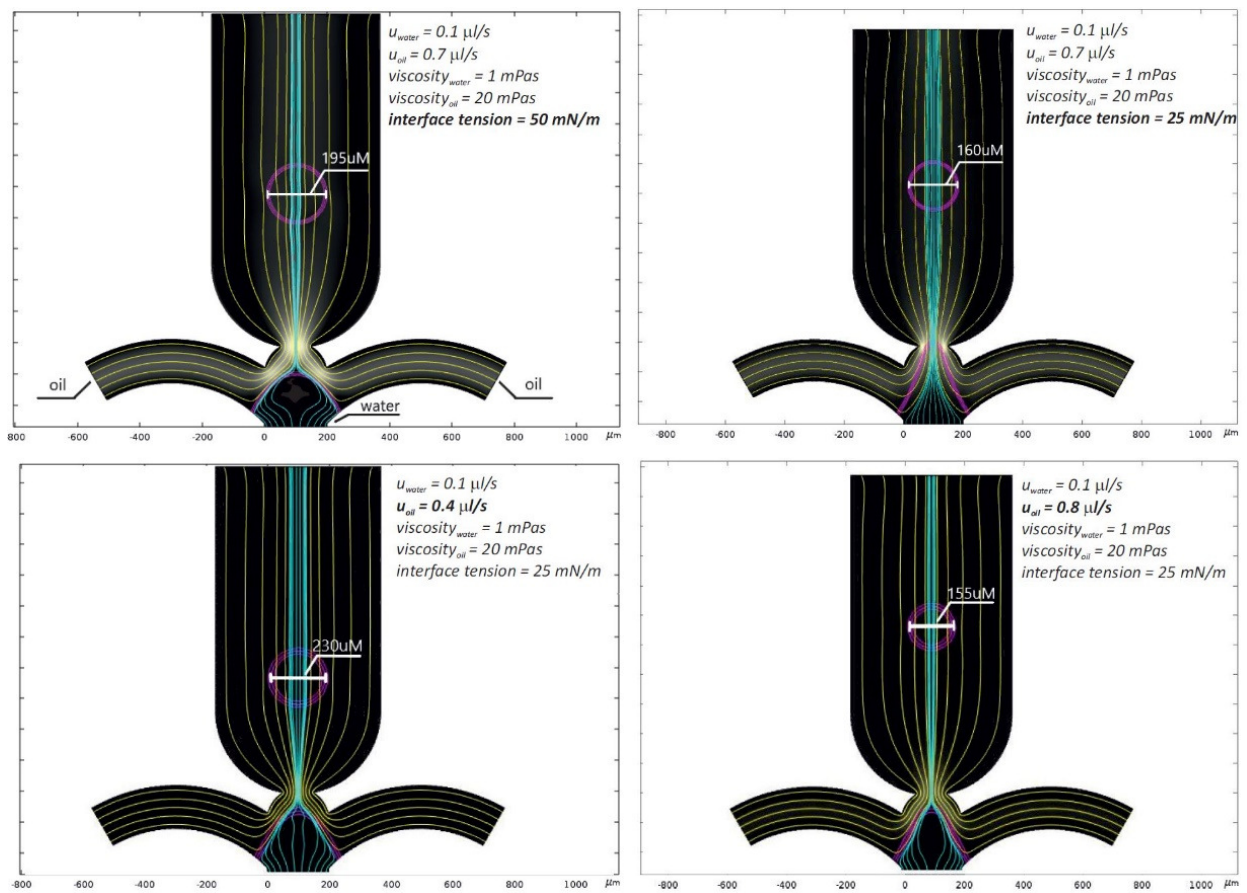


Figure 2: Influence of the interface tension and flow rate ratios on the droplet formation process (droplet size) – FEM simulation

Related publication

- [1] P. Hermann, Zs. Szomor, O. Hakkel, Z. Hajnal, P. Fürjes: *Effects of hydrodynamic parameters of droplet formation in two-phase microfluidic structures*, Lab-on-a-Chip Europe Conference, Rotterdam, The Netherlands, 2019

NEAR INFRARED LED DEVICES FOR SPECTROSCOPIC APPLICATIONS: DEVELOPMENT AND SMALL SCALE PRODUCTION OF NEAR INFRARED LEDs AND LED BASED DEVICES

F. Bíró, I. Réti, G. Battistig, Z. Szabó

Infrared spectroscopy is a very popular measurement technique especially in food industry, pharmaceutical industry and agriculture for the detection and measurement of organic materials. The -OH, -NH and -CH functional groups found in organic substances can frequently be detected by spectroscopy through absorbance measurements at the resonance wavelength of valence-bond vibrations. The measured wavelengths are 4-2.5 μm , while the signal to noise ratio of photon detectors is low due to moderate thermal noise at room temperature. The 1st-3rd harmonic absorption bands are located in the range of the near infrared (NIR), where smaller signals can be measured effectively in practice. NIR LEDs have narrow wavelength, therefore they are suitable for measurements at given wavelength. Further advantages of LEDs compared to incandescent lamps are their small dimensions, high efficiency, and low power consumption, which is critical in small handheld devices.

GaInAsP/InP is an ideal material system for the fabrication of double heterostructure devices as the emission wavelength is easily tuneable between 0.950-1.650 μm . As InP has higher bandgap than the lattice-matched GaInAsP active layer the absorption losses inside the device structure can be minimized. In order to tune the emission wavelength of the LED, the composition of the semiconductor light-emitting layer has to be properly set. When a secondary or multi-peak emission is preferred e.g. in spectroscopic applications, various solid-state solutions can be considered:

1. Application of LED array of different single-peak emissions to cover the whole spectrum or emit at specific peaks the application requires. This approach is widely known and viable, however it suffers from geometric constraints and also from the different temperature dependence of emission of each LED. This makes the intensity control complicated.
2. A more viable solution is our novel single chips what exhibit multiple emission peaks. As we demonstrated earlier (patent pending and publications in 2017) the source of the primary electroluminescent light is the active layer of the diode, but this light also excites a second smaller band gap layer, thereof producing secondary light by photoluminescence. The key element of chip production is liquid-phase epitaxy. Our recent and ongoing development is twofold: Demonstration a measuring technique using double-wavelength LED as light source and wavelength-selective photodiodes as photodetectors.

The photodiodes were fabricated similarly to the NIR LEDs and mounted in a single Transistor Outline (TO)-package. We have chosen ethanol-water system and matching wavelengths to certain -OH and -CH absorption peaks to be able to measure ethanol concentration with 0.1% resolution. Fig. 1 represents the transmission spectra of EtOH-H₂O mixtures as illuminated by a double peak LED.

Moreover, the modified LEDs can be used as photodiodes with proper cut-off at the required wavelength. Also the proper modification of the double-peak LED provides a selective narrow band photodiodes. Demonstration device have constructed using double wavelength LED, two photodiodes in single TO-package and custom-made analogue and digital electronics. The sealed sensor head containing the light source, the photodiodes and a mirror in trans-reflectance configuration sinks in the measured liquid. [1]

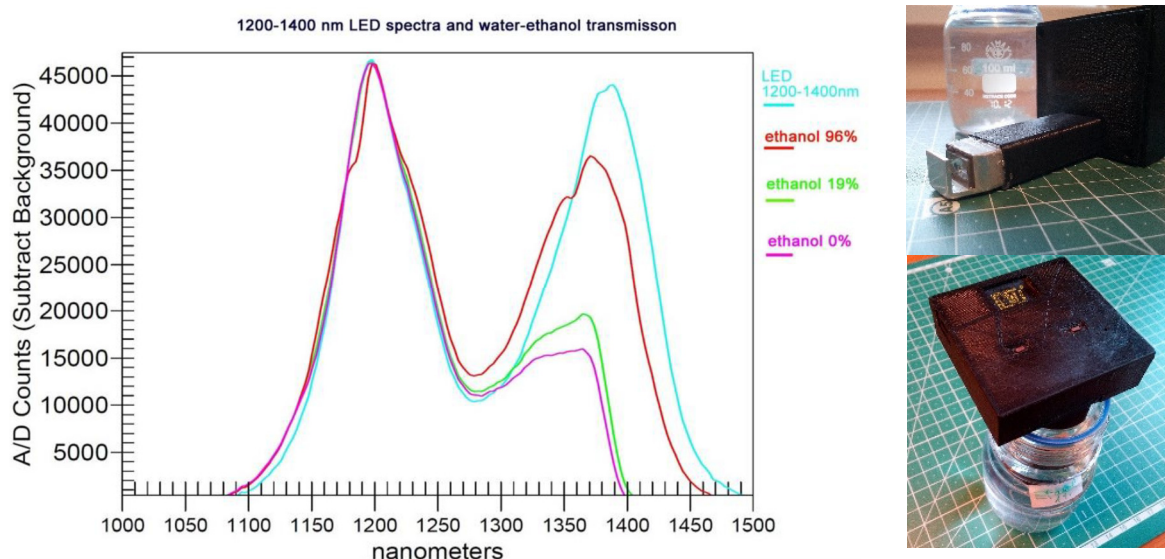


Figure 1: Transmission spectra of water-ethanol mixtures illuminated by a double peak single-chip LED (light blue) (left) and the demonstration device for selective spectroscopic application using dual-wavelength LED (right)

The feasibility of both the 3- and 4-peak single chip LEDs were successfully demonstrated and the early results were presented in the European Materials Research Society (E-MRS) 2019 Spring Meeting (Fig. 2.). However, the reliable fabrication technology is still under development before entering in the market. The promise is to be able to produce a wide band (1000-1700nm) NIR LED with excellent optical and thermal parameters. Manufacturing wide spectra point-like light source opens the way towards miniature spectroscopic devices.

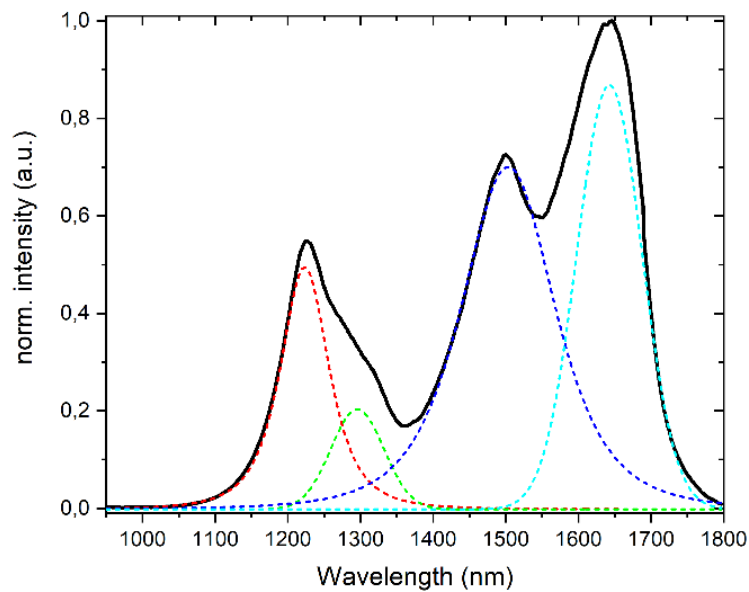


Figure 2: Emission spectrum of the fabricated single LED chip emitting at four different wavelengths

Our business partners are SENOP Oy (Fi) and Anton Paar Ltd. (At). Another Canadian tech company is also interested in high power single emission peak LEDs of the upper wavelength regime for solar simulator purposes.

Related publication

- [1] Z. Szabó: *Wide emission-spectrum NIRLED based on efficient photon-recycling*, E-MRS 2019 Spring Meeting, Nizza, France, 2019

ADHESION FORCE MEASUREMENTS ON FUNCTIONALIZED MICROBEADS: AN IN-DEPTH COMPARISON OF COMPUTER CONTROLLED MICROPIPETTE AND FLUIDIC FORCE MICROSCOPY

ÚNKP-18-3, LP2012-26/2012 Lendület, OTKA KKP129936, OTKA KH126900, OTKA ERC_HU117755

T. Gerecsei, I. Erdődi, B. Peter, Cs. Hős, S. Kurunczi, I. Derényi, B. Szabó, R. Horváth

Characterization of the binding of functionalized microparticles to surfaces with a specific chemistry sheds light on molecular scale interactions. Polymer or protein adsorption are often monitored by colloid particle deposition. Force measurements on microbeads by atomic force microscopy (AFM) or optical tweezers are standard methods in molecular biophysics, but typically have low throughput. Washing and centrifuge assays with (bio)chemically decorated microbeads provide better statistics, but only qualitative results without a calibrated binding force or energy value. In the present work we demonstrate that a computer controlled micropipette (CCMP) is a straightforward and high-throughput alternative to quantify the surface adhesion of functionalized microparticles. However, being an indirect force measurement technique, its in-depth comparison with a direct force measurement is a prerequisite of applications requiring calibrated adhesion force values. To this end, we attached polystyrene microbeads to a solid support by the avidin-biotin linkage. We measured the adhesion strength of the microbeads with both a specialized robotic fluid force microscope (FluidFM BOT) and CCMP. Furthermore, the bead-support contact zone was directly characterized on an optical waveguide biosensor to determine the density of avidin molecules. Distribution of the detachment force recorded on ~50 individual beads by FluidFM BOT was compared to the adhesion distribution obtained from CCMP measurements on hundreds of individual beads. We found that both methods provide unimodal histograms. We conclude that FluidFM BOT can directly measure the detachment force curve of 50 microbeads in 150 min. CCMP can provide calibrated binding/adhesion force values of 120 microbeads in an hour. Schematic illustration of the mentioned methods is in Fig. 1. [1].

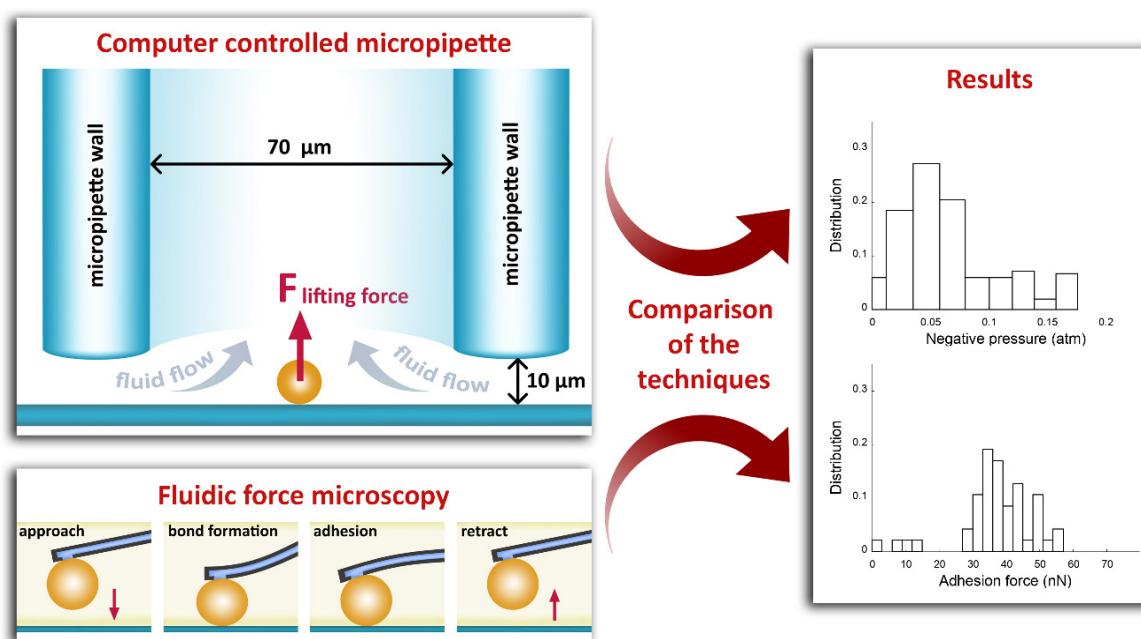


Figure 1: Schematic illustration of the methods. Adhesion force measurements on microbeads were performed by using computer controlled micropipette (CCMP) and Fluidic force microscopy. The obtained results by the two techniques had been compared.

Related publication

- [1] T. Gerecsei, I. Erdődi, B. Peter, Cs. Hős, S. Kurunczi, I. Derényi, B. Szabó and R. Horváth: *Adhesion force measurements on functionalized microbeads: An in-depth comparison of computer controlled micropipette and fluidic force microscopy*, Journal of Colloid and Interface Science **555**, 245-253 (2019)

SPRING CONSTANT AND SENSITIVITY CALIBRATION OF FLUIDFM MICROPIPETTE CANTILEVERS FOR FORCE SPECTROSCOPY MEASUREMENTS

LP2012-26/2012 Lendület, OTKA KKP129936, OTKA KH126900, OTKA ERC_HU117755

Á. G. Nagy, J. Kámán, R. Horváth, A. Bonyár

FluidFM technique can be considered as the nanofluidic extension of the atomic force microscope (AFM). Schematic illustration of the method is in Fig 1. This novel instrument facilitates the experimental procedure and data acquisition of force spectroscopy (FS) and is also used for the determination of single-cell adhesion forces (SCFS) and elasticity. FluidFM uses special probes with an integrated nanochannel inside the cantilevers supported by parallel rows of pillars. However, little is known about how the properties of these hollow cantilevers affect the most important parameters which directly scale the obtained spectroscopic data: the inverse optical lever sensitivity (InvOLS) and the spring constant (k). The precise determination of these parameters during calibration is essential in order to gain reliable, comparable and consistent results with SCFS. Demonstrated by our literature survey, the standard error of previously published SCFS results obtained with FluidFM ranges from 11.8% to 50%. The question arises whether this can be accounted for by biological diversity, or this may be just the consequence of improper calibration. Thus, the aim of our work was to investigate the calibration accuracy of these parameters and their dependence on: (1) the aperture size (2, 4 and 8 μm) of the hollow micropipette type cantilever; (2) the position of the laser spot on the back of the cantilever; (3) the substrate used for calibration (silicon or polystyrene). It was found that both the obtained InvOLS and spring constant values depend significantly on the position of the laser spot. Apart from the theoretically expectable monotonous increase in InvOLS (from the tip to the base of the cantilever, as function of the laser spot's position), we discerned a well-defined and reproducible fluctuation, which can be as high as $\pm 30\%$, regardless of the used aperture size or substrate type. The calibration of spring constant also showed an error in the range of $-13/+20\%$, measured at the first 40 μm from the tip of the cantilever. Based on our results a calibration strategy is proposed. The optimal laser-spot position which yields the most reliable spring constant values was determined and found to be on the first pair of pillars. The proposed method helps in reducing the error introduced via improper calibration and thus increases the reliability of subsequent cell adhesion force or elasticity measurements with FluidFM [1].

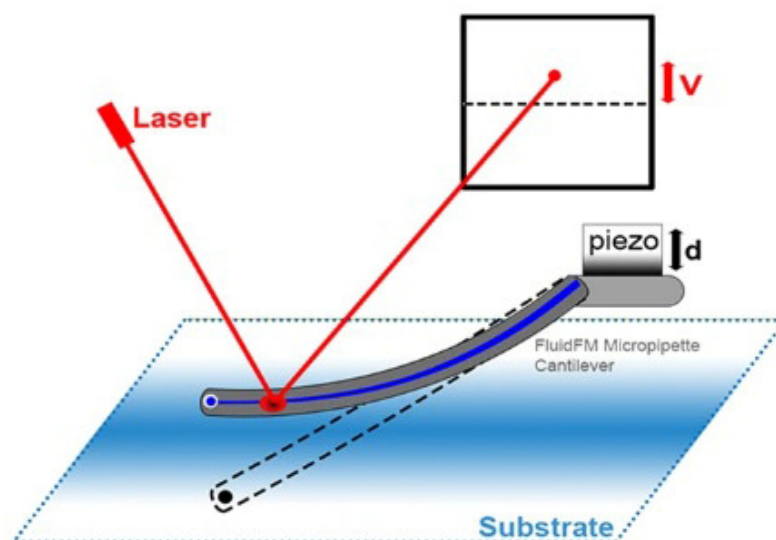


Figure 1: Illustration of the laser beam reflection based optical setup of the FluidFM system

Related publication

- [1] Á. G. Nagy, J. Kámán, R. Horváth, and A. Bonyár: *Spring constant and sensitivity calibration of FluidFM micropipette cantilevers for force spectroscopy measurements*, Scientific Reports **9**, 10287 (2019)

A PRACTICAL REVIEW ON THE MEASUREMENT TOOLS FOR CELLULAR ADHESION FORCE

LP2012-26/2012 Lendület, OTKA KKP129936, OTKA KH126900, OTKA ERC_HU117755, PD 124559, Bolyai Scholarship

R. Ungai-Salánki, B. Peter, T. Gerecsei, N. Orgován, R. Horváth, B. Szabó

Cell-cell and cell-matrix adhesions are fundamental in all multicellular organisms. They play a key role in cellular growth, differentiation, pattern formation and migration. Cell-cell adhesion is substantial in the immune response, pathogen-host interactions, and tumour development. The success of tissue engineering and stem cell implantations strongly depends on the fine control of live cell adhesion on the surface of natural or biomimetic scaffolds. Therefore, the quantitative and precise measurement of the adhesion strength of living cells is critical, not only in basic research but in modern technologies, too. Several techniques have been developed to quantify cell adhesion. All of them have their pros and cons, which has to be carefully considered before the experiments and interpretation of the recorded data. The current review provides guidance to choose the appropriate technique to answer a specific biological question or to complete a biomedical test by measuring cell adhesion (Fig.1.) [1].

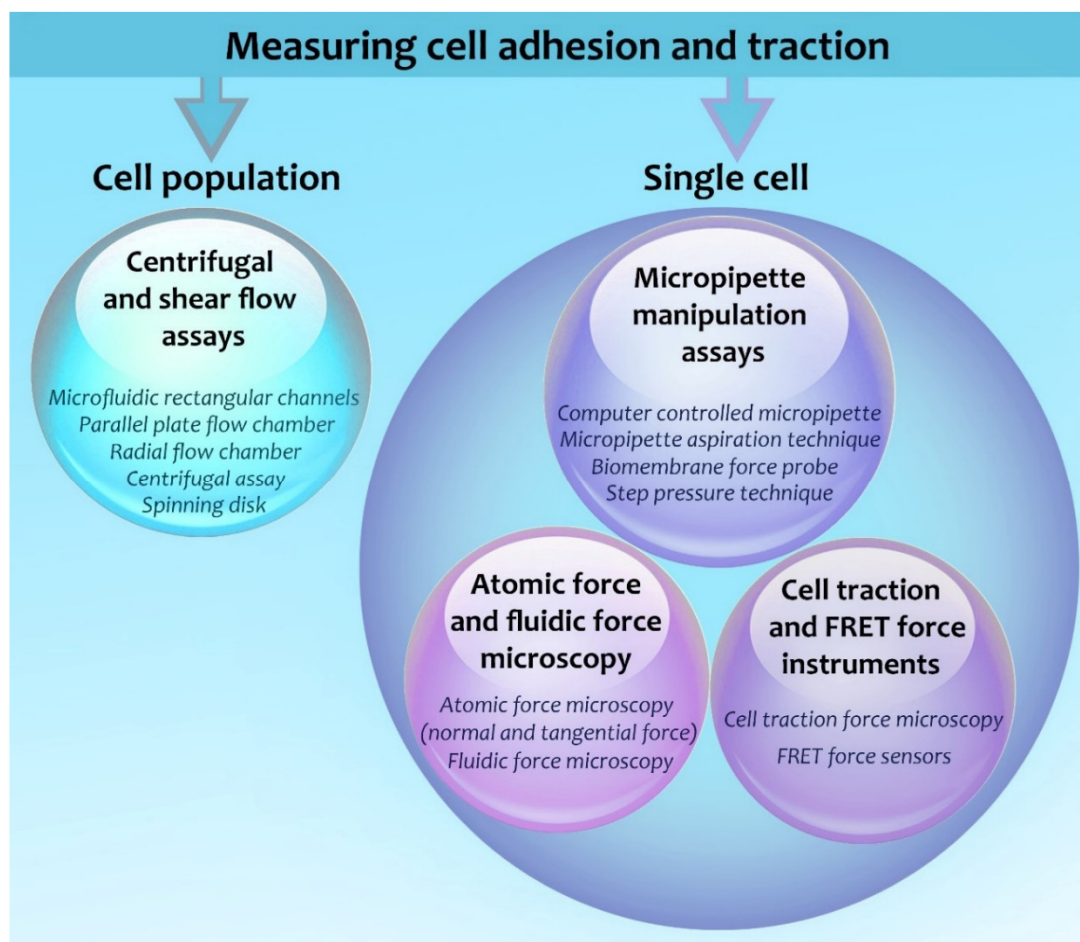


Figure 1: Assays to measure cell adhesion and traction. These techniques are discussed in the review article.

Related publication

- [1] R. Ungai-Salánki, B. Peter, T. Gerecsei, N. Orgován, R. Horváth and B. Szabó: *A practical review on the measurement tools for cellular adhesion force*, *Advances in Colloid and Interface Science* **269**, 309-333 (2019)

MODELLING OF LABEL-FREE OPTICAL WAVEGUIDE BIOSENSORS WITH SURFACES COVERED PARTIALLY BY VERTICALLY HOMOGENEOUS AND INHOMOGENEOUS FILMS

LP2012-26/2012 Lendület, OTKA KKP129936, OTKA KH126900, OTKA ERC_HU117755

B. Kovács, R. Horváth

Optical Waveguide Lightmode Spectroscopy (OWLS) is widely applied to monitor protein adsorption, polymer self-assembly, and living cells on the surface of the sensor in a label-free manner. Typically, to determine the optogeometrical parameters of the analyte layer (adlayer), the homogeneous and isotropic thin adlayer model is used to analyse the recorded OWLS data. However, in most practical situations, the analyte layer is neither homogeneous nor isotropic. Therefore, the measurement with two waveguide modes and the applied model cannot supply enough information about the parameters of the possible adlayer inhomogeneity and anisotropy. Only the so-called quasi-homogeneous adlayer refractive index, layer thickness, and surface mass can be determined. In the present work, we construct an inhomogeneous adlayer model (Fig. 1.). In our model, the adlayer covers the waveguide surface only partially and it has a given refractive index profile perpendicular to the surface of the sensor. Using analytical and numerical model calculations, the step-index and exponential refractive index profiles are investigated with varying surface coverages from 0 to 100%. The relevant equations are summarized and three typically employed waveguide sensor structures are studied in detail. We predict the errors in the calculated optogeometrical parameters of the adlayer by simulating the OWLS measurement on an assumed inhomogeneous adlayer.

We found that the surface coverage has negligible influence on the calculated refractive index for film thicknesses below 5 nm; the calculated refractive index is close to the refractive index of the adlayer islands. But the determined quasi-homogeneous adlayer refractive index and surface mass are always underrated; the calculated quasi-homogeneous thickness is heavily influenced by the surface coverage. Depending on the refractive index profile, waveguide geometry, and surface coverage, the thickness obtained from the homogeneous and isotropic modelling can possess negative and largely overestimated values, too. Therefore, experimentally obtained unrealistic adlayer values, which were dismissed previously, might be important indicators of the layer structure [1].

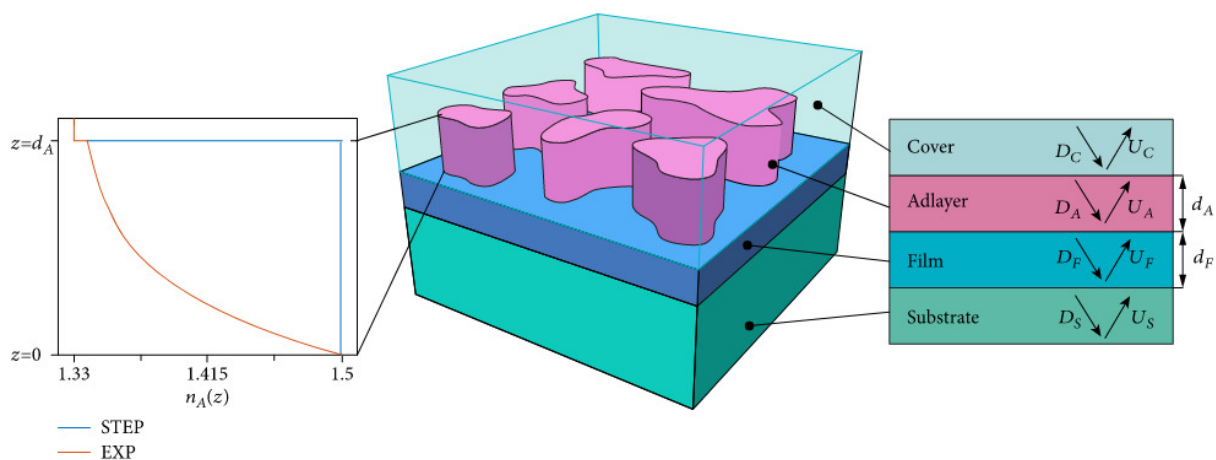


Figure 1: The structure of the modelled OWLS waveguide chips with inhomogeneous adlayer. The modelled multilayered assembly consists of four layers: substrate, waveguide film, adlayer, and cover.

Related publication

- [1] B. Kovacs and R. Horvath: Modeling of label-free optical waveguide biosensors with surfaces covered partially by vertically homogeneous and inhomogeneous films, *Journal of Sensors*, **1762450**, (2019)

BIOMIMETIC DEXTRAN-BASED HYDROGEL LAYERS FOR CELL MICROPATTERNING OVER LARGE AREAS USING THE FLUIDFM BOT TECHNOLOGY

LP2012-26/2012 Lendület, OTKA KKP129936, OTKA KH126900, OTKA ERC_HU117755, OTKA FK128901, Bolyai Scholarship

Saftics, B. Türk, A. Sulyok, N. Nagy, T. Gerecsei, I. Székács, S. Kurunczi, R. Horváth

Micropatterning of living single cells and cell clusters over millimeter–centimeter scale areas is of high demand in the development of cell-based biosensors. Micropatterning methodologies require both a suitable biomimetic support and a printing technology. In this work, we present the micropatterning of living mammalian cells on carboxymethyl dextran (CMD) hydrogel layers using the FluidFM BOT technology (Fig. 1.). In contrast to the ultrathin (few nanometers thick in dry state) CMD films generally used in label-free biosensor applications, we developed CMD layers with thickness of several tens of nanometres in order to provide support for the controlled adhesion of living cells. The fabrication method and detailed characterization of the CMD layers are also described. The antifouling ability of the CMD surfaces is demonstrated by in situ optical waveguide lightmode spectroscopy measurements using serum modelling proteins with different electrostatic properties and molecular weights. Cell micropatterning on the CMD surface was obtained by printing cell adhesion mediating cRGDfK peptide molecules (cyclo(Arg-Gly-Asp-d-Phe-Lys)) directly from aqueous solution using microchanneled cantilevers with subsequent incubation of the printed surfaces in the living cell culture. Uniquely, we present cell patterns with different geometries (spot, line, and grid arrays) covering both micrometre and millimetre–centimetre scale areas. The adhered patterns were analysed by phase contrast microscopy and the adhesion process on the patterns was real-time monitored by digital holographic microscopy, enabling to quantify the survival and migration of cells on the printed cRGDfK arrays [1].

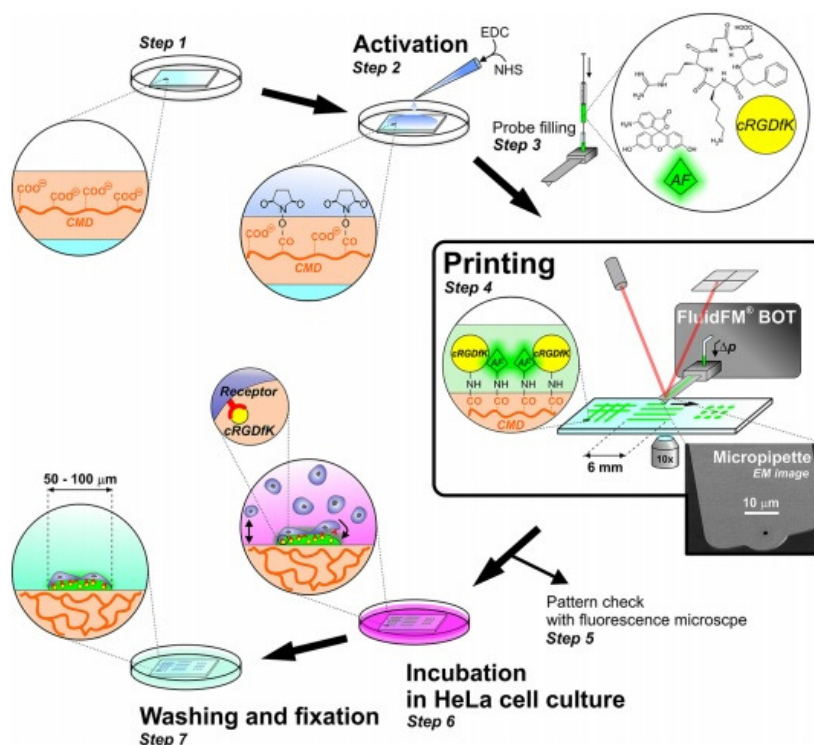


Figure 1: Method used for cell adhesion experiments on the cRGDfK-printed CMD surface, where microprinting was performed with the FluidFM technique

Related publication

- [1] A. Saftics, B. Türk, A. Sulyok, N. Nagy, T. Gerecsei, I. Szekacs, S. Kurunczi and R. Horvath: *Biomimetic Dextran-Based Hydrogel Layers for Cell Micropatterning over Large Areas Using the FluidFM BOT Technology*, *Langmuir*, **35(6)**, 2412-2421 (2019)

OXIDIZATION INCREASES THE BINDING OF EGCG TO SERUM ALBUMIN REVEALED BY KINETIC DATA FROM LABEL-FREE OPTICAL BIOSENSOR WITH REFERENCE CHANNEL

LP2012-26/2012 Lendület, OTKA KKP129936, OTKA KH126900, OTKA ERC_HU117755

B. Péter, A. Saftics, B. Kovács, S. Kurunczi, R. Horváth

Epigallocatechin-gallate (EGCG) is the main polyphenol ingredient of green tea. This compound is a strong antioxidant and oxidizes easily. Numerous studies demonstrated its beneficial effects on the human health, for example its anticancer and anti-inflammatory activity. In the body, EGCG is transported by serum albumin. EGCG easily oxidizes and the interactions of the oxidized form presumably present significant differences. However, the presence of oxidized EGCG is usually neglected in the literature and its effects have not been investigated in detail. Here, we applied the label-free grating coupled interferometry method that performs dual-channel measurements. The measured kinetic signal can be compensated with a signal of a reference channel at each measurement time (Fig. 1.). By testing both hydrophilic and hydrophobic platforms, we found that EGCG can bind to a wide range of surfaces. Exploiting the dual-channel referencing ability as well as the unique sensitivity and throughput of the employed label-free technique, the experiments revealed the specific interactions between bovine serum albumin (BSA) and EGCG and determined the characteristic dissociation constant (K_d) of the binding equilibrium. The obtained binding constants were compared to literature values, showing reasonable agreement with NMR data. Besides the native EGCG, the oxidized form of EGCG was also examined, whose binding behaviours to serum albumins have never been studied. Over-stoichiometric binding obtained; BSA has stronger and weaker binding sites, which could be characterized by two separate K_d values. Furthermore, EGCG oxidization increased the bound amount [1].

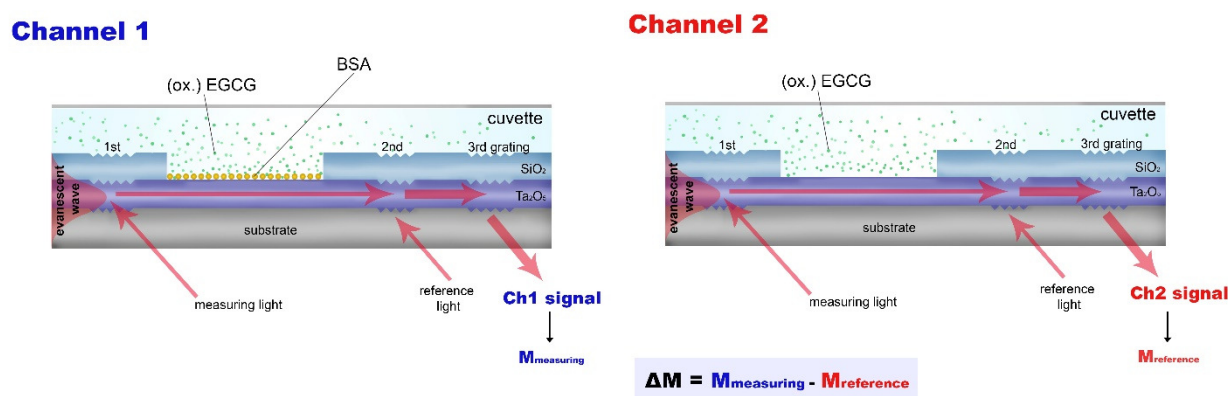


Figure 1: The sensor chips used in the WAVE instrument have two channels; one for measuring the interaction between the immobilized bioreceptor and the analyte (measuring channel, channel 1) and one for subtracting the channel 1 signal by a reference signal (reference channel, channel 2). In our case, BSA was immobilized on channel 1 surface, while channel 2 remained unmodified.

Related publication

- [1] B. Peter, A. Saftics, B. Kovacs, S. Kurunczi and R. Horvath: Oxidization increases the binding of EGCG to serum albumin revealed by kinetic data from label-free optical biosensor with reference channel, *Analyst* **145**(2), (2019)

IN VITRO SOD-LIKE ACTIVITY OF MONO- AND DI-COPPER COMPLEXES WITH A PHOSPHONATE SUBSTITUTED SALAN-TYPE LIGAND

LP2012-26/2012 Lendület, OTKA KKP129936, OTKA KH126900, OTKA ERC_HU117755, OTKA FK128901, Bolyai Scholarship

I. Székács, P. Tokarz, R. Horváth, K. Kovács, A. Kubas, M. Shimura, J. Brasun, V. Murzing, W. Caliebe, Z. Szewczuk, A. Paluch, L. Wojnárovits, T. Tóth, J. S.Pap, Ł. Szyrwił

SALAN- and SALAN-based complexes with catalytically active metal centres are very promising small molecules to be utilized as part of antioxidant therapies. Here we discuss a modified SALAN-type molecule armed with two phosphonate groups that significantly increase its water solubility and aid to furnish mono- or di-nuclear complexes with Cu^{2+} ions. The regulation of the Superoxide dismutase (SOD)-mimicking (i.e., catalytic) disproportionation reaction of the superoxide radical anion ($\text{O}_2^{\bullet-}$) at pH ~ 7.5 could be achieved by adjusting the metal-to-ligand stoichiometry as confirmed by McCord-Fridovich and pulse radiolysis tests. The higher antioxidant activity of the dicopper complex can be explained by the better access of $\text{O}_2^{\bullet-}$ to the copper centres and their more positive $\text{Cu(II)}/\text{Cu(I)}$ redox potential. Simultaneously the analysis of in vitro effect on cells morphology (Fig. 1.) indicates that cytotoxicity is also affected by the metal-to-ligand ratio, however, the active complex molecules do not show notable cytotoxicity that, together with the observed SOD-like activities, makes them potential candidates for antioxidant therapies [1].

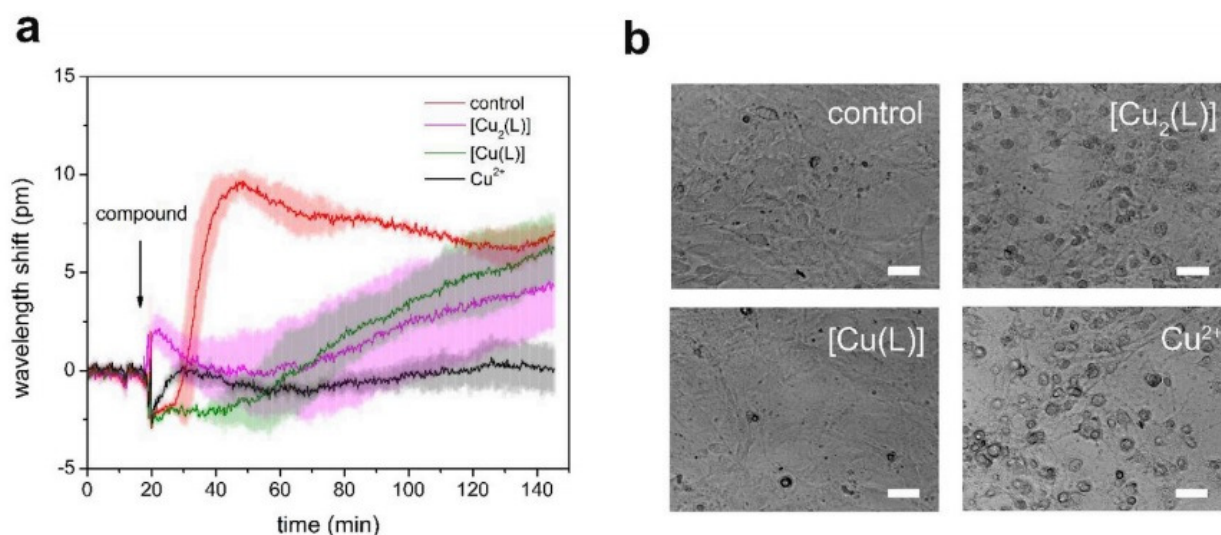


Figure 1: Response of the MC3T3-E1 cells to the treatment with Cu-complexes detected with Epic BT (a). Phase contrast images (scale bar: 50 μm) show morphology of cells on the biosensor surfaces after 24 h incubation with tested compounds (b).

Related publication

- [1] I. Székács, P. Tokarz, R. Horvath, K. Kovács, A. Kubas, M. Shimura, J. Brasun, V. Murzing, W. Caliebe, Z. Szewczuk, A. Paluch, L. Wojnárovits, T. Tóth, J. S.Pap and Ł. Szyrwił: *In vitro SOD-like activity of mono- and di-copper complexes with a phosphonate substituted SALAN-type ligand*, *Chemico-Biological Interactions* **306**, (2019)

AN IMPROVED 96 WELL PLATE FORMAT LIPID QUANTIFICATION ASSAY FOR STANDARDISATION OF EXPERIMENTS WITH EXTRACELLULAR VESICLES

LP2012-26/2012 Lendület, OTKA KKP129936, OTKA KH126900, OTKA ERC_HU117755

T. Visnovitz, X. Osteikoetxea, B. W. Sódar, J. Mihály, P. Lőrincz, K. V. Vukman, E. Á. Tóth, A. Koncz, I. Székács, R. Horváth, Z. Varga, E. I. Buzás

The field of extracellular vesicles (EVs) is an exponentially growing segment of biomedical sciences. However, the problems of normalisation and quantification of EV samples have not been completely solved. Currently, EV samples are standardised on the basis of their protein content sometimes combined with determination of the particle number. However, even this combined approach may result in inaccuracy and overestimation of the EV concentration. Lipid bilayers are indispensable components of EVs. Therefore, a lipid-based quantification, in combination with the determination of particle count and/or protein content, appears to be a straightforward and logical approach for the EV field. In this study, we set the goal to improve the previously reported sulfo-phospho-vanillin (SPV) lipid assay. We introduced an aqueous phase liposome standard (DOPC = Dioleoylphosphatidylcholine) to replace the purified lipid standards in organic solvents (used commonly in previous studies). Furthermore, we optimised the concentration of the vanillin reagent in the assay. We found that elimination of organic solvents from the reaction mixture could abolish the background colour that interfered with the assay. Comparison of the optimised assay with a commercial lipid kit (based on the original SPV lipid assay) showed an increase of sensitivity by approximately one order of magnitude. Thus, here we report a quick, reliable and sensitive test that may fill an existing gap in EV standardisation. When using the optimised lipid assay reported here, EV lipid measurements can be more reliable than protein-based measurements. Furthermore, this novel assay is almost as sensitive and as easy as measuring proteins with a simple Bicinchoninic Acid (BCA) test (Fig. 1) [1].

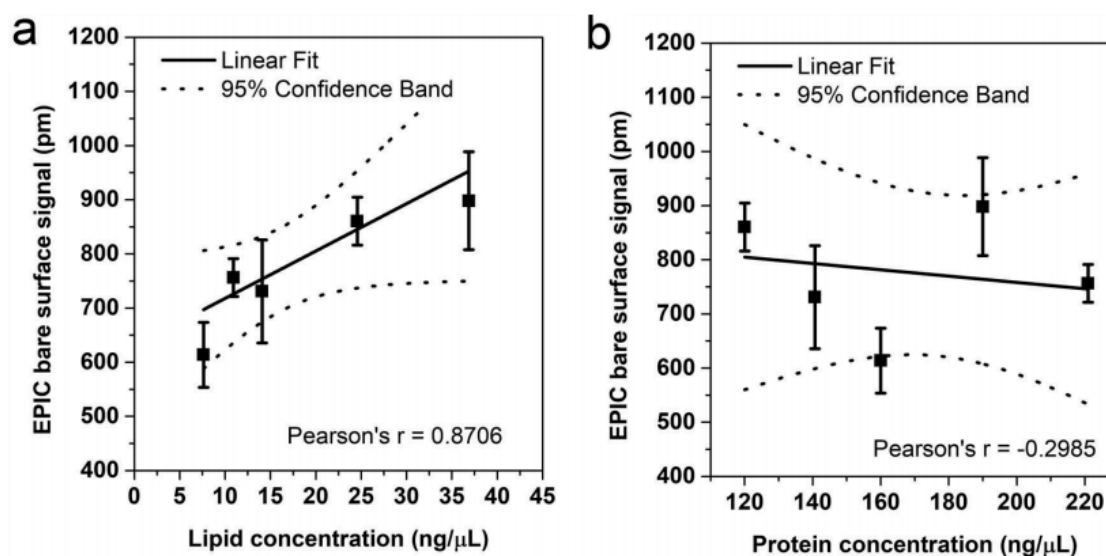


Figure 1: Correlation between the lipid and protein concentrations of EVs with the “bare surface signal” of an EPIC optical biosensor. Correlation between the EPIC “bare surface signal” and the lipid concentration (a) and the protein concentration (b). Small EVs were isolated from serum-free conditioned medium of THP-1 cells. Data points are average of three replicates, error bars represent SD.

Related publication

- [1] T. Visnovitz, X. Osteikoetxea, B. W. Sódar, J. Mihály, P. Lőrincz, K. V. Vukman, E. Á. Tóth, A. Koncz, I. Székács, R. Horváth, Z. Varga and E. I. Buzás: *An improved 96 well plate format lipid quantification assay for standardisation of experiments with extracellular vesicles*, *Journal of Extracellular Vesicles*, 1565263, (2019)

GRAPHENE ADDED MULTILAYER CERAMIC SANDWICH (GMCS) POROUS STRUCTURE PREPARED BY HIP AND SPS TECHNIQUES

FLAG-ERA.NET "Ceranea", OTKA NN127723

K. Balázsi, M. Furkó, Z. Liao, V. Varga, S. Gurbán, A. Kovács, L. Illés, J. Gluch, Zs. Fogarassy, D. Medved, E. Zschech, J. Dusza, C. Balázsi

Multilayer ceramic composites (MCC) consist of two ceramic materials and, considering basic properties, they can be divided into two groups: multilayer composites with weak interfaces and composites with strong interfaces. The sintering of ceramic matrix composites is usually carried out by raising the sintering temperature below melting point of components.

Graphene added multilayer ceramic sandwich (GMCS) structure can be manufactured using various methods, such as the stacking of ceramic sheets produced by tape casting or powder lamination or with in situ layer formation by slip casting, centrifugation or sequential electrophoretic deposition, sintering, among others. Spark plasma sintering (SPS) and hot isostatic pressing (HIP) were used. Multilayered graphene (MLG) and graphene oxide (GrO) were added to Si_3N_4 ceramic matrix in various amount; 5 wt% and 30 wt% (Fig. 1.a). The influence of reinforcing phase on final properties and the relationship between density, porosity and 3-point bending strength of composites were studied. It was shown, that both types of graphene addition had similar trend to the modulus of elasticity, namely, the decrease of strength with increasing graphene content [1, 2].

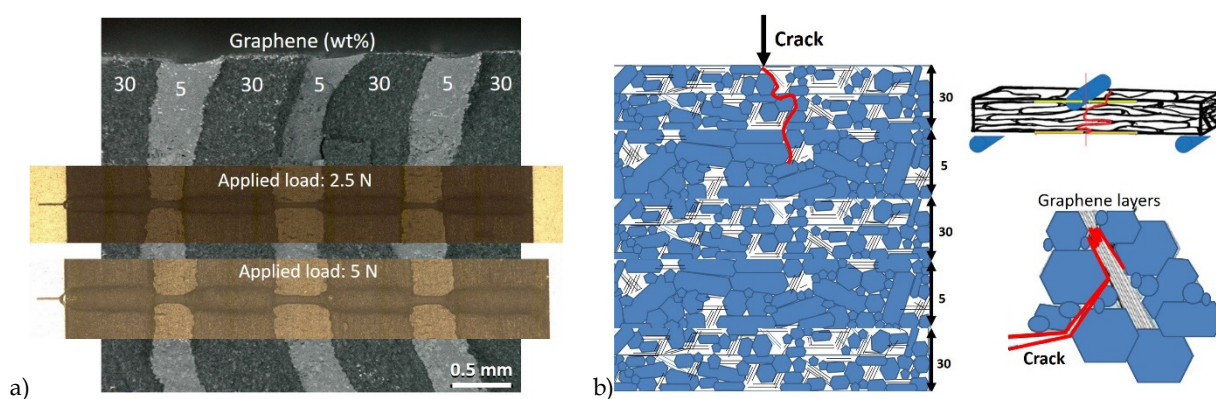


Figure 1: GMCS with seven multilayers. a) SEM image with depth profile, b) schematic view of the crack propagation mechanism in GMCS structure

Detailed elemental analysis of the layers proved the presence of graphene phase after HIP (Fig. 2) and SPS sintering process, as well, the ZrO_2 contamination. The graphene was well dispersed in matrix layers and remained non-oxidized after sintering (Fig 7.2.). The high-temperature liquid phase provided the vehicle for rapid mass transport and the driving force for densification. The 30 wt% of graphene reinforcing phase dispersed between ceramic matrix grains creating a "barrier" layer and blocked the transformation from α to β phase [3].

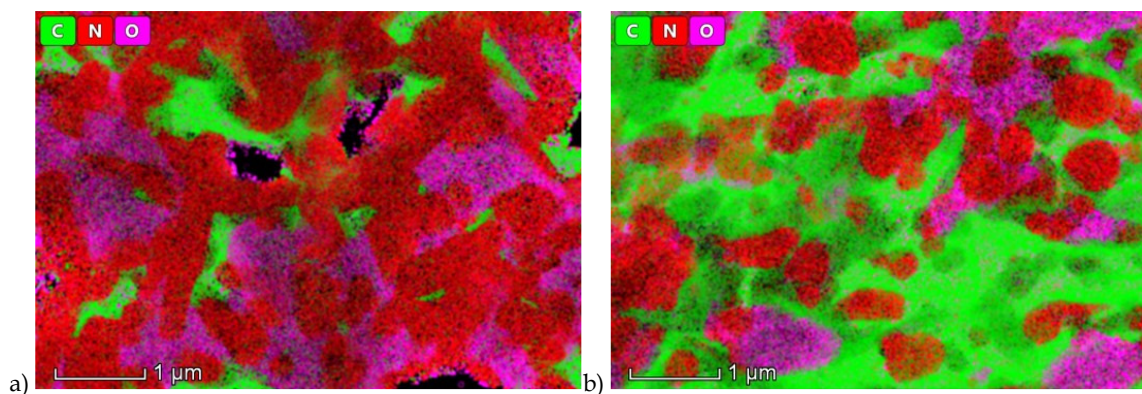


Figure 2: Elemental maps of graphene reinforced Si_3N_4 based composites: a) 5 wt% graphene, b) 30 wt% graphene

The Si_3N_4 / graphene composites exhibited lower friction coefficient (Fig. 3.). A four-time reduction was observed for 30 wt% graphene content, independent of graphene type (MLG, GrO). The friction coefficient (COF) for 5 wt% MLG and GrO containing composites changed between 0.35 and 0.4, while for composites with 30 wt% MLG and GrO content had almost similar COF values of 0.2. These low values are related to the carbon containing tribofilms, the porous structure and characteristic of Si_3N_4 ceramic matrix [4].

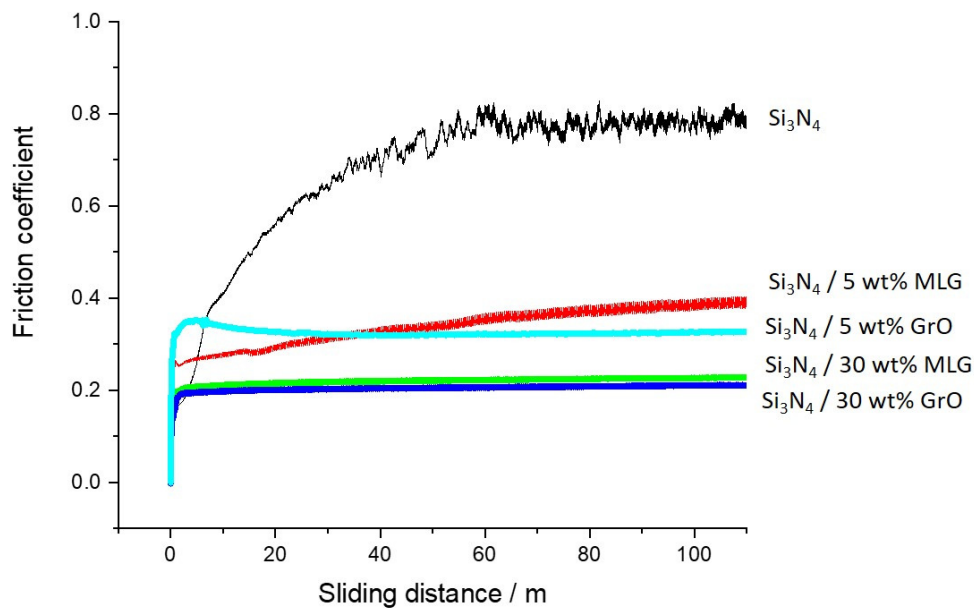


Figure 3: Friction coefficient measurement of Si_3N_4 based composites prepared by SPS

In conclusion, the uniaxial-pressure assisted sintering such as SPS resulted in a preferential alignment of graphene in the ceramic matrix, leading to highly anisotropic properties with lower mechanical behaviour. In the case of HIP, the high-temperature liquid phase provided the vehicle for rapid mass transport and the driving force for densification. The 30 wt% of graphene reinforcing phase dispersed between ceramic matrix grains creating a “barrier” layer and blocked the transformation from α to β phase. In both sintering processes, the homogeneity of graphene addition, the effect of layered structure and porosity influenced the final properties of GMCS structure.

Related publications

- [1] K. Balázs, M. Furkó, Z. Liao, J. Gluch, D. Medved, R. Sedlák, J. Dusza, E. Zschech, C. Balázs: *Porous sandwich ceramic of layered silicon nitride-zirconia composite with various multilayered graphene content*, Journal of alloys and compounds **832**, 154984 (2020)
- [2] K. Balázs, M. Furkó, Z. Liao, Z. Fogarassy, D. Medved, E. Zschech, J. Dusza, C. Balázs: *Graphene added multilayer ceramic sandwich (GMCS) composites: Structure, preparation and properties*, Journal of the European Ceramic Society, (2020), accepted for publ.
- [3] K. Balázs, M. Furkó, P. Klimczyk, C. Balázs: *Influence of Graphene and Graphene Oxide on Properties of Spark Plasma Sintered Si_3N_4 Ceramic Matrix*, Ceramics **3**:**(1)**, 40-50 (2020)
- [4] C. Balázs, Zs. Fogarassy, O. Tapasztó, A. Kailer, C. Schröder, M. Parchoviansky, D. Galusek, J. Dusza, K. Balázs: *Si_3N_4 /graphene nanocomposites for tribological application in aqueous environments prepared by attritor milling and hot pressing*, Journal of the European Ceramic Society **37**:**(12)**, 3797-3804 (2017)

AN ECONOMIC AND FACILE METHOD FOR GRAPHENE OXIDE PREPARATION FROM GRAPHITE POWDER

FLAG-ERA.NET "Ceranea"

M. Furkó, Zs. Fogarassy, L. Illés, K. Balázsi and C. Balázsi

A new method for preparing multi-layered graphene oxide powder was developed. In this method the raw material was commercially available micro-sized graphite powder. The graphite powder was milled by high-speed attritor mill to reduce the particle size of graphite to nanometre and to exfoliate the graphite into multi-layered graphene particles (Fig. 1.). The graphene particles were then oxidized into graphene oxide using the combination of strong oxidizing agents, thermal oxidizing and sonication [1]. Thorough morphological characterizations were carried out to reveal the structure and the size of GrO particles. Results confirmed that the oxidation process was successful (Fig. 2.).

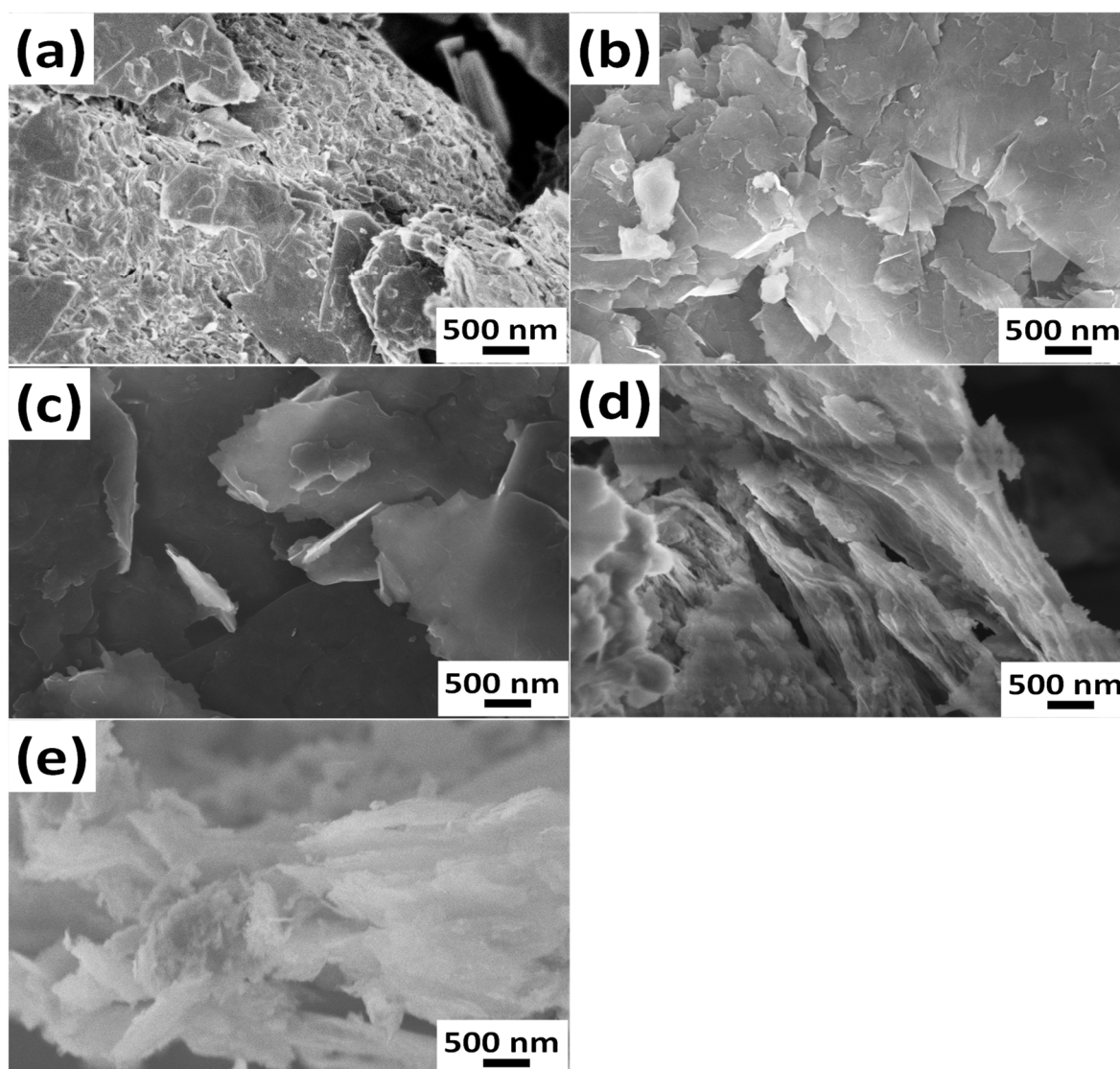


Figure 1: SEM images of graphite (a), graphene platelets (b) and different graphene oxide powders: after oxidation step first (c), oxidation step second (d) and oxidation step third (e)

The graphene nanosheets were oxidized in three steps. First, the powders were dispersed in cc. HNO_3 solution and stirred at 80°C for 4 hours then 50% H_2O_2 was added to the dispersion under continuous stirring and kept at room temperature for 16 hours. The dispersion was then filtered using filter paper grade 3, the filtrate washed/rinsed with 30% H_2O_2 and 96% ethanol and dried at 150°C in air. In the second step, the dried powders were collected and put into oven and heat treated at 850°C for thermal oxidation. Finally, a portion of treated powders were dispersed again in 96% ethanol and sonicated in ultrasonic bath for 3 hours at 70°C to examine the effect of ultrasound on the exfoliation rate of graphene oxide multilayers, then the solvent was evaporated at 80°C .

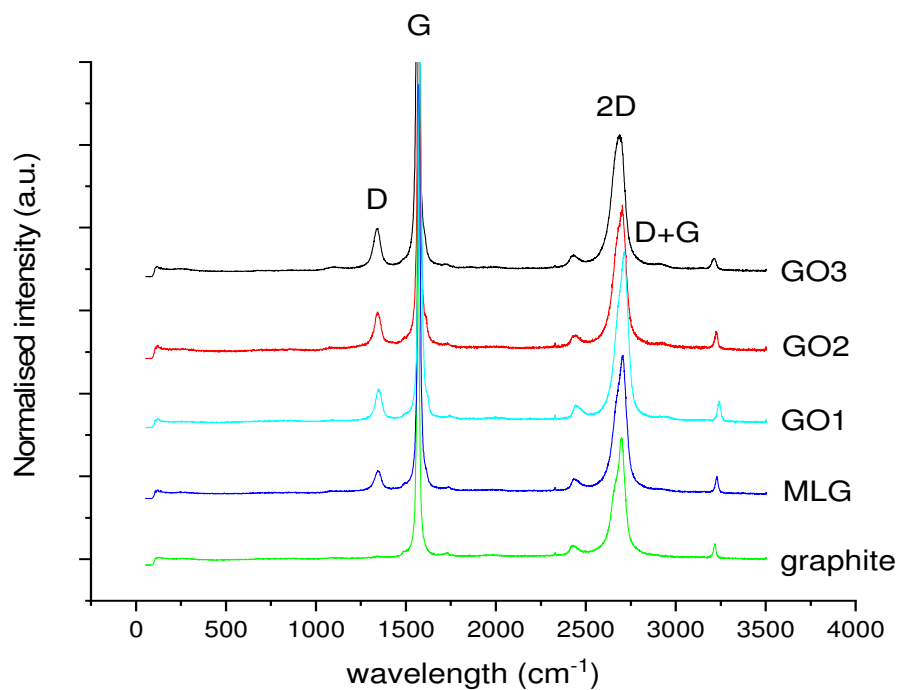


Figure 2: Raman spectra of graphite, MLG and different graphene oxide samples

Related publication

- [1] M. Furkó, Zs. Fogarasy, K. Balázs, C. Balázs: *An economic and facile method for graphene oxide preparation from graphite powder*, *Resolution and Discovery* **4**, 21-25 (2019)

EXAMINATION OF NOVEL ELECTROSPRAYED BIOGENIC HYDROXYAPATITE COATINGS ON Si_3N_4 AND $\text{Si}_3\text{N}_4/\text{MWCNT}$ CERAMIC COMPOSITE

T. Zagyva, K. Balázsi, C. Balázsi

Several types of biomaterials are used for total knee and hip replacements in orthopaedic surgery since the 1970s. Metallic materials, such as titanium alloys and cobalt-chromium have been widely used due to their excellent mechanical strength and corrosion resistance. Silicon nitride (Si_3N_4) ceramic, beside these advantageous properties exert two or three times better fracture toughness than metals, thanks to its microstructure. The high fracture toughness is resulted from the extended crack path along the surface of the elongated grains. Although there is no chemical reaction between bioinert ceramics (e.g. Si_3N_4) and the living tissue, bioactive materials can induce tissue reactions in human body. Using a biodegradable and bioactive temporary coating (e.g., hydroxyapatite HAP) on the implant's surface could induce tissue reactions and help avoid the rejection from the body in the critical early few days, after the operation.

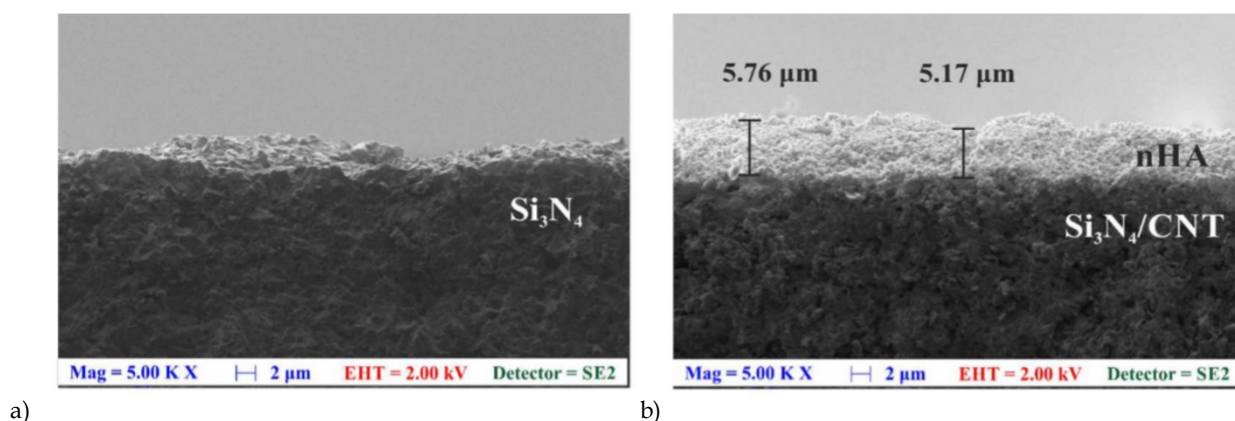


Figure 1: Electrospayed nHAP layer after 45-minute-long ESD process with the same deposition parameter
a) Si_3N_4 , b) $\text{Si}_3\text{N}_4/\text{MWCNT}$ substrates

The aim of our study was to produce thin nanosized HAP layer on silicon nitride implant material by electro spray deposition (ESD) (Fig. 1). To the best of our knowledge, this is the first time that electrospayed nanosized hydroxyapatite coatings were deposited on the ceramics, although this method is more cost-efficient than other widely used deposition techniques like plasma spraying, pulsed laser deposition or RF-magnetron sputtering. In case of electro spraying, electrically conductive materials are required as substrates. Ceramics are mostly insulators, therefore special treatments (e.g., doping) are necessary for creating appropriate substrates for the deposition process. Multiwall carbon nanotubes (MWCNT) (3wt.%) were ideal dopants for increasing the conductivity of Si_3N_4 . The carbon nanotubes occurred only inside the substrate. Using the same deposition parameters, a thin (5 μm) nHAP coating was deposited on the MWCNT doped silicon nitride in 45 minutes (Fig. 1b), while continuous nHAP layer could not form on the pure (insulator) Si_3N_4 surface during this time (Fig. 1.a) [1].

Related publication

- [1] T. Zagyva, K. Balázsi, C. Balázsi: *Examination of novel electrospayed biogenic hydroxyapatite coatings on Si_3N_4 and $\text{Si}_3\text{N}_4/\text{MWCNT}$ ceramic composite*, *Processing and Application of Ceramics* **13**:(2), 132-138 (2019)

ECO-FRIENDLY ALON PROCESSING

OTKA NNE129976

K. Balázs, M. Furkó, V. Varga, S. Gurbán, L. Illés, S. Lamnini, F. Szira, C. Balázs

Aluminium oxynitride (AlON) has a unique thermal and chemical stability that makes it a perfect candidate for a wide range of applications. Currently commercially available AlON material exhibit average grain size in the order of 150–200 μm ; however, development of new methods to control grain size, especially, at the nano-scale could create materials with improved properties. The most promising techniques for AlON preparation are hot pressing (HP), hot isostatic pressing (HIP) and spark plasma sintering (SPS).

According to the thoroughly studied literature data and the state of the art on AlON preparation, the currently available and used techniques are still all expensive, as well as being energy and time consuming [1]. High temperature above 1600–1900 $^{\circ}\text{C}$ is needed for a long time to achieve appropriate phase and densification. We intend to develop an eco-friendly preparation method of AlON in which we develop a novel way to reduce the temperature and/or time thus requiring lower energy (technique, temperature and so on). Moreover, we are planning to recycle and utilize the industrial by-products or aluminium waste (such as aluminium cans) as Al source.

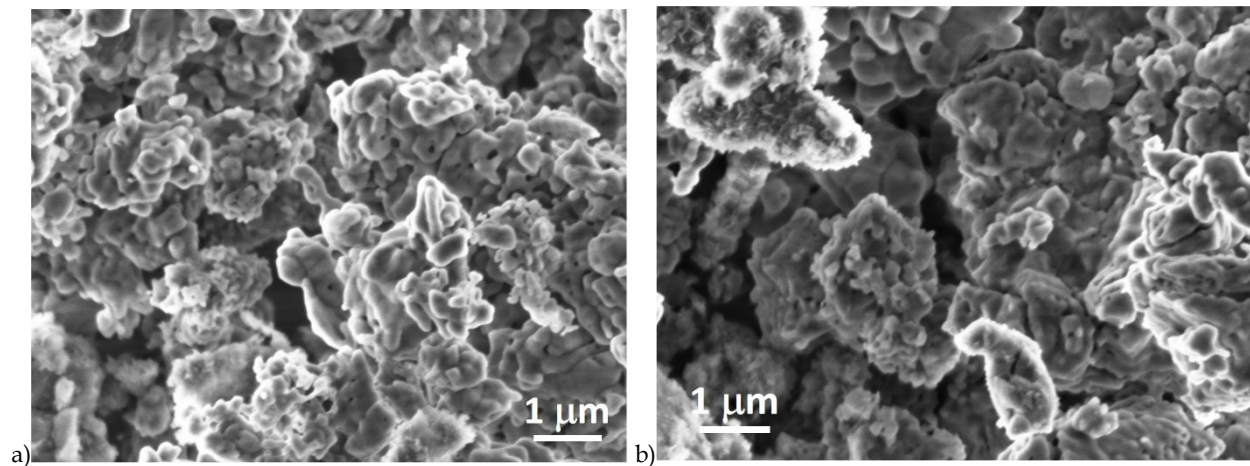


Figure 1: SEM image of oxidized AlN powder. a) 3 h, b) 10 h

The aim of our research is a preparation of cheap AlON by eco-friendly technology. The oxidization of base AlN powder with specific surface area 4.0–8.0 m^2/g and an average particle size of 0.80–1.8 μm for 3, 6 and 10 h at 900 $^{\circ}\text{C}$ in air atmosphere was the first step (Fig. 1.). Hot isostatic pressing for 5 h at 1700 $^{\circ}\text{C}$ in nitrogen was used for sintering of oxidized powders. The increasing the oxidation time significantly improved the tensile strength of sintered samples compared to the reference (Fig. 2). In the case of reference AlN, the measured value is 13.8 MPa on average for the 4-point bending test and 159.2 MPa after 10 h oxidation. It is shown the significant increasing with oxidation time. The oxidation time has influence not only on mechanical properties. We showed, that the increasing of oxidizing time, the higher density, the lower porosity showed the AlON after 10 h oxidation [2].

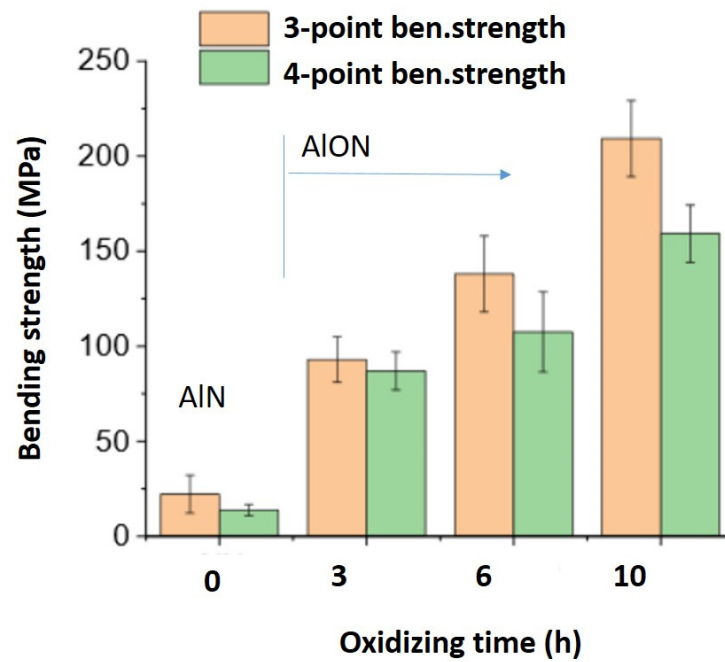


Figure 2: Bending strength of reference (AlN) and sintered AlON ceramics with different oxidation times

Related publications

- [1] C. Balázs, M. Furkó, F. Szira, K. Balázs: *Research on Technical Ceramics and their Industrial Application: Preparation Techniques and Properties of Transparent AlON Ceramics*, *Acta Materialia Transylvania* **2**:(1), 7-12 (2019)
- [2] K. Balázs, M. Furkó, C. Balázs: *Nitrid kerámiák környezetkímélő előállítására és vizsgálata*, In: Barabás, István (szerk.) *XXVIII. OGÉT* 33-36 (2020)

DEVELOPMENT OF MULTIWALL CARBON NANOTUBE REINFORCED YTTRIA STABILIZED ZIRCONIA COMPOSITES

S. Lamnini, L. Illés, Zs. Horváth, Zs. Fogarassy, V. Varga, K. Balázs and C. Balázs

Zirconia (ZrO_2) based materials belong to the most widely investigated and technologically powerful ceramics applied in several fields. Nowadays, multiwall carbon nanotube (MWCNT) reinforced ZrO_2 composites are attracting growing interest, thanks to their ability of self-healing of the crack and the possibility to tailor the desired nanostructured properties. The aim of this PhD work was the experimental synthesis of 8mol% yttria-stabilized zirconia (8YSZ) containing 1, 5 and 10 wt% MWCNTs and study of the microstructure effect on the mechanical and tribological properties of composites (Fig. 1). The powder morphology of pure 8YSZ has been significantly modified after attrition milling to a refined and homogeneous microstructure sized of approximately 400 nm with soft grain edges.

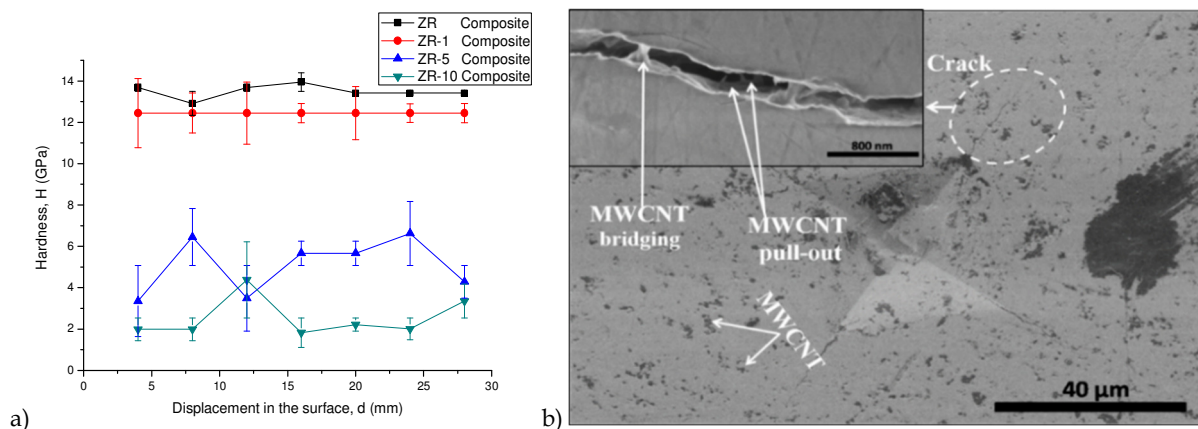


Figure 1: Mechanical properties of 8YSZ/MWCNTs composites. a) hardness measurements, b) crack propagation in composite with 1 wt% MWCNTs

8YSZ / 1 wt% MWCNTs sintered composite owns the highest density 6.76 g/cm^3 , hardness 12 GPa (Fig. 1.a) and bending strength of 502 MPa besides the lowest porosity of 16.5 % among all the tested composites.

The analysis of the crack propagation modes showed the presence of MWCNT pull-out, crack bridging and crack deflections besides more restrained and tapered crack path in the 8YSZ / 1 MWCNTs wt% composite compared to the reference (Fig. 1.b). It was showed that these toughening mechanisms played a vital role in enhancing the resistance to crack propagation. The high degradation of the mechanical and indentation fracture toughness was well approved in case of 5 wt% and 10 wt% MWCNTs addition. This was associated with incoherent and discontinuous matrix, reduced interfacial bonding due to the deep open pores on the surface, which caused a long unrestrained crack path. It was shown an outstanding wear improvement of composite with 1 wt% MWCNTs at low (0.036 m/s) and high (0.11 m/s) sliding speeds attributed to the formation of a perfectly continuous, uniform tribofilm and the improved flexural strength and density. Further, the steady state friction coefficient marked significant decrease at higher sliding speed with 5 and 10 wt% of MWCNTs content [1, 2].

Related publications

- [1] S. Lamnini, Z. Károly, E. Bódis, K. Balázs, C. Balázs: *Influence of structure on the hardness and the toughening mechanism of the sintered 8YSZ/MWCNTs composites*, *Ceramic International* **45**(4), 5058-65 (2019)
- [2] S. Lamnini, C. Balázs, K. Balázs: *Wear mechanism of spark plasma sintered MWCNTs reinforced zirconia composites under dry sliding conditions*, *Wear* **430-431**, 280-289 (2019)

NOVEL METHOD FOR THE PRODUCTION OF SiC MICRO AND NANOPATTERNS

A.S. Rácz, D. Zámbo, G. Dobrik, I. Lukács, Z. Zolnai, A. Németh, P. Panjan, A. Deák, G. Battistig, M. Menyhárd

Recently we have shown that it is possible to produce SiC nano-coating at room temperature by applying ion beam mixing (IBM) on C/Si multilayer structures. Herein we show that the combination of masking layers with IBM allows the fabrication of patterned SiC structures at room temperature and the achievable patterned area is scalable up to wafer size. For this purpose IBM was applied on a Si/C system covered by masks obtained by either conventional lithography technique or nanosphere lithography.

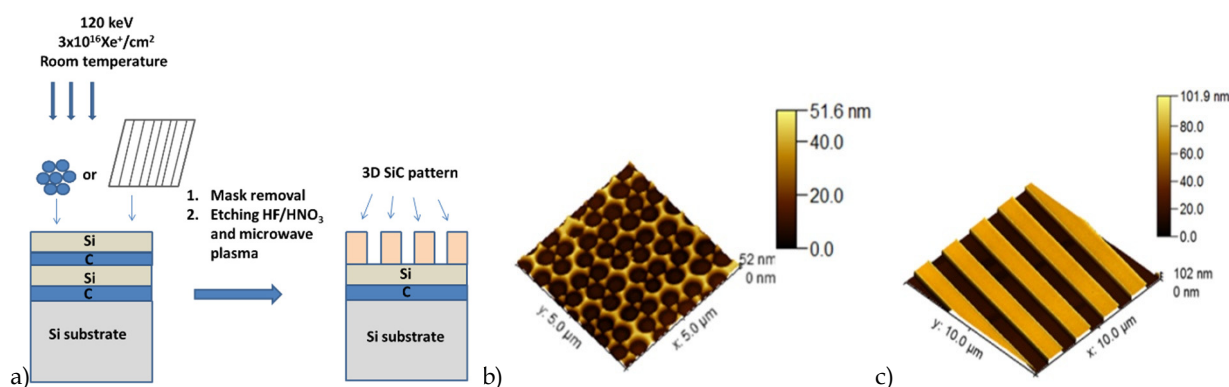


Figure 1: a) Process of producing 3D structures b) AFM image of the LB-masked sample after mask removal and one step HF/HNO₃ etching and one step oxidation. c) AFM image the grid-masked sample after mask removal and HF/HNO₃ etching, oxidation and additional HF/HNO₃ etching

The irradiation conditions were chosen by TRIDYN simulation. Due to IBM a SiC rich layer formation on the non-covered parts of the sample was demonstrated using AES depth-profiling, while the covered regions have not changed. Thus, in a single-step (the compound formation and the creation of patterns happened in one step) a tailor made 2D nanopattern of SiC rich regions alongside pure Si has been constructed at room temperature. Applying additional etching and oxidation processes the 2D pattern has been transformed to a 3D one consisting SiC rich regions in their original place and holes of given depths with either C or Si bottom. The scheme of the 3D structure production is depicted in Fig. 1.a, while Fig. 1.b and 1.c provide the AFM images of the different 3D structures. One of the 3D structure produced by applying the Langmuir-Blodgett film was tested for surface-enhanced Raman scattering (SERS) application. To our knowledge IBM have not been used to produce SERS substrates, yet. The gold coated 3D structure proved to be SERS active allowing the high sensitivity detection of biomolecules both in mild and harsh environments. [1]

Related publication

- [1] A.S. Rácz, D. Zámbo, G. Dobrik, I. Lukács, Z. Zolnai, A. Németh, P. Panjan, A. Deák, G. Battistig, M. Menyhárd: *Novel method for the production of SiC micro and nanopatterns*, Surface and Coatings Technology **372**, 427-433 (2019)

INVESTIGATION OF THE NANOSTRUCTURAL BACKGROUND OF FUNCTIONALITY IN THE CASE OF BIOGENIC AND BIOCOMPATIBLE MINERAL APATITE

OTKA K125100

V. Kovács Kis, Zs. Czigány, Zs. Dallos, D. Nagy, I. Dódony, Zs. Kovács, M. Hegedűs, A. Sulyok, A. Jakab, L. Illés, K. Hajagos-Nagy, Gy. Radnóczy

1) Crystal structure study of bone apatite nanocrystals

While synthesis and characterization of calcium phosphate biomaterials for biomedical applications relies on their similar composition to bone and teeth mineral apatite, the atomic structure and nucleation processes of the biological calcium phosphates themselves are poorly known. Transmission electron microscopy is a powerful tool for studying structures on the nanoscale. While the atomic structure of individual tooth enamel apatite, which have much less organic content (< 5%), has been successfully investigated by high-resolution transmission electron microscopy (HRTEM), nanoscale electron diffraction techniques indicate non-centrosymmetry of the enamel apatite nanocrystals [1]. No published atomic level structural information on bone apatite nanocrystals is known up to now.

In [2] we present the first crystal structure model for bone apatite based on the analysis of individual nanocrystals by HRTEM, see Fig. 1.

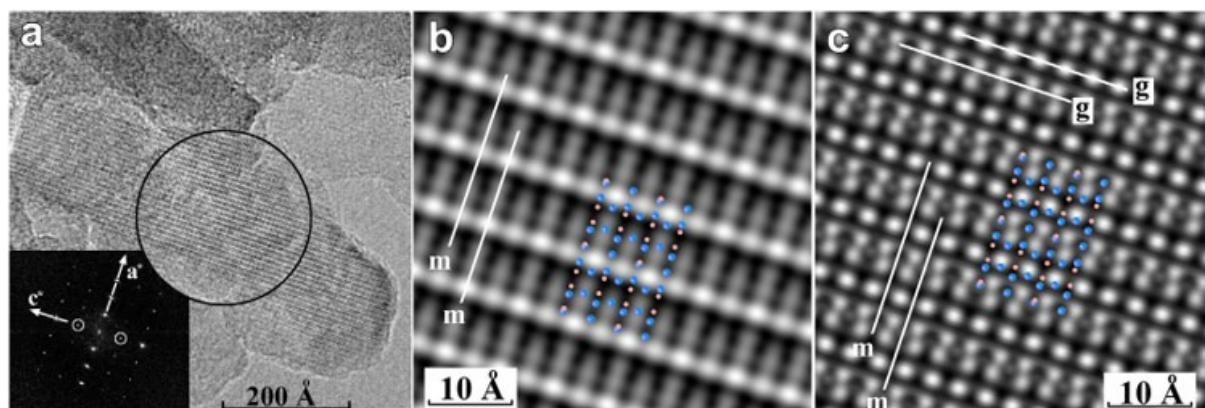


Figure 1: a) [100] HRTEM image of bone apatite nanocrystal is shown with its Fourier transform inserted in the lower left corner. Fourier components forbidden by $P6_3/m$ space group symmetry are encircled. b) Enlarged symmetry imposed image, mirror planes (m) are marked. The inset is the structure model of $P6_3/m$ apatite for 2×2 unit cells. c) Calculated [100] HRTEM image of $P6_3/m$ F-apatite with 2 \AA resolution. The 2D symmetry elements, mirror plane (m) and glide plane (g), are marked. The inset is the structure model of $P6_3/m$ apatite for 2×2 unit cells. Calcium (orange) and phosphorus (blue) atoms are shown, other atoms are omitted for clarity.

By crystallographic image processing we show the loss of hexagonal symmetry along the c axis. To explain our observations, we propose a structure model for B-type carbonate substitution with O vacancies localized in the structural channel along the c axis (Fig. 2.). This model is in agreement with the observed absence of the $[001] 6_3$ screw axis, and the shift of mirror plane is perpendicular to the c axis. Carbonate substitution is deduced from the measured Ca/P=2 ratio.

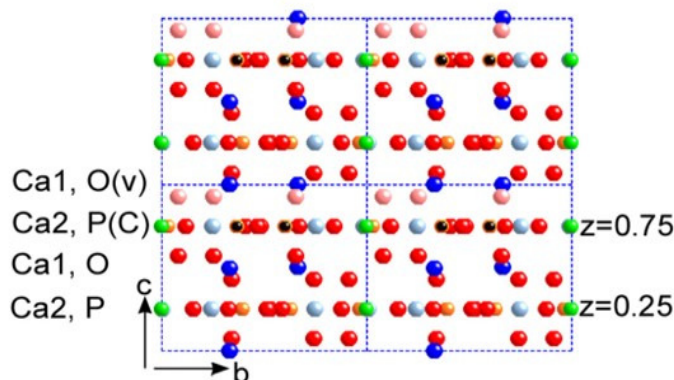


Figure 2: Proposed structural model for carbonated F-apatite to interpret HRTEM observations on bone apatite nanocrystals, 2×2 unit cells. Representation of atoms: blue – Ca (dark and light blue are Ca1 and Ca2 positions, respectively), orange – P, black – C, red – O, pale red – O vacancies, green – F. [100] zone projection.

Besides symmetry reduction, we give evidence for polarity along [010] direction of bone apatite, which implies chemically distinct (0k0) surfaces [1]. First principles study [3] indicate different water adsorption capacities of the two types of surfaces. Bone apatite nanocrystals, which are platy on (010), have relatively large (0k0) surfaces, which according to our results [Ref.2.], are either Ca or P rich. Ca release in exchange for two hydrogens proved to be energetically favourable [Ref.3.], promoting surface hydration. Therefore, we propose that the relative orientation of (0k0) facets has prominent role in resorption processes and also in the adhesion of apatite nanocrystals to the collagen fibres [2].

2) Primary dental enamel: nanostructure and mechanical properties

“XPS clean” surfaces of deciduous dental enamel, obtained according to the cleaning protocol established in the previous year, has been subjected to Mg-exchange experiments. The aim of these experiments was to study under controlled conditions the correlation between Mg-content and mechanical properties, reported in the first year. To check the effect of crystallinity, morphology and particle size on Mg incorporation, nanocrystalline hydroxylapatite and amorphous calcium phosphate (ACP) nanoparticles together with crystalline apatite of pegmatitic origin were also included into the study. Our results indicate that enamel incorporates more Mg than nanocrystalline hydroxylapatite, in spite of its smaller specific surface (related to its character of compact ceramics). ACP dissolves and re-precipitates via forming a metastable nanocrystalline Ca-phosphate phase with stoichiometry Ca:Mg:P = 1:1:2.

Regarding the effect of Mg incorporation on mechanical properties, nanoindentation measurements were performed in parallel on two halves of the same molar, one subjected to the Mg exchange procedure, the other not. This method excludes the effect of individual variations in the thickness of the aprismatic layer, which as reported in the last year, correlates both with native Mg content and with nanohardness. According to our results, Mg incorporation into dental enamel induces a nanohardness increase by cca. 20% with respect to the initial values (Fig. 3). According to preliminary HRTEM, this significant increase is related to a decrease of crystallite size during Mg uptake. These results were presented at two conferences: full-length papers are in preparation.

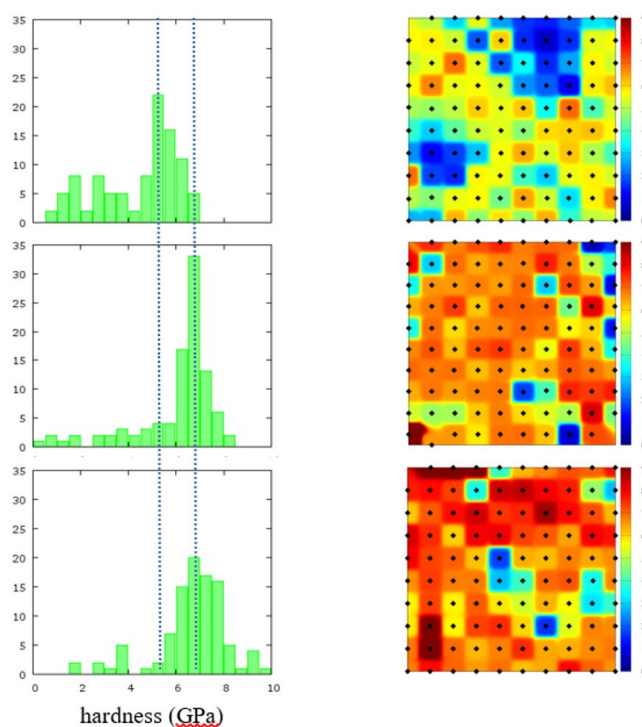


Figure 3: Nanoindentation measurements on pristine (upper row) and Mg-treated (middle and bottom row) primary molar surfaces, array of 10x10 measurement points, 50 μm step size

Related publications

- [1] E. Mugnaioli, J. Reyes-Gasga, U. Kolb, J. Hemmerlé, É.F. Brés: *Evidence of non-centrosymmetry of human tooth hydroxyapatite crystals*, Chem. Eur. J. **20**, 6849–6852 (2014)
- [2] V.K. Kis, Z. Czigány, Z. Dallos, D. Nagy, I. Dódy: *HRTEM study of individual bone apatite nanocrystals reveals symmetry reduction with respect to P63/m apatite*, Mat. Sci. Eng. C **104**, 109966 (2019)
- [3] R. Astala, M.J. Stott: *First-principles study of hydroxyapatite surfaces and water adsorption*, Phys. Rev. B **78**, 075427 (2008)

NANOSTRUCTURE INVESTIGATION OF Mg-NbO-CARBON NANOTUBE COMPOSITE MATERIALS FOR HYDROGEN STORAGE APPLICATIONS

M. Gajdics, T. Spassov, V. Kovács Kis, E. Schafler, Á. Révész

Mg-based nanostructured materials have considerable potential for future applications in hydrogen storage, the main focus of ongoing research activities is improving the desorption properties by applying different additives and processing techniques. In collaboration with colleagues from the Eötvös University, several Mg based nanocomposites before and after absorption-desorption cycles were studied using HRTEM and the effect of the applied additives (Nb₂O₅, carbon nanotubes (CNT) [1, 2], titania nanotubes [3] and their combinations) and processing techniques (ball milling, high pressure torsion (HPT)) on the nanostructure was investigated.

According to our results [1, 2], in the ball milled Mg-CNT nanocomposite sample the interior of the Mg particles contains fairly long CNT sections (several tens of nanometres), which are slightly bent and mainly intact. After HPT, CNTs are still recognized in the disks; however, they are heavily bent considerably shorter than the nanotubes in the corresponding as-milled powder. It is evident from the HRTEM that the torsion procedure does not completely destroy the nanotube structure, which is crucial for the catalytic effect.

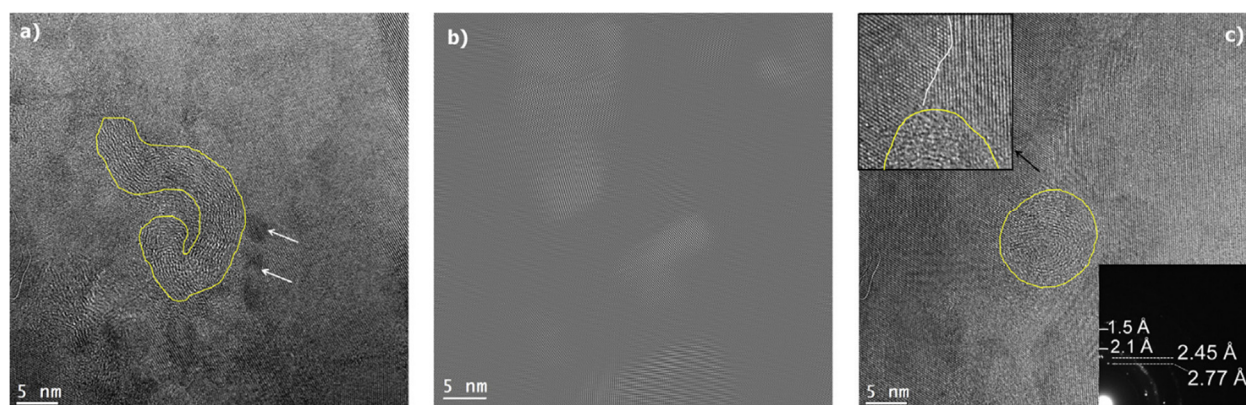


Figure 1: a) A HRTEM images of Mg-NbO-CNT_HPT containing a short nanotube section, b) the corresponding Inverse Fast Fourier Transition (IFFT) image using Nb₂O₅ Fourier maxima. Yellow lines mark the edge of CNT, c) A nanotube lying parallel to the viewing direction close to a grain boundary, marked by white line on the enlarged image at the top left corner. The inset at the bottom right corner shows a typical selected area electron diffraction (SAED) pattern.

It is noteworthy that CNTs and Nb₂O₅ nanoparticles, when applied together, are located in close proximity to each other in the HPT processed samples, which is even more evident on HRTEM images after hydrogen cycling (Fig. 1.a) [1]. We propose that the presence of this kind of agglomerated catalyst structures might be the reason of the noticeably improved sorption kinetics of the Mg catalysed applying both CNT and Nb₂O₅ (Fig. 1.b-c).

Related publications

- [1] M. Gajdics, T. Spassov, V. Kovács Kis, E. Schafler, Á. Révész: *Microstructural and morphological investigations on Mg-Nb₂O₅-CNT nanocomposites processed by high-pressure torsion for hydrogen storage applications*, *Int. J. Hydrogen Energy* **45**, 7917-7928 (2020)
- [2] Á. Révész, T. Spassov, V. Kovács Kis, E. Schafler, M. Gajdics: *The influence of preparation conditions on the hydrogen sorption of Mg-Nb₂O₅-CNT produced by ball milling and subsequent high-pressure torsion*, *J. Nanoscience Nanotechnology* **20**, 4587-4590 (2020)
- [3] M. Gajdics, T. Spassov, V. Kovács Kis, F. Béke, Z. Novák, E. Schafler, Á. Révész: *Microstructural investigation of nanocrystalline hydrogen-storing Mg-titanate nanotube composites processed by high-pressure torsion*, *Energies* **13**, 563 (2020)

STRUCTURAL AND ELECTRICAL PROPERTIES OF ALN THIN FILMS ON GAN SUBSTRATES GROWN BY PLASMA ENHANCED-ATOMIC LAYER DEPOSITION

FLAG-ERA.NET 'Griffone'

E. Schilirò (IMM-CNR), F. Giannazzo (IMM-CNR), F. Roccaforte (IMM-CNR), Zs. Fogarassy, I. Cora, B. Pécz

Aluminum nitride (AlN) thin films have been deposited by Plasma Enhanced Atomic Layer Deposition (PE-ALD) onto GaN-sapphire substrates [1]. The morphological, structural and electrical properties of AlN films with different thicknesses (from 5 to 15 nm see Fig. 1.) have been investigated. They uniformly cover the underlying GaN substrate without pinholes and cracks. All the AlN thin films show c-axis orientation and their in-plane crystalline arrangement perfectly matches the hexagonal structure of GaN substrate. In particular, the cross-sectional TEM analysis demonstrated that the first AlN layers are well aligned with respect to the GaN (001) substrate, while stacking faults formation is observed in the upper part of the films.

Finally, electrical measurements by Hg-probe on as-deposited AlN showed very low current leakage across these layers and the presence of a high density two dimensional electron gas ($> 2 \times 10^{13} \text{ cm}^{-2}$) at the AlN/GaN interface. This latter is a consequence of the above discussed good epitaxial quality of the PE-ALD grown AlN thin films on GaN. These results are promising for future integration of low-temperature deposited AlN thin films with GaN devices technology.

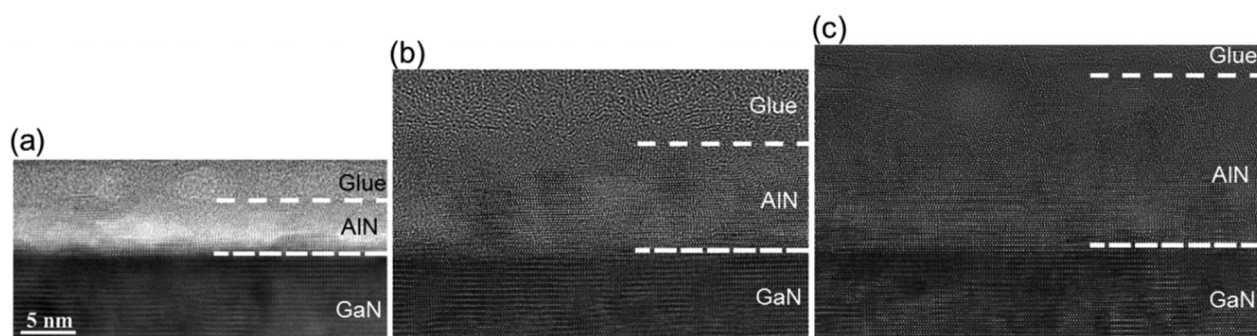


Figure 1: High-resolution cross-sectional TEM images acquired on the AlN layers with 5 nm (a), 10 nm (b) and 15 nm (c) nominal thickness

Related publication

- [1] E. Schilirò, F. Giannazzo, C. Bongiorno, S. Di Franco, G. Greco, F. Roccaforte, P. Prystawko, P. Kruszewski, M. Leszczyński, M. Krysko, A. Michon, Y. Cordier, I. Cora, B. Pecz, H Gargouri, R. Lo Nigro: *Structural and electrical properties of AlN thin films on GaN substrates grown by plasma enhanced-Atomic Layer Deposition*, *Materials Science in Semiconductor Processing* **97**, 35-39 (2019)

STRUCTURE, MECHANICAL PROPERTIES AND THERMAL STABILITY OF WBC AND MOBC COATINGS

M. Alishahi (Brno), S. Mirzaei (Brno), P. Soucek (Brno), L. Zábřanský (Brno), V. Buršíková (Brno), M. Stupavská (Brno), V. Peřina(Rež), K. Balázsi, Zs. Czigány, P. Vašina (Brno)

Characterization of sputtered WBC and MoBC was performed in cooperation with Department of Physical Electronics of Masaryk University, Brno, Czech Republic (Brno) and Nuclear Physics Institute of Academy of Sciences of the Czech Republic, Rež (Rež). The cooperation, which started in 2016 is promising since deposition of layers that are both hard and fracture tough is difficult. The recently applied ceramic coatings are generally fragile. The apparently contradictory properties of high hardness and ductility may be realized in X_2BC systems ($X = Ti, V, Zr, Nb, Mo, Hf, Ta, W$) by ab-initio calculations. In this cooperation WBC [1, 2, 3] and MoBC [4] films were investigated.

In our previous experiments, we have investigated the effect of C/W ratio on bond structure, microstructure, hardness, fracture toughness and scratch resistance at constant B content. This year we added the investigation of the effect of B/W ratio at constant C content. The new results verify former observations. The layers are mostly amorphous, however, a certain level of short range ordering can be observed even in the amorphous films, which are manifested in short, curved and irregular lattice fringes in the HRTEM images. Coatings in the vicinity of W_2BC composition are nanocomposites containing nanocrystals with size of ~ 5 nm embedded into an amorphous matrix. All the layers exhibited high hardness (>20 GPa) so they all can be classified as hard coatings. The level of crystallinity played no crucial role in determining the hardness of the coating, while the effect of the coating structure and bonding was clear – the densest coating with the highest relative amount of W-B bonds exhibited the highest hardness of ~ 29 GPa. Furthermore, the presented coatings exhibited high adhesion to industrially important substrates as well as scratch and crack resistance unmatched by current top-of-the-shelf industrial protective coatings of comparable hardness. The bond state and structure of the amorphous and nanocrystalline WBC coatings were compared with ab-initio calculations [3].

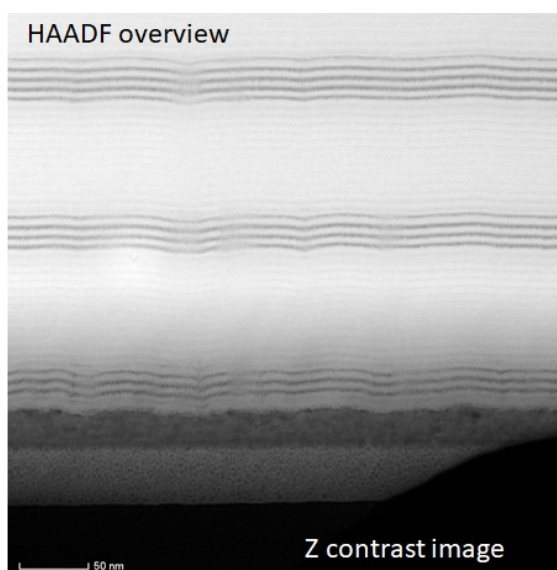


Figure 1: STEM-HAADF image of a WBC coating sputtered in an industrial chamber. The hierarchic multilayer structure, composed of ~ 5 nm layers, was formed due to the double rotation mechanism of the sample holder.

WBC coatings might pave the way to the next generation of coatings for tool protection. As an example the Scanning Transmission Electron Microscope High-Angle Annular Dark-Field (STEM HAADF) image of a WBC coating deposited in an industrial chamber is shown in Fig.1. Based on HAADF and Spectrum Images a hierarchical multilayer structure was revealed which is composed of ~ 5 nm layers. The complicated multilayer structure was formed due to the double rotation mechanism of the sample holder [2].

After annealing at 1000°C of MoBC films Mo_2C and Mo_2BC phases were formed embedded in a nanocrystalline matrix [4]. At high Mo content nanocrystalline Mo_2C phase, at low Mo content Mo_2BC phases were formed. At medium Mo content, the structure was almost amorphous. The hardness and elastic modulus of the layers always increased after annealing, in some cases reaching the 29GPa and 500GPa values, respectively. Co diffusion from the WC(6%Co) substrate and the formed nanocrystalline phases were identified based on HRTEM, STEM HAADF and EDS elemental maps (Fig. 2).

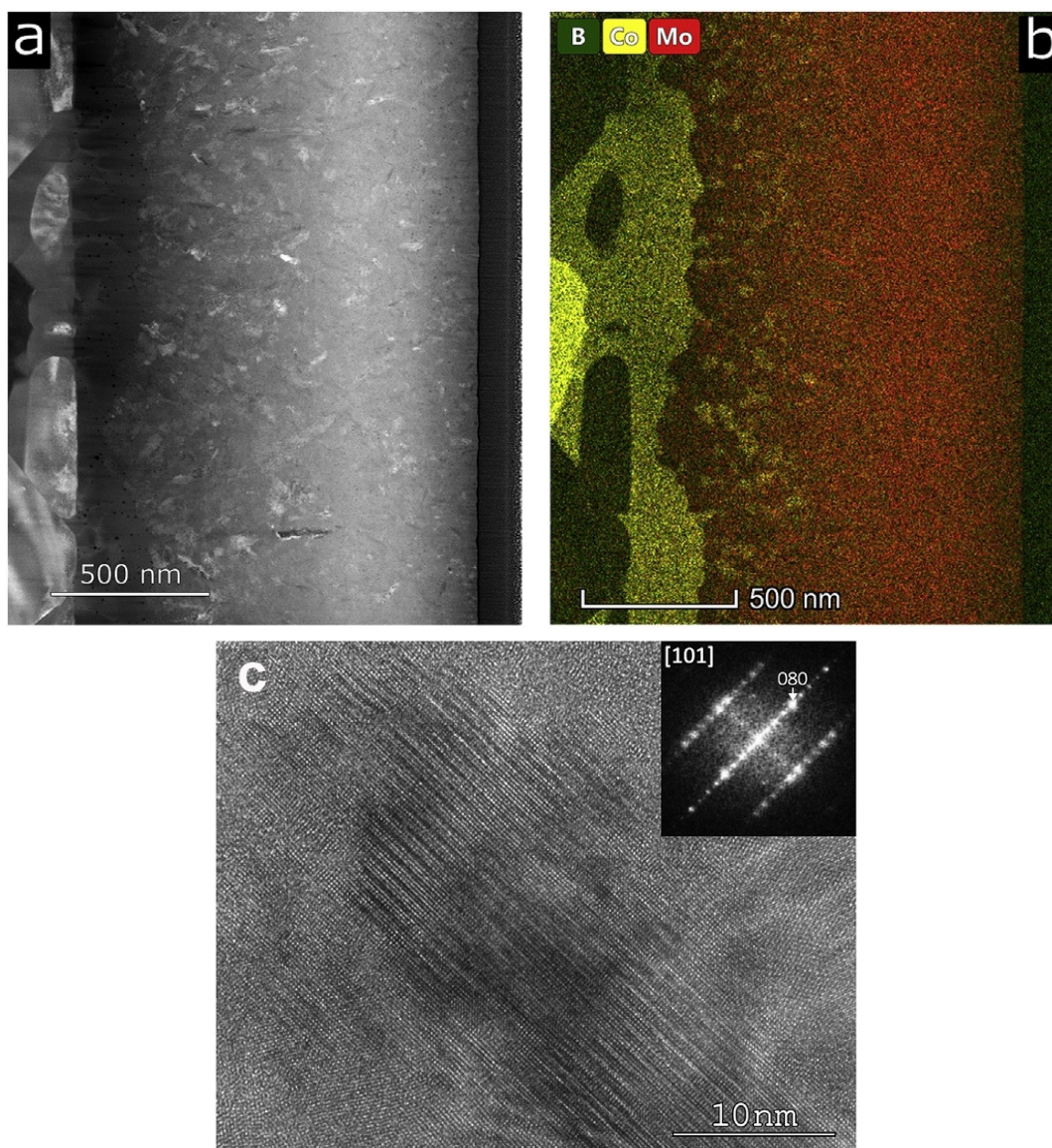


Figure 2: a) HAADF image of a MoBC film with 45 at% Mo content after annealing at 1000°C, b) its EDS elemental map. The interaction between the WC(6%Co) substrate and the film can be observed in the EDS elemental map: the Co content of the substrate diffuses into the film to 100-200nm depth. By the Fourier transform of the HRTEM image (c) orthorhombic Mo₂BC phase can be identified embedded in a nanocrystalline matrix.

Related publications

- [1] S. Mirzaei, M. Alishahi, P. Souček, L. Zábanský, V. Buršíková, M. Stupavská, V. Peřina, K. Balázsi, Zs. Czigány and P. Vašina: *Effects of bonding structure on hardness of fracture resistance of W-B-C coatings with varying B/W ratio*, Surface and Coatings Technology **358**, 843-849 (2019)
- [2] M. Kroker, Zs. Czigány, Z. Weiss, M. Fekete, P. Souček, K. Balázsi, V. Sochora, M. Jílek, P. Vašina: *On the Origin of Multilayered Structure of W-B-C Coating Prepared by Non-Reactive Magnetron Sputtering from a Single Segmented Target*, Surface and Coatings Technology **377**, 124864 (2019)
- [3] S. Mirzaei, M. Alishahi, P. Souček, J. Ženíšek, D. Holec, N. Koutná, V. Buršíková, M. Stupavská, L. Zábanský, F. Burmeister, B. Blug, K. Balázsi, Zs. Czigány, R. Mikšová, P. Vašina: *The effect of chemical composition on the structure, chemistry and mechanical properties of magnetron sputtered W-B-C coatings: Modelling and experiments*, Surface and Coatings Technology **383**, 125274 (2020)
- [4] L. Zábanský, P. Souček, P. Vašina, J. Dugáček, P. Sťahel, J. Buršík, M. Svoboda, R. Mikšová, V. Peřina, K. Balázsi, Zs. Czigány, V. Buršíková: *Microstructural changes of amorphous Mo-B-C coatings upon thermal annealing*, Surface and Coatings Technology **379**, 125052 (2019)

INFLUENCE OF BATH ADDITIVES ON THE THERMAL STABILITY OF THE NANOSTRUCTURE AND HARDNESS OF Ni FILMS PROCESSED BY ELECTRODEPOSITION

T. Kolonits, L. Péter, I. Bakonyi, J. Gubicza and Zs. Czigány

The effect of various organic additives (such as saccharin and trisodium-cytrate) on the microstructure (grain size, dislocation and twin densities), mechanical properties and thermal stability of electrodeposited Ni films was investigated by X-ray diffraction (XRD) line profile analysis and transmission electron microscopy (TEM). The main task of the project is to investigate the thermal stability of different initial microstructures, which could be formed by solving organic additives in the original electrolyte.

The electrodeposited layers were deposited at room temperature at low current density onto copper substrate. The basic electrolyte mainly contained nickel-sulphate ($\text{NiSO}_4 \cdot 7 \text{H}_2\text{O}$) and boric acid (H_3BO_3). XRD and TEM grain size and phase analysis was carried out to determine the microstructure. Hardness tests were made to examine the mechanical properties. Heat treatment (at 400, 500, 600, 750 and 1000 K) was applied to investigate the stability of the micro and macro properties.

During this work, three different initial microstructures were formed: the organic additive free bath resulted a large grain size (90-130 nm), a low dislocation density ($13 \times 10^{14} \text{ m}^{-2}$) and a (220) type texture. Trisodium citrate resulted a moderate grain size (60-80 nm) and dislocation density ($30 \times 10^{14} \text{ m}^{-2}$) and the direction of the texture changed into (200). The additive saccharin resulted in the smallest grain size (20-30 nm), the largest defect density ($160 \times 10^{14} \text{ m}^{-2}$), the highest hardness and the texture was eliminated.

The changes of the hardness and the microstructure during the heat treatment can be followed on Fig. 1. It was found that the layer with additive saccharin which showed the highest hardness at room temperature has the worst thermal stability since the high defect density led to a large driving force for recrystallization; the recrystallization process occurred between 750-1000 K and took place in a few minutes. The best thermal stability was achieved in the layer processed with trisodium-cytrate as recrystallization has not been observed even after heating up to 1000 K [1].

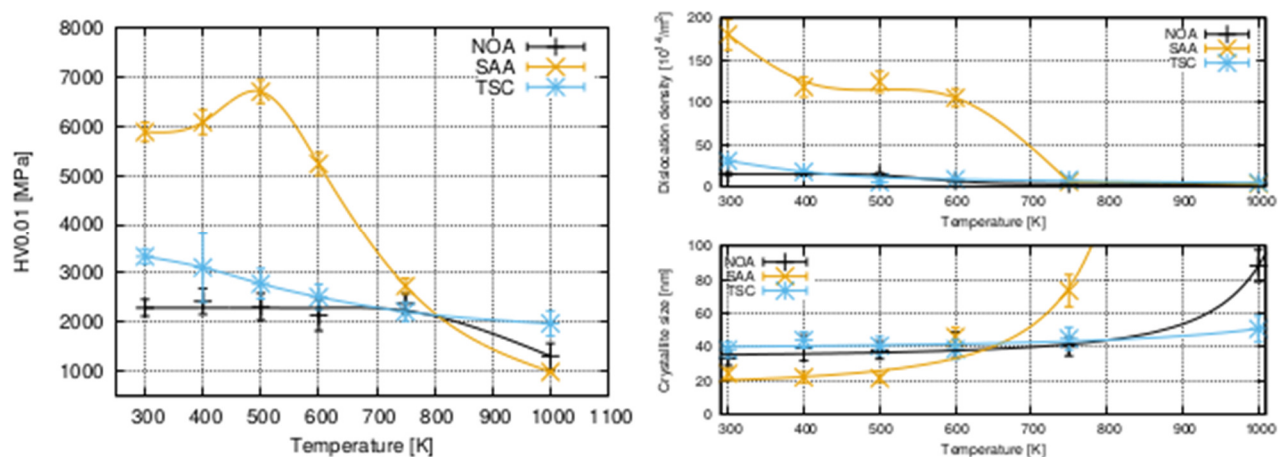


Figure 1: Hardness, dislocation density and crystallite size of heat-treated electrodeposited nanocrystalline nickel layers

Related publication

- [1] T. Kolonits, Zs. Czigány, L. Péter, I. Bakonyi, J. Gubicza, J.: *Influence of Bath Additives on the Thermal Stability of the Nanostructure and Hardness of Ni Films, Processed by Electrodeposition*, *Coatings* **9**, 644 (2019)

TEM STUDY OF NICKEL SILICIDES

E. Dódney, Gy. Z. Radnóczy

Controlled formation of nickel silicide materials is still extensively studied, due to their impact in microelectronics. As the industry is heading towards ever smaller device sizes, new challenges arise. The phase formation and sequence of the nickel silicides differ from the results of the bulk experiments, because of the restricted dimensions. In order to make and optimize devices and their performance, it is necessary to learn how the used materials are formed, what is their atomic structure, and how it transforms as a function of elapsed time.

Due to their importance, we are studying the formation of copper-silicides in thin amorphous silicon (a-Si) films, with the focus on the development and structure of the γ phase $\text{Ni}_{31}\text{Si}_{12}$. The samples – 10nm thick a-Si foils, supported by a Ni microgrid – were heated in-situ to temperatures up to 600 °C, and the silicide formation was investigated. The model structure was created by DC magnetron sputtering a layer of Si in Ar on cleaved NaCl substrate, then, the a-Si layer was transferred to the Ni microgrid by dipping the NaCl in water. The grid acted as the metal source for the silicide formation, where the phases were identified through selected area diffraction (SAED) patterns and high-resolution transmission electron microscopic (HRTEM) images. We have observed polymorphs of the γ phase $\text{Ni}_{31}\text{Si}_{12}$ with ($c_0=6, 12, 18, 24$ and 36 \AA) so called $S_6, S_{12}, S_{18}, S_{24}, S_{36}$. While working on the new Themis microscope of the Thin Film Department, we have observed the S_6 polymorph, which was not documented to date. We have determined its structure using techniques of electron crystallography. The good match between simulated (JEMS) and the gathered experimental data validated the new crystal structure in the $\text{Ni}_{31}\text{Si}_{12}$ composition (Fig. 1). (To be published.)

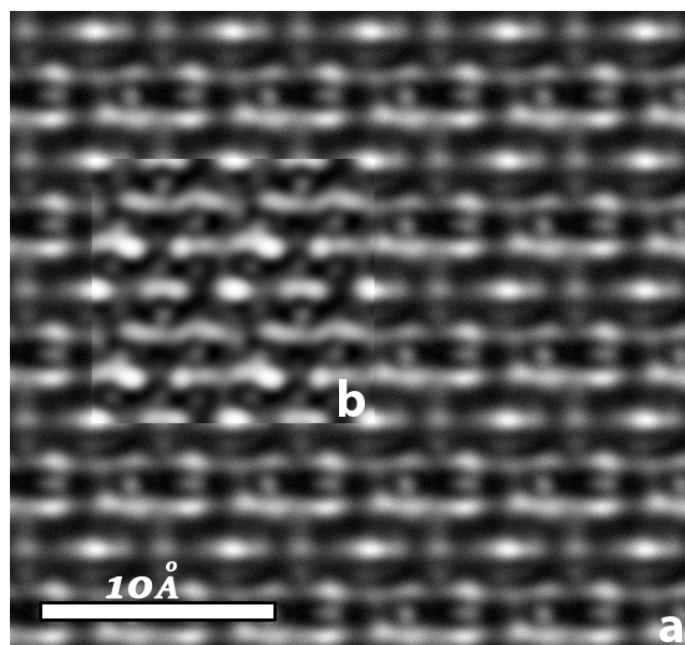


Figure 1: a) Fourier-filtered experimental HRTEM image of S_6 and b) its built structure's simulated HRTEM image

A MICRO-COMBINATORIAL STUDY OF THE OPTICAL PROPERTIES OF A-SiGe:H TOWARDS A DATABASE FOR OPTOELECTRONICS

B. Kalas, Zs. Zolnai, G. Sáfrán, M. Serényi, N. Szász, G. Dobrik, E. Agocs, Tivadar Lohner, Attila Németh, Nguyen Quoc Khanh, M. Fried and P. Petrik

In a co-operation with the Photonics Laboratory the optical parameters of hydrogenated amorphous a-Si_{1-x}Ge_x:H layers were measured with focused beam mapping ellipsometry for photon energies from 0.7 to 6.5 eV. The single-sample micro-combinatorial technique developed at the Thin Films Physics Department enables the preparation of thin binary samples with full range composition spread. Linearly variable composition profile was revealed along the 20 mm long gradient part of the sample by Rutherford backscattering spectrometry and elastic recoil detection analysis. The Cody-Lorentz approach was identified as the best method to describe the optical dispersion of the alloy.

Amorphous Si_{1-x}Ge_x:H samples were prepared on 10 mm x 25 mm size Si wafers by "single-sample" micro-combinatorial that resulted in gradient composition of Si_{1-x}Ge_x with x ranging in 0 ≤ x ≤ 1. The layers with thicknesses of about 100 nm were deposited in an Ultra-high vacuum (UHV) system by dual DC magnetron sputtering using a patented, scaled-up technique and device originally developed for synthesizing micro-combinatorial TEM samples [1, 2]. The device sweeps a shutter with a 1 mm x 10 mm slot in fine steps above the wafer meanwhile the power of the two DC magnetron sources is regulated in sync with the slot movement that creates a gradient of the composition. The details were described earlier for non-hydrogenated a-Si_{1-x}Ge_x samples [3]. The present samples were deposited at a sputtering rate of 0.4 nm/s, in a mixture of H and Ar. The H partial pressures (p_H/p) were 0, 0.05, 0.1 and 0.2 and the total plasma pressure (p) was kept at 3x10⁻³ mbar.

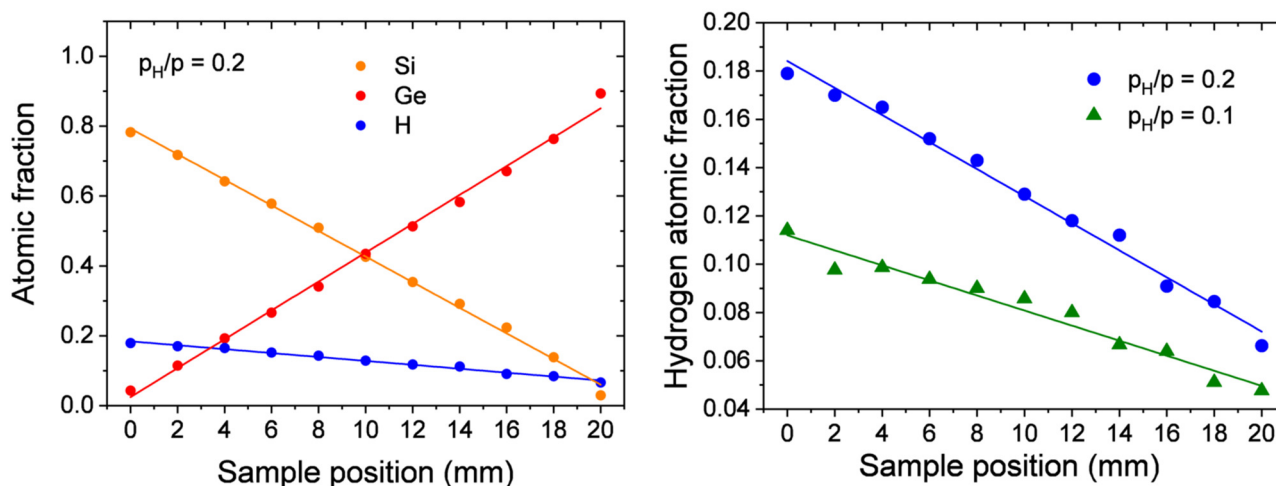


Figure 1: a) Atomic fractions of Si and Ge showing the incorporated H for $p_H/p = 0.2$ of the SiGe layer along the sample measured by RBS, b) atomic fractions of H evaluated from ERDA spectra applying simulations by the RBX software [4] for samples with $p_H/p = 0.1$ and 0.2 , respectively).

The 25 mm long samples exhibit a 20 mm long gradient a-Si_{1-x}Ge_x:H track enclosed between 2.5 mm long lead-in sections of pure Si and Ge, respectively. The sample position "0" belongs to the Si-rich side of the gradient track. Fig. 1.a depicts highly linear curves of Si, Ge and H atomic fractions, along the sample, measured by Rutherford backscattering (RBS) and Elastic Recoil Detection Analysis (ERDA), while Fig. 1.b represents the H-content change with the position from Si-rich to Ge-rich layer, that proves different H-incorporation into Si and Ge. [4].

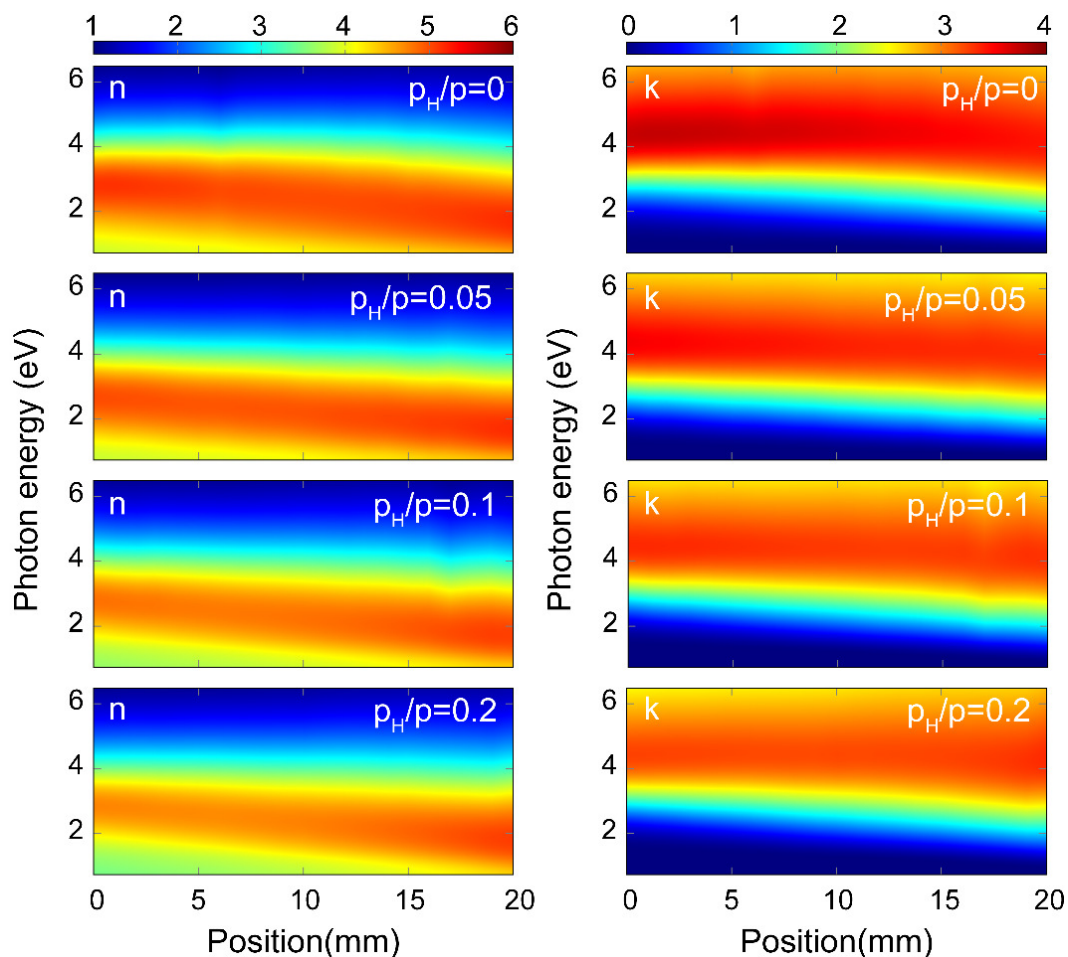


Figure 2: Real and imaginary parts of the complex refractive indices of $a\text{-Si}_{1-x}\text{Ge}_x\text{:H}$ thin films (left and right column, respectively) with different partial pressures of H ($p_{\text{H}}/p = 0; 0.05, 0.1$ and 0.2) as a function of both the position along the 20 mm long gradient section (composition) and photon energy. According to the RBS plots, the position at 0 mm corresponds to the Si-side of the sample.

Fig. 2 shows maps of both n and the extinction coefficient (k) of all samples ($p_{\text{H}}/p = 0, 0.05, 0.1$ and 0.2) in the whole range of compositions, for photon energies from 0.7 to 6.5 eV. The n and k were obtained by fitting the measured spectra using the Cody-Lorentz (CL) optical model. The features in both n and k show a linear change with the position, hence, also with the composition. The single broad peak, characteristic of amorphous semiconductors can clearly be identified in all maps. The peaks are shifted to smaller photon energies as the composition changes from Si to Ge (positions from 0 to 20 mm). There is also a remarkable shift of the peaks vs. H content towards a higher band gap, smaller amplitude and broadening. The maps in Fig. 2 represent a complete database for optical properties of $a\text{-Si}_{1-x}\text{Ge}_x\text{:H}$.

The effect of incorporated H on the optical absorption is explained by the lowering of the density of localized states in the mobility gap. It is shown that in the low-dispersion near infrared range the refractive index of the $\text{Si}_{1-x}\text{Ge}_x$ alloy can be comprehended as a linear combination of the optical parameters of the components. The results revealed above prove that micro-combinatorial sample preparation combined with mapping ellipsometry is not only suitable for the fabrication of samples with controlled lateral distribution of the concentrations, but also opens new prospects in creating databases of composition dependent properties of compounds for optical and optoelectronic applications.

This work was supported by the Economic Development Innovation and Operative Program. GINOP # 2.1.7-15.

Related publications

- [1] G. Sáfrán: Hung. Patent No. P150 050 0 (2015)
- [2] G. Sáfrán: "One-sample concept" micro-combinatory for high throughput TEM of binary films, *Ultramicroscopy* **187**, 50–55 (2018)
- [3] T. Lohner, et al.: Refractive index variation of magnetron-sputtered $a\text{-Si}_{1-x}\text{Ge}_x$ by "One-Sample Concept" Combinatory, *Appl. Sci.* **8**, 826 (2018)
- [4] E. Kotai: Computer methods for analysis and simulation of RBS and ERDA spectra, *Nucl. Inst. Meth. B* **85**, 588–596 (1994)

CERAMIC DISPERSION STRENGTHENED SINTERED STAINLESS STEELS AFTER THERMAL AGEING

MTA Hungarian – Japan Bilateral project (CeramODS)

C. Balázsi, K. Balázsi, H. R. Ben Zine, M. Furkó, Zs. Czigány, L. Almásy, V. Ryukhtin, H. Murakami, G. Göller, O. Yucel, F. C. Sahin, S. Kobayashi, Á. Horváth

Oxide dispersion strengthened (ODS) ferritic steels can be used as large scale structural materials in many industrial applications owing to their excellent corrosion resistance in oxidising and/or sulphidising environments. The ODS steels are useful base materials for boilers and turbines of power generation plant co-firing coal or gas with renewable fuels such as biomass for high temperature, high pressure tubing applications, fast breeder reactors and blanket applications for fusion reactors.

The aim of research was the development of the ultrafine grained silicon nitride by powder technology has been studied. The effect of the yttria addition to the morphological, structural, mechanical and magnetic properties of the ceramic dispersion strengthened 316L stainless steels was studied.

Two ceramic dispersion strengthened (CDS) composites have been prepared: 316L/0.33 wt% Si₃N₄ and 316L/1 wt% Si₃N₄. Spark plasma sintering (SPS) was used for fast compaction of milled composite powders (Fig. 1.a) [1].

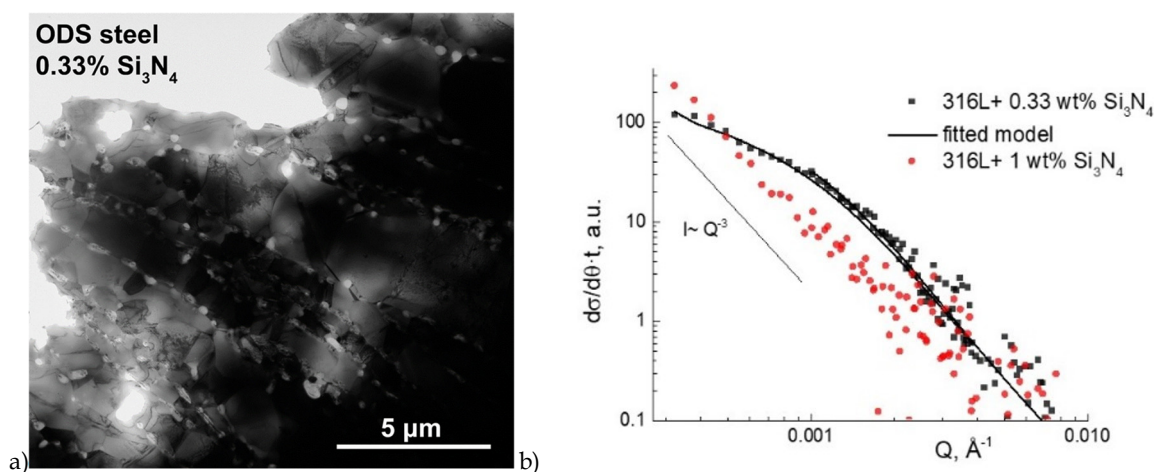


Figure 1: Si₃N₄ ceramic dispersed strengthened steel. a) structure, b) SANS measurements

The samples were enclosed in a vacuum quartz tube and then aged at 600 °C in a high-temperature furnace up to 10 h and 20 h. For CDS with 1wt% Si₃N₄ ageing was carried out also at 800 °C. The hardness values have been found to be twice as high (300 HV) in the cases of CDS samples in comparison to reference sample.

SANS data measured on the sintered samples at double-bent-crystal (DBC-SANS) facility are presented in Fig. 1.b. The scattering curves obey Porod law ($I \sim Q^{-3}$) over the whole measured q -range. This corresponds to the interface scattering from particles larger than several micrometres. This scattering behaviour is observed for sample with 1wt% of Si₃N₄ (Fig. 1.b). However, SANS on 316L+ 0.33 wt% of Si₃N₄ has demonstrated presence of smaller (submicron) size particles. The scattering data were fitted to a model scattering of spherical particles with log-normal size distribution, and the fitted averaged diameter is obtained as $\langle D \rangle = 441 \pm 33$ nm. The presence of smaller grains in this sample is probably caused by their better dispersion in the steel matrix, and contribute to the favourable mechanical properties of these CDS.

To investigate possible microstructural changes with ageing, Electron backscatter diffraction (EBSD) measurements were performed for CDS sample with 1.0 wt.% Si₃N₄ aged at 800°C. The average grain size is ~14 microns and small amount of bcc iron structure ($< \sim 0.2\%$) was also detected for this sample (Fig. 2.a). The magnetic characterization of samples demonstrated that the samples exhibit ferromagnetic property already before ageing and a larger ferromagnetic component was observed as a result of thermal aging.

Fig. 2.b shows data for CDS samples with 1.0 wt% Si₃N₄ inclusion, aged at 800°C. The sample exhibits ferromagnetic property before ageing, associated with a hysteresis around zero magnetic field. In particular, for the sample used for ageing at 800°C, we observed a large ferromagnetic component, which evolves with thermal ageing.

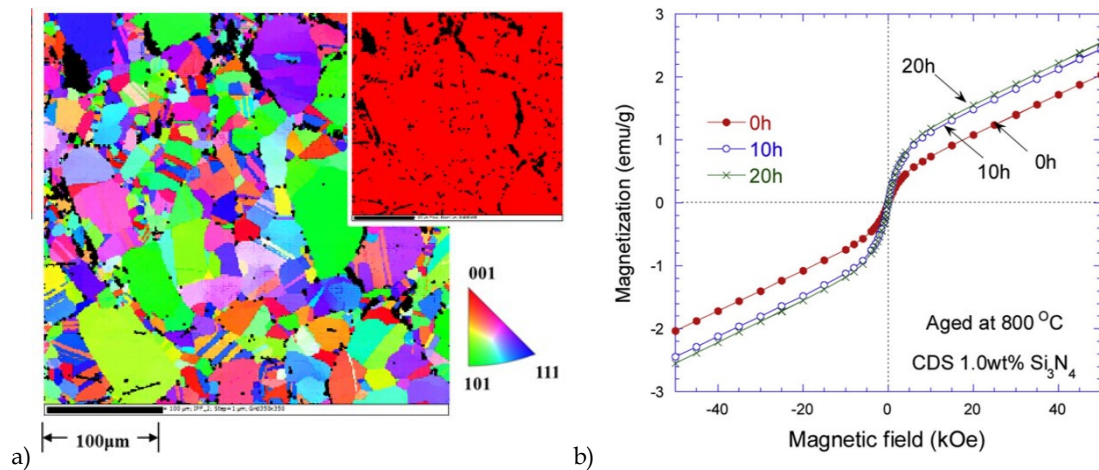


Figure 2: a) EBSD inverse pole figure (IPF) map of CDS samples with 1.0 wt% Si₃N₄ for ageing time of 20 h, showing crystal orientation along the normal direction of sample surface. The insets show phase colour map. The crystal structure of Si₃N₄ was not considered in this analysis, b) Magnetization curves for 1.0 wt.% Si₃N₄ CDS samples aged at 800 °C.

The magnetic characterization of samples demonstrated that the samples exhibit ferromagnetic property before ageing and a large ferromagnetic component was observed, which evolved with thermal aging [2]. It was proven that for ODS and CDS samples with a low amount of Y₂O₃ or Si₃N₄, the saturation magnetization was slightly dependent on ageing time, however, it exhibited a noticeable change with ageing both at 600 and 800 °C for samples containing higher amount of additives.

Related publications

- [1] H.R. Ben Zine, K. Balázs, C. Balázs: *Effect of the α -Si₃N₄ addition on the tribological properties of 316L stainless steel prepared by attrition milling and spark plasma sintering*, *Anyagok Világa (Materials World)* **1**, 9-16 (2018)
- [2] C. Balázs, H. R. Ben Zine, M. Furko, Z. Czigány, L. Almásy, V. Ryukhtin, H. Murakami, G. Göller, O. Yucel, F.C. Sahin, K. Balázs, S. Kobayashi, A. Horváth: *Microstructural and magnetic characteristics of ceramic dispersion strengthened sintered stainless steels after thermal ageing*, *Fusion Engineering and Design* **145**, 46-53 (2019)

SI(B) A PROSPECTIVE MATERIAL FOR QUANTUM ELECTRONIC APPLICATIONS

VEKOP-2.3.3-15-2016-00002

J.L. Lábár, M. Menyhárd, A. Sulyok, L. Illés, F. Chiodi, S. Lequien, F. Lefloch, F. Nemouchi

Gas Immersion Laser Doping (GILD) of Si with boron provided shallow, box-like regions, where B concentration exceeds thermodynamic equilibrium level without forming precipitates. In such material, superconductivity was measured below 1 K. However, to detect either the concentration, or spatial distribution of B is a difficult task. In the present paper, we show a TEM-based method for measuring B concentration and determining the extent of the heavily B-doped region.

Preparation of the TEM lamella and examination of the native sample with SEM/EDS was done in a SCIOS-2 type dual-beam Field Emission Gun - Scanning Electron Microscope (FEG-SEM)/Focused Ion Beam (FIB) equipped with Oxford X-maxN 20 type EDS. FIB-lamellae were cut by Ga⁺-ions with special care taken to avoid heating of the samples during preparation. The selected region was protected by Pt-deposition prior to cutting. First an <100 nm thick Pt was deposited by e-beam assisted deposition (2 kV, 3.2 nA), followed by a thicker (1.5 μm) ion-beam assisted deposited Pt layer (30 kV, 300 pA). The trenches at the two sides of the lamella were milled with a 30 kV Ga-ion beam (15 nA). When the lamella reached 3 μm thickness, it was further thinned in the bulk with 30kV, 7 nA ion current down to a thickness of 1.5 μm. Then it was cut out (30 kV, 5 nA) and welded to the TEM-grid (using back-sputtering at 30kV 5 nA) for further thinning. The thinning started with 16 kV 50 pA Ga-beam. Polishing in two steps: 5 kV 48 pA followed by 2 kV 27 pA till proper transparency.

TEM and energy-disperse X-ray spectroscopy (EDS) examinations were performed in a Titan Themis G2 200 STEM equipped with a four-segment Super-X EDS detector. The corrector for the spherical aberration (C_s) was applied at the imaging part, while no probe-correction was present. Image resolution limit is 0.08 nm in phase-contrast HRTEM mode, while resolution is 0.16 nm in STEM Z-contrast imaging mode (by using a Fishione high-angle annular dark-field (HAADF) detector). HRTEM images were recorded at 200 keV with a 4k × 4k CETA 16 CMOS camera.

Auger Electron Spectroscopy (AES) depth profiling of B was done in STAIB DESA 150 analyser with pre-retarded Cylindrical Mirror Analyser (CMA). Depth profiling with AES did not require any preparation prior to insertion into the UHV. Depth profiling: projectile Ar⁺, energy 1 keV, angle of incidence 75° (with respect to surface normal), specimen rotation during sputtering. Using these parameters for sputter removal, bombardment induced roughness is not expected.

First, we proved that the layer close to the surface really contains B, as expected. A sample without any prior preparation was inserted into the SEM and an EDS spectrum was recorded with 1 kV primary electron beam energy, to ensure that the excited volume is within the top 30 nm of the sample. Fig. 1. shows that B K-line and Si L-line are clearly present. However, the commercial program of the EDS could not give quantitative result at that energy with the Si L-line.

Next, Auger electron depth profiling was carried out starting from the native surface. Fig. 2 demonstrates that B is only present in the layer close to the surface and its concentration does not vary with depth. Thus, the procedure resulted in a good quality homogeneous B doping. Both the depth scale and the concentration value were fitted to the TEM result.

Finally, the cross-sectional TEM lamella was examined by TEM. Note that EDS in the TEM was unable to measure B properly, due to the extremely high overvoltage. Electron diffraction proved that the crystal structure in the layer is identical to that of Si. Measurement of both the B concentration and the thickness of the B-doped layer were based on observation of the change in the lattice parameter due to the difference in the atomic radii of Si and B. The resulting strain and lattice defects made the layer visible even in the bright field (BF) image in the TEM. However, it was only the lattice resolution image (HRTEM) recorded by phase contrast (Fig. 3.), that facilitated measuring quantitatively the change in the local lattice parameter. That difference in lattice parameter was converted into local B concentration by using the Vegard's law. Boron in pure form cannot be found in cubic structure, so Vegard's law cannot be applied to the pure end-members of the oversaturated Si(B). However, the x-ray diffraction database contains Si-1%B, which has the same crystal structure as Si, which still allows to rely on Vegard's law. As it is seen in Fig. 3, the thickness of the B-doped layer is 30 nm. It also contains stacking faults occasionally. Selecting regions without crystal defects, we can measure the lattice parameter both in the layer and in the pure Si substrate. The latter one was used to fine-tune the calibration of the magnification of the TEM. Table 1 summarizes the measurement results on several images. As a result the B-content is 7,15±2,86 at% in a 30 nm thick layer. The scatter is probably a superposition of both local variation and measurement uncertainty.

Table 1: B-concentration determined from HRTEM images on the basis of Vegard's law

FFT #	Miller index	d-in-layer	d-in-Si	d-in-Si-%B	B[at%]	Magnification of HRTEM
915	333	1,035	1,0450	1,0424	3,88	630 k
921	333	1,033	1,0450	1,0424	4,85	800 k
923	333	1,029	1,0450	1,0424	6,21	380 k
924	333	1,015	1,0450	1,0424	11,65	380 k
927	333	1,022	1,0450	1,0424	9,13	380 k

This research was supported by VEKOP-2.3.3-15-2016-00002 of the European Structural and Investment Funds.

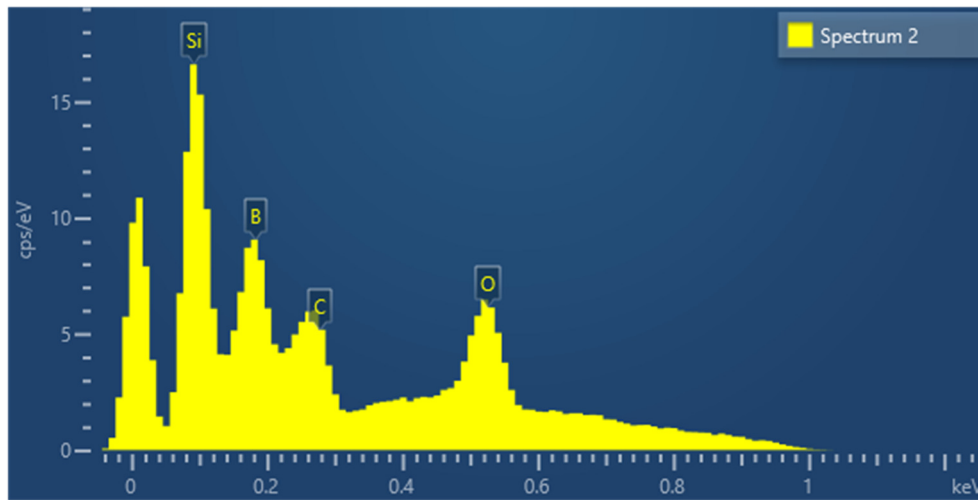


Figure 1: EDS spectrum recorded at 1 kV in the SEM from native surface of the implanted layer

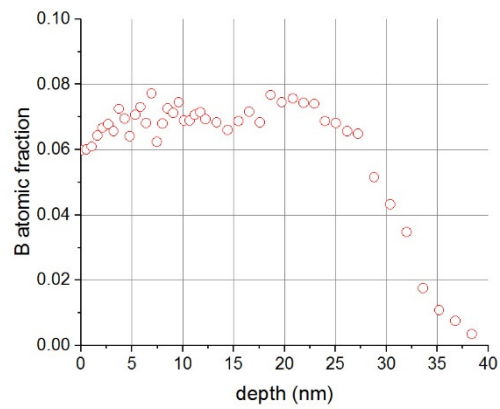


Figure 2: AES depth profile from native surface of the implanted layer

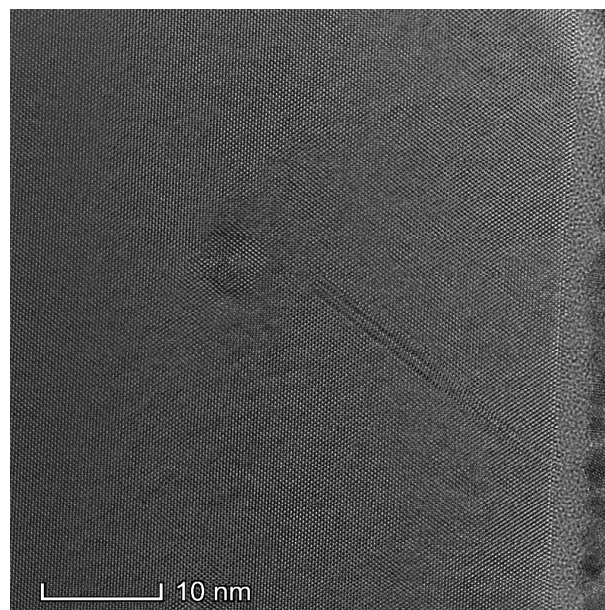


Figure 3: HRTEM image from a cross section of the sample

BURSTS IN THREE-STRATEGY EVOLUTIONARY GAMES ON A SQUARE LATTICE

OTKA K120785

G. Szabó, B. Király, and K. Hódsági

The evolutionary potential games exhibit thermodynamic behaviour if the strategy updates are controlled by the so-called logit rule, which is a consecutive selfish one-site strategy updates resembling dynamics used widely in Monte Carlo analyses of many-particle systems. Now we have considered three-strategy evolutionary games on a square lattice when the pair interactions are composed of three types of elementary interactions. The first component is equivalent to the three-state Potts model and it results in the formation of one of the three equivalent homogeneous states at low noise levels. The second component favours the first strategy similarly to the application of a suitable external field in spin systems. The third component describes Rock-Paper-Scissors type cyclic dominance. In contrary to the naive expectation the presence of cyclic component yields paradoxical effect. Namely, instead of the externally supported (first) strategy the system will be dominated by its predator (second strategy). The homogeneous state of the second strategy, however, is unstable. Due to the cyclic dominance a sufficiently large island of the third strategy can expand as illustrated in Fig. 1.

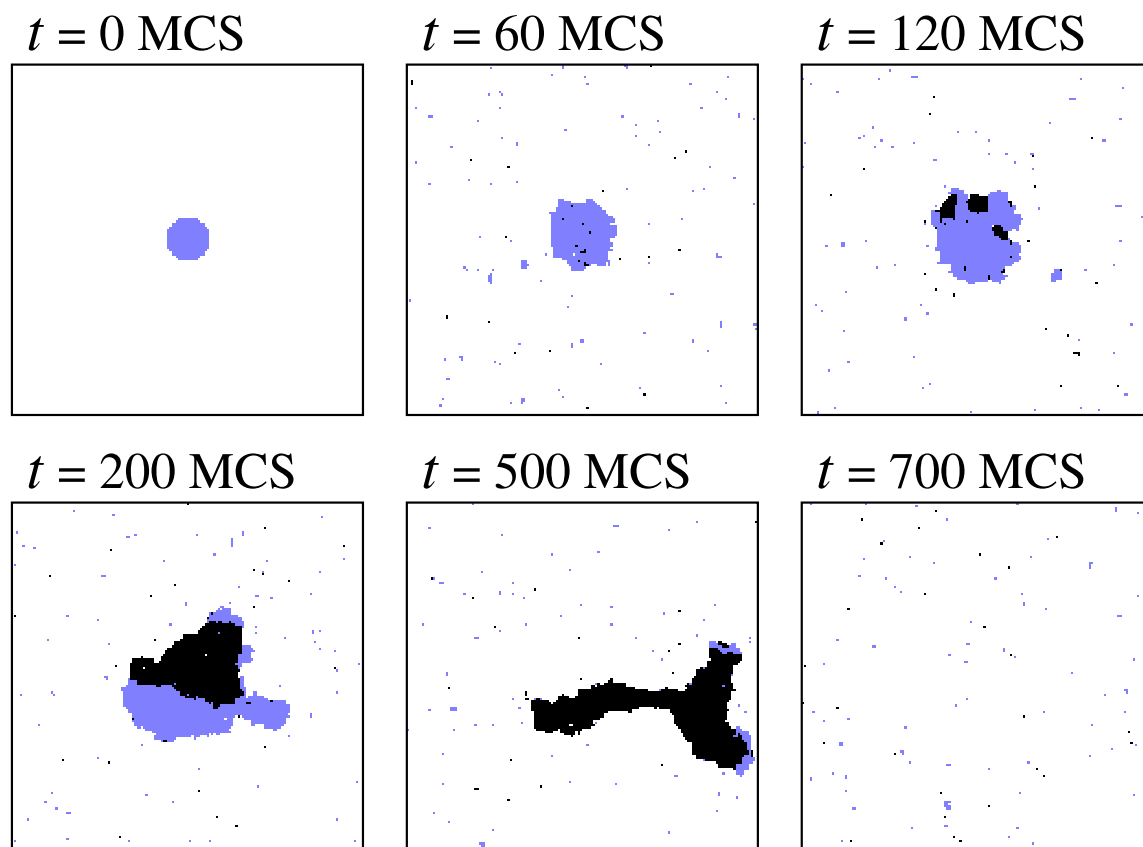


Figure 1: Evolution of strategy distribution if a sufficiently large circular island of strategy 3 (blue pixels) is inserted into the sea of strategy 2 (white pixels). The growth of the island of strategy 3 is reversed when the strategy 1 (black pixels) occurs and invades the territory of 2s. Sooner or later, however, the black domains are also shrunken via the same mechanism.

In the homogeneous states the sufficiently large predator domains can occur via a nucleation mechanism which is well described in material sciences. The curiosity of these phenomena is that here two (or more) consecutive nucleation processes drive the system back to the state dominated by strategy 2. Notice that for three-state cyclic dominance the most aggressive strategy cannot expand after having eliminated its prey and finally its predator invades the whole system because of the extinction of its predator.

In these systems similar bursts can occur anywhere via the stochastic processes mentioned above. The frequency of these bursts is proportional to the system size and it decreases with the noise. At the same time, the maximum extension of these bursts increases when the noise level is reduced. Fig. 2 shows the frequency of strategy 3 for parameters when the bursts are well separated in time.

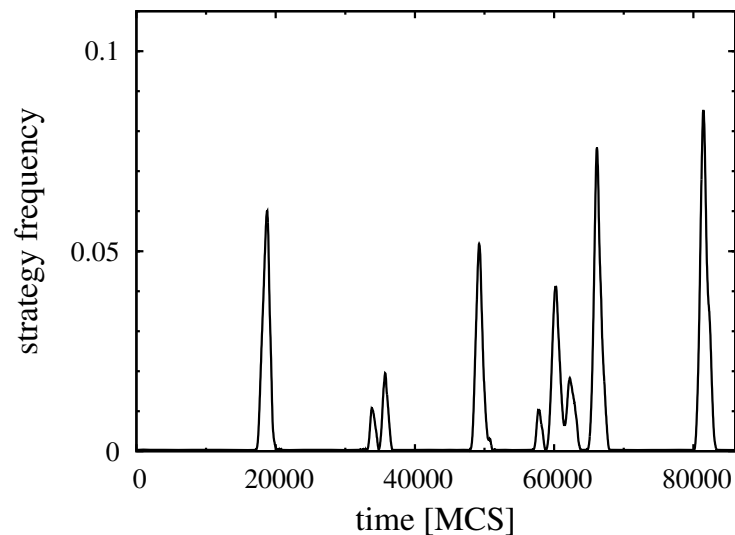


Figure 2: Typical time-dependence of the frequency of strategy 3 in a large system for low noise levels when the bursts (illustrated in Fig. 1) occur rarely. In these Monte Carlo simulations we used large linear system size (it is varied from $L=1000$ to 2800), thus these bursts may include more than $100,000$ lattice sites.

The quantitative analyses of the fluctuations in the strategy frequencies have indicated huge increase at low noises despite of the relevant reduction of the average bursts frequencies.

Finally it is worth to mention that the above model represents a type of social dilemma when the paradoxical effect of cyclic dominance drives the system into a social trap where the average income is not optimal at low noise levels. It is found, however, that in a narrow range of noise level these systems can achieve higher average income [1, 2].

Related publications

- [1] K. Hódsági and G. Szabó: *Bursts in three-strategy evolutionary ordinal potential games on a square lattice*, *Physica A* **525**, 1379-1387 (2019)
- [2] B. Király and G. Szabó: *Interplay of Elementary Interactions Causing Social Traps in Evolutionary Games*, *Frontiers in Physics* **8**, 59 (2020)

SEASONAL PAYOFF VARIATIONS AND THE EVOLUTION OF COOPERATION IN SOCIAL DILEMMAS

OTKA K120785

A. Szolnoki and M. Perc

Varying environmental conditions affect relations between interacting individuals in social dilemmas, thus affecting also the evolution of cooperation. Oftentimes these environmental variations are seasonal and can therefore be mathematically described as periodic changes. Accordingly, we here study how periodic shifts between different manifestations of social dilemmas affect cooperation. We observe a non-trivial interplay between the inherent spatiotemporal dynamics that characterizes the spreading of cooperation in a particular social dilemma type and the frequency of payoff changes. In particular, we show that periodic changes between two available games with global ordering best be fast, while periodic changes between global and local ordering games best be slow for cooperation to thrive. We also show that the frequency of periodic changes between two local ordering social dilemmas is irrelevant, because then the process is fast and simply the average cooperation level of the two is returned. The structure of the interaction network plays an important role too in that lattices promote local ordering, whilst random graphs hinder the formation of compact cooperative clusters. Conversely, for local ordering the regular structure of the interaction network is only marginally relevant as role-separating checkerboard patterns do not rely on long-range order.

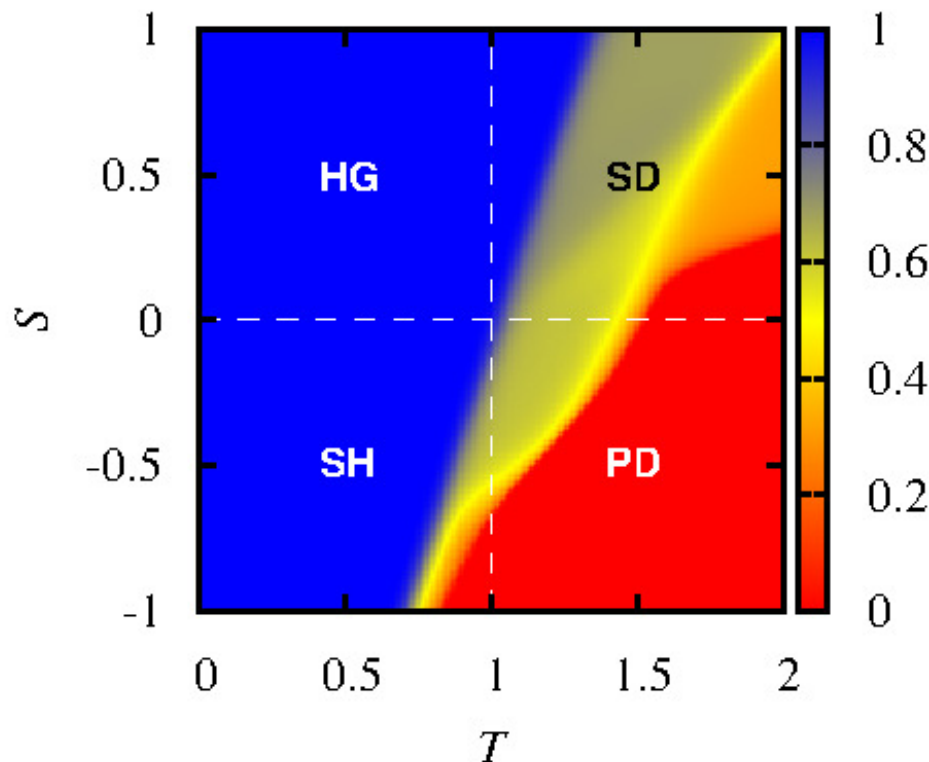


Figure 1: Colour maps encoding the stationary density of cooperators on the full T - S plane obtained on square lattice. The payoff values ($T_1 = 0.9$, $S_1 = 0.1$) and ($T_2 = T$, $S_2 = S$) are exchanged periodically with period $\tau = 1$. In the snowdrift quadrant (SD), seasonal effects have a very similar impact on cooperation regardless of the applied interaction network. Conversely, in the stag-hunt (SH) and the prisoner's dilemma quadrant (PD), cooperators fare better under seasonal variations.

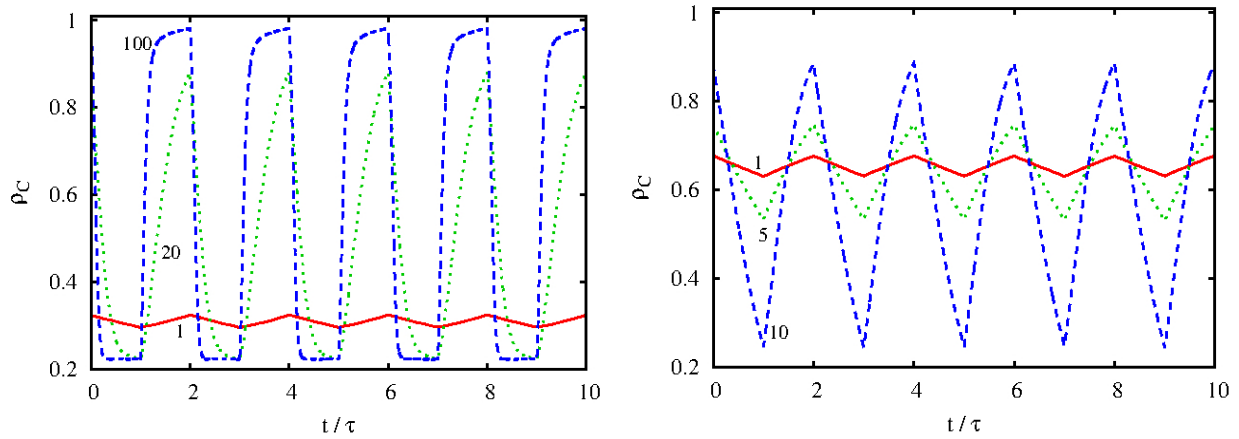


Figure 2: Left: Time evolution of the cooperation level f_C in the stationary state, as obtained for different values of τ in the snowdrift game ($T=2$, $S=0.5$). Right: Time evolution of the cooperation level f_C in the stag-hunt game ($T=0.92$, $S=-0.5$). It can be observed that the relaxation dynamics for the snowdrift game is fast, while for the harmony game and the stag-hunt game, it is comparatively much slower.

We have shown that there exists a non-trivial interplay between the inherent spatio-temporal dynamics that characterizes the spreading of cooperation in a particular social dilemma type and the frequency of payoff changes. The inherent spatiotemporal dynamics is affected by the parameterization of the two games entailed in the switch, and by the structure of the interaction network. In particular, when cooperation proliferates by means of compact clusters, as is the case in the harmony game, the stag-hunt game, and the prisoner's dilemma game, the relaxation times are longer and the translation invariant feature of an interaction graph promotes the local emergence of a coordinated state that is necessary for a spreading process to reach a global ordering. Accordingly, we have shown that periodic changes between two games with global ordering should be fast for cooperation to be promoted, and preferably unfold on a network without long-range links, like a square lattice. If an interaction network with long-range links is used, like a regular random graph, then the irregular structure hinders the formation of compact clusters, which in turn impairs the evolution of cooperation. Since the observed behaviour is strongly related to the diverse speed of spreading at different payoff values, we may expect conceptually similar behaviour in scale-free and multilayer complex networks as well. [1].

Related publication

- [1] A. Szolnoki and M. Perc: *Seasonal payoff variations and the evolution in cooperation in social dilemmas*, Scientific Reports **9**, 12575 (2019)

CRITICAL SYNCHRONIZATION DYNAMICS OF THE KURAMOTO MODEL ON CONNECTOME AND SMALL WORLD GRAPHS

OTKA K128989

G. Ódor, J. Kelling, R. Juhász and G. Deco

We considered the Kuramoto model on sparse random networks such as the Erdős–Rényi graph or its combination with a regular two-dimensional lattice and study the dynamical scaling behaviour of the model at the synchronization transition by large-scale, massively parallel numerical integration. By this method, we obtain an estimate of critical coupling strength more accurate than obtained earlier by finite-size scaling of the stationary order parameter. Our results confirm the compatibility of the correlation-size and the temporal correlation-length exponent with the mean-field universality class [1].

The hypothesis, that cortical dynamics operates near criticality also suggests, that it exhibits universal critical exponents, which marks the Kuramoto equation, a fundamental model for synchronization, as a prime candidate for an underlying universal model. Here, we determined the synchronization behaviour of this model by solving it numerically on a large, weighted human connectome network, containing 836733 nodes, in an assumed homeostatic state. Since this graph has a topological dimension $d < 4$, a real synchronization phase transition is not possible in the thermodynamic limit, still we could locate a transition between partially synchronized and desynchronized states. At this crossover point we observe power-law-tailed synchronization durations, with $\tau_t \approx 1.2(1)$, away from experimental values for the brain. For comparison, on a large two-dimensional lattice, having additional random, long range links, we obtain a mean-field value: $\tau_t \approx 1.6(1)$. However, below the transition of the connectome we found global coupling control-parameter dependent exponents $1 < \tau_t \leq 2$, overlapping with the range of human brain experiments. We also studied the effects of random flipping of a small portion of link weights, mimicking a network with inhibitory interactions, and found similar results. The control parameter dependent exponent suggests extended dynamical criticality below the transition point [2, 3].

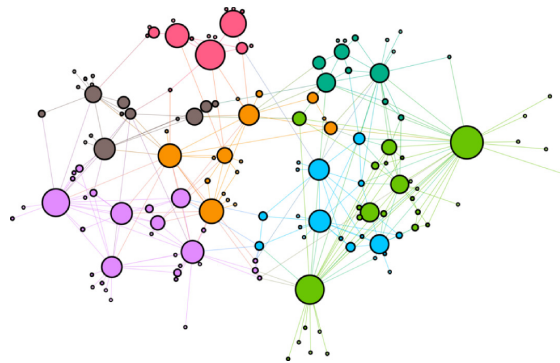


Figure 1: Network of the modules of the KKI-18 human connectome graph is shown. The size of circles is proportional with the number of nodes.

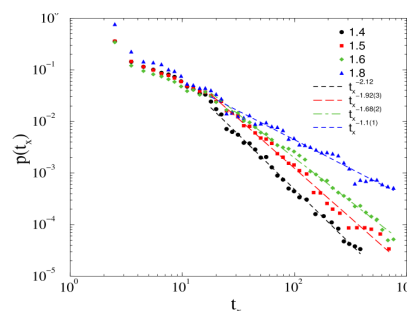


Figure 2: Duration distribution of on the KKI-18 model for growth $K = 1.4$ (bullets), 1.5 (boxes), 1.6 (diamonds), 1.8 (triangles). The dashed line shows power-law (PL) fits to the tail region: $t_x > 20$.

Related publications

- [1] R. Juhász, J. Kelling, and G. Ódor: *Critical dynamics of the Kuramoto model on sparse random networks*, J. Stat. Mech. 053403 (2019)
- [2] G. Ódor and J. Kelling: *Critical synchronization dynamics of the Kuramoto model on connectome and small world graphs*, Scientific Reports **9**, 19621 (2019)
- [3] G. Ódor, J. Kelling and G. Deco: *The effect of noise on the synchronization dynamics of the Kuramoto model on a large human connectome graph*, [arXiv:1912.06018](https://arxiv.org/abs/1912.06018)

ABBREVIATIONS

2D	Two-dimensional
8YSZ	8mol% Ytria-stabilized Zirconia
ACP	Amorphous Calcium Phosphate
ACTOF	Accident Tolerant Fuels
AEKI	Institute for Atomic Energy Research
AER	Atomic Energy Research
AES	Auger Electron Spectroscopy
AFM	Atomic Force Microscopy
a-Ge	Amorphized Ge
AMTD	Activity Median Thermodynamic Diameter
ANOVA	Analysis of Variance
ANP	Analytical Network Process
AQ	Amodiaquine
ALD	Atomic Layer Deposition
ALLEGRO	Experimental Helium Gas Cooled Fast Reactor Developed by the European V4G4
ATLAS+	Advanced Structural Integrity Assessment Tools for Safe Long Term Operation
ATOMKI	MTA Institute for Nuclear Research
BAGIRA	New Irradiation Device at the Budapest Research Reactor
BC	Black Carbon
BCA	Bicinchoninic Acid
BCC	Body Centred Cubic
BCS	Boron Coated Straw
BDD	Boron Doped Diamond
BEMA	Bruggeman Effective Medium Approximation
BF	Bright Field
BITS	Bin Type Statistical Simulation
BME	Budapest University of Technology and Economics
BNC	Budapest Neutron Centre
BRR	Budapest Research Reactor
BSA	Bovine Serum Albumin
BzO	Benzaldehyde (C ₆ H ₅ CHO)
BzOH	Benzyl alcohol (C ₆ H ₅ CH ₂ OH)
BZN	Bay Zoltán Nonprofit Ltd. for Applied Research
CAD	Computer-Aided Design
CAK	Zirconium Material Studies
CCMP	Computer Controlled Micropipette
CDS	Ceramic Dispersion Strengthened
CEFR	China Experimental Fast Reactor
CERIC	Central European Research Infrastructure Consortium
CERN	Centre Européen pour la Recherche Nucléaire (French name of the European Organization for Nuclear Research)
CFD	Computational Fluid Dynamics
CL	Cody-Lorentz
CNA	Complex Network Analysis
CNS	Cold Neutron Source
CNT	Carbon Nanotube
CMA	Cylindrical Mirror Analyser
CMD	Classical Molecular Dynamics, Carboxymethyl dextran
CMUT	Capacitive Micromachined Ultrasonic Transducer
COD	Chemical Oxygen Demand
COF	Friction Coefficient

CONCERT	EU H2020 Project for the Integration of Radiation Protection Research
CONFIDENCE	Consortia of an European Joint Programme (COping with uNcertainties For Improved modelling and DEcision making in Nuclear emergenCIes)
COPD	Chronic Obstructive Pulmonary Disease
CPE	Controlled Potential Electrolysis
CRP	IAEA Coordinated Research Project
CPL	Coplanar Transmission Line
CV	Cyclic Voltammetry
CVD	Chemical Vapour Deposition
D&D	Decommissioning and Dismantling
DBA	Design Basis Accident
DBC	Double-bent-crystal
DBTT	Ductile-to-brittle Transition Temperature
D3S	Distributed Space Weather Sensor System
DFT	Density Functional Theory
DFT-LSDA	Density Functional Theory with the Local Spin-density Approximation
DGA	Diglycol Amide
DLD	Deterministic Lateral Displacement
DLR	German Aerospace Centre
DOPC	Dioleoylphosphatidylcholine
DP	Deposition Precipitation
DRIFTS	Diffuse Reflectance Fourier Transform Infrared Spectroscopy
DRM	Dry Reforming
DSB	Double Strand Break
DSP	Dithiobis(succimidyl propionate)
DUV	Deep Ultraviolet
EB	Electron Beam
EBB	Elegant Breadboard Model
EB GL	Electricity Balancing Guidelines
EBSD	Electron Backscatter Diffraction
ECR	Equivalent Cladding Reacted
EDS, EDX	Energy-dispersive X-ray Spectroscopy
EDXRF	Energy-dispersive X-ray Fluorescence
EELS	Electron Energy Loss Spectroscopy
EEW	Electric Explosion of Wires
EGCG	Epigallocatechin-gallate
EMR	Electron Magnetic Resonance
ELTE	Eötvös Loránd University, Budapest
EMA	Effective Medium Approximation
EMR	Electron Magnetic Resonance
E-MRS	European Materials Research Society
EPS	Environmental Protection Service
EQM	Engineering Qualification Model
ERDA	Elastic Recoil Detection Analysis
ESA	European Space Agency
ESD	Electrospray Deposition
ESS	European Spallation Source, Lund
EURADOS	European Radiation Dosimetry Group
EVs	Extracellular Vehicles
EXAFS	Extended X-ray Absorption Fine Structure
FAZ	Fly Ash Zeolites
FC	Field Cooling
FCC	Face Centred Cubic
FEG	Field Emission Gun
FEM	Finite Element Method

FFT	Fast Fourier Transform
FIB	Focused Ion Beam
FluidFM BOT	Specialized Robotic Fluid Force Microscope
FS	Force Spectroscopy
FTO	Fluorine-doped Tin Oxide
GC	Glassy Carbon
GDML	Geometry Description Markup Language
GFR	Gas-Cooled Fast Reactor
GILD	Gas Immersion Laser Doping
GINOP	Economic Development Innovation and Operative Program
GLE	Ground Level Enhancement
GM	Geiger–Müller
GMCS	Graphene Added Multilayer Ceramic Sandwich
GPU	Graphics Processing Unit
GRAS	Geant4 Radiation Analysis for Space
GSTP	General Support Technology Programme
HAADF	High-angle Annular Dark-field
Hap	Hydroxyapatite
HIP	Hot Isostatic Pressing
HLW	High-level Radioactive Waste
HOPG	Highly Oriented Pyrolytic Graphite
HP	Hot Pressing
HPGe	High-purity Germanium
HPT	High Pressure Torsion
HRTEM	High Resolution Transmission Electron Microscopy
HSA	Human Serum Albumin
HV	High Voltage
IAEA	International Atomic Energy Agency
IBM	Ion-beam Mixing
IBMP	Institute for Biomedical Problems, Moscow
ICP-MS	Inductively Coupled Plasma Mass Spectrometry
ICP-OES	Inductively Coupled Plasma Optical Emission Spectrometry
IFFT	Inverse Fast Fourier Transition
ILL	Institut Laue-Langevin
ILW	Intermediate Level Waste
INCLUDING	INnovative CLUster for raDIological and Nuclear emerGencies
INSIDER	Improved Nuclear Site characterisation for waste minimisation In Decommissioning and dismantling operations under constrained EnviRonment
InvOLS	Inverse Optical Lever Sensitivity
IOD	In-Orbit Demonstration
IoT	Internet of Things
IPERION CH	EU Funded Project (Integrated Platform for the European Research Infrastructure ON Cultural Heritage)
IPF	Inverse Pole Figure
IR	Infrared
ISO	International Organization for Standardization
ISS	International Space Station
ITO	Indium Tin Oxide
KFKI	Former Name of the Research Centre, Nowadays the Campus Name
KIKO3DMG	Nodal Reactor Physics Calculation Code Developed in the CER
KIT	Karlsruhe Institute of Technology
KVSZ	Environmental Protection Service (Hungarian acronym)
LDOS	Local Density of States
LEL	Lower Explosion Limit
LET	Linear Energy Transfer

LLW	Low Level Waste
LOC	Lab-on-a-Chip
LOCA	Loss of Coolant Accident
LSC	Liquid Scintillation Counting
LTO	Long Term Operation
MAT	Magnetic Adaptive Testing
MCB	Moiré Commensurate Bilayer
MCBJ	Mechanically Controlled Break Junctions
MCC	Multilayer Ceramic Composite
MCD	Multi-criteria Decision
MCNP	Monte Carlo N-Particle Transport Code
MCNPX	Monte Carlo N-Particle eXtended
MELODI	Multidisciplinary European Low Dose Initiative
MEMS	Microelectromechanical System
MFA	Institute of Technical Physics and Materials Science (Hungarian acronym)
MIC	Minimum Inhibitory Concentration
MLG	Multi-layered Graphene
MOX	Mixed Oxide
MS	Mass Spectrometry or Mössbauer Spectroscopy or Member States
MU	Mock-ups
EK	Centre for Energy Research (Hungarian acronym)
MWCNT	Multiwall Carbon Nanotube
MU	Mock-up
MVM	Hungarian Power Companies
NAA	Neutron Activation Analysis
NAL	Nuclear Analysis and Radiography Department, MTA EK
ND	Neutron Diffraction
NDE	Non Destructive Evaluation
NEAAA	Neutron-based Element Analysis and Activation Assessment
NIPS	Neutron Induced Prompt Gamma-ray Spectroscopy
NIPS-NORMA	Neutron-Induced Prompt Gamma-ray Spectroscopy & Neutron Optics and Radiography for Material Analysis
NIR	Near InfraRed
NKFIH	National Research, Development and Research Office (Hungarian acronym)
NMR	Nuclear Magnetic Resonance
NMX	Neutron Macromolecular Diffraction
NNKP	National Nuclear Research Program (Hungarian acronym)
NOMAD	Non-destructive Evaluation System for the Inspection of Operation-Induced Material Degradation in Nuclear Power Plants (EU H2020 project)
NP	Nanoparticle
NPP	Nuclear Power Plant
NR	Neutron Radiography, Nanorod
NR/NT	Neutron Radiography and Tomography
NS	Nanosphere
NUBIKI	Nuclear Safety Research Institute
O&M	Operation and Maintenance
OAH	Hungarian Atomic Energy Authority (Hungarian acronym)
ODS	Oxide Dispersion Strengthened
OECD	Organisation for Economic Co-operation and Development
OTKA	Hungarian Scientific Research Fund (Hungarian Acronym)
OWLS	Optical Waveguide Light Mode Spectroscopy
Paks NPP	Paks Nuclear Power Plant
PBI	2,2'-(2-pyridyl)benzimidazole
PCA	Principal Component Analysis
PCB	Printed Circuit Board

PD	Prisoner's Dilemma
PDMS	Polydimethylsiloxane
PE-ALD	Plasma Enhanced Atomic Layer Deposition
PEG	Polyethylene Glycol
PFM	Protoflight Model
PGAA	Prompt-gamma Neutron Activation Analysis
PGAI	Prompt-gamma Activation Imaging
PGAI-NT	Prompt-gamma Activation Imaging – Neutron Tomography
PL	Power-Law
PLA	Polylactic Acid
PoC	Point of Care
PPKE	Pázmány Péter Catholic University (Hungarian acronym)
PSD	Position Sensitive Detector
PSF	Photon Strength Function
PURAM	Public Limited Company for Radioactive Waste Management
PXRD	Powder X-ray Diffractometry
pXRF	Portable XRF Spectrometer
PWR	Pressurized Water Reactor
RAD	Static/dynamic Thermal-neutron and X-ray Imaging Station at BNC
RADACT	Alpha Particle – Epithelial Cell Interaction Model
RADCUBE	A Joint Mission Name of the ESA
RadMag	Instrument for Measuring Space Radiation and Magnetic Field Parameters
RBC	Red Blood Cell
RBS	Rutherford Backscattering Spectrometry
REXUS/BEXUS	Rocket and Balloon Experiments for University Students
RF	Radio Frequency
RID	Radioisotope Identification Detector
RM	RadMag
RMC Method	Reverse Monte Carlo Method
RMS	Root Mean Square
RPV	Reactor Pressure Vessel
RT	Room Temperature
SAA	South Atlantic Anomaly
SAED	Selected Area Electron Diffraction
SAFEST	EU Funded Project: Severe Accident Facilities for European Safety Targets
SANS	Small Angle Neutron Scattering
SAXS	Small Angle X-ray Scattering
SBO	Station Blackout
SBR	Signal-to-Background Ratio
SCK•CEN	Belgian Nuclear Research Centre
SCFS	Single-Cell Adhesion Forces
SD	Snowdrift Quadrant
SE	Spectroscopic Ellipsometry
SEM	Scanning Electron Microscopy
SERS	Surface Enhanced Raman Spectroscopy (or scattering)
SH	Stag-Hunt
SINE2020	EU Funded Project: Science and Innovation with Neutrons in Europe in 2020
SINAC	Simulator Software for Interactive Consequences of Nuclear Accidents
SLM	Stochastic Lung Model
SMAD	Solvated Metal Atom Deposition
SMPS	Scanning Mobility Particle Sizers
SOD	Superoxide Dismutase
SO GL	System Operational Regulation Guidelines
SOI	Silicon-on-Insulator
SPR	Surface Plasmon Resonance

SPS	Spark Plasma Sintering
SPV	Sulfo-phospho-vanillin
SRA	Strategic Research Agenda
SSNTD	Solid State Nuclear Track Detector
SURET	SUBchannel REactor Thermohydraulics
STEM	Scanning Transmission Electron Microscopy
STEM HAADF	Scanning Transmission Electron Microscope High-Angle Annular Dark-Field
STM	Scanning Tunnelling Microscopy
STS	Scanning Tunnelling Spectroscopy
SWE	Space Weather Service Network
SWV	Square Wave Voltammetry
TDC	Time-to-Digital Conversion
TEM	Transmission Electron Microscopy
TENORM	Technologically Enhanced Naturally Occurring Radioactive Materials
TÉT	Bilateral Research Program (Hungarian acronym)
TG	Thermogravimetric
TL	Thermoluminescent
TLD	Thermoluminescent Dosimeter
TLG	Trilayer Graphene
TMCs	Transition Metal Chalcogenides
TMP	Turbomolecular Pump
TNA	Technology Needs Assessment Project, Transnational Access
TO	Transistor Outline
TOC	Total Organic Carbon
TOF-ND	Time of Flight Neutron Diffraction
TPO	Temperature Programed Oxidation
TPR	Temperature Programmed Reduction
TQCM	Thermoelectric Quartz Crystal Microbalances
T-VAC	Thermal-Vacuum Test
TXRF	Total-reflection X-ray Fluorescence
UHV	Ultra-High Vacuum
UOX	Uranium Oxide
UV-VIS	Ultraviolet-Visible (Spectroscopy)
VERONA	Reactor Core Monitoring and the Reactivity Measurement System for VVER Type NPPs
VOC	Volatile Organic Compounds
VVER	Water-Cooled Water-Moderated Energetic Reactor, Russian acronym
XANES	X-ray Absorption Near Edge Structure
XAS	X-ray Absorption Spectrometry
XAFS	X-ray Absorption Fine Structure
XPS	X-ray Photoelectron Spectroscopy
XRD	X-ray Diffraction
XRF	X-ray Fluorescence Analysis
XTEM	Cross-sectional Transmission Electron Microscopy
WG	Work Group
WI	Wet Impregnation
Wigner FK	Wigner Research Centre for Physics
ZFC	Zero Field Cooling

IMPRINT

Editors

*László Redler
Attila R. Imre*

Lector

*Ferenc Szlávik
Jesse Weil*

Publisher

*Ákos Horváth
Tamás Belgya
Centre for Energy Research
H-1121, Budapest, Konkoly Thege M. út 29-33.
Hungary*

Design

Anikó Jécsai

Picture credits

Centre for Energy Research,

Accessibility

<http://www.energia.mta.hu/>

Contact

*Centre for Energy Research, Hungarian Academy of Sciences
Location: KFKI Campus 29-33 Konkoly-Thege Miklós street 1121 Budapest, Hungary
Mailing address: 1525 Budapest 114., P.O. Box 49., Hungary
Phone: (+36 1) 395 91 59 **Fax:** (+36 1) 395 92 93
E-mail addresses: info@energia.mta.hu*



